

PHYSICS OF MAGNETIC FLUX COMPRESSION USING PLASMA ARMATURES USING FINITE DIFFERENCE TIME DOMAIN METHOD

By

Sijoy C. D.

Enrolment No: PHYS01200804008

**BHABHA ATOMIC RESEARCH CENTRE, VISAKHAPATNAM
INDIA**

*A thesis submitted to the
Board of Studies in Physical Sciences*

*In partial fulfillment of requirements
For the Degree of*

DOCTOR OF PHILOSOPHY

of

HOMI BHABHA NATIONAL INSTITUTE



Nov 2013

Homi Bhabha National Institute

Recommendations of the Viva Voce Board

As members of the Viva Voce Board, we certify that we have read the dissertation prepared by **Sijoy C. D.** entitled "Physics of magnetic flux compression using plasma armatures using finite difference time domain method" and recommend that it may be accepted as fulfilling the dissertation requirement for the Degree of Doctor of Philosophy.

----- A. K. Das ----- Date : _____

Chairman : Dr. A. K. Das, BARC, Mumbai

----- A. Chaturvedi ----- Date : 29/11/13

Convener : Dr. Shashank Chaturvedi, BARC, Visakhapatnam

----- Anurag Shyam ----- Date : 20/11/13

Member : Dr. Anurag Shyam, BARC, Visakhapatnam

----- R. Srinivasan ----- Date : _____

Member : Dr. R. Srinivasan, IPR, Gandhinagar

----- Manjit Singh ----- Date : 20/11/2013

External Examiner : Dr. Manjit Singh, TBRL, Chandigarh

Final approval and acceptance of this dissertation is contingent upon the candidate's submission of the final copies of the dissertation to HBNI.

I hereby certify that I have read this dissertation prepared under my direction and recommend that it may be accepted as fulfilling the dissertation requirement.

Date: 20/11/13

Guide: A. Chaturvedi

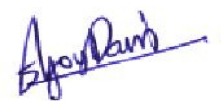
Place: MUMBAI

(Dr. Shashank Chaturvedi)

STATEMENT BY AUTHOR

This dissertation has been submitted in partial fulfillment of requirements for an advanced degree at Homi Bhabha National Institute (HBNI) and is deposited in the Library to be made available to borrowers under rules of the HBNI.

Brief quotations from this dissertation are allowable without special permission, provided that accurate acknowledgement of source is made. Requests for permission for extended quotation from or reproduction of this manuscript in whole or in part may be granted by the Competent Authority of HBNI when in his or her judgment the proposed use of the material is in the interests of scholarship. In all other instances, however, permission must be obtained from the author.



Sijoy C. D.

DECLARATION

I, Sijoy C. D., hereby declare that the investigation presented in the thesis has been carried out by me. The work is original and the work has not been submitted earlier as a whole or in part for a degree/diploma at this or any other Institution or University.

A handwritten signature in blue ink, appearing to read 'Sijoy C. D.', with a horizontal line extending to the right.

Sijoy C. D.

CERTIFICATION FROM GUIDE

This is to certify that the corrections suggested by the examiners of the thesis have been incorporated in the thesis submitted to HBNI

Date: 20/4/13

Guide:*A. S. Chaturvedi*.....

(Dr. Shashank Chaturvedi)

To my family...

ACKNOWLEDGEMENTS

First and above all, I Thank God, the Almighty for His blessings throughout my life and for granting me this opportunity and the ability to successfully complete this study.

This thesis appears in its current form due to the assistance, guidance and support of several people. It is my pleasure to offer my sincere thanks to all of them. I apologize in advance for any omissions.

I feel honoured to express my sincere gratitude to my supervisor Dr. Shashank Chaturvedi for his thoughtful guidance, critical comments, constant support and excellent advices throughout this period. I offer my special thanks to him for patiently revising the thesis and several manuscripts related to this work. I also thank him for teaching me various numerical techniques related to the hydrodynamics simulation during the early days of my career.

Special acknowledgment is due to the Chairman of the Doctoral Committee Dr. A. K. Das for his critical suggestions to improve the quality of this work. I also thank other members of my Doctoral Committee, Dr. Anurag Shyam and Dr. R. Srinivasan for their support and valuable suggestions in my annual reviews.

Special thanks are due to the administrative and Academic staff of the HBNI and particularly to Dean Academic Physical Sciences Dr. B. N. Jagatap for their assistance.

I take this opportunity to thank my colleagues in CAD, BARC Visakhapatnam for their support and valuable comments. My special thanks to Vinayak Mishra, Gursharn Singh, Sunil Rawat, and Rohit Shukla for their help.

Some of the simulations reported in this thesis required large computing power

and were carried out on a parallel computing facility set up by the Computational Analysis Division (CAD) in BARC Visakhapatnam. I am thankful to N. Sakthivel and the High Performance Computing (HPC) Team of CAD for their assistance in parallel computing.

I would like to offer my special regards to my friends of IPR, Jinto Thomas and P. V. Subhash for their constant moral support and many fruitful discussions.

Most importantly, I express my thanks to my wife Sherin and son Leonel for their immense patience, understandings, encouragement, love and support.

My deepest gratitude goes to my parents and my brother for their unflagging love and support throughout my life. I am indebted to my parents for everything they have done for my education and for constantly providing me the much needed moral and emotional support at every stage. It is only because of their love, affection and blessings that I could complete this thesis.

Finally, I express my gratitude to all persons who have not been listed here but helped to complete this work.

A handwritten signature in blue ink, appearing to read 'Sijoy C. D.', with a horizontal line extending to the right.

Sijoy C. D.

Abstract

Various schemes have been analysed over the years for extracting energy from Inertial Fusion Energy systems such as laser-driven fusion. The method examined here is to directly convert a part of the plasma kinetic energy into pulsed electrical energy, through the medium of magnetic flux compression. The present work involves a computational study of the physics of flux compression inside a current-carrying coil by an expanding inertial fusion plasma sphere. The numerical analysis has been performed using two-dimensional MHD and FDTD simulations.

The overall efficiency of the system is determined numerically for a typical set of initial plasma and system parameters. It is found that the proposed system is promising in terms of overall efficiency, but the system produces ultrahigh inter-turn voltages in the coil, necessitating the use of magnetic self-insulation to avoid inter-turn breakdown.

The plasma sphere, expanding across a magnetic field, is subject to the Magnetic Rayleigh-Taylor (MRT) instability. For a detailed analysis of this concept, especially plasma dynamics under large deformations, a two-dimensional Eulerian multi-material MHD model has been developed for the first time. The algorithm is found to be capable of accurately handling complex plasma dynamics inside the MFC system. Magnetic field diffusion into the plasma during the expansion phase is found to be negligible. 2D MHD simulations of random, single and multi-mode MRT instability growth have been performed to analyze the MRT instability and its implications for the proposed MFC system. The simulation takes into account the effects of MFC and geometric divergence due to spherical plasma expansion. The dominant modes obtained in the random seed analysis show a progressive transition to the intermediate wavelength regime ($\sim 4-8$ cm) in the spectrum. Single-mode evolution exhibits linear exponential growth followed by a non-linear phase towards stagnation time. In the multi-mode analysis, with initial amplitudes

(α_{in}) comparable to the perturbation wavelength (λ_{in}), there is clear evidence of mode coupling and the generation of harmonic and inverse cascade modes. We also find that near the time of stagnation, the growth in amplitude of the modes, although exponential in nature, is much lower than that predicted by linear theory. Furthermore, the instability amplitudes are not large enough for $\alpha_{in} \leq 0.1\lambda_{in}$ to severely disturb the smooth MFC during the first expansion phase. However, the growth of modes with $\alpha_{in} \geq \lambda_{in}$ causes plasma jetting, especially for longer λ modes, and can lead to significant reduction in MFC efficiency.

We have also investigated the application of finite difference time domain (FDTD) schemes, involving direct solution of Maxwell's equations. The FDTD algorithm has been modified, for the first time, by including motional e.m.f terms in the standard FDTD update equations. This algorithm can be applied to MFC systems with moving parts. This new approach is validated with standard analytical solutions for planar flux compression systems and magnetic field diffusion in moving conductors with non-relativistic velocity. Finally, in order to demonstrate the utility of this powerful scheme to MFC problems, we have applied it to a sample problem involving plasma armatures. To our knowledge, this is the first application of this powerful technique to such systems. We have also identified, through extensive numerical tests, critical constraints that must be satisfied while performing magnetic diffusion problems using FDTD scheme.



Homi Bhabha National Institute

Ph.D. PROGRAMME

1. Name of the Student:	Shri Sijoy C. D.
2. Name of the Constituent Institution:	Bhabha Atomic Research Centre
3. Enrolment No.:	PHYS01200804008
4. Title of the Thesis:	Physics of magnetic flux compression using plasma armatures using finite difference time domain method
5. Board of Studies:	Physical Sciences

SYNOPSIS

Introduction

Magnetic flux compression (MFC) generators [1–7] convert the chemical energy of explosives into high-power electrical pulses through the compression of magnetic flux. These systems typically consist of a high-explosive charge contained inside a metallic conductor (“armature”). Detonation of the explosive produces high-pressure gases, which cause the armature to expand outward at a high velocity. The armature is subjected to an externally-imposed magnetic field, e.g. by being placed inside a current-carrying solenoid. Since the armature is a good electrical conductor, it pushes against the magnetic field and compresses the magnetic flux into a smaller space. This *magnetic flux compression* leads to amplification of the electrical energy in the solenoid. The net result is that the chemical energy of the explosive is partially converted into output electrical energy. MFC generators have

found widespread use as pulsed power sources for a broad range of applications such as fusion, electromagnetic accelerators, high-power micro-wave (HPM) sources, laser, electron, ion, or neutron sources, high magnetic field research and many others.

Most existing MFC devices use solid metal armatures to compress the magnetic field, although the use of imploding liquid and plasma liners has also been explored [8–13]. for the generation of high magnetic fields.

In Inertial Fusion Energy (IFE) systems, such as laser-driven fusion, the implosion and burn process produces a *fireball* consisting of a high-density, high-temperature plasma. Several schemes have been examined for converting the thermal and kinetic energy of this fireball into electrical energy [14–20]. Since the IFE plasma fireball is a good electrical conductor, it could, in principle, act as an armature in an MFC system. Plasma armatures can expand much faster than metal armatures, yielding shorter-duration electrical pulses and higher flux efficiencies. On the other hand, the expanding plasma could be subject to MHD instabilities due to its interaction with the magnetic field.

Hence it is necessary to perform a detailed numerical study of the interaction between the IFE fireball and an externally-imposed magnetic field. The objective of this thesis work is to computationally examine the physics of expanding plasma armatures using numerical schemes based on MHD as well as Finite Difference Time Domain (FDTD) approaches.

The following studies have been performed in this thesis:

- *Development of a Lagrangian MHD scheme coupled self-consistently with external circuit equations for the analysis of MFC inside a solenoid driven by a fusion plasma sphere.*
- *Preliminary analysis of the conversion of plasma energy into pulsed electrical energy using the above mentioned MHD scheme.*

- *Development of an Eulerian MHD model using volume-of-fluid material interface tracking for studying the plasma dynamics across the magnetic field.*
- *The study of large-deformation plasma dynamics in the proposed MFC system using an Eulerian MHD model.*
- *Analysis of magnetic Rayleigh-Taylor instability in a MFC system driven by fusion plasma sphere.*
- *Development and validation of computational algorithms relevant to MFC systems based on the FDTD scheme for electromagnetics.*
- *Application of FDTD scheme for electromagnetics for the analysis of MFC by an expanding cylindrical plasma.*

The important work carried out and the major results of the thesis are summarized below.

1. MFC inside a solenoid by an expanding fusion plasma sphere and its application as a direct energy conversion scheme

Introduction and Motivation

In this chapter, we report on a conceptual study of magnetic flux compression inside a solenoid by an expanding IFE plasma sphere. The plasma expands across the magnetic field produced by the coil itself. The study has been performed numerically using two-dimensional magneto-hydrodynamic (MHD) simulations. The basic idea is to use a conducting surface (a solenoid in this work) enclosing an expanding diamagnetic plasma expanding across an external magnetic field. The external magnetic field will be excluded by the diamagnetic plasma due to currents produced in the plasma. The inductive

electromotive force (e.m.f) induces currents in the shielding conductor and thus convert the plasma kinetic energy into electrical energy. Fig. 1 shows a schematic of the proposed MFC system.

Earlier work in this area [14–17] had considered separate coils for producing the primary field and for carrying the induced (output) currents. The present study is the first to consider a single coil. Similarly, Ref. [14] analyses a different plasma parameter range, starting with an initial radius of ~ 1 m and system dimensions of ~ 14 m in radius. Since the pickup coil is located at a radius of ~ 9 m, a low initial magnetic field is sufficient to stop the plasma close to the coil radius. Therefore, a magnetic field of ~ 0.57 T is used in Refs. [14]. We have examined the case of a much smaller system having a radius ~ 1.5 m, a higher-pressure plasma ($\sim 10^7$ Pa) with an initial radial expansion velocity $\sim 10^7$ m/s, which requires a higher magnetic field (5 T) to extract enough energy from the plasma.

We examine the dynamics of plasma expansion across the magnetic field and the energy conversion efficiency. We start our simulation from the time when plasma is created and the initial magnetic field is setup. The initial plasma conditions are chosen from earlier published works for a D-3He fusion plasma with energy of 140 MJ with mass ~ 6 mg. Although the required ignition energy is substantially higher for D-3He, the reaction products will consist predominantly of charged particles, which can be electromagnetically manipulated. The initial magnetic field is varied from 2 to 10 Tesla. The coil radius and length were taken as 1.5 m and 2-3 m respectively.

Results and conclusions of this study

- During the expansion phase, the characteristic scale length of the plasma is much larger than the ion skin-depth and orbit radius. Hence plasma

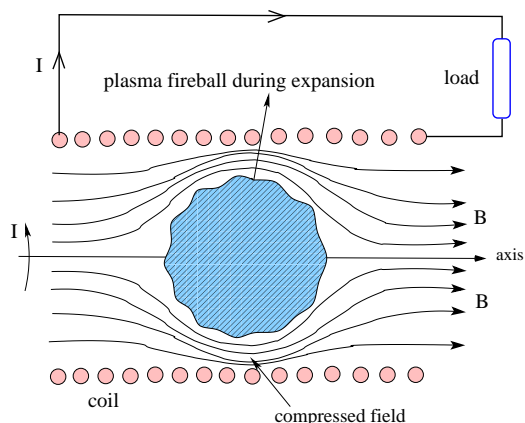


Figure 1: Schematic showing magnetic flux compression during expansion phase (not to scale).

dynamics is modeled using single fluid MHD equations assuming quasi-neutrality in plasma. A 2D-Lagrangian code has been developed and validated to solve the governing two-dimensional MHD equations. The code has an explicit finite-difference scheme for hydrodynamic equations. A filamentary model [21,22], which includes the effect of plasma dynamics, is used to update the coil current and the induced currents in the plasma.

- The plasma dynamics and the efficiency of the proposed system with different inductive and resistive load conditions are studied numerically. An overall efficiency $\sim 56\%$ is obtained with an inductive load having an inductance ~ 1 mH for a typical system (coil radius = 1.5 m and length ~ 4.5 m and initial magnetic field ~ 5 T) and plasma parameters (energy 140 MJ and mass ~ 6 mg) considered.
- However, ultra-high inter-turn voltages ~ 25 MV are predicted across the coil turns. Therefore, the feasibility of magnetic self-insulation for avoiding coil inter-turn break-down has been examined. It has been found that breakdown could indeed be prevented by self-insulation for

the parameter range considered here. We have also found that the inter-turn voltages can be reduced with increased operational time (by decreasing initial \vec{B} and increasing coil radius). For example, with an increase of 33 % in coil radius, with an initial magnetic field of 3.8 T and coil length equal to three times the coil radius, the inter-turn voltage decreases to 19 MV ($E=95$ MV/m); corresponding to a 42% reduction in the voltage and a reduction in inter-turn electric field by 2.8 times.

- The variation of plasma stopping radius with different applied external magnetic fields has been calculated numerically and compared with a simple analytical expression. Reasonable agreement is found, except for cases with low initial magnetic fields. The difference in results, especially for low magnetic field cases, is due to the fact that the analytical expression neglects the effect of field amplification, leading to over-estimation of the stopping radius. This effect is more significant for cases with low initial magnetic fields, where the radial plasma expansion is higher, leading to considerable difference between initial and final magnetic fields.
- It is observed that during the final stage of MFC, the plasma shape becomes distorted (non-spherical) due to non-uniform deceleration caused by the magnetic field outside the plasma sphere. In particular, there is elongation of the plasma in the axial direction. These effects, collectively, lead to a non-spherical expansion of the plasma with large deformation.

To the best of our knowledge, this is the first analysis of an MFC system driven by an IFE plasma, conducted with an MHD scheme self-consistently coupled to external circuit equations.

This work has been published in [23].

2. Development of an Eulerian MHD model using volume-of-fluid material interface tracking and its application to study the plasma dynamics in an MFC system

Introduction and motivation

Numerical studies described in the last section (Ref. [23]) have shown that plasma expansion in an MFC system is highly non-uniform due to magnetic deceleration. In particular, the plasma exhibits non-spherical expansion, i.e., axial expansion of the plasma is higher than radial expansion. Towards the end of the expansion phase, Magnetic Rayleigh-Taylor (MRT)-like instabilities are observed at the plasma surface. Under conditions where such instabilities reach large amplitudes, there are large distortions of the plasma shape, hence Lagrangian algorithms fail. In order to study these effects in detail, it is necessary to develop an Eulerian MHD model.

Important work, results and conclusions of this study

- We have developed and validated an Eulerian multi-material algorithm with Volume-of-Fluid (VOF) based material interface tracking. The algorithm is capable of handling large material deformations. A Volume-weighted averaging technique is used to handle mixed computational cells.
- The Eulerian code is then extended to MHD form. The magnetic induction equation is solved implicitly using magnetic vector potential. An iteration procedure using Alternating Direction Implicit (ADI) scheme is used for free space field calculation. The fields are transported using a second order MUSCL scheme.

- The validated algorithm is applied to study the dynamics of plasma inside an MFC system described in the last section. We start with a spherically-symmetric initial plasma, which means that the MRT instability is seeded by numerically-generated perturbations. Simulations indicate the development and evolution of MRT instabilities at the plasma-vacuum interface near stagnation time, i.e., close to the time when the outer surface comes to a halt. The wavelength of this perturbation is found to be ~ 6.8 cm. In the $r - z$ plane, these instabilities are more marked near the center of the solenoid where the magnetic deceleration is comparatively higher.
- The plasma sphere forms a shell-like geometry near the stagnation point as the outer surface slows down due to \vec{B} and the inner region catches up with the outer surface. The resulting high temperature plasma region has high electrical conductivity. Therefore the \vec{B} diffusion into the plasma is found to be negligible even around stagnation time.

This work has been published in [24–25].

3. Analysis of magnetic Rayleigh-Taylor instability in an MFC system driven by plasma armatures

Introduction and motivation

In the previous sections, we have described the direct energy conversion scheme to convert plasma kinetic energy in an IFE system into pulsed electrical energy [23,24]. Preliminary numerical studies [23,24] indicate that the proposed system, with an inductive load, is promising in terms of overall conversion efficiency. However, such a plasma, expanding across a magnetic field, is subject to the Magnetic Rayleigh Taylor (MRT) instability. The

MRT instability occurs when an electrically conducting fluid, e.g. plasma, is decelerated or supported by the magnetic field. For efficient operation of the proposed MFC system [23,24], the instability amplitude must remain small so that the irregular surface, caused by growth of the MRT instability, does not disturb the smooth compression of the magnetic field between the plasma and solenoid. Large amplitude flute modes and plasma jetting can damage the cavity wall [14].

The majority of numerical and experimental studies performed by other workers on plasma expansion in an external magnetic field consider a uniform background magnetic field. This means that magnetic field increase due to flux compression are ignored. This is not valid in MFC systems examined here.

Ref. [14] has examined the problem of plasma energy conversion, taking into account the role of MFC. The system examined in the present work differs from Ref. [14] in several respects. Firstly, Ref. [14] analyses a different parameter range, starting with an initial radius of ~ 1 m and system dimensions of ~ 14 m in radius. Since the pickup coil is located at a radius of ~ 9 m, a low initial magnetic field is sufficient to stop the plasma close to the coil radius. Therefore, a magnetic field of ~ 0.57 T is used in Ref. [14]. In our last study [23,24], we had examined the case of a much smaller system having a radius ~ 1.5 m, a plasma with higher initial pressure ($\sim 10^7$ Pa) and having an initial radial expansion velocity $\sim 10^7$ m/s, which requires a higher magnetic field (5 T) to extract enough energy from the plasma.

Secondly, the simulation results given in Ref. [14] start with an unperturbed initial plasma state, so that instabilities are seeded by numerically-produced perturbations. This was also the case in our last study [24]. In reality, perturbations with different wavelengths and amplitudes would exist on the

surface of the plasma sphere even before it starts expanding. For a real-life system, therefore, it is necessary to study the growth of pre-existing perturbations with different wavelengths and amplitudes.

In the present section, therefore, the study has been done for different cases of applied initial perturbations (different wavelengths and amplitudes), taking into account the effects of magnetic field amplification (time dependent g) and the geometric divergence due to spherical plasma expansion. The purpose of this study is to numerically analyze, using MHD fluid simulations, the MRT instability on the surface of the plasma liner and its implications for the proposed MFC system. The initial plasma parameters are taken from earlier published data for D-3He plasma. The plasma energy E_p and mass m_p used in this study are 280 MJ and 4.4 mg respectively [14–17,27,28]. The value of seed magnetic field \vec{B} used in the simulation is 5 T and the system parameters are taken from Refs. [23,24].

Important work, results and conclusions of this study

In Ref. [23], we had developed a pure Lagrangian MHD scheme, self consistently coupled with external circuit equations, to solve the governing equations. That scheme, however, is not suitable for the present study as large material deformations are expected. In such situations, the pure Lagrangian scheme fails just around the time the problem becomes interesting, i.e., when plasma deformation becomes significant. Consequently, in Ref. [24] we have formulated an Eulerian MHD scheme with volume-of-fluid material interface tracking [25] to handle large plasma deformations in the MFC system. However, for the present study, it demands a prohibitively large number of cells in the simulation. This is due to an order of magnitude difference between the different scale lengths involved in the system, such as MFC system di-

mensions of the order of few meters, plasma initial perturbation amplitude α_{in} of the order of few μm and wavelength λ ranging from few mm to cm. Note that for numerical convergence with respect to the mesh size, at least 10–20 cells per λ are required. This demands an unacceptably large number of computational cells in the simulation.

In this work, therefore, we have used an unstructured Lagrangian scheme [29] with sub-zonal mass and pressure [30] to control artificial grid distortion and hourglass type motion. Further, to stabilize the grid a node based tensor viscosity [31] and an artificial grid distortion control algorithm [30] are used. This allows us to simulate the plasma evolution till the stagnation or turn-around time t_s (the time at which the plasma radial expansion halts) without leading to numerical instability. Approximately at this time the inductive energy across the load goes to maximum [23,24]. Therefore, in the present work, we are only interested in studying the evolution of MRT instability till the stagnation time. We have obtained a substantial reduction of the overall computational time with the help of an unstructured Lagrangian scheme, since the total number of cells required in the simulation are considerably reduced.

The following are the important works, results and conclusions of this study.

- We have developed an unstructured Lagrangian scheme [29] with sub-zonal mass and pressure [30] to control artificial grid distortion and hourglass type motion. Further, to stabilize the grid a node based tensor viscosity [31] and an artificial grid distortion control algorithm [30] are used.
- Two-dimensional MHD simulations of random, single and multi-mode perturbation growth in an MFC system driven by a fusion plasma sphere have been carried out for different initial perturbation amplitudes and

wavelengths. The simulation takes into account the effects of magnetic flux compression and geometric divergence due to spherical plasma expansion.

- In the random seed perturbation analysis, we have found that the dominant modes in the spectrum show a progressive transition from the short-wavelength to the intermediate-wavelength regime, $\lambda \sim 4\text{--}8$ cm – this is consistent with the observations in Ref. [24]. The cross-correlation analysis indicates the mode coupling between dominant modes and other modes in the spectrum.
- The multi-mode (sinusoidal) analysis, with two different fundamental modes (say n_1 & n_2) and with $\alpha_{in} \sim 500$ μm , shows the appearance of higher harmonics of the individual modes, as well as the shorter wavelength ($n_1 + n_2$) and higher wavelength inverse cascade ($n_2 - n_1$) modes created by non-linear interaction of fundamental and harmonic modes. This indicates that the modes upon saturation exhibits strong interaction with other modes in the spectrum.
- In the case of single-mode perturbation, the modes continue to grow exponentially with nearly constant γ and make a transition into the non-linear phase (mode saturation). That is the amplitude growth of the modes towards stagnation time, although exponential in nature, is lower than the growth predicted by linear theory.
- We also note that extremely large flute structures and plasma jetting, which could damage or reach the cavity-wall/coil and to severely disturb the smooth compression of the magnetic field, are not seen during the time period of our interest, viz., the first expansion phase of the plasma. This means that it is feasible to have efficient flux compression during the first expansion phase in the proposed system, for perturba-

tion amplitudes $\alpha_{in} \leq \lambda_{in}/10$. However, for $\alpha_{in} \geq \lambda_{in}$, the instability amplitudes are large enough, especially for longer λ modes, to cause plasma jetting leading to significant reduction in the flux compression efficiency.

This work has been published in [32] and some part of this work has been presented in [33].

4. **Development, validation and application of finite-difference time-domain (FDTD) schemes for electromagnetics based on first principle calculations to MFC systems**

Introduction and motivation

Numerical simulations of MFC systems with solenoids as stator/pick-up coil require accurate calculations of the inductance and resistance of complex geometries, such as arbitrarily-wound helical coils. Analytical, closed-form expressions are available, and have long been used, for calculating the coil resistance, taking into account skin and proximity effects [34–36]. However, for an arbitrarily-wound coil, involving a variable pitch, turn splitting and inter-turn potting, calculation of the proximity and skin effects is complicated by a complex geometry and the presence of multiple materials, conductors as well as dielectrics. One example of such a dielectric is the inter-turn potting material. Even if these factors were not a consideration, the analytical methods are applicable for a single frequency, while flux compression systems typically involve complex temporal waveforms which cannot be approximated by a single frequency. To our knowledge, none of the closed-form expressions can handle these complexities.

The most general method is to solve the magnetic field diffusion equation for

the system [38]. Such a solution yields the spatio-temporal distribution of the magnetic field, and hence the current density, throughout the domain, from which the resistance can be calculated. However, the electrical conductivity, and hence the magnetic field diffusion coefficient, can vary by orders of magnitude through the coil assembly. This leads to numerical problems in obtaining this solution using “standard” solvers for such equations. In particular, the inter-turn insulation has a near-infinite magnetic field diffusion coefficient, requiring a near-zero timestep. This last problem can be handled by using flux-limited transport, but the problem of small timesteps remains. The problem is further complicated by imperfectly-known boundary conditions for the magnetic field. There is thus a need for a more general method that can handle real-life problems with all the complexities listed earlier.

We have used the Finite Difference Time Domain (FDTD) method for electromagnetics [37] to handle such problems. This method directly updates Maxwell’s curl equations in time, using an explicit algorithm, to yield spatial variation of electric and magnetic fields. It allows setting up of complex, multi-material configurations. Furthermore, the time domain analysis allows handling of arbitrary time-dependent waveforms of current. This technique thus allows a study of real-life configurations with practically no limitations on the geometric complexity, the materials used or the temporal waveforms. **To our knowledge, this is the first application of this powerful technique to such systems.**

The objective of the work described in this section is the development and validation of a computational tool using FDTD method for electromagnetics for studying various phenomena (magnetic diffusion and flux loss, skin and proximity effects in stator coils, inclusion of motional e.m.f terms in standard FDTD equations for studying magnetic induction in moving conductors, etc)

in MFC systems.

- (a) **Step-1:** A computational tool using 3D-FDTD method for electromagnetics is developed to calculate accurate resistance and inductance of arbitrarily wound helical coils of interest in MFC systems. For this a FDTD method for electromagnetics, which is adapted for magnetic-field diffusion problems, has been developed. The simulations have been performed using a locally developed 3D variable-mesh FDTD code. The resistance calculations automatically take account of skin and proximity effects and are capable of handling arbitrarily complex multi-material systems. The simulations also yield a detailed 3D picture of magnetic field diffusion through a complex multi-material coil in the presence of arbitrary time dependent current waveforms. Hence these methods can provide critical insight into coil performance in real-life MFC systems.
- (b) **Step-2:** MFC systems involve the motion of the conductors (liner or armature) across the magnetic field. The FDTD calculations performed so far include only the coil (stator); the inclusion of material movement in standard FDTD equations is, therefore, necessary. Worldwide, the FDTD algorithms for electromagnetics are used mainly for static problems.

Therefore, we have developed a new 2D-FDTD algorithm for electromagnetics by including motional e.m.f terms in standard FDTD update equations, which can be applied to flux compression systems with moving parts. Material movement is implemented by continuously changing material properties in each computational cell consistent with material advection. The magnetic flux carried by the moving conductors in a fixed Eulerian mesh is transported using a flux corrected transport (FCT) scheme. A higher time-step is achieved by artificially increas-

ing the permittivity of the medium. This new approach is validated with standard analytical solutions for planar flux compression systems and magnetic field diffusion in moving conductors with non-relativistic velocity. *This work is the first approach to use FDTD method for electromagnetic problems involving material motion.*

- (c) **Step-3:** Finally, in order to demonstrate the utility of the powerful FDTD-based scheme to MFC problems, we have applied it to a sample problem involving plasma armatures [15]. Here, an ideal cylindrical plasma expansion in an applied magnetic field ~ 0.27 T is considered. The initial conditions are taken from Ref. [15] with plasma energy 270 MJ and pickup coil (single turn) radius 8.25 m. In Ref. [15], the electrical energy is extracted across a resistive load connected to the pickup coil. The hydrodynamic calculation provide the spatial variation of plasma conductivity and velocity at a given instant of time. This information is used in the FDTD calculation to update electromagnetic fields. The updated electromagnetic fields are then used in the hydrocode for calculating magnetic deceleration on the surface of the plasma. We have compared the plasma energy conversion efficiency ($\sim 28\%$) at the end of first expansion phase with the reported values $\sim 30\%$ in Ref. [15]. A reasonable agreement with the results are obtained. However, the dynamics of the plasma after the first expansion phase is found to be different from the predictions made by the 0D-model described in Ref. [15]. This is due to the neglect of plasma compressibility in their 0D-model. As expected, the diffusion of magnetic field into the plasma is found to be negligible.

Important works, results and conclusions of this study

- We have developed and validated a 3D parallel variable-mesh FDTD scheme by directly solving Maxwell's equations adapted for magnetic field diffusion problems. An exponential difference scheme was used for the stability of the numerical solution in the conductor region.
- To permit higher time-steps in FDTD calculations, artificial scaling of permittivity was considered.
- Identified important issues that must be kept in mind (e.g. cell-size, distance to computational boundary, maximum permittivity scaling factor, etc) while performing magnetic diffusion problems using FDTD scheme for electromagnetics. *Some new constraints were identified for the first time.*
- The resistance, inductances and proximity factor calculated for sample problems are validated with known models/results. However, the technique also suffers from the disadvantage of being extremely demanding in terms of computational power. Hence the method can be regarded as a first exploratory step, rather than as a mature technique ready for application to design.
- Developed and validated a parallel variable-mesh 2D-FDTD algorithm with an exponential difference scheme, adapted for magnetic field diffusion problems involving material movement, by directly solving Maxwell's equations including motional e.m.f terms. The algorithm is validated with the known analytical solutions for a planar MFC system.
- The validated algorithm is then applied to study MFC by an expanding cylindrical plasma [15]. The energy conversion efficiency at the end of the first expansion phase is calculated and compared with the results

given in Ref. [15]. Reasonable agreement in the results is obtained.

- This method accurately predicts magnetic field diffusion into a moving conductor and field amplification in the compression volume for complex situations. However, it suffers from the disadvantage of being extremely demanding in terms of computational power, even for sample problems with typical dimensions of a few cm with conductivity of the order of 10^6 S/m.

This work has been published in [39–42].

References

1. L. L. Altgilbers et al, Magnetocumulative Generators, Springer-Verlag, (2000)
2. G. Knoepfel, Pulsed High Magnetic Fields, North-Holland Publishing Company, Amsterdam, (1970)
3. C. M. Fowler et al, Megagauss Technology and Pulsed Power Applications, Plenum Press, New York, (1987)
4. B. M. Novac and I. R. Smith, Electromagnetic Phenomena, **3**, pp 358-365, (2004)
5. I. R. Smith, B. M. Novac and H. R. Stewardson, Engineering Science & Technology Journal, **4**, pp 52-56, (1995)
6. I. R. Smith and B. M. Novac, Power Engineering Journal, **9**, pp 97-101, (1995)
7. B. M. Novac et al, J. Phys. D Appl. Phys., **28**, pp 807-823, (1995)
8. L. I. Rudakov et al, Physics of plasmas, **10**, pp 4435-4447, (2003)

9. F. S. Felsber, M. A. Liberman and A. L. Velikovich, *Appl. Phys. Lett.*, **46**, pp 1042, (1985)
10. A. L. Velikovich et al, *Sov. Phys. JETP*, **61**, pp 261, (1985)
11. F. S. Felsber, M. A. Liberman and A. L. Velikovich, *Phys. Fluids.*, **31**, pp 3675, (1988)
12. F. S. Felsber et al, *J. Appl. Phys.*, **64**, pp 3831, (1988)
13. C. M. Fowler, W. B. Carn and R. S. Caird, *J. Appl. Phys.*, **31**, pp 588, (1960)
14. H. Nakashima, Y. Inoue and Y. Kanda, *Fusion Technology*, **22**, pp 73-81, (1992)
15. K. Mima et al, *Fusion Technology*, **22**, pp 56, (1992)
16. H. Shoyama, H. Nakashima and Y. Kanda, *Fusion Engineering and Design*, **69**, pp 1250-1259, (1993)
17. H. Nakashima, Masaya Takada and Y. Kanda, *Fusion Engineering and Design*, **15**, pp 225-262, (1992)
18. Yu. P. Zakharov et al, *J. Appl. Mech. and Tech. Phys.*, **42**, pp 185-195, 2001
19. Yu. P. Zakharov et al, *Fiz. Plazmy.*, **12**, pp 1170-1176, 1986
20. Yu. P. Zakharov et al, *Trans. Fusion Technol.*, **35**, pp 283-287, 1999
21. B. M. Novac and I. R. Smith, *Jap. J. Appl. Phys.*, **45**, pp 2807, 2006
22. B. M. Novac, I. R. Smith and M. Hubbard, *IEEE Trans. Plasma Sci.*, **32**, pp 1896, 2004

23. C. D. Sijoy and Shashank Chaturvedi, Fusion Engineering Design, **86**, pp 174-182, (2011)
24. C. D. Sijoy and Shashank Chaturvedi, Fusion Engineering Design, **87**, pp 104-117, (2012)
25. C. D. Sijoy and Shashank Chaturvedi, Journal of Computational Physics, **229**, pp 3848-3863, (2010)
26. C. D. Sijoy et al, Journal of Physics Conference Series, **377**, pp 012106, (2012)
27. T. Honda, Y. Nakao, Y. Honda, K. Kudo and H. Nakashima, Nuclear Fusion, **31**, pp 851-865, (1991)
28. T. Shiba, H. Nakashima, Y. Yoshioka and K. Kanda, Nuclear Fusion, **28**, pp 699-705, (1991)
29. E. J. Caramana et al, Journal of Computational Physics, **146**, pp 227-262, (1998)
30. E. J. Caramana and M. J. Shashkov, Journal of Computational Physics, **142**, pp 521-561, (1998)
31. J. C. Campell and M. J. Shashkov, Journal of Computational Physics, **172**, pp 739-765, (2001)
32. C. D. Sijoy and Shashank Chaturvedi, Annals of Nuclear Energy, **62**, pp 81-85, (2013)
33. C. D. Sijoy, G. Singh and S. Chaturvedi, Presented in 27th National Symp. on Plasma Sci. and Tech., (2012)
34. Glenn S. Smith, Journal of Applied Physics, **43**, pp 2196-2203, (1972)

35. Arnold A.H.M, Journal of the Institution of Electrical Engineers, **88**, pp 349-359, (1941)
36. M. Jones, Proc. Int. Conf. on Megagauss Mag. Field Gen. and Related Topics, Ed. P. J. Turchi, USA (1978)
37. K.S. Kunz et al, The Finite Difference Time-Domain Method for Electromagnetics, CRC press, (1993)
38. John R. Freeman and Samuel L. Thompson, Journal of Computational Physics, **25**, pp 332-352, (1977)
39. C. D. Sijoy and Shashank Chaturvedi, IEEE Transactions on Plasma Science, **36**, pp 70-79, (2008)
40. C. D. Sijoy and D. Sharma and S. Chaturvedi, VIII Khariton Readings, RFNC-VNIIF, Russia, (2006)
41. C. D. Sijoy and S. Chaturvedi, Int. Conf. on Megagauss Mag. Field Gen. and Related Topics, USA (2006)
42. C.D. Sijoy and Shashank Chaturvedi, Journal of Computational Physics, **228**, pp 2282-2295, (2009)

LIST OF PUBLICATIONS

Peer Reviewed International Journals

1. **Analysis of magnetic Rayleigh-Taylor instability in a direct energy conversion system which converts inertial fusion plasma kinetic energy into pulsed electrical energy,**
Sijoy C. D. and Shashank Chaturvedi, *Annals of Nuclear Energy*, **62**, pp 81-85, (2013)
2. **An Eulerian MHD model for the analysis of magnetic flux compression by expanding diamagnetic plasma sphere,**
Sijoy C. D. and S. Chaturvedi, *Fusion Engineering and Design*, **87**, pp 104-117, (2012).
3. **Conversion of plasma energy into electrical pulse by magnetic flux compression,**
Sijoy C. D. and S. Chaturvedi, *Fusion Engineering and Design*, **86**, pp 174-182, (2011).
4. **Volume of fluid algorithm with different modified dynamic material ordering methods and their comparison,**
Sijoy C. D. and S. Chaturvedi, *Journal of Computational Physics*, **229**, pp 3848-3863, (2010).
5. **Finite difference time domain algorithm for electromagnetic problems involving material movement,**
Sijoy C. D. and S. Chaturvedi, *Journal of Computational Physics*, **228**, pp 2282-2295, (2009).
6. **Calculation of Accurate Resistance and Inductance for Complex**

Magnetic Coils using the Finite Difference Time Domain Technique,

Sijoy C. D. and S. Chaturvedi, *IEEE Transactions on Plasma Science*, **36**, pp 70-79, (2008).

7. A VOF based multi material method to study impact and penetration problems,

Sijoy C. D., V. Mehra, V. Mishra and S. Chaturvedi, *Journal of Physics Conference Series*, **377**, pp 012106, (2012)

Conferences and presentations

1. Parallel Finite-Difference Time Domain Methods For Electromagnetic and Particle In Cell Simulation Codes, Sijoy C D, G. Singh and

S. Chaturvedi, *22nd National Symposium on Plasma Science and Technology*, Ahmedabad, (2007).

2. Three Dimensional Calculations of Electrical Parameters in Flux compression Systems,

Sijoy C. D. and S. Chaturvedi, *Proc. 2006 International Conference on Megagauss Magnetic Field Generation and Related Topics*, Santa Fe, New Mexico, USA, pp 385-390 (2006).

3. Magnetic Flux compression by expanding plasma sphere,

Sijoy C. D. and S. Chaturvedi, *Invited talk delivered at School on Pulsed power Technology (SPPT-2001)-(Pulsed power and Electro-magnetics)*, Mumbai, May (2011).

4. Magnetic Flux Compression for Direct Energy Conversion in Pulsed Fusion Systems: A Computational Study,

Sijoy C. D., S. Madhavan and S. Chaturvedi, *Invited talk delivered at International Symposium on Waves, Coherent Structures and Turbulence in Plasmas*, IPR, Gandhinagar, 12-15 Jan (2010).

5. Accurate Resistance and Inductance Calculations for High Magnetic Field Systems,

Sijoy C. D., D. Sharma and S. Chaturvedi, *VIII Khariton Readings: Conference on High Energy Densities*, RFNC-VNIIF, Sarov, Russia, (2006).

6. A VOF based multi material method to study impact and penetration problems,

Sijoy C. D., V. Mehra, V. Mishra and S. Chaturvedi, *23rd International Conference on High Pressure Science and Technology (AIRAPT)*, Mumbai, (2011)

7. Rayleigh-Taylor instability analysis in a direct energy conversion system based on magnetic flux compression by expanding fusion plasma,

Sijoy C. D., G. Singh and S. Chaturvedi, *27th National Symposium on Plasma Science and Technology*, University of Pondichery, Pondichery, Dec. (2012).

ACKNOWLEDGEMENTS	1
ABSTRACT	3
SYNOPSIS	5
LIST OF PUBLICATIONS	26
Table of Contents	29
List of Figures	33
List of Tables	45
1 Introduction	47
1.1 Magnetic flux compression generator	47
1.1.1 Basic theory of magnetic flux compression	48
1.1.2 Governing circuit equations	51
1.2 MFC using plasma armatures/liners	53
1.2.1 Imploding plasma liners	53
1.2.2 Expanding plasma armatures	54
1.2.3 Motivation for present work	55
1.3 Proposed concept of MFC by a plasma armature	57
1.3.1 Basic description	57
1.3.2 Typical initial conditions	60
1.3.3 Major difference with past work in this area	61
1.4 Plan of the thesis	63

2	Analysis of energy conversion efficiency and related issues using Lagrangian MHD simulations	67
2.1	Introduction	67
2.2	Computational model	68
2.3	Initial conditions	70
2.4	Issues to be addressed	72
2.4.1	MHD instabilities	72
2.4.2	Choice of the load	73
2.4.3	Coil inter-turn breakdown	74
2.5	Results and discussion	76
2.6	Limitations of the study	86
2.7	Conclusions of this study	87
 3	 An Eulerian MHD model to study the dynamics of plasma	 89
3.1	Introduction	89
3.2	Equations of MHD model	92
3.2.1	Multi-material model	92
3.2.2	MHD model using magnetic vector potential	94
3.3	Computational method	96
3.3.1	Implicit field diffusion using vector potential	97
3.3.2	Lagrangian step	99
3.3.3	Advection or remap step	101
3.3.4	Iteration procedure in free space	104
3.3.5	Volume-of-fluid (VOF) method	105
3.3.6	Boundary conditions (BC)	107
3.4	Validation of the algorithm	107
3.4.1	Sedov problem (cylindrical geometry)	107

3.4.2	Flux compression by expanding perfect electric conductor . .	110
3.4.3	Magnetic Flux diffusion into an imploding resistive liner . .	113
3.4.4	Check for $\nabla \cdot \vec{B} = 0$ condition	116
3.5	MFC by an expanding fusion plasma sphere	117
3.6	Limitations of the study	123
3.7	Conclusions of this study	124
4	Analysis of Magnetic Rayleigh-Taylor (MRT) instability	126
4.1	Introduction	126
4.2	MHD model and Computational Scheme	128
4.3	Initial conditions	130
4.4	Results and Discussion	132
4.4.1	Random perturbation	132
4.4.2	Single mode sinusoidal perturbation	140
4.5	Conclusions of this study	151
5	FDTD based first principle analysis of MFC systems	154
5.1	Introduction	154
5.2	Application to problems with stationary conductors	156
5.2.1	Computational method	156
5.2.2	Geometry setup and excitation	158
5.2.3	Important issues	159
5.2.4	Important new constraint observed in simulations	162
5.2.5	Quasi-DC Excitation	164
5.2.6	AC Excitation	170
5.2.7	Sample calculations for different P/D ratios	174
5.2.8	Sample Calculations for different applied frequencies	175

5.2.9	Sample calculation with a variable pitch coil	175
5.2.10	Parallel Performance of the 3D-Code	177
5.3	Application to dynamic problems	179
5.3.1	Algorithm	180
5.3.2	Theoretical Model for a simple system	184
5.3.3	Computational Model	186
5.3.4	Application to 2D planar MFC systems	192
5.3.5	Sensitivity to permittivity scaling factor	196
5.3.6	Convergence Test	198
5.3.7	Parallel Performance of the 2D-Code	199
5.4	MFC by an expanding cylindrical plasma	200
5.5	Limitations of the Study	204
5.6	Conclusions	204
6	Summary and conclusions	207
6.1	Overall summary	207
6.2	Suggestions for future work	213
	Appendix	215
A	Volume-of-fluid (VOF) scheme	215
A.1	Structured Staggered Mesh	215
A.2	Interface Construction	216
A.3	Volume behind interface line	217
A.4	Volume Iteration	218
A.5	Multi-material interface construction	220
A.6	Dynamic Material Ordering	221
A.7	Calculation of transport volume	224

B	Unstructured compatible Lagrangian hydrodynamics scheme	226
B.1	Introduction	226
B.2	Staggered unstructured mesh	227
B.3	Discrete Lagrangian hydrodynamics	227
B.4	Sub-zonal pressure method	230
B.5	Tensor artificial viscosity	231
	Bibliography	232

List of Figures

1	Schematic showing magnetic flux compression during expansion phase (not to scale).	9
1.1	Schematic of one dimensional planar flux compression by incompressible electrical conductors. (a) Initial configuration, (b) During the flux compression process.	50
1.2	Equivalent circuit diagram for a general MFC system.	52
1.3	Cross-section of a cylindrical MFC system driven by plasma liners in imploding and expanding geometries. (a) Compression of axial magnetic field by an imploding cylindrical plasma liner. (b) The expanding central plasma column compress the axial magnetic field between the plasma and the outer co-axial cylindrical conductor. . .	54
1.4	Schematic of magnetic flux compression system inside a solenoid, driven by an expanding plasma sphere (not to scale)	59
1.5	Schematic of the proposed magnetic flux compression system during the plasma expansion phase (not to scale)	60
2.1	The Lagrangian mesh which shows the different stages of plasma expansion ($t=0.03 \mu s$, $0.08 \mu s$, $0.15 \mu s$ and $0.18 \mu s$). The square dots represents the coil loop locations. Only one quarter of the system is shown because of the symmetry.	79
2.2	Evolution plasma density (kg/m^3) contours (the contour lines are spaced linearly) at different times during expansion phase. Only one quarter of the system is shown because of the symmetry.	79
2.3	The variation of plasma radius at $z = 0$ and normalized magnetic field with respect to initial magnetic field ($B_0 \sim 5 \text{ T}$).	80

2.4	The radial variation of normalized density at different times for $z=0$ plane. The normalization factor is the maximum value of the density along the radial direction for a given time.	80
2.5	The radial velocity profile at different times for $z=0$ plane.	81
2.6	Contours of magnetic field lines represented by magnetic vector potential (A_θ in Tesla-meter), at different times ($t=0, 0.056\mu s, 0.08\mu s$ and $0.18\mu s$)	81
2.7	Time variation of normalized load energy (E_L/E_0), coil current (I/I_0) and system inductance (L/L_0); where E_{L0} , I_0 and L_0 are the initial load energy, coil current and inductance respectively. . .	82
2.8	Variation of plasma stopping radius for different values of initial magnetic fields	84
2.9	Time evolution of coil inter-turn voltage (MV) for different cases with load inductance 1.0 mH	85
2.10	Time evolution of α_V defined in Eq. 2.9 for two different locations. It is clear that, the ratio $\alpha_V \leq 1$. See text for the discussion.	86
3.1	A schematic of the grid used in the two-region solution. The shaded area corresponds to the plasma region and the unshaded region to the vacuum. The Eq. (3.14) is solved in the plasma region and Eq. (3.17) is solved in the vacuum region.	99
3.2	Comparison of normalized pressure profile (normalized to peak pressure, $p_{peak} = 4.0$ Pa) with semi-analytical solution for Sedov problem at $t = 0.05$ s.	108
3.3	Comparison of normalized velocity profile (normalized to peak velocity, $v_{peak} = 1.84$ m/s) with semi-analytical solution for Sedov problem at $t = 0.05$ s.	109

3.4	Profile of B/B_{max} obtained with various advection algorithms at different times during compression phase.	112
3.5	Comparison of L_1 norm error vs. mesh-size for different schemes/limiters. MC – monotonized centered limiter.	113
3.6	The no. of iterations required to solve Eq. (3.17) vs. mesh size for different values of tolerance factor ξ	113
3.7	Comparison of the diffused flux $\Phi_B(t)$ into the resistive liner calculated using two different advection schemes (MUSCL and FCT) with analytical solution given in Ref. [78]. The left and right side figures correspond to $R_m \sim 315$ and 150, respectively.	115
3.8	The L_1 norm error in Φ_B at $t = t_o$ (for $R_m \sim 315$) for different mesh-sizes used in the radial direction.	115
3.9	Spatial variation of the magnetic field vector for plasma expansion problem	117
3.10	The temporal evolution of maximum divergence error for different mesh-size used. Here, $\tau = t_f/t$ is the normalized time.	118
3.11	Spatial variation of scaled density ($\rho \times 10^6$ kg/m ³) at different times ($t = 0.072, 0.14, 0.19$ and $0.24 \mu s$). The elongation of the plasma sphere along the axial direction and the development of shell like plasma structure are clearly visible towards the end of the radial expansion phase.	120
3.12	The radial variation of normalized density at different times for $z = 0$ plane. The normalization factor is the maximum value of the density along the radial direction for a given time.	121

3.13	Contours of magnetic field lines represented by magnetic stream function ($\Psi = 2\pi r A_\theta$), at different times, $t = 0.072$ and $0.21 \mu s$ respectively.	122
3.14	The radial variation of B_z at different times for $z = 0$ plane.	122
3.15	The distribution of plasma current density (contours) at different times.	122
3.16	Zoomed in plot (plotted on a coarse mesh for clarity) of plasma-vacuum interface near stagnation point ($\sim 0.21 \mu s$) indicates development of RT like instability on the plasma surface.	124
3.17	Zoomed-in plot of velocity vector inside the plasma region at a time $\sim 0.21 \mu s$. The plot indicate the development of instabilities on the plasma surface. The velocities within the plasma shell are considerably lesser than the velocities on the surface and at regions below the shell.	125
4.1	A typical unstructured Lagrangian mesh used in the plasma region. A larger number of cells is used near near the surface of the plasma, where large material deformations are expected.	130
4.2	Initial radial plasma profiles for density, temperature and velocity. The profiles are normalized to the peak value; $\rho_{peak} = 2.5 \times 10^{-4} \text{ kg/m}^3$, $T_{peak} = 0.275 \text{ keV}$ and $v_{peak} = 1.63 \times 10^7 \text{ m/s}$	131
4.3	(a) Plasma pressure (normalized to 10^7 Pa) vs radius at different times during the initial phase of the plasma expansion. The plasma forms a shell like geometry [52, 82]. (b) The temporal evolution of g of the outer surface (normalized to 10^{14} ms^{-2}) during the initial phase of plasma expansion.	134

4.4	Spectral evolution of perturbations in plasma liner at different times, starting with an initial random perturbation. We have drawn an envelope over the wave structure, adapted from [104], (dashed blue line) to easily identify the dominant modes and corresponding wavelength regime. Figures (a)–(f) are at $t=0, 0.04 \mu\text{s}, 0.044 \mu\text{s}, 0.048 \mu\text{s}, 0.058 \mu\text{s}$ and $0.081 \mu\text{s}$, respectively. The corresponding average plasma radii are 0.2 m, 0.78 m, 0.9 m, 0.95 m, 1.0 m and 1.2 m respectively.	136
4.5	Cross-correlation factor (f_{cr}) for few dominant modes ($n = 22, 34, 38$ and 50) with other modes in the spectrum.	137
4.6	Temporal variation of λ for mode number 80. The λ for this mode changes from 4 mm to 2.25 cm.	138
4.7	Spectral evolution of plasma liner at different times from an initial random amplitude perturbation (with $n_\theta = 600$). We have drawn an envelope over the wave structure (dashed blue line) to easily identify the dominant modes and corresponding wavelength regime.	139
4.8	Fourier spectrum obtained for two different values of α_n (random initial perturbation). The initial spectrum obtained for these two cases are as shown in the first plot of Fig. 4.4 with a multiplication factor of 10 and 100 respectively.	140
4.9	Density ($\times 10^5 \text{ kg/m}^3$) profile near the plasma surface towards $t = t_s$ for the case with $\lambda_{in} = 3.14 \text{ cm}$ ($n = 10$) and $\alpha_{in} = \lambda_{in}/10$. Right side plot is the corresponding Lagrangian Mesh with a mesh-size $\sim \lambda/12$	144

4.10 The left side plot shows the spectrum amplitude (mm) at different times (single mode analysis) with $\lambda_{in} = 3.14$ cm ($n = 10$) and $\alpha_{in} = \lambda_{in}/10$. The FFT spectrum shows the evolution of harmonic modes. Right side plot shows the normalized spectrum amplitude (α/α_{peak}) at $t \sim 0.04$ μ s obtained in the multi-mode analysis (modes 10 & 40, $\alpha_{in} = 500$ μ m) and single mode analysis ($n = 40$, $\alpha_{in} = \lambda/10$). 145

4.11 The normalized spectrum amplitude (α/α_{peak}) obtained in the multi-mode perturbation analysis with $\alpha_{in} \sim 500$ μ m. The left and right side plots are for modes 30 & 40 at $t = 0.04$ μ s and modes 60 & 80 at $t = 0.03$ μ s respectively. 146

4.12 The evolution of perturbation amplitude α (single mode analysis) for $n = 10$ with $\alpha_{in} = \lambda_{in}/10$. Here, α_L is the analytical variation assuming constant linear growth rate $\gamma_L \sim (2\pi g_{avg}/\lambda_{avg})^{1/2}$. Similarly $\alpha_L(t)$ is obtained by using instantaneous values for $\gamma_L(t) \sim (2\pi g(t)/\lambda(t))^{1/2}$ 146

4.13 The temporal evolution (single mode analysis) of the spectrum amplitude (normalized to initial value) for modes 5, 25 and 45 with $\alpha_{in} = \lambda_{in}/1000$ 147

4.14 The variation of maximum α/α_{in} and α ($\times 10^2$ m) for different values of initial mode number n and perturbation amplitude α_{in} ($\lambda/1000$, $\lambda/100$ and $\lambda/10$). 147

4.15 Temporal evolution of spectrum amplitude (single mode analysis with $n = 10$) and plasma outer surface radius (both normalized to their initial values) with $m_p \sim 4.4$ mg and $E_p = 140$ and 280 MJ. . 148

4.16	Initial plasma configuration (blue color plot) and the plasma configuration at $t = 0.033\mu s$ obtained in the single mode analysis for $n = 10$ with $\alpha_{in} = \lambda_{in}$	149
4.17	The snap shots of MRT instability evolution at different times (left and right side plots are at $0.035\mu s$ and $0.09\mu s$ respectively.) with an Eulerian MHD scheme for $n = 10$ with $\alpha_{in} = \lambda_{in}$	150
4.18	The plasma density (normalized to $1.0 \times 10^{-5} \text{ kg/m}^3$) at $0.09 \mu s$ obtained with an Eulerian MHD scheme for $n = 10$ with $\alpha_{in} = \lambda_{in}$. The plot is shown only near the surface of the plasma for better clarity.	150
4.19	The plasma pressure (normalized to $7.0 \times 10^7 \text{ Pa}$) at $0.09 \mu s$ obtained with an Eulerian MHD scheme for $n = 10$ with $\alpha_{in} = \lambda_{in}$. The plot is shown only near the surface of the plasma for better clarity. . . .	151
4.20	Flux compression efficiency (defined in the text) vs mode number for two different values of α_{in}	152
5.1	Yee cell with electric and magnetic field locations	159
5.2	Schematic of a typical two turn coil geometry setup used in FDTD modeling, including different current observation loops as well as the applied electric field driving a current through the coil.	160
5.3	A typical two turn coil, $n\lambda$ is the distance to the FDTD domain boundary ($n = 1, 2, 3 \dots$)	161
5.4	Schematic of a typical single-turn coil geometry setup with different current observation loops and source excitation gap. Inset shows line ‘ab’ along which electric field measurements are reported. . . .	163
5.5	Applied Half-gaussian pulse for Quasi-DC excitation with a rise-time of $1 \mu s$	166

5.6	Mean current for single-turn coil with quasi-DC excitation	166
5.7	Steady-state electric field E_x (V/m) distribution through the conductor as a function of radial position (along the line \vec{ab} as shown in Figure 5.4) inside the conductor, for a single turn coil with Quasi-DC excitation.	167
5.8	Meshing used near the conductor cross-section with mesh size of 0.09 mm	168
5.9	Mean Current calculated for two-turn coil with quasi-DC excitation	170
5.10	Absolute value of the difference in currents with respect to the mean current	170
5.11	Schematic of a typical two-turn coil which shows the current density observation planes across the conductor cross-section for individual turns in the coil	171
5.12	Current density distribution (A/m^2) over the conductor cross-section for a two turn coil at different times during current ramp-up. The last frame is close to steady state.	171
5.13	The current density (A/m^2) diffusion in to the conductor cross-section as a function of axial distance (along the line \vec{cd} as shown in Figure 5.11) for a two turn coil at different times during current ramp-up. The last frame is close to steady state.	172
5.14	Currents (mA) observed at different locations and the applied voltage (scaled up by 10) for a single-turn coil with AC excitation . . .	172
5.15	Currents (μA) observed at different locations for two-turn coil for AC excitation	173
5.16	Time dependent inductance (nH) for two-turn coil with AC excitation	174

5.17	Current density (A/m^2) distribution over conductor cross-section for two-turn coil for AC excitation. The snap-shots are for a typical cycle after reaching steady state.	175
5.18	Current density (A/m^2) distribution over conductor cross-section for two-turn coil for AC excitation. The snap-shots are for a typical cycle after reaching steady state.	176
5.19	Comparison of R_{ac}/R_{dc} using FDTD calculations with those obtained from Arnold's expression, as a function of the P/D ratio. Calculations are reported for a two-turn coil with an applied frequency of 1 GHz.	177
5.20	Comparison of R_{ac}/R_{dc} using FDTD calculations with those from Arnold's expression, for a two-turn coil having a P/D ratio of 1.3. The frequency is varied from 0.5 to 1.3 GHz	178
5.21	Sketch of a typical 4 turn variable pitch coil having two sections with different P/D ratio	179
5.22	Speedup vs. no. of processors used for two different cases, namely, parallelization along one direction and prallelization along multiple directions	181
5.23	Electromagnetic induction model with a moving conductor and fixed end conductors at $x = -b$ and $x = +d$. B_{10} , B_{20} are the initial transverse magnetic fields to the left and right of the conductor. The symbol V_c marks the 'compression volume'.	185
5.24	FDTD setup, with source excitation points and magnetic field observation points (B_1 and B_2). D is the distance to computational boundary.	186

5.25 Two-dimensional (2D) Yee cell, showing locations of field components and material quantities.	189
5.26 Magnetic field inside the compression volume, B_2 , as a function of time. Dotted curve is the analytical solution and solid line represents results from the FDTD calculation. $t=0$ refers to the time when the source magnetic field reaches its peak value.	193
5.27 Time history of normalized magnetic flux inside the system. The normalization factor is the initial flux in the system = $3.14 \times 10^{-5} Tm^2$ (Weber)	194
5.28 Magnitude of induced EMF (kilo volts/m) on the surface of the slab ($E_v = v_x \times B_z$). Both analytical and computed values are shown.	194
5.29 Spatial variation of magnetic field inside the compression volume, illustrating field amplification. Three different plots correspond to field variations at three different times during compression. Points represent analytical solutions while line plots shows numerical results.	195
5.30 Inductance as a function of time. Analytical and FDTD results match well.	196
5.31 Spatial variation of magnetic field inside the compression volume. Dots and solid lines represent analytical and computational solutions, respectively.	196
5.32 Normalized magnetic fields inside ($B_2(t)/B_{peak}$) and outside ($B_1(t)/B_{10}$) the compression volume, as functions of time. B_{peak} is the peak magnetic field reached in the compression volume. Dots and solid lines represent analytical and computational solutions, respectively. $t=0$ refers to the time when the source magnetic field reaches its peak, and conductor motion starts.	197

5.33	Percentage error between analytical and numerical solutions, as a function of the permittivity scaling factor (ϵ_r).	198
5.34	Percentage error between analytical flux conservation factor and numerical solutions, as a function of mesh-size.	199
5.35	Speedup achieved as a function of the number of processors, for the problem described in Sec. 5.3.4.	200
5.36	Schematic of FDTD setup for the simulation of MFC by an expanding cylindrical plasma. The pickup coil is a single turn cylindrical coil. The current in the coil is determined by constructing an integration loop around the cross-section of the loop in 2D r-z plane. . .	202
5.37	Radial profile of plasma density (kg/m^3) at different times during the first expansion phase	203
5.38	The plot of velocity vector defined at nodes along with the distorted Lagrangian mesh (plotted on a coarse mesh for clarity) indicates the evolution of instability.	203
5.39	The variation plasma outer surface radius w.r.t time during the first expansion phase.	204
A.1	Schematic of staggered computational grid	216
A.2	Geometry of linear interface construction for Material interface . . .	217
A.3	Different types of possible material interface orientation. Here, $d = \alpha$ (in the text) is the perpendicular distance from a local origin and \vec{n} is the exterior normal to the interface line.	219
A.4	Onion-skin order of material interfaces in a computational cell . . .	220
A.5	Priority checking by Mosso-Clancy method	223
A.6	Priority checking by Benson's method of least square fit to the set of the centroids	224

A.7 Material polygon before and after Lagrangian deformation for two
different orientations 224

B.1 A typical unstructured staggered mesh, including zone z and point
 p . The solid lines define the mesh and the dashed lines show the
sub-cell or median mesh. The sub-cell of each node is formed by
connecting the zone centroid and edge centers. 228

2.1	System performance for different inductive load conditions. L is the load inductance, E_i is the initial electrical energy, E_L is the inductive energy stored in the load, and η is the conversion efficiency. 83
2.2	System performance for different resistive loads. R is the load resistance, E_L is the resistive energy across the load, and η is the conversion efficiency. The total initial energy is 400 MJ. 83
3.1	L_1 norm error ($\times 10^3$) for density ρ vs. mesh-size used for Sedov problem for different flux limiters. In the Table MC stands for monotonized centered limiter. 109
3.2	Convergence rate obtained for Sedov problem with superbee limiter. 110
5.1	No. of cells and cell-size used in each directions 165
5.2	No. of cells and cell-size used in each directions 168
5.3	Speedup achieved with no. of processors used in each directions . . 180
A.1	Different cases of intersection among pairs of interface lines [62]; ‘y’ and ‘n’ stands for an intersection and non-intersection respectively. 222

1

Introduction

1.1 Magnetic flux compression generator

Conventional high explosive (HE) driven Magnetic Flux Compression (MFC) generators (also known as magneto cumulative generators) convert the chemical energy of explosives into high-power electrical pulses or high magnetic fields through the compression of magnetic flux [1–10]. These systems typically consist of a high-explosive charge contained inside a metallic conductor (“armature”). Detonation of the explosive produces high-pressure gases, which cause the armature to expand outward at a high velocity (few km/s). The armature is subjected to an externally-imposed magnetic field, e.g. by being placed inside a current-carrying solenoid. Since the armature is a good electrical conductor, it pushes against the magnetic field and compresses the magnetic flux into a smaller space. This *magnetic flux compression* (MFC) leads to amplification of the electrical energy in the solenoid. The net result is that the chemical energy of the explosive is partially converted into output electrical energy. MFC generators have found widespread use as pulsed power sources for a broad range of applications such as fusion, elec-

tromagnetic accelerators, high-power micro-wave (HPM) sources, laser, electron, ion, or neutron sources, high magnetic field research and many others.

1.1.1 Basic theory of magnetic flux compression

A brief theoretical introduction to MFC is given in the following. The Faraday induction law states that the electric field appearing at the open circuited terminals of a loop with contour ‘C’ and area ‘S’ is equal to the time rate of change of the flux $\Phi = \int_S \vec{B} \cdot d\vec{S}$ through the loop:

$$\int_C \vec{E} \cdot d\vec{l} = -\frac{d\vec{\Phi}}{dt} = -\frac{d}{dt} \int_S \vec{B} \cdot d\vec{S} \quad (1.1)$$

For an ideal conductor (infinite electrical conductivity σ), the flux loss in to the conductor is zero. That is the total flux is conserved.

$$\frac{d\vec{\Phi}}{dt} = \frac{d}{dt} \int_S \vec{B} \cdot d\vec{S} = 0 \quad (1.2)$$

$$\vec{\Phi} = \int_S \vec{B} \cdot d\vec{S} = \text{const.} \quad (1.3)$$

Therefore, for an ideal case, if the area of the loop is reduced, the magnetic flux density \vec{B} in the loop has to increase so as to conserve the total flux Φ . This is the working principle of MFC. Work has to be performed to decrease the area of the loop. In the case of explosive driven MFC systems, this work is done by the explosive.

In terms of electrical notations, the above phenomena can be described as follows. The magnetic flux is defined as $\Phi = LI$, where L is the system inductance and I is the current. The work is done so as to decrease the system inductance. Therefore, for an ideal case, the current and hence \vec{B} in the confining conductor

has to increase so as to conserve the flux.

The two expressions $\int_S \vec{B} \cdot d\vec{S} = \text{const}$ and $LI = \text{const}$, are equivalent but they best describes different types of devices. The imploding devices used for the generation of high magnetic fields are best described by the expression $\int_S \vec{B} \cdot d\vec{S} = \text{const}$ and are called MK-1 devices, whereas exploding devices, called as MK-2 devices [1], delivering high currents are best described by the expression $LI = \text{const}$.

For practical cases, the magnetic flux diffuses into the confining conductors due to finite electrical conductivity (resistive loss). Therefore, the magnetic flux has to be compressed within a time frame such that the magnetic flux does not have time to diffuse through the conductors and out of the compression volume. The diffusion of magnetic field into the conductor is governed by the following equation.

$$\frac{\partial \vec{B}}{\partial t} = -\nabla \times \frac{1}{\mu\sigma} \nabla \times \vec{B} = -\nabla \times \frac{\eta}{\mu} \nabla \times \vec{B} \quad (1.4)$$

Here, μ , σ and $\eta = 1/\sigma$ are the permeability, electrical conductivity and resistivity of the conductor material respectively. The term $1/(\mu\sigma)$ is called the *magnetic diffusivity*. For a one-dimensional planar case (see Fig 1.1) and neglecting the spatial gradient of resistivity η , the equation reduces to

$$\frac{\partial B_z}{\partial t} = \frac{1}{\mu\sigma} \frac{\partial^2 B_z}{\partial x^2} = \frac{\eta}{\mu} \frac{\partial^2 B_z}{\partial x^2} \quad (1.5)$$

where, B_z is the perpendicular magnetic field component. From Eq. (1.5), the diffusion time-scale for the magnetic field to diffuse the conductor is given by

$$t_B = \mu\sigma L^2 \quad (1.6)$$

where, L is the conductor thickness. For effective magnetic flux compression,

the flux compression time $t_c = L_c/v \gg t_B$, where L_c and v are the compression length and velocity of the conductor respectively, see Fig 1.1.

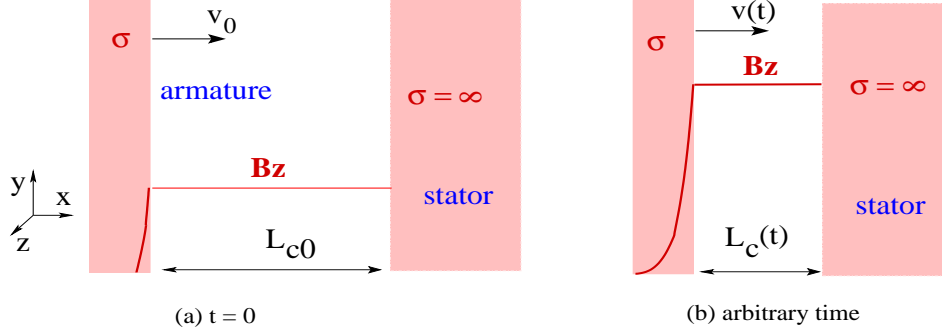


Figure 1.1: Schematic of one dimensional planar flux compression by incompressible electrical conductors. (a) Initial configuration, (b) During the flux compression process.

For steady state sinusoidal variation of field with angular frequency ω , the solution of Eq. (1.5) is given by

$$B_z(x, t) = B_0 e^{-x/\delta} \sin\left(\omega t - \frac{x}{\delta}\right) \quad (1.7)$$

where, B_0 is the magnitude of the field and $\delta = \sqrt{\frac{2}{\omega\sigma\mu}}$ is the skin depth.

The variation of the current density ($\vec{J} = \frac{1}{\mu} \nabla \times \vec{B}$) along the thickness of the conductor produces non-uniform Joule heating in the conductor, leading to non-uniform electrical conductivity ($\sigma = \sigma(T)$, where T is the temperature). The magnetic field diffusion, therefore, is non-linear and is governed by the following equation for the one-dimensional planar case.

$$\frac{\partial B_z}{\partial t} = \frac{\partial}{\partial x} \frac{1}{\mu\sigma} \frac{\partial B_z}{\partial x} \quad (1.8)$$

Here, $\sigma = \sigma(x, T, t)$; is a function of space, local heating and time.

The practical implication of magnetic field diffusion is that the conductor thick-

ness in a flux compression generator should be chosen such that the skin depth is smaller than the conductor thickness to avoid excessive loss of flux during the compression.

During the process of MFC, the magnetic field in the compression volume and the associated $\vec{J} \times \vec{B}$ force on the conductor increases. This will slow down the armature and hence the compression. The increased magnetic field may eventually stop the armature and even cause it to reverse direction. This is called ‘turn-around’ or ‘armature rebound’. At the turn-around point, the magnetic energy inside the system equals the sum of initial kinetic energy of the armature and magnetic energy in the system.

1.1.2 Governing circuit equations

The equivalent circuit diagram for a MFC system is shown in Fig. 1.2. The flux conservation equation with resistive elements can be represented by the following differential equation.

$$L \frac{dI}{dt} + I \frac{dL}{dt} + IR = 0 \quad (1.9)$$

Here, $L = L_g + L_L$ and $R = R_g + R_L$ are the total system inductance and resistance respectively. The terms L_g and R_g are represent the generator inductance and resistance. Similarly, L_L and R_L are the load inductance and resistance respectively. The current I , flowing through the circuit can be found by solving the Eq. (1.9). The analytical solution of the equation is given by

$$LI = L_i I_i \exp \left(- \int_0^t \frac{R}{L} dt \right) \quad (1.10)$$

where, I_i is the initial seed current and L_i is the initial total inductance of the

system. From Eq. (1.9), the necessary condition for $dI/dt > 0$ can be deduced as follows:

$$-\frac{dL}{dt} > R \quad (1.11)$$

In order to account for intrinsic flux losses [1] in HE-driven MFC systems, dL/dt is usually multiplied by a constant parameter $0 < \alpha \leq 1$ in the above equation. The value of α is typically 0.6–0.7.

$$-\alpha \frac{dL}{dt} > R \quad (1.12)$$

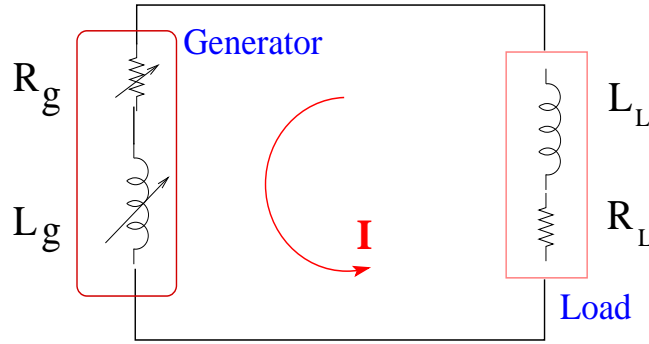


Figure 1.2: Equivalent circuit diagram for a general MFC system.

Multiplying Eq. 1.9 by current I , we get the rate of change of electrical energy.

$$\frac{d}{dt} \left(\frac{1}{2} L I^2 \right) + \frac{I^2}{2} \frac{dL}{dt} + I^2 R = 0 \quad (1.13)$$

The analytical solution of the above equation is given by

$$E(t) = E_i \frac{L_i}{L(t)} \exp \left(-2 \int_0^t \frac{R}{L} dt \right) \quad (1.14)$$

where the subscript i refers to the initial value. The necessary condition for positive energy gain is given by

$$-\frac{dL}{dt} > 2R \quad (1.15)$$

Using the intrinsic flux loss parameter, α , the above equation can be written as

$$(1 - \alpha) \frac{dL}{dt} > 2R \quad (1.16)$$

1.2 MFC using plasma armatures/liners

Most existing MFC devices use solid metal armatures to compress the magnetic field. However, the use of imploding liquid and plasma liners has also been explored for the generation of high magnetic fields [12, 18–20]. A schematic representation of MFC systems used for the compression of an axial seed magnetic field in cylindrical geometry is shown in Fig. 1.3. The left side plot in Fig. 1.3 shows an MFC system driven by an imploding plasma/liquid liner (converging geometry) whereas the right side plot shows the compression of magnetic field between an expanding cylindrical plasma and an outer co-axial confining conductor (diverging geometry). In the following sections, we present a brief review of MFC by plasma armatures/liners in both converging and diverging geometries.

1.2.1 Imploding plasma liners

Many authors have examined the process of MFC by an imploding liquid/plasma liner. Analytical theory and numerical simulations of the confinement and compression of magnetic flux by plasma shells are given in Ref. [11]. Ref. [12] has examined the production of ultra-high magnetic fields ~ 100 megagauss (MG) by the compression of an axial magnetic field inside a radially imploding gas-puff Z

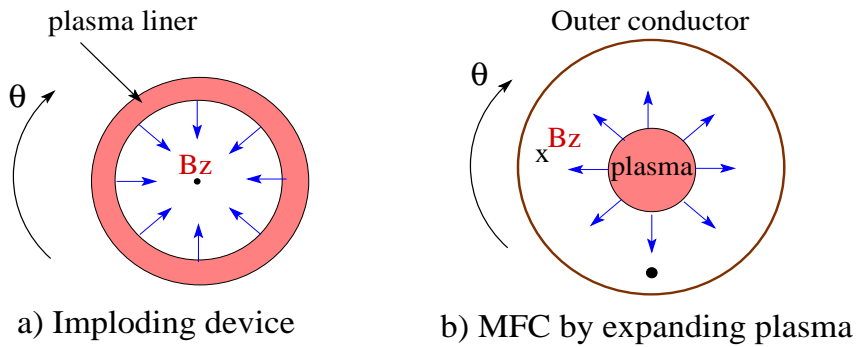


Figure 1.3: Cross-section of a cylindrical MFC system driven by plasma liners in imploding and expanding geometries. (a) Compression of axial magnetic field by an imploding cylindrical plasma liner. (b) The expanding central plasma column compresses the axial magnetic field between the plasma and the outer co-axial cylindrical conductor.

pinch plasma. The compression of an axial field can also be achieved by a laser driven ablative implosion of a thin liner [12–14]. In Ref. [15], self-similar solutions have been obtained for the compression of the plasma with a frozen-in magnetic field by an imploding thin cylindrical wall. Self-similar solutions for supersonic and subsonic compression of a magnetized plasma-filled liner is provided in Ref. [16,17]. The production of high axial magnetic fields $\sim 2\text{--}40$ MG by imploding an annular gas puff Z pinch has been studied in Ref. [18,19]. The production of $10\text{--}15$ MG fields by using an HE-driven liner compressing an initial seed flux has been studied in Ref. [20].

1.2.2 Expanding plasma armatures

Several works have been reported in the past which explore MFC by an expanding plasma armature. A spherical expansion configuration compressing an azimuthal field was proposed by Fowler et al. [4]. The general idea of MFC by an expanding *plasma sphere* has been proposed by Artsimovich [21]. This has been applied to inertial fusion energy (IFE) systems by Haught et al. [22]. The basic idea is to use

a conducting surface that encloses a diamagnetic plasma expanding across an external magnetic field. The external field is excluded by the diamagnetic plasma due to the currents produced in the plasma. The induced electromotive force (e.m.f) drives currents in the shielding conductor and thus converts the plasma kinetic energy into electrical energy [37]. Raizer [23] obtained, theoretically, a conversion efficiency of up to 80 % when a plasma sphere is allowed to expand in an external homogeneous magnetic field in the absence of a shielding conductor. Also, using a simple theoretical model, an efficiency of about 50% in the presence of short-circuited pickup coils were obtained in the development of rocket thrust using fusion micro-explosions [24]. A preliminary analytical study with an assumption of cylindrical plasma expansion is provided in Ref. [25]. Cowan et al. [34–36] proposed a pulsed power conversion system with inductive storage, called PULSAR, that could be powered by the expanding plasma from fusion micro-explosions to compress the magnetic flux. They expected an energy conversion efficiency $>80\%$ with a fusion reactor scale PULSAR design. A first quantitative study, using a two-dimensional particle-in-cell (PIC) simulation [26,27] for an ICF fusion reactor with D-3He fuel, predicts a maximum efficiency of 20 % with a resistive load. An experimental study [28–30] using laser-produced plasma clouds shows a conversion efficiency of about 30%.

1.2.3 Motivation for present work

Plasma armature, as compared to a metal armature, has several advantages. The major advantages are summarized below.

- High electrical conductivity, leading to higher flux efficiency (lower flux losses due to magnetic flux leakage into the armature).

- Much higher expansion velocity, leading to smaller expansion times, in turn increasing flux efficiency.
- Greater expansion ratio, i.e., ratio of maximum to minimum radii of plasma. With a metal armature, fracture precludes the use of expansion ratios higher than 2 for aluminium (Al) armatures and ~ 2.5 for copper (Cu) armatures.
- Unlike conventional explosive driven flux compression generators where the stator coil is permanently destroyed, the plasma armature driven flux compression system gives lower impulse to generator structure. Reusable coil structures can be designed [26,27]. However, to protect the coil from plasma radiations, a cylindrical protective shield between the coil and plasma may be required.

On the other hand the plasma armature driven MFC systems have some major disadvantages as summarized below.

- Plasma is subject to instabilities: Instabilities can also arise in metal armatures, but are stabilized due to material strength. A plasma has no material strength.
- Short operational time may lead to ultra high voltages, leading to problems with insulation & electrical breakdown.

The advantages of plasma armatures over metallic liners make this subject attractive. The plasma armatures can expand much faster than metal armatures, yielding shorter-duration electrical pulses and higher flux efficiencies. However, they are subjected to MHD instabilities due to its interaction with the magnetic field. Also, the short operation time may lead to ultra-high voltages. Hence it is necessary to perform a detailed numerical study of the interaction between the

plasma and an externally-imposed magnetic field. In the present work, we explore the physics of MFC using an expanding *spherical plasma armatures*. The concept may find application in inertial fusion energy (IFE) systems as a direct energy conversion scheme to convert a part of fusion plasma kinetic energy into pulsed electrical energy.

1.3 Proposed concept of MFC by a plasma armature

1.3.1 Basic description

In Inertial Fusion Energy (IFE) systems, such as laser-driven fusion, the implosion and burn process produces a *fireball* consisting of a high-density, high-temperature plasma [25, 31, 32]. Since the IFE plasma fireball is a good electrical conductor, it could, in principle, act as an expanding armature in an MFC system. Plasma armatures can expand much faster than metal armatures, yielding shorter-duration electrical pulses and higher flux efficiencies.

Schematic representations of the basic concept are shown in Fig. 1.4 and 1.5. The first figure shows the initial configuration of the system, where the coil is driven by a power source (e.g. a charged capacitor) to set up the initial magnetic field. Following earlier works [24–26, 28], we assume that a spherical plasma is created at the center of the coil, e.g. from fusion micro-explosions [24–26, 28]. Also, we assume that the system is isolated from the power source by opening the switch s_1 . The sequence of switch operation is as follows. At time $t=0$, the switch s_1 is closed and the switch s_2 is held open. This allows the capacitor to discharge into the coil and set up the initial magnetic field. Simultaneous (ideally) opening and closing of

the switches s_1 and s_2 respectively, prior to the plasma expansion, will exclude the capacitor from the system. The circuit breakers or opening switches can be SF6 gas switches capable of handling high voltages, as suggested in earlier works [25, 26]. Such circuit breakers or opening switches and near-simultaneous switching actions are realized in many magnetic flux compression generator experiments using plasma opening switches (POS), two-stage exploding foil switches (EFS), SF6 gas switches etc. However, for the time-scales involved, the possible options are either a plasma opening switches (POS) or an exploding foil switches (EFS). It is worth noting here that for these opening switches a large energy has to be dissipated inside the switches. Also, the switch must be capable of absorbing hundreds of MJ energies. At present, similar to earlier works [25, 26], we assume that these requirements can be achieved with near-term engineering technologies.

The whole system, excluding the load and source, should be kept inside a vacuum chamber similar to the designs given in Ref. [25, 26]. Similarly, to protect the cylindrical coil from plasma radiation, a cylindrical protective shield may be placed between the coil and plasma, see Fig. 1.4. For a typical case of plasma and system parameters, an ultra-high single-turn EMF of the order of 25 million volts (MV) is produced. In order to be able to handle such voltages, the radiation shield must be electrically insulating in the azimuthal direction. These requirements can be achieved with existing or near-term engineering technologies. A brief discussion on these issues and possible methods to overcome those are given in Ref. [25], which can also be found in many IFE reactor design concepts.

The expanding plasma performs work against the magnetic field and thereby loses energy. The increase in the magnetic energy due to magnetic flux compression is accompanied by an increase in the coil current (See Fig 1.5). In other words, a part of the plasma kinetic energy can be converted into electrical energy by the

compression of magnetic flux between the coil and plasma. The concept may find application in inertial fusion energy (IFE) systems as a direct energy conversion scheme.

However, the expanding plasma, working against a magnetic field, is subject to MHD interchange instabilities, e.g. magnetic Rayleigh-Taylor (MRT) instability, flute mode instability etc. Therefore, the plasma parameters, system dimensions and initial magnetic field should be chosen in such a way that MHD instabilities do not grow significantly during the *first expansion phase* of the plasma. Here, the *first expansion phase* is defined as the time duration from the start of plasma expansion up to the stagnation point, where the plasma expansion velocity along the radial direction falls to zero.

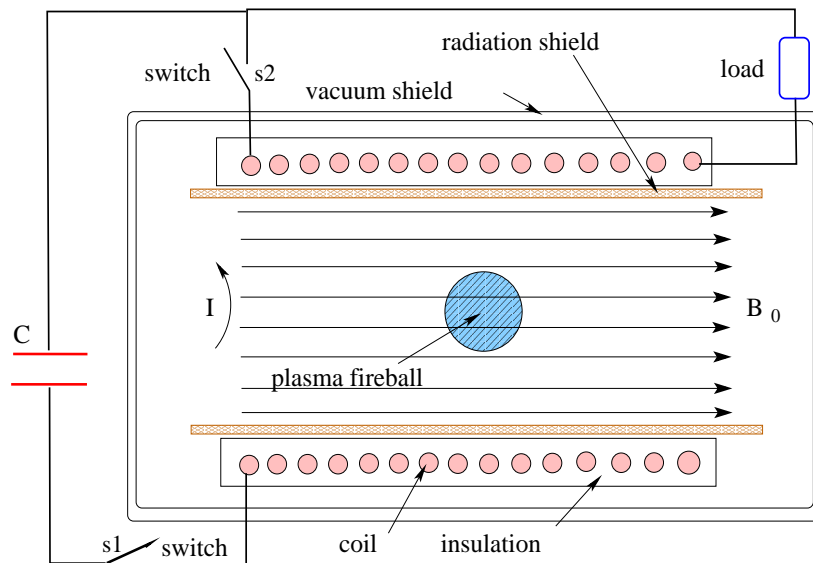


Figure 1.4: Schematic of magnetic flux compression system inside a solenoid, driven by an expanding plasma sphere (not to scale)

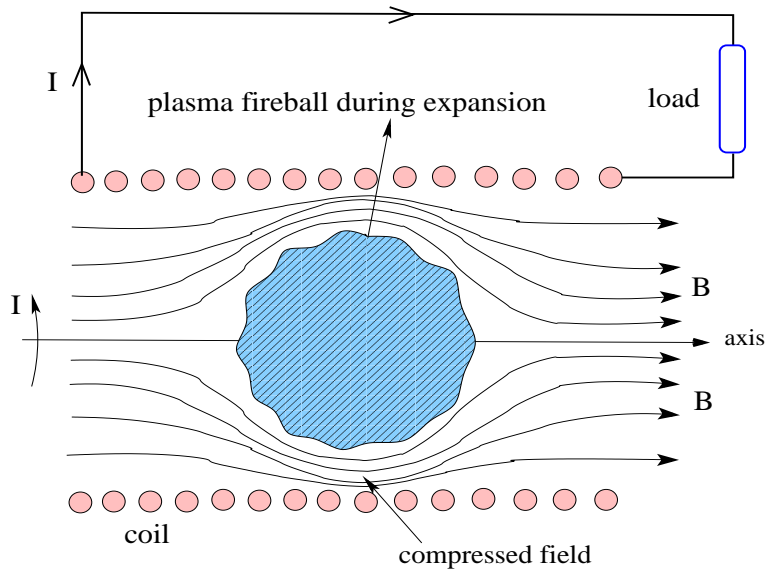


Figure 1.5: Schematic of the proposed magnetic flux compression system during the plasma expansion phase (not to scale)

1.3.2 Typical initial conditions

In the present computational work, we focus on the dynamics of plasma expansion across the magnetic field, the energy conversion efficiency and an analysis of magnetic Rayleigh-Taylor (MRT) instability in such systems. Therefore, similar to earlier works, we start our analysis/simulation from the time when plasma is created and the initial magnetic field is set up.

The initial plasma conditions are chosen from earlier published works [25–28] for a D-3He fusion plasma. Although the required ignition energy is substantially higher for D-3He, the reaction products will consist predominantly of charged particles, which can be electromagnetically manipulated. In D-3He fusion products, about 80% of the fusion energy is carried by 14-MeV protons ($D_1^2 + He_2^3 \rightarrow He_2^4$ (3.6 MeV) + p_1^1 (14.7 MeV)). Shortly after fusion reactions start, the plasma reaches a state of extremely high temperature (few tens of keV) and density ($\sim 10^6$ kg/m³), and has a radius of 150-250 μ m. Therefore, initially, it undergoes free expansion

in the applied initial magnetic field. Considering this fact, we start our simulation with an initial plasma radius of about 1.0 cm with a coil of radius 1.5 m. Therefore, the ratio of initial plasma radius (r_{pi}) to coil radius (r_c) is $\sim 7 \times 10^{-3}$. A higher initial radius of about 1 m is reported in Ref. [25, 26], with $r_{pi}/r_c \sim 0.1$ ($r_c \sim 10$ m). Hence the system dimensions used here are much smaller than those given in Ref. [25–27]. We have taken the coil axial length as approximately 2–4 times the radius. The initial plasma kinetic energy is typically varied from 140–280 MJ. with plasma mass equal to 1–6 milligrams (mg) [25–27]. The initial magnetic field is varied from 2 to 10 Tesla, which is considerably higher than the magnetic field values used in earlier works [25–27].

1.3.3 Major difference with past work in this area

Major differences with earlier works [25–27] described above are in terms of the system dimensions, parameter regime, feeding magnetic field source, computational model used etc.

Ref. [33] analyses a different plasma parameter range, starting with an initial radius of ~ 1 m and system dimensions of ~ 14 m in radius. Since the pickup coil is located at a radius of ~ 9 m, a low initial magnetic field is sufficient to stop the plasma close to the coil radius. Therefore, a magnetic field of ~ 0.57 T is used in Refs. [33]. We have examined the case of a compact system having a radius ~ 1.5 m. That is the plasma expansion radius is much smaller than that described in Refs. [25–27], leading to higher-density and higher-pressure plasma ($\sim 10^7$ Pa) with an initial radial expansion velocity $\sim 10^7$ m/s. This requires a higher magnetic field (~ 5 T) to extract enough energy from the plasma.

Also, earlier work in this area [25–27, 33] had considered separate coils for producing the primary field and for carrying the induced (output) currents. The

present study is the first to consider a single coil. This makes the design similar to conventional explosive driven helical generator. Also, the complexity of two coils with a cylindrical shielding conductor between the coils [25–27, 33] can be eliminated. However, since the same coil is used for providing initial magnetic field and energy extraction, it is necessary to have fast switching devices to isolate the primary power supply.

Most of the existing works are based on simple analytical (Zero-D) models except the two-dimensional (2D)-PIC simulations given in Ref. [26,27]. The non-uniform deformation of plasma (larger expansion along the axial direction) is reported in Refs. [26,27]. Therefore, it is necessary to analyse the plasma dynamics in 2D. Apart from this, for a detailed analysis of plasma RT instabilities the development of 2D scheme is necessary. In Refs. [26,27], the simulations are started with an initial plasma radius of about 1 m and the plasma is allowed to expand up to a radius of ~ 14 m. That is the plasma had already expanded to a very low density. Therefore, PIC simulations are sufficient to study the plasma dynamics. However, for the present work, since we are dealing with a higher-density plasma (hence fluid-like), MHD simulations are required. We have used a 2D axisymmetric MHD model coupled self-consistently to an external circuit equations with load. To the best of our knowledge, it is the first time such a calculation is performed for an MFC system driven by spherical plasma armatures.

The analysis of MHD instabilities on the surface of the plasma armature is one of the objective of this work. The instability analysis (using 2D PIC simulations) reported in Refs. [26,27] are for comparatively lower initial magnetic field and larger plasma expansion. We have performed a detailed 2D instability analysis (random and single mode perturbation analysis) for different values of initial perturbation amplitudes and wavelengths using 2D MHD simulations.

Finally, we examine the utility of Finite-Difference Time-Domain (FDTD) scheme for electromagnetics for studying MFC systems. This is done by including velocity-dependent terms in the standard FDTD equations. The validated algorithm is then applied to a sample problem involving plasma armatures. To our knowledge, this is the first application of this powerful technique to such systems.

1.4 Plan of the thesis

The objective of this thesis work is to computationally examine the physics of expanding plasma armatures using numerical schemes based on MHD as well as Finite Difference Time Domain (FDTD) approaches.

During the expansion phase, for typical system and plasma parameters used in this work (discussed earlier in Sec. 2.3), the characteristic scale length of the plasma is much larger than the ion skin-depth and orbit radius. Hence plasma dynamics can be modeled using single fluid MHD equations assuming quasi-neutrality in the plasma. In Chapter 2, therefore, we have presented a study of plasma dynamics across the magnetic field and the energy conversion efficiency using a 2D Lagrangian MHD scheme coupled self-consistently with an external circuit equation solver [52]. The main objective is to introduce the concept of MFC inside a solenoid and its potential application as a direct energy conversion scheme to convert plasma kinetic energy into pulsed electrical energy. A brief discussion of a few important theoretical and technical issues that need to be addressed are also included. The work includes the development of a 2D Lagrangian hydrodynamic code and an external circuit equation solver using the filamentary model [49, 50] to update the coil and plasma currents. The modules are self-consistent coupled, and an analysis performed of the energetics of the proposed system.

Numerical studies described in Chapter 2 have shown that plasma expansion in an MFC system is highly non-uniform due to magnetic deceleration. In particular, the plasma exhibits non-spherical expansion, i.e., axial expansion of the plasma is higher than radial expansion. Towards the end of the expansion phase, Magnetic Rayleigh-Taylor (MRT)-like instabilities are observed at the plasma surface. Under conditions where such instabilities reach large amplitudes, there are large distortions of the plasma shape, hence Lagrangian algorithms fail. In order to study these effects in detail, it is necessary to develop an Eulerian MHD model.

In Chapter 3, we have described the details of an Eulerian MHD model [82] developed to study large deformation plasma dynamics in the proposed MFC system. The plasma expands into an ambient medium (vacuum or low density material). The treatment of mixed computational cells (a cell containing more than one material) is therefore necessary for the Eulerian method. Therefore, a multi-material formulation based on a volume-of-fluid (VOF) method [60] is used. The details of the benchmarking of the code against known results and the convergence analysis are also given in Chapter 3. The details of the new volume-of-fluid (VOF) algorithm developed [60] for material interface tracking are given briefly in Appendix A. Details of the analysis of large deformation plasma dynamics in the proposed MFC system are also given in Chapter 3. We have also demonstrated the observation of magnetic Rayleigh-Taylor (MRT) instability on the surface of the plasma near the stagnation time by using this new computational tool.

The simulation results given in Chapter 3 start with an unperturbed initial plasma state, so that instabilities are seeded by numerically-produced perturbations. In reality, perturbations with different wavelengths and amplitudes would exist on the surface of the plasma sphere even before it starts expanding. For a real-life system, therefore, it is necessary to study the growth of pre-existing

perturbations with different wavelengths and amplitudes. Therefore, Chapter 4 is exclusively dedicated for this instability analysis for different applied perturbations and initial plasma conditions. The algorithm described in Chapter 3 was able to handle large plasma deformations in the MFC system. However, for the present instability analysis, it demands a prohibitively large number of cells in the simulation. This is due to an order of magnitude difference between the different scale lengths involved in the system, such as MFC system dimensions of the order of few meters, plasma initial perturbation amplitude α_{in} of the order of few μm and wavelength λ ranging from few mm to cm. Therefore, we have used an unstructured Lagrangian scheme [98] with sub-zonal mass and pressure [99] for this analysis. In Chapter 4, we provide details of an unstructured Lagrangian scheme and the results of instability analysis with random, single and multi-mode perturbations.

In Chapter 5, we examine the utility of a three-dimensional Finite-Difference Time-Domain (FDTD) scheme for electromagnetics for studying magnetic field diffusion in complex geometries relevant to MFC systems [53, 54]. As a first step, the FDTD scheme is applied to static problems, in particular to determine accurate resistance and inductance of simple magnetic field coils, taking account of skin and proximity effects. In the second step, the algorithm is extended to study MFC systems involving material movement by including velocity-dependent terms in the standard FDTD equations. This work is the first attempt at extending the FDTD method for electromagnetic problems involving material motion. Finally, in order to demonstrate the utility of the powerful FDTD-based scheme to MFC problems, we have applied it to a sample problem involving plasma armatures [25]. Details of these steps and related issues are discussed in Chapter 5.

Finally, in Chapter 6, we present the overall summary/conclusions of the work reported in the present thesis and suggestions for future work.

Some of the simulations [53, 54] reported in this thesis required large computing power and were carried out on a parallel computing facility set up by the Computational Analysis Division in BARC Visakhapatnam.

2

Analysis of energy conversion efficiency and related issues using Lagrangian MHD simulations

2.1 Introduction

In this chapter, we present results from two-dimensional MHD simulations to explore the possibility of direct energy conversion of plasma kinetic energy into electrical pulses. Details of the proposed concept and a brief summary of related works are given in Chapter 1. The major differences with earlier works described in Chapter 1 are in terms of the parameter regime, the external source of the seed magnetic field and the computational model, as explained in Chapter 1. For the present study, we assume that the load is predominantly inductive – this is a major difference from earlier works [25–27], where a resistive or capacitive load was considered. A brief discussion on a few important theoretical and technical issues

that have to be addressed are given in the following sections. Also, we report the overall efficiency of the system with different load conditions.

2.2 Computational model

During the expansion phase, $L_n \gg r_{Li}, c/\omega_{pi}$ and r_D ; where L_n is the characteristic scale length of the plasma, $r_{Li} \sim v_i/\Omega_i$ is the ion Larmor radius, $v_i \sim (T_i/m_i)^{1/2}$ is the ion thermal speed, Ω_i is the ion cyclotron frequency, ω_{pi} is the ion plasma frequency and r_D is the Debye radius. Similarly, the time scale (plasma radial expansion time $\sim t_s$) is longer than an ion cyclotron period. Therefore, a single-fluid MHD model (assuming quasi-neutrality) can be used to describe the plasma. In addition to this, we assume that the plasma behaves like an ideal gas. The governing equations are as follows [39]:

$$\frac{\partial \rho}{\partial t} + \nabla \cdot (\rho \vec{u}) = 0 \quad (2.1)$$

$$\rho \left(\frac{\partial \vec{u}}{\partial t} + \vec{u} \cdot \nabla \vec{u} \right) = -\nabla p + \vec{J} \times \vec{B} \quad (2.2)$$

$$\frac{\partial}{\partial t} \left(\rho I + \frac{\rho u^2}{2} \right) + \nabla \cdot \left[\rho \vec{u} \left(I + \frac{u^2}{2} \right) + p \vec{u} \right] = 0 \quad (2.3)$$

where, ρ is the density, \vec{u} is the velocity vector, p is the pressure, \vec{J} is the current density, \vec{B} is the magnetic field and I is the internal energy. We have neglected the resistive heating term required in Eq. 3.3, because of the high conductivity of the plasma and short time scales involved. Similarly, the energy flux from thermal heat conduction is neglected.

The two-dimensional MHD equations are solved using a locally-developed 2D-

Lagrangian code based on the formulations given in [38]. The code uses an explicit finite-difference scheme for hydrodynamic equations.

For the present geometry setup, only the θ -component of current exists in both coil and plasma. A filamentary model, similar to the formulations given by Novac et al. in Refs. [49–51], is used to update the coil current and the induced currents in the plasma. This model includes the effect of plasma dynamics. For this, each coil turn is broken up into a number of coaxial circular loops. Similarly, each computational cell used to describe the plasma region in the hydrodynamic calculation is assumed to be a circular loop with a rectangular cross-section. Each such loop may carry a different current, which is updated self-consistently using coupled circuit equations given below:

$$L_T \frac{dI_c}{dt} + \sum_{j=1}^{N_a} M_{cj} \frac{dI_j}{dt} = -I_c R_T - \sum_{j=1}^{N_a} I_j \frac{dM_{cj}}{dt} \quad (2.4)$$

$$M_{cj} \frac{dI_c}{dt} + L_j \frac{dI_j}{dt} + \sum_{i,j=1;i \neq j}^{N_a} M_{ij} \frac{dI_i}{dt} = S_j \quad (2.5)$$

$$S_j = -I_j R_j - \sum_{i,j=1;i \neq j}^{N_a} I_i \frac{dM_{ij}}{dt} - I_c \frac{dM_{cj}}{dt} - I_j \frac{dL_j}{dt} \quad (2.6)$$

where, L_T , R_T and I_c are the total inductance (coil+stray+load), total resistance and coil current respectively. L_j , R_j and I_j are the self-inductance, resistance and induced current respectively for the j^{th} plasma filament. M_{ij} is the mutual inductance between the plasma filaments i and j . Similarly, M_{cj} is the mutual inductance between coil and j^{th} plasma filament. The coupled Eqs. 2.4 and 2.5 are solved simultaneously. The cell-centered current density is obtained by dividing the current obtained using Eq. 2.4 and 2.5 by the area of the computational cell in the R-Z plane, which represents a fluid element. The node-averaged current

density is then calculated to estimate the Lorentz force. The self-inductance of a circular loop and the mutual inductance between the loops are calculated using analytical equations in terms of elliptic integrals. The magnetic field at any given point in the computational domain is calculated using the contributions from all plasma filaments and the coil loops. The field from a circular filament loop is calculated using an analytical formula in terms of elliptic integrals. The self and mutual inductances of the current loops can be calculated more accurately by using standard Finite-Element method [141]. However, for the present system involving large number of current carrying filaments, the application of Finite-Element method [141] to calculate the self and mutual inductances of the filaments at each time-step will be computationally expensive. Therefore, we have used analytical formula in terms of elliptic integrals. The estimated maximum error w.r.t. to the results of Finite-Element method [141] was about 2–3 %.

2.3 Initial conditions

A brief discussion on typical initial conditions used in this work has been given in Chapter 1. However, some important parameters are given below for the sake of completeness. The initial plasma kinetic energy and mass are taken as 140 MJ and 6 milligrams (mg) [25–27, 31, 32] respectively. Initially, the plasma undergoes free expansion in the applied magnetic field, since the kinetic pressure, p_k is far higher than the magnetic pressure, p_B (high $\beta = p_k/p_B$ plasma). Considering this fact, we start our simulation with an initial plasma radius of about 1.0 cm. We have taken the coil axial length as approximately 2-4 times the radius. The coil radius (r_c), length (l_c) and no. of turns (n_c) are 1.5 m, 4.5 m and 30 respectively. For higher efficiency, the plasma should stagnate at a radius, $r_p \sim r_c$. The seed

field should be sufficient to stop the plasma expansion within this distance, which means that the initial magnetic field has a strong effect on the recovery efficiency. An initial magnetic field of ~ 5 T is assumed, corresponding to an initial current of ~ 750 kA.

Ideally, the magnetic field profile inside the plasma sphere, at the time simulation starts, must be evaluated by considering magnetic field diffusion into the sphere as it expands rapidly across the magnetic field, from an initial radius $\sim 200\mu\text{m}$ to 1 cm. However, magnetic field diffusion into the plasma sphere during those early time-scales can be neglected, due to high temperature and electrical conductivity. Hence we assume a uniform magnetic field through the sphere at $t=0$. The subsequent evolution of this field, as the sphere expands, is calculated using the frozen-field approximation, which conserves total magnetic flux ($\propto B_0$) connected with each plasma mass element. We have examined the difference in plasma dynamics as well as overall system efficiency for two cases. The first case assumes that the initial magnetic field inside the plasma is (and therefore remains) zero at all times. The second case assumes a constant initial magnetic field in the plasma, which is evolved according to the frozen-field approximation. We have found that the choice of initial B_0 has negligible effect on the overall system dynamics and efficiency for the system parameters considered in this work. Hence, in the rest of this chapter, we have assumed a uniform initial magnetic field in the plasma.

We have also analyzed the dependence of overall system efficiency on the initial radius of the plasma sphere, r_p . Negligible variation is observed for $0.01\text{m} \leq r_p \leq 0.1\text{m}$. Therefore, in the present study, we have assumed an initial plasma radius of $r_p = 1\text{cm} \ll r_c$. The initial coil and load inductances (L_c and L_L) were ~ 1.4 millihenry (mH) and 1.0 mH respectively.

2.4 Issues to be addressed

In this section, we discuss a few theoretical and technical issues that need to be addressed.

2.4.1 MHD instabilities

Performance degradation due to MHD interchange instabilities of the expanding plasma are a major concern with this concept. The plasma expanding into the magnetic field can undergo Rayleigh-Taylor (RT) instability. The instability amplitude should be small enough so that the expanding plasma layer is stable at least during first expansion phase. From MHD theory, the RT instability growth rate $\gamma = \sqrt{g/L_n}$; for $kL_n \gg 1$ and $\gamma = \sqrt{kg}$; for $kL_n \ll 1$, where, k is the wave number, g is the deceleration and L_n is the density scale-length.

From the simulation, the average deceleration and density scale-length are found to be $1 \times 10^{14} \text{ ms}^{-2}$ and 0.2 m respectively. The large Larmor radius (LLR) effect on RT instability growth rate [47, 48] can be neglected during the first expansion phase for the present case. This is because the ratio $r_{Li}/L_n \ll 1$, where $r_{Li} \sim 10^{-3} \text{ m}$ is the time-averaged ion Larmor radius, defined as the ratio of thermal expansion velocity to the cyclotron frequency based on the magnetic field. The growth rate thus evaluated for the wavelength perturbations in the range 10^{-3} to 0.5 m is found to be of the order of 10^7 s^{-1} , which is comparable with the inverse of plasma expansion time. Therefore, we expect the RT instability may not be so critical for *small amplitude* initial perturbations during the first expansion phase of the plasma.

Similarly, in Ref. [40], Winske has reported a detailed theoretical and numerical study which could explain the experimentally observed results (see references given

in Ref. [40]) on the development of flute modes (similar to RT instability) on expanding plasma clouds. From various experimental results observed and numerical simulations performed, Winske [40] has concluded that the single most important parameter which determines the evolution of flute mode instability is the ratio of ion Larmor radius, r_{Li} to the plasma confinement radius, R_w . When $r_{Li}/R_w > 1$, large flute modes are observed which shows nonlinear dynamics. For $r_{Li}/R_w \leq 1$, the flute modes are smaller and the non-linear surface modes appear only at the time of maximum expansion. When $r_{Li}/R_w \ll 1$, only a weak instability is detected. According to Winske [40], such results are consistent with linear theory. A detailed discussion, including non-linear effects, can be found in Ref. [40]. For the present case, the ratio r_{Li}/R_w is $\sim 10^{-3}$. Therefore, only a weak instability is expected during the first expansion phase of the plasma.

The MHD interchange instabilities, however, need to be analysed separately with different initial conditions of applied perturbations. In Chapter 4, we have presented this analysis in detail.

2.4.2 Choice of the load

Depending on the application, the load can be purely resistive, inductive, capacitive or a combination of these. Most of the earlier works have examined the case of a purely resistive load. Higher efficiency is achieved by using an optimized capacitor-diode load where a capacitor is switched to the coil circuit at the moment of peak current in the coil [26]. However, this demands a coil discharge on a timescale which is short relative to that of plasma expansion time [27] ($\frac{\pi}{2}\sqrt{L_c C} \ll t_p$, where t_p plasma expansion time $\sim 10^{-7}$ s, L_c is the coil inductance and C is the capacitance).

For the present study, we assume that the load is predominantly inductive – this is an important difference as compared to earlier works [25–27], where a resistive or

capacitive load was considered. The inductive load could be electrically decoupled from the pickup coil after the completion of first expansion phase of the plasma and could be subsequently switched into a different load (not shown in Fig. 1.4) for $t \geq t_p$. The decoupling of the inductive load from the pickup coil will be necessary due to the fact that, after the *first expansion phase* of the plasma, the amplitude of perturbations on the irregular surface of the plasma caused by RT instability is likely to be so large that the plasma can not maintain its stability [33]. The remaining plasma energy in the form of inductive energy of its diamagnetic current will convert into plasma heating due to the penetration of the field into the plasma at a late stage.

In this work, we focus on system performance with an inductive load. However, to facilitate comparison, we have also performed a sample simulation with a resistive load.

2.4.3 Coil inter-turn breakdown

Since the inductive energy recovery system proposed here has a total operational time less than $\sim 0.2 \mu s$, extremely high voltages (few hundreds of MV) across the coil are expected. Ultra-high voltages ~ 500 MV were predicted in earlier work [25, 26]. One possible method to prevent the inter-turn voltage break-down is to use magnetic insulation. The concept of magnetic insulation has been investigated by many authors, such as Hirsch [43] and Winterberg [41]. Mima et al. [25] has discussed the effect of magnetic insulation to reduce the possibility of electric breakdown between neighboring pickup coil segments. Therefore, in Ref. [25], they expected the breakdown voltage to be very high (~ 10 MV) for their design. The application of this concept in high voltage transformers have been investigated by Winterberg [42], Novac et al. [44] and Istenic et al. [45]. Magnetic insulation

has proved to be the practical technique for use in the development of high-voltage components like transmission lines and plasma opening switches etc (see Ref. [44] and References therein). The magnetic field required for insulation can either be provided externally or by the system itself (magnetic self-insulation). Magnetic self-insulation is more appropriate for the present system. More details on magnetic self-insulation method used in high voltage helical transformer coils can be found in Ref. [44, 45].

From our simulation results for the present case, the maximum average inter-turn voltage is found to be ~ 25 MV, which is higher than the break-down voltage ~ 0.5 MV obtained using the equations provided in Ref. [45, 46] without considering magnetic insulation. Considering magnetic insulation, the relation between the breakdown voltage (V_b) and magnetic field is given by [43, 45]

$$B \geq \sqrt{\frac{2mE}{ed_g}} \quad (2.7)$$

where, $E = V/d_g$ is the electric field, V is the voltage and m and e are the mass and charge of an electron. Using this formulation, Novac et al. [44, 45] have studied the application of magnetic self insulation to eliminate breakdown between the coil turns of a helical transformer. For helical coils, the inter-turn electric field is along the axial (E_z) direction. Therefore, the radial component of magnetic field (B_r) should be used in Eq. 2.7, assuming axisymmetry. From the simulation results, we have found that the magnetic field component, $B_r \geq 0.25$ T between the coil turns. Therefore, the breakdown voltage $V_b \geq 125$ MV for $d_g = 0.15$ m. This is higher than the average inter-turn voltage (~ 25 MV) obtained in our simulation. A detailed discussion, including the effect of field variation along the pitch of the coil, is given in Sec. 2.5.

Finally, with an optimized design having longer plasma expansion time, e.g. by

increasing the coil mean radius, and increasing inter-turn separation (pitch) of the coil, the voltage level can be reduced to an acceptable level. A brief discussion of this is provided in later sections.

In short, we have listed a few methods to mitigate the problem of inter-turn break-down. However, a detailed optimization study in this direction may be required to maintain the internal voltage levels within the acceptable range of existing technologies.

2.5 Results and discussion

The initial conditions used are within the range of parameters given in Sec. 2.3. The plasma sphere is assumed to be centered at $(r,z) = (0,0)$ and because of the symmetry only one quarter of the system is simulated. Fig. 2.1 shows the different stages of plasma expansion.

In the early phase of plasma dynamics, the plasma sphere has high initial directed velocity $\sim 10^7 \text{ ms}^{-1}$ and moderately high plasma β value. Therefore, it expands freely across the magnetic field (radial direction) as well as along the magnetic field (axial direction). Expansion perpendicular to the field is decelerated by the progressive increase in magnetic field due to magnetic flux compression. Expansion along the axial direction, at radii close to the axis, is not significantly affected. This is because motion along the z-direction is opposed by B_r , and $B_r \rightarrow 0$ for $r \rightarrow 0$. Hence the plasma sphere tends to elongate in the direction of the magnetic field. This can be readily seen from the density contour plots of Fig. 2.2 at different times. This is consistent with the earlier reported results [25–27]. Pure Lagrangian computational scheme fails when Large deformations occurs. Consequently, the simulations presented here are performed with a coarse mesh

(only near the axis) and the calculations are stopped when the radial expansion of the plasma comes to a halt at $z = 0$ location. This does not significantly change the calculated system efficiency. We see that plasma expansion nearly stops at a radius ~ 1.23 m at $z = 0$ location. The plasma stopping radius can be roughly obtained by equating the magnetic energy excluded by the plasma to the initial plasma energy; $(4\pi r_{max}^3/3)(B^2/2\mu_0) \sim E_p$, where E_p is the initial plasma energy. This leads to $r_{max} \sim 8.5 \times 10^{-3}(E_p/B^2)^{1/3}$. The maximum radius thus evaluated is ~ 1.5 m, which is higher than the r_{max} obtained from simulation. The analytical estimate for r_{max} is likely to over estimate the radius since it has neglected the field amplification due to magnetic flux compression. However, considering the average magnetic field during the expansion phase (~ 6.3 T), the r_{max} evaluated is ~ 1.28 m, which is close to the numerical result.

The plasma expansion radius along the field lines can be roughly estimated (neglecting the deceleration produced by magnetic field component, B_r) using the typical expansion velocity $\sim 10^7$ m/s and total radial expansion time $\sim 2 \times 10^{-7}$ s, which is found to be ~ 2 m and is consistent with the simulation value ~ 1.99 m.

The time evolution of plasma radius and the magnetic field on the surface of the plasma at $z=0$ are shown in Fig. 2.3. As mentioned earlier, because of the high initial directed velocity and β value, the early stage of plasma expansion is less affected by the magnetic pressure. However, as the plasma expands, its pressure and density decreases continuously and the magnetic field inside the compression volume increases. Therefore the deceleration by the magnetic pressure dominates in the later stages of expansion. It is clear from Fig. 2.3 that the magnetic pressure tends to dominate at a time $t \sim 0.1\mu\text{s}$.

Fig. 2.5 shows the radial velocity profile at different times for an axial location $z=0$. The initial velocity profile is almost linear and then decreases due to magnetic

pressure. The velocity at the outer radius of the plasma decreases faster (high magnetic field on the surface) and goes to zero at the ‘stagnation point’. The magnetic field on the plasma surface at the stagnation point is 7.6 T. The radial profile of the normalized density, for the $z=0$ plane, and at different times, is shown in Fig. 2.4. The plasma forms a near shell-like geometry at the stagnation point, where the outer surfaces slow down due to magnetic pressure and the inner region catches up with the outer region, as shown in Fig. 2.2 and 2.4. The plasma density scale length, L_n varies over the range ~ 0.1 to 0.2 m.

One important parameter which determines the efficiency of the flux compression system is the ratio of magnetic diffusion time ($t_d = \mu_0 \sigma L^2$) to the compression time ($t_c \sim 10^{-7}$); where L is the system dimension and σ is the conductivity. The necessary condition is that this ratio, $R_e = t_d/t_c \gg 1$. For the present case $R_e \sim 10^7$ (for $L \sim 0.1$ m and resistivity at stagnation point $\sim 10^{-8} \Omega\text{m}$), indicating negligible magnetic field diffusion over the time-scales of interest.

Fig. 2.6 shows the spatial variation of the magnetic vector potential, A_θ . This represents field line contours inside the coil, including the plasma region, at different times. The magnetic field is given by: $B_z = \frac{1}{r} \frac{\partial \psi}{\partial r}$, where $\psi = rA_\theta$ is the stream function. The magnetic field outside the plasma is amplified by magnetic flux compression, while the field inside the plasma gets reduced by the diamagnetic (θ) current produced by the plasma. As expected, the maximum magnetic field between the coil and plasma, inside the flux compression volume, is observed at the axial midplane $z=0$.

Fig. 2.7 shows the time variation of normalized electrical energy stored in the load, coil current and inductance. The normalizations are performed with respect to their initial values (initial inductive energy in the load is $E_{L0}=281$ MJ). The plasma energy conversion efficiency is defined by $\eta_p = \frac{E_{Lf}-E_{L0}}{E_p}$, where E_{Lf} and

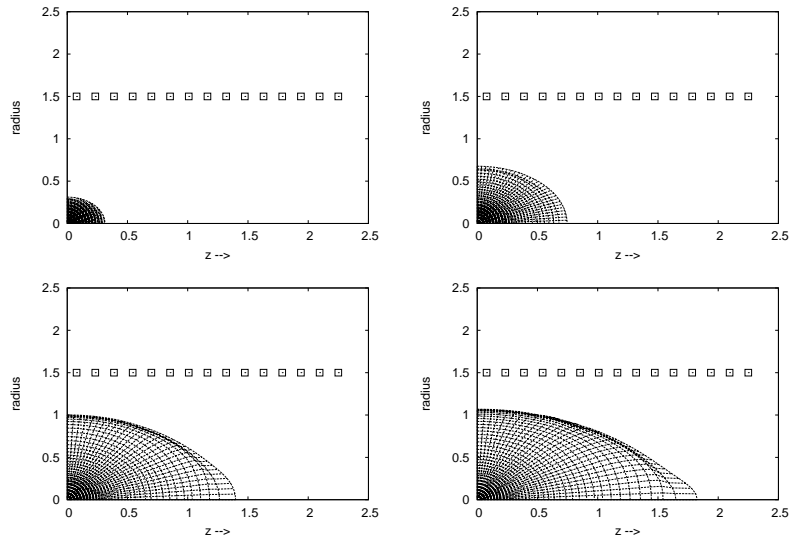


Figure 2.1: The Lagrangian mesh which shows the different stages of plasma expansion ($t=0.03 \mu\text{s}$, $0.08 \mu\text{s}$, $0.15 \mu\text{s}$ and $0.18 \mu\text{s}$). The square dots represents the coil loop locations. Only one quarter of the system is shown because of the symmetry.

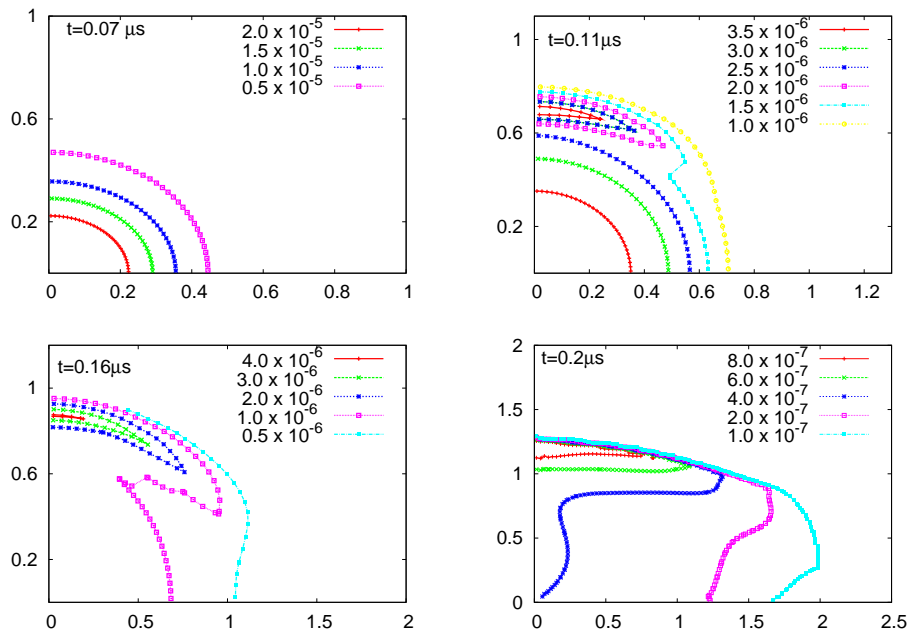


Figure 2.2: Evolution plasma density (kg/m^3) contours (the contour lines are spaced linearly) at different times during expansion phase. Only one quarter of the system is shown because of the symmetry.

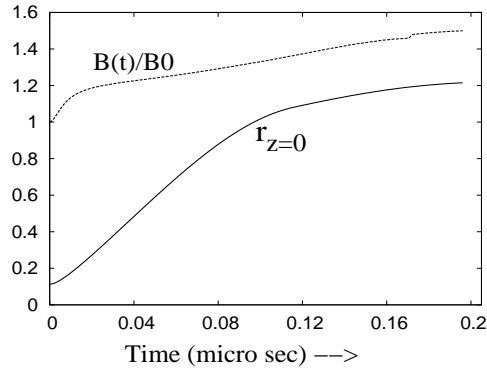


Figure 2.3: The variation of plasma radius at $z = 0$ and normalized magnetic field with respect to initial magnetic field ($B_0 \sim 5$ T).

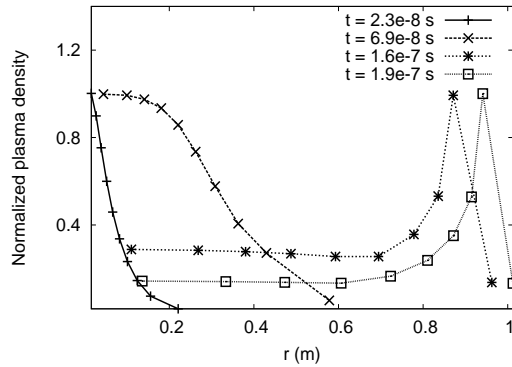


Figure 2.4: The radial variation of normalized density at different times for $z=0$ plane. The normalization factor is the maximum value of the density along the radial direction for a given time.

E_p are the final load and initial plasma energy. The plasma energy recovered in the inductive load is 97 MJ, corresponding to an efficiency of 69 %. The inductive energy increase in the coil and the residual plasma energy (kinetic + internal energy) were 15 MJ and ~ 28 MJ respectively. We have defined the *overall system efficiency*, η_s for $t \leq t_p$ as below:

$$\eta_s = \frac{E_L}{E_i + E_p} \quad (2.8)$$

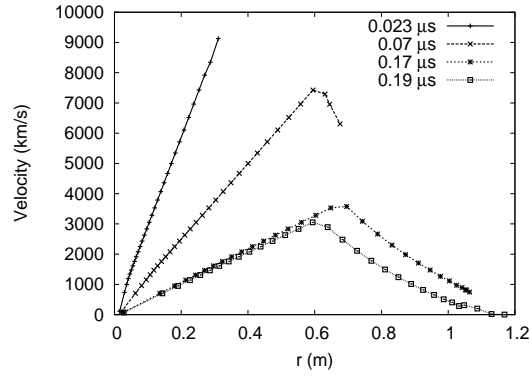


Figure 2.5: The radial velocity profile at different times for $z=0$ plane.

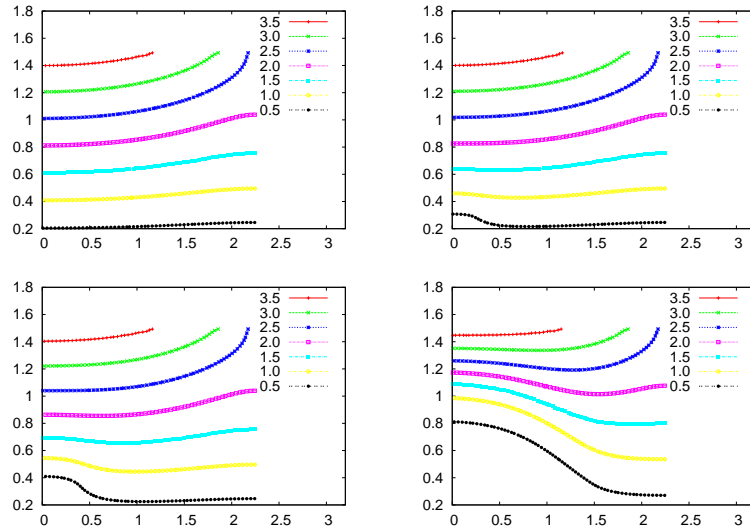


Figure 2.6: Contours of magnetic field lines represented by magnetic vector potential (A_θ in Tesla-meter), at different times ($t=0$, $0.056\mu s$, $0.08\mu s$ and $0.18\mu s$)

where, $E_i = \frac{1}{2}(L_c + L_L)I_0^2$ is the total initial electrical energy in the system. Note that E_i is defined after the exclusion of the capacitor by the simultaneous switching action of switches s_1 and s_2 , and t_p is the time required to complete the first expansion phase. The above expression assumes that the inductive energy remaining in the coil (not the load) cannot be recovered after the completion of first expansion phase. Also, we assume the load is decoupled from the system

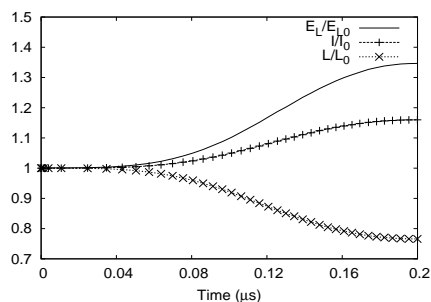


Figure 2.7: Time variation of normalized load energy (E_L/E_0), coil current (I/I_0) and system inductance (L/L_0); where E_{L0} , I_0 and L_0 are the initial load energy, coil current and inductance respectively.

for $t \geq t_p$, as discussed earlier. The overall system efficiency, η_s calculated using Eq. 2.8 is found to be equal to 56 %. The peak coil current obtained is 870 kA.

The effect of load inductance on the conversion efficiencies (η_p and η_s) is shown in Table 2.1. It is clear from the table that higher efficiency is achieved as load inductance increases. For the cases with low load inductance compared to the coil inductance, the energy efficiency in the load is found to be low. This is because most of the energy will be inductively stored in the coil. It is worth noting that as the load inductance increases, despite higher η_s value, the initial electrical energy requirement increases since we are keeping the initial magnetic field constant at ~ 5 T. This is because we assume that the load is active in the circuit during the priming of the system.

Next, for the sake of comparison, we have analysed the system efficiency with different resistive loads. Table 2.2 summarizes these results. The efficiency increases as the load resistance increases and tends to saturate, which is consistent with the observations reported in Ref. [27], where the maximum efficiency was reported with a resistive load of $\sim 1400 \Omega$. In contrast to inductive loads, the initial energy required for different cases listed in Table 2.2 are the same ~ 400 MJ.

Next, we have examined the variation of plasma stopping radius, r_{max} at the

Table 2.1: System performance for different inductive load conditions. L is the load inductance, E_i is the initial electrical energy, E_L is the inductive energy stored in the load, and η is the conversion efficiency.

L (mH)	E_i (MJ)	E_L (MJ)	η_p (%)	η_s (%)
0.05	407	8	5.7	5.5
0.1	421	16	11.5	10
0.3	478	41	29	26
0.5	534	63	45	38
0.7	590	79	56	47
1.0	675	97	69	56

Table 2.2: System performance for different resistive loads. R is the load resistance, E_L is the resistive energy across the load, and η is the conversion efficiency. The total initial energy is 400 MJ.

R (Ω)	E_L (MJ)	η_p (%)	η_s (%)
100	8	9	2
250	31	22	7
500	61	43	15
750	90	64	22.5
900	99	70	24.7
1000	101	72	25

axial midplane ($z=0$) for different initial magnetic fields. The coil radius, length and number of turns are 3 m, 9 m and 30 respectively. The initial magnetic field is varied from 1.4 to 6.3 T. A comparison of simulation results with a simple analytical expression described earlier this section is shown in Fig. 2.8. Reasonable agreement is found, except for the cases with low initial magnetic field. The difference in results for the cases with low magnetic field is due to the fact that the analytical expression neglects the effect of field amplification, and hence over-estimate the stopping radius. This effect will be higher for the cases with low initial magnetic fields, where the radial plasma expansion will be higher and likely to have considerable difference between initial and final magnetic fields. The variation of B_f/B_0 is shown in Fig. 2.8, where B_0 and B_f are the initial and final magnetic fields. Another reason for the difference in simulation results and

analytical result is the assumption of uniform expansion of the plasma sphere while deriving the expression for r_{max} . In reality, the plasma sphere expands non-uniformly, expanding more along the axial direction. This leads to underestimation of r_{max} at $z=0$.

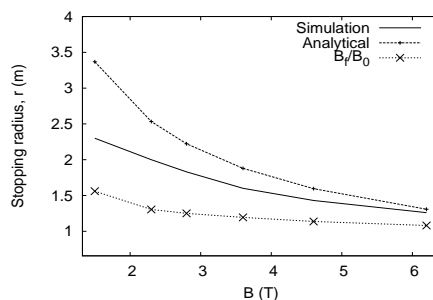


Figure 2.8: Variation of plasma stopping radius for different values of initial magnetic fields

The time evolution of coil inter-turn voltage for typical system dimensions described in the beginning of this section (Case-1) is shown in Fig. 2.9. The change in flux inside the coil is high during the period where the magnetic deceleration is small ($t \leq 0.1 \mu s$). The voltage increases to a peak value of about ~ 27 MV (peak electric field of 180 MV/m, for pitch of the coil equal to 0.15 m) during this period and then decreases continuously due to the magnetic pressure driven deceleration of the plasma expansion. This is because the change in flux decreases due to deceleration of the plasma. An optimized design with appropriate coil dimensions and initial magnetic field can reduce the average inter-turn voltage. For example, with an increase of 33 % in coil radius (case-2), with an initial magnetic field of 3.8 T and coil length equal to three times the coil radius, the inter-turn voltage decreases to 19 MV ($E=95$ MV/m); corresponds to a 42 % decrease in the voltage (see Fig. 2.9, case-2). The electric field between the coil turns are reduced by 2.8 times. However, with increased coil dimensions the initial energy required will

increase by 20 %. Similarly, keeping the system dimensions are the same as case-1 and increasing the magnetic field from 5 to 6.4 T (case-3) the voltage and electric field are reduced by 12.5 % despite the short operational time (see Fig. 2.9, case-3). Even though the internal voltages are within the range of values discussed in Sec. 2.4.3, a detailed optimization study in this direction is needed to maintain the voltage levels within the acceptable range without reducing overall system efficiency.

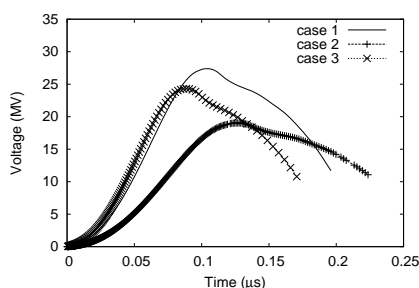


Figure 2.9: Time evolution of coil inter-turn voltage (MV) for different cases with load inductance 1.0 mH

Finally, we have analysed the magnetic self-insulation process for the entire pulse duration. Eq. 2.7 can be written as $B_r d_g \geq \sqrt{2mV/e}$, where V is the inter-turn voltage. Integrating this equation along the pitch of the coil turn (to account for the variation of B_r along the axial direction between coil turns), the following equation can be derived as a necessary condition to satisfy magnetic self-insulation criteria [44, 45].

$$\alpha_V = \left(\sqrt{2mV/e} \right) / \left(\int_0^{p/2} B_r(r_c, z) dz \right) \leq 1 \quad (2.9)$$

where, r_c is the coil radius and p is the pitch. It is known that that the magnetic component, B_r , produced by a helical coil is smallest near the center of the coil. Therefore, the present analysis concentrates on this region. However, for purposes

of comparison, we have provided the results obtained for two turns located at the axial end of the coil. The variation of α_V , the ratio given in Eq. 2.9, for two different locations (center and axial end point) are shown in Fig. 2.10. It is clear from the figure that the criteria for magnetic self-insulation is fairly satisfied. It is worth noting that the factor α_V is high (\sim a factor of 2) for the turns located at the center of the coil.

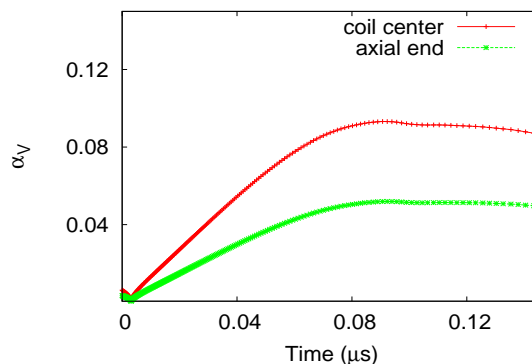


Figure 2.10: Time evolution of α_V defined in Eq. 2.9 for two different locations. It is clear that, the ratio $\alpha_V \leq 1$. See text for the discussion.

2.6 Limitations of the study

In the present work we have mainly focused on the introduction of the concept, the dynamics of plasma across the magnetic field and the energy conversion efficiency. Therefore, similar to earlier works, we have started our simulation from the time when plasma is created and the initial magnetic field is setup. Also, we have not considered the implications of D-3He systems for inertial fusion energy (IFE) drivers and targets. We have assumed that the fast opening switches capable of absorbing hundreds of MJ energies can be realized with existing or near-term engineering technologies. We assume such systems and technologies will be devel-

oped in the near future. The main limitation of this concept is the handling of ultra-high voltages across the conductors. This fact is also reported in most of the earlier works. The optimization study of the system to reduce the coil inter-turn voltage (increasing operational time), analysis of possible energy extraction after first expansion phase, conversion of residual energy stored in the coil (not the load), detailed analysis of radiation effects on shielding material, electromagnetic stress analysis acting on the coil, etc. are omitted in the present study. Therefore, the system dimensions and parameters used in the simulations may vary for an optimized system. The present study should, therefore, be treated as a first exploratory step.

2.7 Conclusions of this study

A conceptual study of magnetic flux compression inside a cylindrical coil by an expanding fusion plasma sphere have been performed numerically using 2D magneto-hydrodynamic (MHD) simulations. Preliminary theoretical analysis shows that, for an unperturbed initial plasma, MHD interchange instabilities would not grow during the first expansion phase of the plasma for typical system parameters examined here. A few important theoretical and technical issues that need to be addressed have been discussed.

It is observed that during the final stage of MFC, the plasma shape becomes distorted (non-spherical) due to non-uniform deceleration caused by the magnetic field outside the plasma sphere. In particular, there is elongation of the plasma in the axial direction. These effects, collectively, lead to a non-spherical expansion of the plasma with large deformation.

The concept can be used as a method to convert a part of fusion plasma kinetic

energy into pulsed electrical energy. An *overall system efficiency* of $\sim 56\%$ obtained for a typical system with appropriate load conditions. Approximately 78% of plasma kinetic energy is converted into electrical energy with appropriate inductive load conditions. The system performances with different inductive and resistive load conditions are studied.

The simulation results indicate that the proposed system is promising in terms of overall efficiency. However, ultrahigh coil inter-turn voltages (~ 25 MV) are predicted. Therefore, the application of magnetic self-insulation to avoid coil inter-turn break-down is considered. Even though the voltage levels are within the theoretically acceptable range, a detailed optimization study is required to avoid coil inter-turn break-down without reducing the system efficiency.

3

An Eulerian MHD model to study the dynamics of plasma

3.1 Introduction

In Chapter 2, a Lagrangian computational method with a filamentary model [49, 50, 52] self-consistently coupled with external circuit equations is used to study the proposed MFC system. It is observed that during the final stage of MFC, the plasma becomes distorted due to non-uniform deceleration caused by the magnetic field outside the plasma sphere. Also, similar to Refs. [27, 33, 52], an elongation of the plasma ‘blob’ in the axial direction is observed since the plasma expands almost freely along the axial direction. These effects, collectively, lead to a non-spherical expansion of the plasma with large deformations. Consequently, the simulations described in Chapter 2 are stopped when the radial expansion of the plasma at the axial midplane ($z=0$) comes to a halt.

For a detailed analysis of plasma dynamics under non-uniform expansion, it is necessary to use an algorithm that can handle large material deformation. We

have, therefore, developed an Eulerian magneto-hydrodynamic (MHD) model to overcome the limitations of the computational model described in Chapter 2. Each step in the Eulerian algorithm involves a Lagrangian step followed by a remap to the initial mesh.

For the present geometry setup, only the θ -component of current exists in both the confining conductor and plasma. Similarly, the boundary conditions are either known explicitly or can be specified in terms of θ -component of current. In addition to that, all non-zero field components (B_r , B_z and E_θ) can be calculated using the θ -component of vector potential (A_θ). Therefore, for the present case, the MHD algorithm is formulated using A_θ . This offers some advantages. Firstly, only the θ -component of vector potential needs to be transported instead of two magnetic field components. Therefore the algorithm is computationally less expensive. Secondly, it may reduce the numerical error in the divergence of magnetic field ($\nabla \cdot \vec{B} \neq 0$) as compared to the case where two components of magnetic field are transported.

A few examples of MHD calculations using vector potential (relevant to the present context of MFC systems) can be seen in Refs. [57, 58]. In Ref. [58], the expansion of a cylindrical plasma across an external unconfined background magnetic field is studied using a vector potential formulation, where a second order differenced piecewise linear Lax-Wendroff method is used for both hydrodynamic and field transport calculations. A numerical study of an MFC system using vector potential formulation with an iterative solver to couple to the external circuit equations is given in Ref. [57], where the convective terms are solved using flux corrected transport (FCT) [59] and field diffusion is calculated using an explicit method.

In the present algorithm, magnetic field diffusion into the plasma sphere is solved implicitly using magnetic vector potential. This differs from the explicit

treatment used in Refs. [57,58]. The advection terms are computed using a second-order monotonic upwind scheme (MUSCL) due to van Leer [64] (a non-linear total variation diminishing (TVD) limiter); whereas a Lax-Wendroff method was used in Ref. [58] and an FCT scheme in Ref. [57]. The MUSCL scheme used here is less diffusive as compared to the Lax-Wendroff and FCT schemes. An iteration procedure, using a second-order-accurate alternating direction implicit (ADI) scheme, is used to calculate the field components in free space with the help of known boundary conditions at plasma and conducting surfaces. Our algorithm is formulated using a ‘dimensionally-split’ approach to extend the calculations to two-dimensions. Similarly, an ‘operator-split’ approach is used with three distinct phases in each direction (axial and radial): electromagnetic diffusion, Lagrangian motion (predictor-corrector scheme), and Eulerian advection or remap (back to initial mesh). To avoid unnecessary material diffusion, the interface between plasma and vacuum or low density material is explicitly tracked by using volume-of-fluid (VOF) method along with a multi-material hydrodynamic formulation (different from Refs. [57,58]).

The algorithm has been validated against the semi-analytical solutions of cylindrical magnetic convective-diffusion equations for MFC problems in the limit of large magnetic Reynolds number. The Reynolds number is defined as $R_m = \mu\sigma Lv$, where σ is the conductivity, L is the scale length and v is the liner velocity. A comparative study with different advection procedures (MUSCL scheme and methods given in Refs. [57,58]) is given. Following validation, the scheme has been applied to study the non-spherical expansion of plasma sphere in an MFC system, special attention being paid to plasma dynamics, field amplification due to MFC, magnetic field diffusion and the evolution of the plasma-vacuum interface for a typical set of system parameters.

3.2 Equations of MHD model

The plasma dynamics can be modeled using single fluid MHD equations. Also, we assume that the plasma behaves like an ideal gas. The governing equations are as follows [39, 52].

$$\frac{\partial \rho}{\partial t} + \nabla \cdot (\rho \vec{u}) = 0 \quad (3.1)$$

$$\rho \left(\frac{\partial \vec{u}}{\partial t} + \vec{u} \cdot \nabla \vec{u} \right) = -\nabla p + \nabla \cdot \vec{T}_{ij} \quad (3.2)$$

$$\frac{\partial}{\partial t} \left(\rho I + \frac{\rho u^2}{2} \right) + \nabla \cdot \left[\rho \vec{u} \left(I + \frac{u^2}{2} \right) + p \vec{u} \right] = -\vec{J} \cdot \vec{E} \quad (3.3)$$

$$\vec{T}_{ij} = \frac{1}{\mu_0} (B_i B_j - \frac{1}{2} \delta_{ij} B^2) \quad (3.4)$$

where, ρ is the density, \vec{u} is the velocity vector, p is the pressure, \vec{T}_{ij} is the Maxwell stress tensor, \vec{J} is the current density, \vec{E} is the electric field, B_i is the magnetic field component and I is the internal energy. For the present study, we have neglected the energy flux due to thermal heat conduction and viscosity terms.

3.2.1 Multi-material model

The plasma expands into an ambient medium (vacuum or low density material). The treatment of mixed computational cells (a cell containing more than one material) is therefore necessary for the Eulerian method. Therefore, a multi-material formulation [61, 62] using the VOF method [60] is used. A detailed discussion of

this multi-material formulation and the derivations of the relevant equations are given in Refs. [61, 62]. A complete description of this formulation lies beyond the scope of this work. However, in the following, we have listed a few important equations.

The mass conservation equation (Eq. (3.1)) for individual materials, in terms of their volume fractions f^m in a mixed cell, is given by [61, 62].

$$\frac{\partial (f^m \rho^m)}{\partial t} + \nabla \cdot (f^m \rho^m \vec{u}) = 0; \quad m = 1, \dots, M \quad (3.5)$$

Here, M is the total number of materials present in a mixed cell. The f^m of each material in a mixed cell should satisfy the following condition.

$$f^m = 0 \leq f^m \leq 1; \quad \sum_m f^m = 1 \quad (3.6)$$

The total density and average pressure are calculated using a volume-weighted average.

$$\begin{aligned} \rho &= \sum_m f^m \rho^m \\ p &= \sum_m f^m p^m \end{aligned} \quad (3.7)$$

The total density ρ and average pressure p are used to solve the momentum equation Eq. (3.2) by assuming a common velocity field for all materials present in a mixed cell [61]. The assumption of locally adiabatic evolution of internal energy [62] leads to the following equation for internal energy update in multi-material cells, as explained in Ref. [62].

$$\frac{\partial e^m}{\partial t} + (\vec{u} \cdot \nabla) e^m = -\frac{p^m}{\rho^m} \nabla \cdot \vec{u} + Q_s^m; \quad m = 1, \dots, M \quad (3.8)$$

Here, an additional term Q_s^m is added due to Joule heating. One more equation, apart from the equation of state (EOS) of each material, is required to close the system which is given by the following:

$$\frac{\partial f^m}{\partial t} + (\vec{u} \cdot \nabla) f^m = 0; \quad m = 1, \dots, M \quad (3.9)$$

The above equation for the volume fraction is solved using a volume-of-fluid algorithm given in Ref. [60] – this is discussed briefly in later sections and detailed in Appendix A.

3.2.2 MHD model using magnetic vector potential

Since, for the present case, the term $\vec{J} \times \vec{B} - \nabla p_e$ in the generalized Ohm's law has no θ -component, the magnetic vector potential in the plasma is governed by the following equation:

$$\frac{\partial \vec{A}}{\partial t} = \frac{\eta}{\mu_0} \nabla^2 \vec{A} + \vec{u} \times \nabla \times \vec{A} \quad (3.10)$$

where η and μ_0 are the resistivity of the plasma and permittivity of free space, respectively. We have used the condition $\nabla \cdot \vec{A} = 0$ to derive Eq. (3.10). In free space, the vector potential satisfies a Laplace-like equation:

$$\nabla^2 \vec{A} = 0 \quad (3.11)$$

The field components are calculated using the vector potential.

$$\vec{B} = \nabla \times \vec{A}; \quad \vec{E} = -\frac{\partial \vec{A}}{\partial t} \quad (3.12)$$

For the non-zero component, A_θ in cylindrical co-ordinates, Eq. (3.10) can be written as below.

$$\frac{\partial A_\theta}{\partial t} = \frac{\eta}{\mu_0} \left(\nabla^2 \vec{A} \right)_\theta + \left(\vec{u} \times \nabla \times \vec{A} \right)_\theta \quad (3.13)$$

Introducing the magnetic stream function $\Psi = rA_\theta$ in cylindrical co-ordinates, the Eq. (3.13) can be written as follows:

$$\frac{\partial \psi}{\partial t} + u_r \frac{\partial \psi}{\partial r} + u_z \frac{\partial \psi}{\partial z} = \frac{\eta}{\mu_0} \left[\frac{\partial^2 \psi}{\partial r^2} + \frac{\partial^2 \psi}{\partial z^2} - \frac{1}{r} \frac{\partial \psi}{\partial r} \right] \quad (3.14)$$

Here, u_r and u_z are the velocity components in the radial and axial directions respectively. Splitting the above equation into two separate equations for diffusion and advection (solved using operator split method in two different phases: Lagrangian and remap steps) following two equations can be obtained.

$$\frac{\partial \psi}{\partial t} = \frac{\eta}{\mu_0} \left[\frac{\partial^2 \psi}{\partial r^2} + \frac{\partial^2 \psi}{\partial z^2} - \frac{1}{r} \frac{\partial \psi}{\partial r} \right] \quad (3.15)$$

$$\frac{\partial \psi}{\partial t} + u_r \frac{\partial \psi}{\partial r} + u_z \frac{\partial \psi}{\partial z} = 0 \quad (3.16)$$

Similarly, the free space Eq. (3.11) in terms of A_θ in a cylindrical co-ordinate system can be expressed as below [57].

$$\frac{\partial^2 \psi}{\partial r^2} + \frac{\partial^2 \psi}{\partial z^2} - \frac{1}{r} \frac{\partial \psi}{\partial r} = 0 \quad (3.17)$$

The field components B_r , B_z and E_θ are calculated from the θ component of

vector potential, A_θ as follows:

$$B_r = -\frac{\partial A_\theta}{\partial z}; \quad B_z = \frac{1}{r} \frac{\partial (r A_\theta)}{\partial r}; \quad E_\theta = -\frac{\partial A_\theta}{\partial t} \quad (3.18)$$

3.3 Computational method

A fixed Eulerian mesh is used with a virtual Lagrangian calculation. The effect of Lagrangian deformations are remapped, at each time-step, on to the original mesh during Eulerian advection or remap step (making the overall algorithm into Eulerian). We have used a spatially staggered mesh, where velocities are defined at cell faces, while density, internal energy, pressure, etc. are defined at the mid point of the cell, as shown in Fig. A.1.

Physical variables are updated using a ‘dimensionally split’ method to extend the calculations into the two-dimensional case. Similarly, the algorithm is formulated using an ‘operator-split’ approach with three distinct phases in each direction (axial and radial): electromagnetic diffusion, Lagrangian motion (predictor-corrector scheme), and Eulerian advection or remap (using VOF scheme). The predictor and corrector step assumes the same magnetic stress-tensor calculated in the magnetic diffusion step prior to the Lagrangian step. To avoid biasing, the sequence of steps in radial and axial directions is alternated during subsequent time-steps. The details of the numerical algorithm are described in the following sections. The radial part of the equations are more complicated than the axial part. Therefore, detailed discussions are given only for the calculations in the radial direction in a one-dimensional manner.

3.3.1 Implicit field diffusion using vector potential

Magnetic field diffusion into the plasma sphere is expected to be negligible due to high electrical conductivity of the plasma and short time-scales involved. However, for MFC systems with increased operational time (larger stopping radius), field diffusion into the plasma may be significant towards the time of stagnation. Also, a generalized algorithm must handle magnetic field diffusion. Considering these, we have formulated the MHD algorithm by including magnetic field diffusion.

Diffusion is performed only in the plasma region. A grid point is defined to be plasma if $n_i \geq n_c$ and vacuum if $n_i < n_c$ as shown in Fig. 3.1, where n_i and n_c are the plasma number density and cutoff density respectively. The diffusion equation for the radial step is obtained by dropping axial terms from Eq. (3.15). The advection terms in each direction are treated separately during the remap step.

$$\frac{\psi^{n+1} - \psi^n}{\Delta t} = \frac{\eta}{\mu_0} \left[\frac{\partial^2 \psi^{n+1}}{\partial r^2} - \frac{1}{r} \frac{\partial \psi^{n+1}}{\partial r} \right] \quad (3.19)$$

The above equation can be linearized as below.

$$a_{j-1} \psi_{j-1}^{n+1} + b_j \psi_j^{n+1} + c_{j+1} \psi_{j+1}^{n+1} = d_j \psi_j^n \quad (3.20)$$

Here, j is the cell edge and a common subscript $i + \frac{1}{2}$ is omitted. The coefficients in the matrix are given in the following.

$$\begin{aligned}
a_j &= -\frac{\Delta t}{\mu_0 \sigma \Delta r_{j+1}} \left[\frac{1}{\Delta r_{j+1}} + \frac{1}{r_{j+1}} \right] \\
b_j &= \left[1 + \frac{2\Delta t}{\mu_0 \sigma \Delta r_j^2} \right] \\
c_j &= -\frac{\Delta t}{\mu_0 \sigma \Delta r_{j-1}} \left[\frac{1}{\Delta r_{j-1}} - \frac{1}{r_{j-1}} \right] \\
d_j &= 1 \\
\Delta r_j &= \frac{1}{2}(\Delta r_{j-1/2} + \Delta r_{j+1/2})
\end{aligned} \tag{3.21}$$

A tri-diagonal matrix can be constructed if one linearize the Eq. (3.19) as given in Eq. (3.20) for all other nodes in the plasma region along the radial direction for a given axial cell ($i + \frac{1}{2}$). The vector potential on the cell edges (on the y-faces of the cells for the radial direction update) $A_{\theta_{i+1/2,j}}$ are obtained by the inversion of tri-diagonal matrix. These values are then averaged into the cell center, $A_{\theta_{i+1/2,j+1/2}}$. The A_θ values at $r = 0$ along the axis are obtained using boundary conditions, see Sec. 3.3.6. The process is repeated for all the axial locations. The numerical scheme to solve the magnetic field diffusion equation in the axial direction follows the same. The derivations of the governing equations and the matrix coefficients are straight forward and are omitted here for brevity.

The electrical conductivity of a mixed cell (cell containing plasma and vacuum/background medium) is determined using a volume weighted average ($\sigma = \sum_m f^m \sigma^m$), where the the volume fraction of each material, f^m in a mixed cell is calculated using volume-of-fluid algorithm [60] (discussed later). The conductivity at the cell edge is the average of these cell centered quantities.

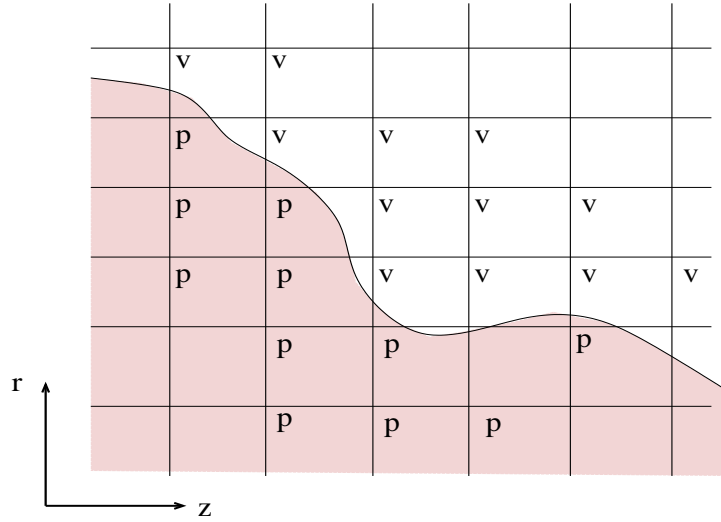


Figure 3.1: A schematic of the grid used in the two-region solution. The shaded area corresponds to the plasma region and the unshaded region to the vacuum. The Eq. (3.14) is solved in the plasma region and Eq. (3.17) is solved in the vacuum region.

3.3.2 Lagrangian step

A predictor-corrector scheme is used to integrate the fluid equations. The solution is advanced to $t^{n+1/2}$ by a half time-step with a forward Euler differencing. The derivative is evaluated at the half time-step using this approximate solution. This time-centered derivative is used to advance the solution from t^n to t^{n+1} . The displacements are advanced using a trapezoidal rule. In the following, we describe the Lagrangian step in detail.

First, the tentative half time-step velocities $u_r^{n+1/2}$ and $u_z^{n+1/2}$ are calculated by using an explicit time integration of Eq. (3.2) with time-step $\Delta t/2$.

$$\begin{aligned}
 u_r^{n+1/2} &= u_r^n + \frac{\Delta t}{2\rho^n} \left[-\nabla p^n + \nabla \cdot \left(\vec{T}_{ij}^n \right) \right]_r \\
 u_z^{n+1/2} &= u_z^n + \frac{\Delta t}{2\rho^n} \left[-\nabla p^n + \nabla \cdot \left(\vec{T}_{ij}^n \right) \right]_z
 \end{aligned}
 \tag{3.22}$$

The half time-step values of Lagrangian energy (for each material) are updated for the radial step using the following equation.

$$(e^m)^{n+1/2} = (e^m)^n - \frac{\Delta t (p^m)^n}{2} \frac{1}{(\rho^m)^n} \frac{\partial (ru_v^n)}{r \partial r} + (Q_s^m)^n \quad (3.23)$$

Here, Q_s^m is the energy deposition rate per unit volume due to Joule heating. The Eq. (3.23) is solved for $m = 1, \dots, M$, where M is the total number of materials in a mixed cell. The Lagrangian step conserve the total mass and volume fraction of each material in a cell. Therefore, the tentative radial locations $\tilde{r}_j = r_j^n + \Delta t \tilde{u}_r / 2$, where $\tilde{r}_v = (u_{rj}^n + u_{rj}^{n+1/2}) / 2$ can be used to determine the half time-step volume and hence the density $(\rho^m)^{n+1/2}$ of each material. The predicted half time-step pressure $(p^m)^{n+1/2}$ is evaluated using equation of state (EOS) of the material ($p^m = f_{\text{eos}} [e^m, \rho^m]$). The predicted mean cell pressure in a mixed cell is determined using volume weighted average.

Now, a corrected step is applied to advance the physical variables from time-step n to $n + 1$ using the above determined predicted half time-step values. The corrected velocity \vec{u}^{n+1} is updated as follows.

$$\begin{aligned} u_r^{n+1} &= u_r^n + \frac{\Delta t}{\rho^{n+1/2}} \left[-\nabla p^{n+1/2} + \nabla \cdot (\vec{T}_{ij}^n) \right]_r \\ u_z^{n+1} &= u_z^n + \frac{\Delta t}{\rho^{n+1/2}} \left[-\nabla p^{n+1/2} + \nabla \cdot (\vec{T}_{ij}^n) \right]_z \end{aligned} \quad (3.24)$$

We have used the magnetic stress tensor defined at the beginning of the time-step for the predictor as well as corrector steps. The corrected Lagrangian energy at $n + 1$ for the radial step is calculated using the following equation.

$$\tilde{e}^m = (e^m)^n - \frac{\Delta t (p^m)^{n+1/2}}{(\rho^m)^{n+1/2}} \frac{1}{r} \frac{\partial (r u_r^*)}{\partial r} + (Q_s^m)^{n+1/2} \quad (3.25)$$

Here, $u_r^* = (u_r^n + u_r^{n+1})/2$ is the time centered velocity. The radial locations are updated using these time centered velocities, $r_j^{n+1} = r_j^n + \Delta t u_r^*$. Eq. (3.25) is solved for $m = 1, \dots, M$, where M is the total number of materials in a mixed cell. The corrected volume and density for each material are updated using these corrected node locations. Finally, the EOS of the material is used to calculate corrected pressure at $n + 1$; i.e. $((p^m)^{n+1} = f_{\text{eos}}[\tilde{e}^m, (\rho^m)^{n+1}])$. The mean pressure in a mixed cell is the volume weighted average of individual material pressures; $p^{n+1} = \sum_m f^m (p^m)^{n+1}$. This completes the Lagrangian predictor-corrector step in the radial direction.

3.3.3 Advection or remap step

The Eulerian advection terms are treated in the remap step of the algorithm. All the solution variables are advected in a conservative manner.

Mass and energy advection

The Lagrangian step strictly conserves the mass. Therefore, only the advected mass contained in the overlap region in between the Eulerian and Lagrangian grid after a time-step (Δt) has to be found, see Fig. A.7. Let M_j^m denotes the signed advected mass (same sign of velocity at that face) along the radial direction of material m through cell face j . Then the mass flux, $\Pi_j^m = M_j^m / (\Delta z \Delta t)$ for each material through the face can be determined. The quantity M_j^m is evaluated using VOF algorithm [60]. Now, the continuity equation for material m can be updated

using the following.

$$(f^m \rho^m)_{j+1/2}^{n+1} = (f^m \rho^m)_{j+1/2}^n + \frac{\Delta t (\Pi_j^m - \Pi_{j+1}^m)}{r_{j+1/2} \Delta r_{j+1/2}} \quad (3.26)$$

The conservative advection equation (for radial direction) for the energy of individual materials in terms of the volume fraction is given below. Details can be found in Ref. [61,62].

$$\frac{\partial(f^m \rho^m e^m)}{\partial t} + u_r \frac{\partial(f^m \rho^m e^m)}{\partial r} = 0 \quad (3.27)$$

Therefore, the advected energy flux is obtained by multiplying internal energy resulting after the Lagrangian step with the mass flux. The Eulerian update equation for internal energy, using an upwind scheme, is given by

$$(f^m \rho^m e^m)_{j+1/2}^{n+1} = (f^m \rho^m e^m)_{j+1/2}^n + \frac{\Delta t (\tilde{e}_j^m \Pi_j^m - \tilde{e}_{j+1}^m \Pi_{j+1}^m)}{r_{j+1/2} \Delta r_{j+1/2}} \quad (3.28)$$

where, the upwind values of \tilde{e}_j^m are: $\tilde{e}_j^m = \tilde{e}_{j-1/2}^m$; if $u_{r_j}^* > 0$ and $\tilde{e}_j^m = \tilde{e}_{j+1/2}^m$; if $u_{r_j}^* \leq 0$. The ratio of quantities obtained using Eq. (3.28) and Eq. (3.26) yield specific internal energy of the material m after the advection step.

Momentum advection

Momentum is advected using the method given in Ref. [63]. We have used the following differencing scheme for momentum remap, refer Fig. A.1 for the subscripts used.

$$P_j^{n+1} = P_j^n + (\Pi_{j-1/2} \hat{u}_{r_{j-1/2}} - \Pi_{j+1/2} \hat{u}_{r_{j+1/2}}) \Delta t \quad (3.29)$$

Here, a common subscript $i + \frac{1}{2}$ is omitted. Also, $P_j = m_j u_{r_j}$ is the momentum defined at the cell edge where m_j is the node mass, $\Pi_{j+1/2}$ is the geometrically weighted average of face centered (on y-edges of the cell for radial step) mass flux summed over all the materials advected through that edge (see Eq. (3.30) and also Ref. [62]) and $\hat{u}_{r_{j+1/2}}$ is the monotonized second-order flux limited interpolated velocity at the center of the cell. Presently, four different limiter functions are implemented: superbee, monotonized center (MC), minmod and van Leer.

$$\Pi_{j+1/2} = \frac{1}{2} \left[\left(1 + \frac{r_{j+1} - r_j}{2r_{j+1/2}} \right) \Pi_j + \left(1 - \frac{r_{j+1} - r_j}{2r_{j+1/2}} \right) \Pi_{j+1} \right] \quad (3.30)$$

For axial momentum ($P_i = m_i u_{z_i}$) advection during the radial step, the face centered (on y-edges of the cell for radial step) mass fluxes are first geometrically averaged to cell corners.

$$\Pi_{i,j} = \frac{1}{2} (\Pi_{i-1/2,j} + \Pi_{i+1/2,j}) \quad (3.31)$$

Finally, the axial momentum is updated using these corner located mass fluxes and monotonized second-order flux limited velocities.

$$P_{i,j+1/2}^{n+1} = P_{i,j+1/2}^n + (\Pi_{i,j+1} \hat{u}_{z_{i,j+1}} - \Pi_{i,j} \hat{u}_{z_{i,j}}) \Delta t \quad (3.32)$$

Here, $\hat{u}_{z_{i,j}}$ is the monotonized second-order flux limited interpolated velocity at cell corners.

Magnetic field transport using A_θ

The advection term in Eq. (3.16) for vector potential is treated in the material remap step. The advection equation for the radial direction is obtained by dropping axial terms from Eq. (3.16). The solution update is as given by Eq. (3.33).

$$\phi_{j+1/2}^{n+1} = \frac{1}{V_{j+1/2}^{n+1}} \left[\phi_{j+1/2}^n V_{j+1/2}^n + \tilde{\phi}_j \Delta V_j - \tilde{\phi}_{j+1} \Delta V_{j+1} \right] \quad (3.33)$$

In Eq. (3.33), the nodes are numbered as $j, j + 1$ etc. and the cell defined by nodes j and $j + 1$ is $j + \frac{1}{2}$. Also, $\phi = A_\theta$ is the vector potential, ΔV is the signed volume advected across the node j and $\tilde{\phi}_j$ is the upwind values of stress components at node locations. We have used a second order accurate monotonic upwind scheme (MUSCL) due to van Leer [64] as it is one of the simplest and most efficient algorithms that is both second order accurate and monotonic. The essential idea of MUSCL algorithm is to replace the piecewise constant distribution of ϕ within a cell with a piecewise linear distribution. The details of the algorithm can found in Ref. [64].

3.3.4 Iteration procedure in free space

The free-space Eq. (3.17) for vector potential is solved iteratively at each time-step in the vacuum region between the plasma and the conductor, using the boundary conditions at both plasma and conductor surfaces. The iterations along the radial and axial directions are performed in a single step. The iteration is performed at the end of each time-step, once the diffusion, Lagrangian and advection steps in each direction (radial and axial) are completed. The iteration procedure may also be performed in each direction separately, along with the other calculations in the ‘dimensionally-split’ algorithm. However, we have observed no significant differ-

ence in the physical solutions obtained by using these two different approaches. On the other hand, the first approach is computationally less expensive. As this part of the algorithm (iteration procedure) takes most of the computational time, the above fact is critical for an optimized algorithm.

For numerical convenience, the equation is written in terms of ψ , see Eq. (3.17). A second-order-accurate difference scheme [65], using an alternating direction implicit (ADI) method, is used to solve Eq. (3.17). An optimization study has been performed to determine an optimum initial tolerance factor for convergence. Also, the convergence parameters are varied at each iteration to improve the convergence. The number of iterations required to converge the solution with a tolerance factor $\xi \sim 10^{-8}$ typically lies in the range of 10-20. Here, $\xi = \max [f_i^n - f_i^{n+1}]_{i=1}^N$; where, f_i^n is the solution at n^{th} iteration and N is the total number of cells.

3.3.5 Volume-of-fluid (VOF) method

A detailed description of the VOF method can be found in many references [66–70] and a review of VOF methods can be found in [71]. The formulation used in this thesis follows our work described in Ref. [60]. The algorithm consists of three parts: Interface reconstruction, Lagrangian deformation of material interfaces and finally Eulerian transport (advection). A ‘directional-split’ advection procedure is used to extend this method into the two-dimensional case. More details of this VOF scheme can be found in Ref. [60] and also in Appendix A. A few important points are given below for ready reference.

Interface construction and volume iteration

A piecewise linear interface construction (PLIC) method is used. The interface line is represented by $\vec{n} \cdot \vec{x} - \alpha = 0$; where, $\vec{n} = \hat{i}n_x + \hat{j}n_y$ is the exterior normal

to the line and α is the perpendicular distance from a local origin in a cell, see Fig. A.3. The local origin in a cell for each material is decided by checking the slope of the interface line for that material [60]. The slope of a material interface line and hence the normal vector ($\vec{n} = \vec{\nabla} f^m / |\vec{\nabla} f^m|$) are determined using LVIRA method [72]. Having obtained interface normals the interface parameter α has to be determined so that volume behind the interface line is equal to the material volume. The volume behind an interface line is calculated using an algorithm given by Sijoy et al. in Ref. [60]. The interface parameter α is found when the function $f(\alpha) = V(\alpha) - V_{actual}$, becomes zero (root-finding). Here, $V(\alpha)$ is the material volume in the cell bounded by the interface line with line parameter α . We have used Brents method [65] to find α with $\alpha_{\min} = 0$ and $\alpha_{\max} = d$ as initial bracket; where d is the cell diagonal distance.

Dynamic material ordering

The material interfaces in a mixed cell are constructed using ‘onion-skin’ or ‘layered’ model (see Fig. A.4) with the help of a ‘material order list’ determined dynamically. The ‘material order list’ is also used for specifying the order of transport for each material in a mixed cell to its neighboring cells. We have used a simple combination of centroid check algorithm [73] and Benson’s least squares fit to centroid algorithm [74] for dynamic material ordering (see Ref. [60] and Appendix A for details).

Material advection

The material volume advected (V_i^m) is evaluated using a generalized algorithm given in Ref. [60] and also in Appendix A. The material volume fraction for each material is updated using formulations given in [62] for cylindrical co-ordinates.

The advected mass (M_i^m) is calculated using a characteristic trace back method [62] by assuming a linear interpolation of velocity along the streamline in a computational cell. Authors in Ref. [62] have demonstrated that this method conserve total mass in cylindrical co-ordinate system.

3.3.6 Boundary conditions (BC)

The fluid boundary conditions (outflow, extrapolative, symmetric, etc.) are implemented using methods given in Ref. [75]. The BC for A_θ along the axis for field diffusion calculation in the axis-symmetric case is set equal to zero. Similarly, during the iterative procedure, the condition $\psi_{r=0} = 0$ is used ($\psi = rA_\theta \rightarrow 0$ as $r \rightarrow 0$). For conductor boundary at the outer radius, we assume the magnetic flux ($\Psi = 2\pi\psi$) is conserved because of the short time scales involved $\sim 0.1 - 1 \mu\text{s}$. Therefore, at the conducting wall (r_w), the magnetic flux remains ‘pinned’ to its initial value; hence, $\Psi_{r_w} = \Psi_{initial} \rightarrow \psi_{r_w} = \psi_{initial}$. For symmetric BC along the r-axis in r-z geometry; a simple fist-order implementation of $\frac{\partial\psi}{\partial z} = 0$ is used.

3.4 Validation of the algorithm

The MHD algorithm described so far has been validated against known analytical results. A comparative study between different existing advection methods and van Leer MUSCL scheme has also been done. Finally, a convergence study with respect to mesh size has been performed.

3.4.1 Sedov problem (cylindrical geometry)

The validation of the hydrodynamic part of the algorithm is done with various test cases. A particular case, which is relevant to the present context, is described

below. The Sedov point blast problem (Sedov 1959) is often used to test the capability of an algorithm to deal with strong shock waves in curvilinear co-ordinates. In this case, the resulting shock wave evolves in a self-similar fashion in which the shock radius, shock velocity, peak pressure, etc. can be found analytically [39, 76]. For a comparison of spatial profiles of the density, pressure, velocity, etc, semi-analytical solutions with the help of numerical methods are used. Details of the solution procedure are described in Refs. [39, 76, 77]. We deposit a quantity of energy $E = E_0$ into few computational cells surrounding the origin, which corresponds to a small radius ∂r at the beginning. The density is set equal to unity everywhere, with an extremely small value of pressure, $p_0 = 10^{-5}$ Pa. Also, the initial velocity is set to zero throughout the computational domain. The computational domain extends from zero to 0.5m. The grid consists of 300 cells along the radial direction. Fig. 3.2 and Fig. 3.3 show the normalized pressure and velocity profiles for a cylindrical Sedov problem at $t = 0.05$ s. Reasonable agreement with a semi-analytical solution is found.

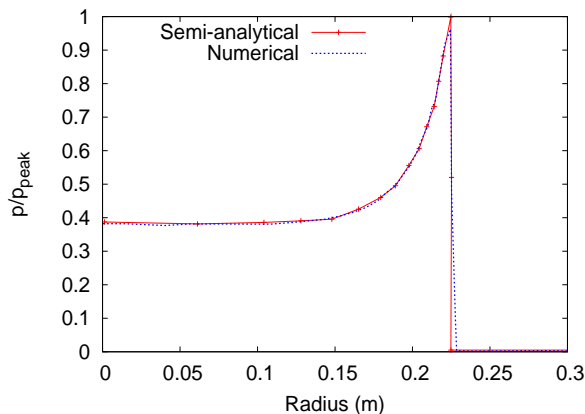


Figure 3.2: Comparison of normalized pressure profile (normalized to peak pressure, $p_{peak} = 4.0$ Pa) with semi-analytical solution for Sedov problem at $t = 0.05$ s.

Table 3.1 lists the L_1 norm error (multiplied by a factor 10^3) in the density for

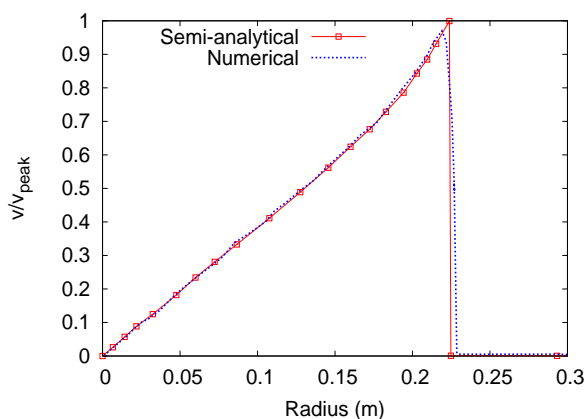


Figure 3.3: Comparison of normalized velocity profile (normalized to peak velocity, $v_{peak} = 1.84$ m/s) with semi-analytical solution for Sedov problem at $t = 0.05$ s.

varying mesh-size (Δr) and flux limiter function used for momentum advection. The L_1 norm error is calculated as $L_1 = (\sum_{i=1}^N |f_i^c - f_i^e|) / N$; where $f_i^{c,e}$ are the computed and exact solutions respectively, and N is the total number of cells. The Superbee limiter performed slightly better than others for this particular problem. The rate of convergence ($3.32 \log(L_{12h}/L_{1h})$, where L_{1h} and L_{12h} are the L_1 norm errors with grid-size ‘h’ and ‘2h’ respectively) calculated for this problem is summarized in Table 3.2. For this test problem, the predictor-corrector algorithm yielded an average order convergence rate ~ 1.73 .

Table 3.1: L_1 norm error ($\times 10^3$) for density ρ vs. mesh-size used for Sedov problem for different flux limiters. In the Table MC stands for monotonized centered limiter.

Limiter	$\Delta r = 5$ mm	$\Delta r = 2.5$ mm	$\Delta r = 1.25$ mm
Superbee	6.816	2.005	0.613
MC	6.824	2.088	0.635
Minmod	6.827	2.103	0.668
van Leer	6.828	2.107	0.671

Table 3.2: Convergence rate obtained for Sedov problem with superbee limiter.

Δr (mm)	L_1	rate
5	6.816×10^{-3}	–
2.5	2.005×10^{-3}	1.76
1.25	6.131×10^{-4}	1.7

3.4.2 Flux compression by expanding perfect electric conductor

Next, the phenomenon of magnetic flux compression by an expanding cylindrical liner (shell) with a given velocity profile is used to validate the MHD algorithm. An important characteristic required for any Eulerian fluid dynamics algorithm is its ability to advect distributions of the dependent variables with as little numerical diffusion as possible. Since the accuracy of advection schemes used for hydrodynamic variables are given in the previous test case, this problem is designed to verify the ability of the proposed MHD algorithm to advect distributions of magnetic field. The liner is assumed to be a perfect electric conductor (PEC), similar to the expansion of highly electrically conducting fusion plasma across magnetic field. The initial axial magnetic field is assumed to fill the region between the liner and the outer co-axial cylindrical shell. In this case, the magnetic flux contained in-between the liner and outer PEC cylinder will be compressed, as the liner expands radially outward, without flux diffusion into the walls. Therefore, the magnetic flux contained in the compression volume at any instant can be determined analytically. This particular example is a stringent test of the advection algorithm used for field transport. Any diffusive advection algorithm will show an unphysical flux diffusion (numerical diffusion) into the liner.

System parameters are chosen so as to yield a large magnetic Reynolds number, $R_m \gg 1$, since it is the limit of efficient flux compression and hence the case of

experimental interest. Also, the present case of interest (expansion of fusion plasma sphere across external applied magnetic field) falls in this regime. The Reynolds number is defined as $R_m = \mu\sigma Lv$, where σ is the conductivity, L is the scale length and v is the liner velocity. A velocity profile of the form, $v_l(t) = (R_w - R_l(t))/t_R$, is used; where, v_l is the velocity of the liner, R_w and R_l are the radius of the outer PEC wall and the liner respectively and t_R is a constant $\sim 10^{-6}$. A mesh resolution of 100 cells with $\Delta r = 1$ mm along the radial direction is used. The liner is modeled by solving only the advective terms in the Eq. (3.14), disabling diffusion calculation, in the conductor region.

Fig. 3.4 shows the normalized magnetic field profile at different times with three different schemes used for the advection of vector potential: MUSCL scheme with van Leer limiter (present method), FCT [57] scheme and Lax-Wendroff [58]. Field transport using the Lax-Wendroff scheme results in an oscillatory solution in the conductor region where, ideally, the diffused field should be zero. Both FCT and van Leer schemes are free from these numerical oscillations. However, the FCT scheme produces a slightly more diffusive solution as compared to the van Leer scheme.

Fig. 3.5 shows a comparison of L_1 norm error, $L_1 = \max (|f_i^c - f_i^e| \Delta x)_{i=1}^N$, for different linear and non-linear schemes/limiters; where $f_i^{c,e}$ are the computed and exact solutions in the compression volume respectively, N is the total number of cells and Δx is the mesh-size. The L_1 norm error produced by the van Leer scheme is the smallest among the compared schemes. Despite the numerical ripples in the conductor region, the Lax-Wendroff scheme gives almost the same accuracy as that obtained with the non-linear superbee limiter for the solutions in the compression region. It is worth noting that, with increased resolution, the accuracy of FCT scheme and non-linear limiters (superbee and MC) give almost the same

accuracy as the van Leer scheme. An algorithm which yields reasonable accuracy on a coarse Eulerian mesh is attractive for the analysis of plasma expansion with a ratio of final plasma radius to initial radius $r_f/r_i \sim 10 - 50$, since a considerable reduction in computational cost can be achieved. This fact makes the proposed algorithm attractive. The convergence rate derived using the L_1 norm error, $L_1 = (\sum_{i=1}^N |f_i^c - f_i^e|) / N$; shows an average rate of convergence ~ 1.82 with MUSCL scheme and van Leer limiter.

It is also of interest to determine the number of iterations required to converge the free space iteration calculation, for a given tolerance factor ξ , as a function of mesh size. This variation is shown in Fig. 3.6. As this part of the algorithm takes most of the computational time, proper choice of initial ξ for a given mesh-size is important to reduce the overall computational time. We have observed that, for a majority of problems tested so far, a tolerance factor ξ in the range of $\sim 10^{-7} - 10^{-8}$ yields satisfactory results (in terms of accuracy and total computational time) with $\sim 8 - 16$ iterations per time-step.

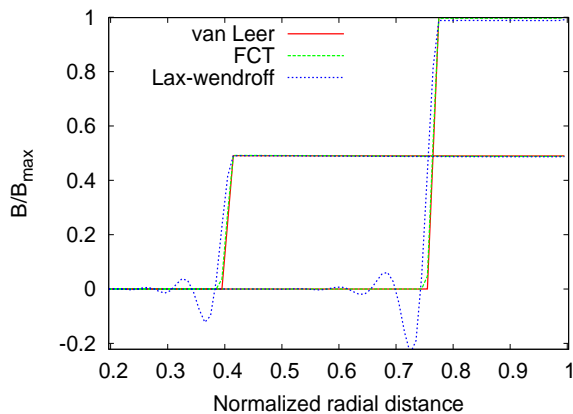


Figure 3.4: Profile of B/B_{max} obtained with various advection algorithms at different times during compression phase.

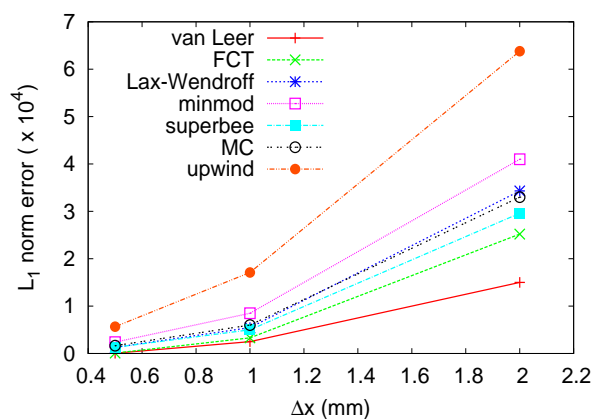


Figure 3.5: Comparison of L_1 norm error vs. mesh-size for different schemes/limiters. MC – monotonized centered limiter.

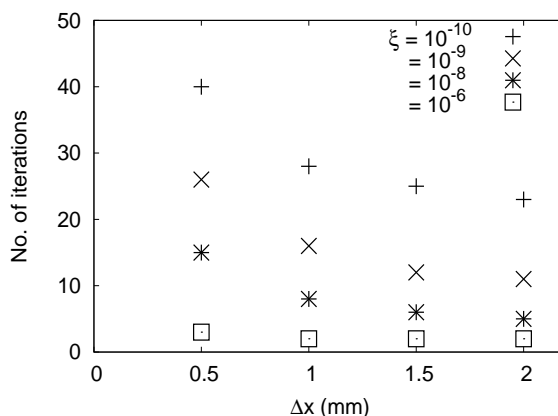


Figure 3.6: The no. of iterations required to solve Eq. (3.17) vs. mesh size for different values of tolerance factor ξ .

3.4.3 Magnetic Flux diffusion into an imploding resistive liner

Next, a magnetic convective-diffusion problem [53, 78–81] is chosen for the validation of magnetic field diffusion into a moving conductor. The flux compression problem [53, 78] is formulated in a cylindrical co-ordinate system. A cylindrical incompressible resistive liner surrounding a vacuum region is imploded to compress

a uniform axial magnetic field in the vacuum region. The initial inner radius, conductivity and velocity of the liner are chosen so as to satisfy the condition of large magnetic Reynolds number. The analytical solution of the problem can be found [78–81]. A parabolic liner trajectory of the form $r^2(t) = r_o^2 [1 + a(1 - t/t_o)^2]$ is used to have consistency with the analytical solutions provided in Ref. [78]; where $r(t)$ is the instantaneous inner radius of the liner, r_o is the turn-around radius, t_o is the turn-around time and a is a constant equal to ~ 9.0 in our simulation. An initial axial magnetic field of 2 T is used. The initial liner and the turn-around radius were 0.2 and 0.1 m respectively (radial compression length of 10 cm). The liner thickness was 2 cm. The σ and t_o of the liner were taken as 1×10^4 S/m and 0.1 μ s respectively. This leads to a magnetic Reynolds number, $R_m \sim 315$ (here, we define $R_m = \mu_0 \sigma r_o^2 / 4t_o$ as given in Ref. [78]). We have used a mesh-size of ~ 0.16 mm in the radial direction. A Neumann boundary condition (BC) of the form $\frac{\partial \psi}{\partial r} = 0$ is used for ψ at outer radius of the liner.

The diffused magnetic flux is defined as $\Phi_B = 2\pi \int_{r_1}^{r_2} B_z r dr$; where r_1 and r_2 are the inner and outer radius of the liner respectively. Fig. 3.7 compares the computed value of diffused flux with the analytical solution given in Ref. [78] for two different values of R_m . For the case with $R_m \sim 315$, corresponding to lower flux diffusion, the solution obtained with the MUSCL scheme shows better match with the analytical solution. For example, at turn-around time, the MUSCL scheme yields a $\sim 3\%$ difference, compared to 10% in the FCT scheme. The results obtained with both MUSCL and FCT scheme for $R_m \sim 150$, i.e., more diffusion than for $R_m = 315$, show better agreement with the analytical solution, viz., $\sim 2.9\%$ with MUSCL and $\sim 4.2\%$ with FCT. The two schemes, however, over-predict the diffused field for both cases. For a quantitative analysis, the variation of L_1 norm error in Φ_B at $t = t_o$ (for $R_m \sim 315$) with different mesh-size used in the

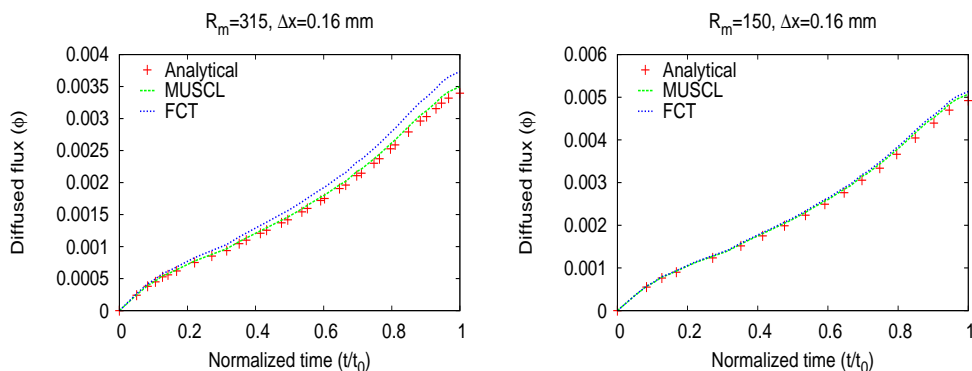


Figure 3.7: Comparison of the diffused flux $\Phi_B(t)$ into the resistive liner calculated using two different advection schemes (MUSCL and FCT) with analytical solution given in Ref. [78]. The left and right side figures correspond to $R_m \sim 315$ and 150, respectively.

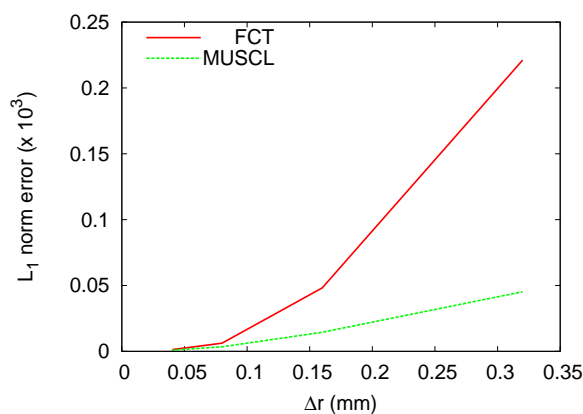


Figure 3.8: The L_1 norm error in Φ_B at $t = t_o$ (for $R_m \sim 315$) for different mesh-sizes used in the radial direction.

radial direction (Δr) is shown in Fig. 3.8. On a coarse mesh, the accuracy of our MUSCL scheme is better than the FCT scheme. However, with increased spatial resolution, both the FCT and MUSCL schemes give similar accuracy. The convergence rate calculated using L_1 norm error (with MUSCL scheme) shows an average rate of convergence ~ 1.8 for this particular problem.

3.4.4 Check for $\nabla \cdot \vec{B} = 0$ condition

The MHD schemes used in this work evolve only Maxwell's curl equations, without explicitly taking the Gauss law of magnetism ($\nabla \cdot \vec{B}=0$) into account. Hence an additional check on the suitability of the algorithm is the requirement of divergence free solution for the magnetic field. In the following, therefore, we have analysed the divergence error produced by the algorithm. On a staggered mesh in cylindrical geometry, the numerical divergence of \vec{B} at a time-step n is defined by the following equation.

$$(\nabla \cdot \vec{B})^n = \frac{(B_{z_{i+1,j}}^n - B_{z_{i,j}}^n)}{\Delta z_{j+1/2}} + \frac{(r_{j+1}B_{r_{i,j+1}}^n - r_j B_{r_{i,j}}^n)}{r_{i+1/2}\Delta r_{i+1/2}} \quad (3.34)$$

For an efficient algorithm, the divergence at the n -th time-step remains zero to machine round-off, provided that $(\nabla \cdot \vec{B})^{n-1}$ equal to zero.

The expansion of a spherical magnetized plasma across an external confined axial magnetic field is chosen as a test problem. A monatomic ideal gas plasma with $\gamma = 1.67$ is confined by a reflecting cylindrical shell with axial and radial dimensions of 4.8 m ($z = -2.4$ to 2.4 m) and 1.5 m, respectively. The plasma is separated from the surrounding low density medium by a membrane shaped like a sphere, centered at the origin with an initial radius of 0.2 m. The initial plasma temperature is assumed to be equal to ~ 100 keV. The density of the plasma and surrounding medium were 1.8×10^{-4} kg/m³ and 10^{-10} kg/m³ respectively. The initial velocity is zero throughout the simulation region. The magnetic field is assumed to be uniform, with only the axial component initially nonzero and equal to ~ 4 T. Only one quarter of the system is simulated in two dimensions because of axisymmetry.

The total magnetic field \vec{B} at a time 0.12 μ sec is shown in Fig. 3.9, where

the direction and length of the vectors indicate the direction and magnitude of the local magnetic field, respectively. It is clear from the figure that the field outside the plasma sphere is amplified due to flux compression and the field inside the plasma gets diluted. Also, the initial uniform field lines get modified by the plasma currents, and a finite B_r is observed near the plasma surface.

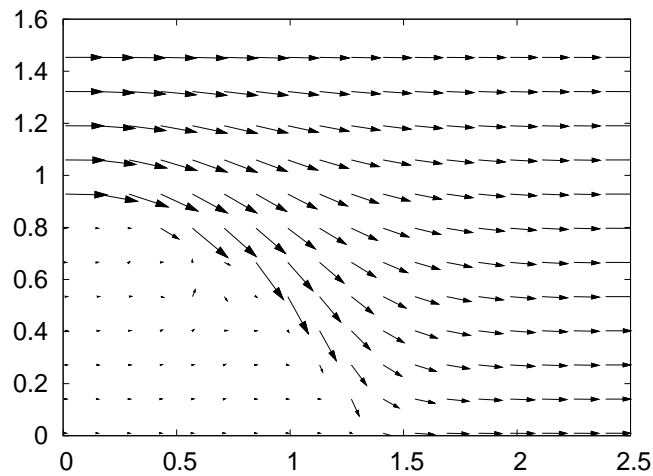


Figure 3.9: Spatial variation of the magnetic field vector for plasma expansion problem

Fig. 3.10 shows the temporal evolution of maximum absolute divergence error on the grid, obtained with the van Leer scheme, for different mesh-sizes used. The error remains within the acceptable limits and does not grow in time. Also, it is found that the divergence error depends weakly on the tolerance factor ξ used for the iteration. This indicates that a high tolerance factor will only produce an error in the spatial profile of magnetic field without much divergence error.

3.5 MFC by an expanding fusion plasma sphere

The validated algorithm is applied to study the expansion of a diamagnetic fusion plasma sphere across an external magnetic field [52], with special attention to the

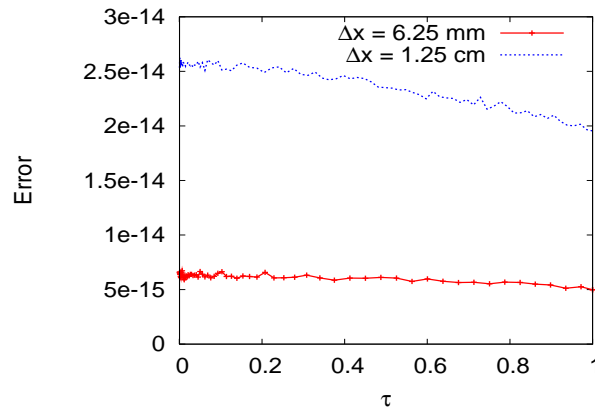


Figure 3.10: The temporal evolution of maximum divergence error for different mesh-size used. Here, $\tau = t_f/t$ is the normalized time.

dynamics of the plasma and the evolution of the plasma-vacuum interface. Also, this test will demonstrate the capability of the algorithm to simulate complex dynamics of high energy fusion plasma across an external magnetic field. The initial plasma conditions are chosen from earlier published works for D-3He fusion plasma (see Ref. [52] and references therein). The initial plasma kinetic energy and mass are assumed to be 140 MJ and 6 mg with an initial plasma radius (r_p) equal to 10 cm [52]. The shielding conductor (a solenoid in Ref. [52]) has a radius of 1.5 m and an axial length of ~ 4.5 m. An initial magnetic field of ~ 3.5 T is used. Other details of the MFC system and its dimensions and parameters are given in Ref. [52]. Magnetic field diffusion into the plasma sphere during the initial expansion phase ($r \leq r_p$) can be neglected due to high magnetic Reynolds number, $R_m \gg 1$. Therefore, the plasma sphere can be assumed to be initially free from the applied axial field. Also, we assume the plasma sphere is centered at $(r,z) = (0,0)$ and because of the symmetry only one quarter of the system is simulated. A mesh resolution of 900×600 is used. A symmetry boundary condition is used along the radial direction (y-axis) at $z=0$ location. Fixed and extrapolative boundary

conditions are used at the outer radius ($r = r_{\max}$) and the axial ends ($z = z_{\max}$) of the system, respectively. Details of the boundary conditions applied on the stream function Ψ are discussed in Sec. 3.3.6. The vector potential as a function of (r, z) on the computational domain is initialized using analytical equations in terms of elliptic integrals, taking contributions from all the turns in the shielding coil, and based on the initial coil current. This procedure is similar to the initialization of magnetic field in Ref. [52].

Fig. 3.11 shows the spatial variation of scaled density ($\rho \times 10^6 \text{ kg/m}^3$) at different times. Initially the plasma exhibits a uniform spherical expansion. The expansion of the plasma across the field lines (radial direction) reduces in time due to magnetic deceleration. Expansion along the field lines (axial direction) is essentially not affected by the axial magnetic field, as explained in chapter 2. The radial expansion at $z = 0$ is stopped at a radius $\sim 1.15 \text{ m}$ at $\sim t = 0.19 \mu\text{s}$. On the other hand, expansion continues at axial locations $z \geq 0.6 \text{ m}$ beyond this time, as shown in the last two plots in Fig. 3.11 at $t = 0.19$ and $0.24 \mu\text{s}$ respectively. A small quantity of plasma $\sim 0.05\%$ leaves the axial length of the system. This is because, as mentioned earlier, the plasma expansion along the axial direction is essentially free. It was not possible to simulate this free streaming using the Lagrangian method [52] explained in Chapter 2. Even though neglect of axial streaming does not significantly change the calculated system efficiency, it is clear that the MHD algorithm used in the present work offers an advantage over the purely Lagrangian MHD method [52].

Fig. 3.12 shows the normalized radial profile of density at $z=0$ at different times, the normalization being done with respect to the peak density at each time. As observed in Chapter 2, the plasma forms a shell-like geometry at the stagnation point, where the outer surface slows down due to magnetic pressure and the inner

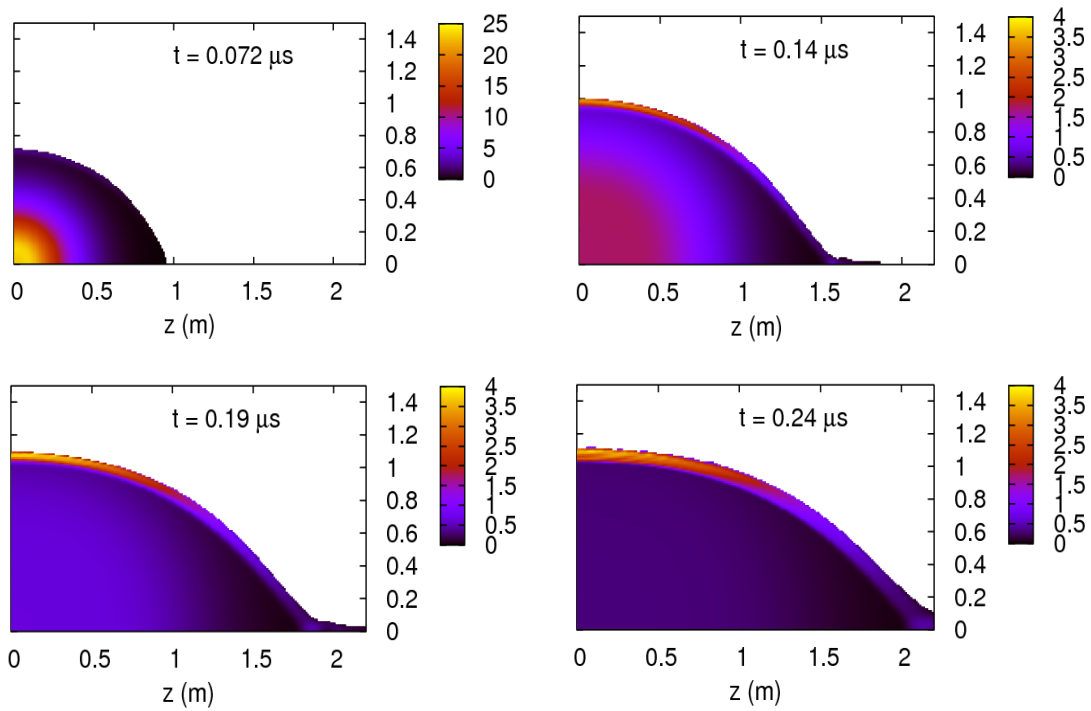


Figure 3.11: Spatial variation of scaled density ($\rho \times 10^6 \text{ kg/m}^3$) at different times ($t = 0.072, 0.14, 0.19$ and $0.24 \mu\text{s}$). The elongation of the plasma sphere along the axial direction and the development of shell like plasma structure are clearly visible towards the end of the radial expansion phase.

region catches up with the outer region. This can be seen from Figs. 3.11 and 3.12. The thickness of the shell is $\sim 0.1 \text{ m}$ with an average temperature of $\sim 37 \text{ keV}$ at $t = 0.23 \mu\text{s}$. Note that the electrical conductivity of the plasma shell formed near the stagnation point, is high enough ($\sim 10^9 \text{ S/m}$) to prevent magnetic field penetration. This means that the high temperature plasma shell that exists near stagnation time does not allow magnetic field diffusion, even though plasma motion stops for some time.

Next, we have analysed the temporal and spatial evolution of magnetic field inside the MFC system. Fig. 3.13 shows the contour levels of magnetic stream function (representing magnetic field lines) at different times during the flux com-

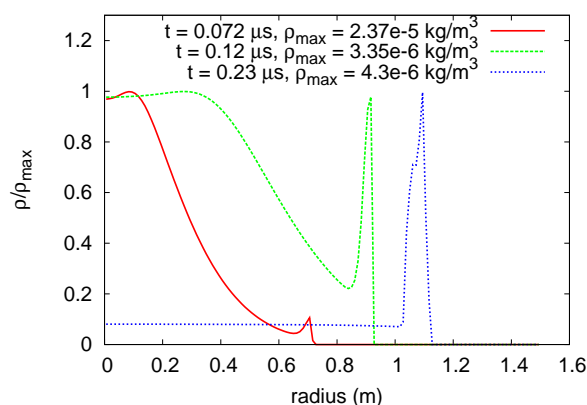


Figure 3.12: The radial variation of normalized density at different times for $z = 0$ plane. The normalization factor is the maximum value of the density along the radial direction for a given time.

pression phase. The magnetic field outside the plasma is amplified by magnetic flux compression, while the field inside the plasma gets reduced due to the diamagnetic (θ -directed) current produced by the plasma. The maximum magnetic field between the coil and plasma is observed at the axial midplane $z=0$. These are consistent with the results given in Ref. [52]. The radial variation of B_z at $z=0$ plane at different times is shown in Fig. 3.14. A spike-like increase in the magnetic field near $r = 1.5$ m is due to the presence of shielding conductor (solenoid loops). The final amplified field is ~ 6.6 T at $z=0$ plane. The distribution of current density at different times during the expansion phase is shown in Fig. 3.15. The diamagnetic current produced in the plasma has its maximum value near the plasma surface, as expected.

Finally, the dynamics of the plasma-vacuum interface is investigated, with special attention to the evolution of the Rayleigh-Taylor (RT) instability driven by the magnetic field. The plasma-vacuum interface near the stagnation point ($\sim 0.21 \mu\text{s}$) is shown in Fig. 3.16 (plotted on a coarse mesh for clarity). The figure indicates the development and the evolution of RT-like instability near the stagnation point.

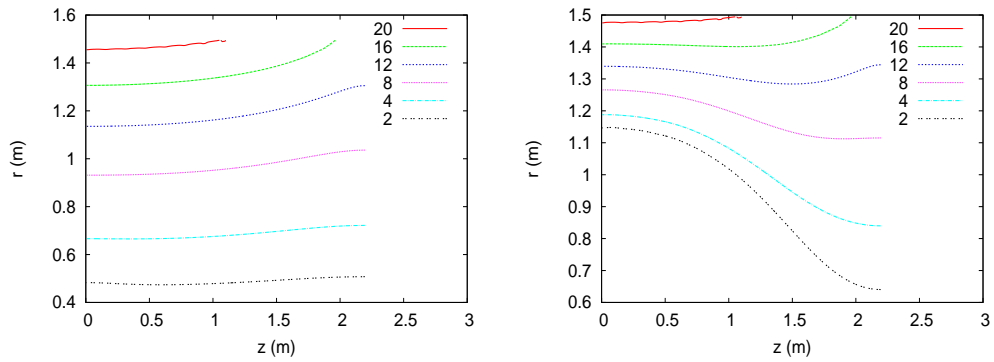


Figure 3.13: Contours of magnetic field lines represented by magnetic stream function ($\Psi = 2\pi r A_\theta$), at different times, $t = 0.072$ and $0.21 \mu\text{s}$ respectively.

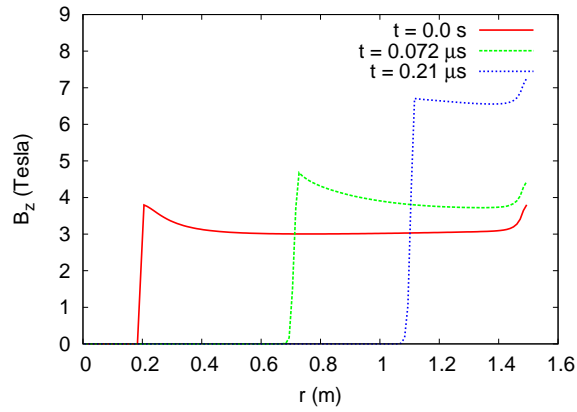


Figure 3.14: The radial variation of B_z at different times for $z = 0$ plane.

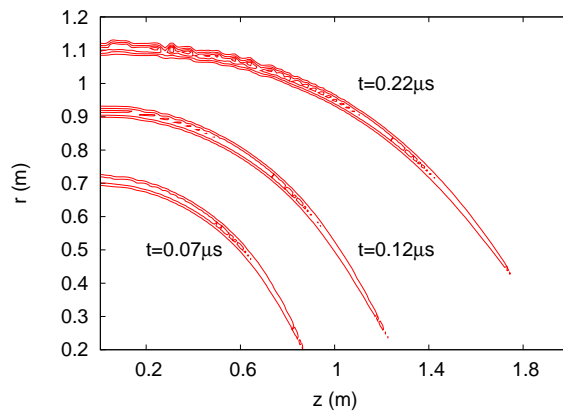


Figure 3.15: The distribution of plasma current density (contours) at different times.

If we start with a perfectly spherical initial plasma, these instabilities appear only around the end of the expansion phase, i.e., $\sim 0.18 \mu\text{s}$ for the problem considered here. The amplitude of the instability at $\sim 0.21 \mu\text{s}$ is $\sim 2 \text{ mm}$ with a wavelength of $\sim 6.8 \text{ cm}$. Fig. 3.17 shows velocity vectors inside the plasma region at a time $\sim 0.21 \mu\text{s}$, where the length of the vector shows the magnitude of the velocity at that location. The figure clearly shows a non-uniform velocity distribution on the surface. The variations in the directions of the velocity vectors clearly show the development of instability. The velocities within the plasma shell are considerably lesser than the velocities on the surface and at regions below the shell. Even though the instabilities are observed only around stagnation time for the problem considered above, it is possible that for different system parameters instabilities may play a more significant role. Hence a detailed plasma stability analysis is clearly necessary, assuming initial surface perturbations with different amplitudes and wavelengths. This forms the subject of the next chapter.

3.6 Limitations of the study

In this chapter, we have focused on the dynamics of the plasma and the evolution of MRT instability near the stagnation point. Therefore, although we consider this MFC system in the context of the energy conversion from a hot plasma sphere to usable electrical energy, we have not studied the conversion efficiencies of the proposed system using this MHD model. However, the conversion efficiencies of the proposed system with different inductive and resistive load conditions were described in Chapter 2. In order to study the possible inefficiencies of the system including resistive elements (confining conductor with finite conductivity), the perfectly conducting external boundary condition must be replaced with a diffusion

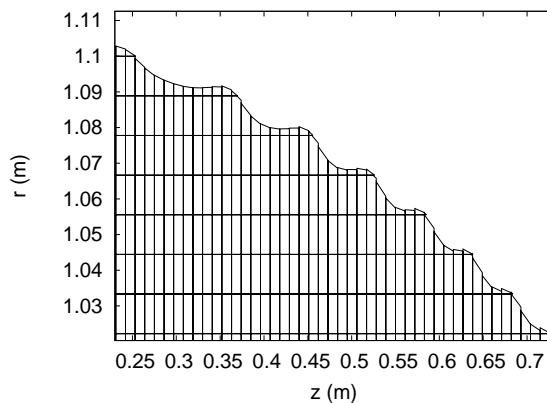


Figure 3.16: Zoomed in plot (plotted on a coarse mesh for clarity) of plasma-vacuum interface near stagnation point ($\sim 0.21 \mu s$) indicates development of RT like instability on the plasma surface.

calculation into a resistive wall with a self-consistently coupled circuit equation model [52, 57].

3.7 Conclusions of this study

In this chapter we have described the development and validation of an Eulerian multi-material MHD model to study the dynamics of expanding plasma sphere across external magnetic field with a special attention to plasma dynamics and the evolution of MRT instability at plasma-vacuum interface. The MHD algorithm is formulated using magnetic vector potential. In order to treat the expansion of plasma into surrounding vacuum or low density medium a multi-material hydrodynamic formulation is used. Different materials in a computational cell are assumed to be separated by a sharp material interface. These interfaces are tracked using classical volume-of-fluid (VOF) method. The magnetic field diffusion is solved implicitly using a vector potential formulation. The advection terms in the field diffusion equation are computed using a second-order monotonic upwind scheme

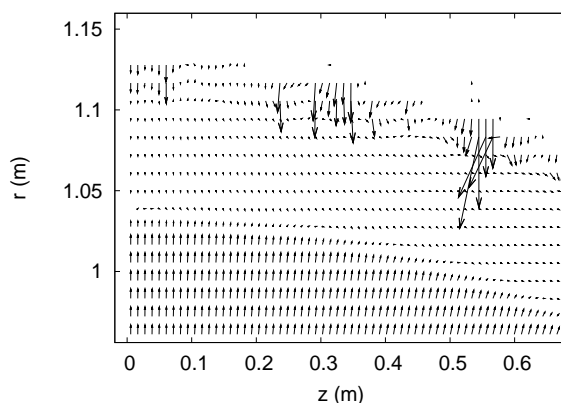


Figure 3.17: Zoomed-in plot of velocity vector inside the plasma region at a time $\sim 0.21 \mu\text{s}$. The plot indicate the development of instabilities on the plasma surface. The velocities within the plasma shell are considerably lesser than the velocities on the surface and at regions below the shell.

due to van Leer. A second-order accurate alternating direction implicit iteration procedure is used to calculate the field components in free space. Results obtained for various test cases show good qualitative and quantitative agreement with theoretical solutions. A convergence rate of ~ 1.7 is obtained.

The validated algorithm has been applied to study the proposed MFC system described in Ref. [52]. The algorithm was able to handle complex physics/dynamics involved in the MFC system such as non-uniform plasma expansion and magnetic pressure driven deceleration, magnetic field amplification due to flux compression, magnetic field diffusion and its advection, material interface tracking at plasma-vacuum boundary, etc.

The simulation results indicate the growth of the magnetic Rayleigh-Taylor (MRT) instability on the surface of the plasma around the time of stagnation. The plasma sphere forms a shell-like geometry near stagnation point. The electrical conductivity of the plasma shell is sufficiently high for the system parameters used in this simulation, to prevent magnetic field diffusion into the plasma.

4

Analysis of Magnetic Rayleigh-Taylor (MRT) instability

4.1 Introduction

In previous Chapters, we have examined a direct energy conversion scheme to convert plasma kinetic energy in an Inertial Fusion Energy system into pulsed electrical energy. Preliminary numerical studies [52, 82] described in Chapters 2 and 3 indicate that the proposed system is promising in terms of overall conversion efficiency. However, such a plasma, expanding across a magnetic field, is subject to the Magnetic Rayleigh Taylor (MRT) instability. The growth of MRT instability on the surface of the plasma, around the time of stagnation, is evident from the results presented in Chapter 3. A detailed analysis of such instabilities forms the subject of this chapter.

The MRT instability occurs when an electrically conducting fluid, e.g. plasma, is decelerated or supported by the magnetic field. The classical linear MRT growth rate [83] is defined as, $\gamma_L = (kg)^{1/2}$ for $kL_n \ll 1$ and $\gamma_L = (g/L_n)^{1/2}$ for $kL_n \gg 1$;

where k is the wave number, g is the deceleration, $L_n \sim [\partial \ln(n)/\partial x]^{-1}$ is the density scale length of the plasma and n is the plasma density. For efficient operation of the proposed MFC system [52, 82], the instability amplitude must be small so that the irregular surface caused by growth of the MRT instability does not disturb the smooth compression of the magnetic field between the plasma and solenoid. Large amplitude flute modes and plasma jetting can damage the cavity wall [33].

Numerical and experimental studies on plasma expansion in an external magnetic field and the analysis of interchange instabilities in space and laboratory plasmas can be found in Refs. [40, 84–97] (also see references therein). The majority of the above-mentioned works examine plasma expansion in a uniform unconfined background magnetic field where there is negligible compression of the magnetic field. In the MFC system, however, the magnetic field outside the plasma increases due to magnetic flux compression.

Previous work related to plasma energy conversion and including the role of MFC has been reported in Ref. [33]. There are, however, two major differences between that work and the present work. Firstly, Ref. [33] analyses a different plasma parameter range, starting with an initial radius of ~ 1 m and system dimensions of ~ 14 m in radius. Since the pickup coil is located at a radius of ~ 9 m, a low initial magnetic field is sufficient to stop the plasma close to the coil radius. Therefore, a magnetic field of ~ 0.57 T is used in Refs. [33]. In our last study [52, 82], described in Chapter 2 and 3, we had examined the case of a much smaller, practically-relevant system having a coil radius ~ 1.5 m, higher-pressure plasma ($\sim 10^7$ Pa) with an initial radial expansion velocity $\sim 10^7$ m/s, which requires a higher magnetic field (5 T) to extract enough energy from the plasma.

Secondly, the simulation results given in Ref. [33] start with an unperturbed initial plasma state, so that instabilities are seeded by numerically-produced per-

turbations. This was also the case in our last study [82], described in Chapter 3. In reality, perturbations with different wavelengths and amplitudes would exist on the surface of the plasma sphere even before it starts expanding. For a real-life system, therefore, it is necessary to study the growth of pre-existing perturbations with different wavelengths and amplitudes. In the present work, therefore, the study has been done for different cases of applied initial perturbations (different wavelengths and amplitudes), taking into account the effects of magnetic field amplification (time dependent g) and the geometric divergence due to spherical plasma expansion.

The purpose of this study is to numerically analyze, using MHD fluid simulations, the MRT instability on the surface of the plasma liner and its implications for the proposed MFC system.

4.2 MHD model and Computational Scheme

The equations of the MHD model used in this work have been described in Chapter 3. In Chapter 2, we have developed a pure Lagrangian MHD scheme self consistently coupled with external circuit equations to solve the governing equations. That scheme, however, is not suitable for the present study as large material deformations are expected. In such situations, use of a purely Lagrangian scheme leads to severe mesh distortion. Consequently, in Chapter 3, we have formulated an Eulerian MHD scheme with volume-of-fluid material interface tracking [60] to handle large plasma deformations in the MFC system. The method was successful in analysing large deformation plasma dynamics in the proposed MFC system. However, for the present study, it demands a prohibitively large number of cells in the simulation. This is due to the order of magnitude difference between the

different scale lengths involved in the system, such as MFC system dimensions of the order of few meters, plasma initial perturbation amplitude α_{in} of the order of few μm and wavelength λ ranging from few mm to cm. Note that for numerical convergence with respect to the mesh size, at least 10–20 cells per λ are required. This demands an extremely large number of cells in the simulation. Hence neither of the two foregoing techniques can be used for analysing MRT instabilities in an MFC system. In this chapter, we report on the development and use of an unstructured Lagrangian scheme [98] for such problems.

This unstructured Lagrangian scheme [98] helps control artificial grid distortion and ‘hourglass’-type motion. Further, to stabilize the grid, a node based tensor viscosity [100] and an artificial grid distortion control algorithm [99] are used. This allows us to simulate plasma evolution till the stagnation or turn-around time t_s without numerical instabilities. Approximately at this time, the inductive energy across the load reaches a maximum [52, 82]. Therefore, in the present work, we are only interested in studying the evolution of the MRT instability till the stagnation time. We have obtained a substantial reduction of the overall computational time with the help of an unstructured Lagrangian scheme, since the total number of cells required in the simulation are considerably reduced.

A typical unstructured mesh used in the simulation is given in Fig. 4.1. Only one quarter of the system is simulated due to symmetry. Details of the unstructured Lagrangian scheme can be found in Refs. [98–100], and essential details are given in Appendix B. Similarly, the details of the MHD scheme can be found in Ref. [52, 60, 82] and are omitted here for the sake of brevity.

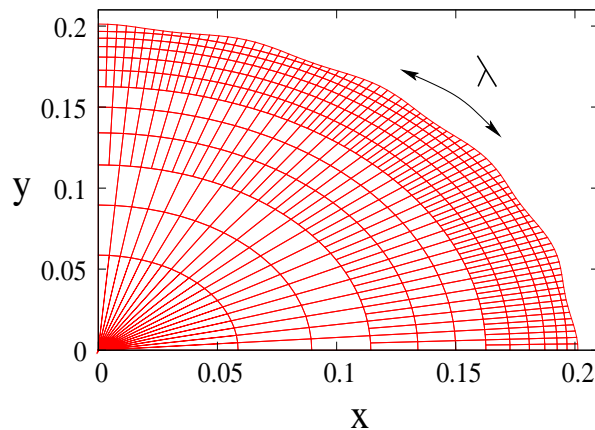


Figure 4.1: A typical unstructured Lagrangian mesh used in the plasma region. A larger number of cells is used near the surface of the plasma, where large material deformations are expected.

4.3 Initial conditions

The initial plasma parameters are taken from earlier published data for a D-3He plasma. The plasma energy E_p and mass m_p used in this study are 280 MJ and 4.4 mg respectively [25–27, 31, 32]. A 5 Tesla seed magnetic field is used in the simulation and the system parameters are the same as described in Chapters 2 and 3. Initially, therefore, the plasma undergoes free expansion across the B (see Chapters 2 and 3 and Refs. [25–27, 52, 82]). Therefore, we have started our simulation with an initial plasma radius of ~ 0.2 m. Initial radial profiles for the plasma density, temperature and velocity are generated using a separate 2D simulation without considering the effect of B (free expansion up to a radius equal to 0.2 m). The initial conditions thus obtained are shown in Fig. 4.2 as a function of plasma radius.

The overall computational approach in this work is summarized below. We have analyzed the evolution of MRT instability in two steps.

1. In the first step, we have applied random amplitude perturbations. The

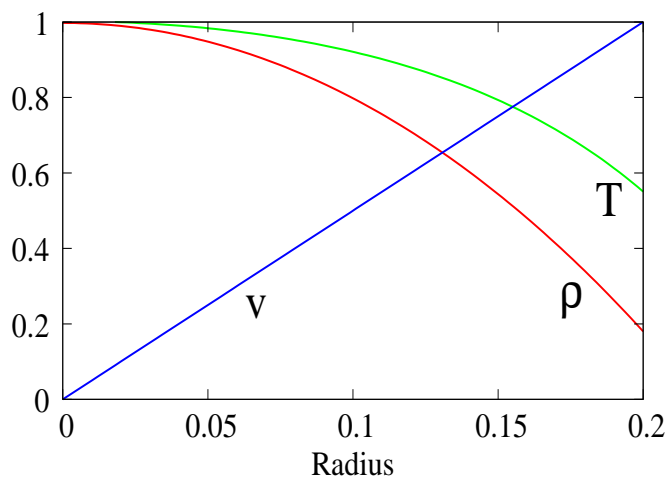


Figure 4.2: Initial radial plasma profiles for density, temperature and velocity. The profiles are normalized to the peak value; $\rho_{peak} = 2.5 \times 10^{-4} \text{ kg/m}^3$, $T_{peak} = 0.275 \text{ keV}$ and $v_{peak} = 1.63 \times 10^7 \text{ m/s}$.

instability has been seeded by adding a random fraction of the initial amplitude α_{in} to the plasma radius on the outer surface. In this method, the non-linear evolution of different modes can be studied simultaneously. Also, it helps to identify the dominant modes in the spectrum. However, this study is subject to the limitation that the shortest wavelength that can be studied is restricted to the mesh-size used in the θ direction near the surface of the plasma.

2. In the second step, we have used a single-mode sinusoidal perturbation. The initial wavelength λ_{in} of this perturbation is varied typically around the wavelength of the dominant modes found in the previous analysis (random perturbations). The perturbation is imposed by defining the outer radius as

$$R(x, y) = R_0 + \alpha_{in} \sin(2\pi r / \lambda_{in})$$

where $r = \sqrt{x^2 + y^2}$ and α_{in} are the radius and perturbation amplitude re-

spectively.

In the random seed analysis, the mesh-size is typically governed by the shortest wavelength that has to be studied. For single mode analysis, we have used a mesh-size ranging from $\sim \lambda/20$ to $\lambda/12$, which is found sufficient to yield numerical convergence with respect to the mesh-size.

4.4 Results and Discussion

The simulation results are analyzed using a Fast Fourier Transform (FFT) technique. The Fourier spectrum of modes in the plasma liner at different times is obtained as follows. The simulation yields $R(\theta, t)$ on the outer surface of the plasma. We subtract the $R(\theta, t)$ from the average outer radius to yield the deviations $\Delta R(\theta, t)$. A fast Fourier transform is performed on these values to yield the Fourier spectrum.

4.4.1 Random perturbation

The plasma has an initial radius $r_p = 0.2$ m. A random perturbation is imposed on the outer surface of the plasma, as described in Sec. 4.3 with $\alpha_n = 5 \mu\text{m}$. We have used 160 cells in the θ direction ($n_\theta = 160$) near the surface of the plasma. Since only one quarter of the system is simulated, we have a spherical plasma liner with a circumference $C = \pi r_p/2$. The mode number corresponding to a wavelength λ is given by $n = C/\lambda$. Therefore, the shortest and largest wavelength that can be studied with this mesh-size are $2C/n_\theta \sim 4$ mm and $C \sim 0.3$ m respectively. Note that these values change along with the instantaneous plasma radius $r_p(t)$ (geometric divergence effect).

The early phase is characterized by plasma expansion, a comparatively low

value of acceleration g and hence a low growth rate γ . A high pressure plasma region is created near the surface [52,82] as the outer surface slows down due to B and the inner region catches up with the outer surface, as shown in Fig. 4.3(a). This pressure build up near the plasma surface tends to smooth out the perturbations. Hence, for a very short initial period, the amplitudes of all the modes decrease. As the plasma expands further, the B outside the plasma increases due to MFC and hence the interface deceleration g increases, as shown in Fig. 4.3(b). This in turn increases the growth rate of the modes.

Fig. 4.4 shows snapshots of the Fourier spectrum at different times for this case. The initial figure at $t = 0$ shows a spectrum with comparatively larger amplitudes for longer wavelength modes. Fig. 4.4(b), corresponding to $t \sim 0.036 \mu\text{s}$, shows that the amplitudes of all modes become comparable, with an average amplitude of $\sim 30 \mu\text{m}$. During this time, the amplitudes of short λ modes are increased by ~ 10 times while the amplitudes of longer λ modes essentially remain constant. This is because of the faster growth of shorter wavelength modes (comparatively higher γ). However, these short wavelength modes also tend to saturate earlier. For $t \geq 0.05 \mu\text{s}$, all the modes grow with nearly equal γ , with a comparatively higher-amplitude spectrum in the intermediate wavelength range (modes 20–50). This is due to the non-linear evolution of the modes. For the present system dimensions and plasma parameters, the time scales of magnetic field diffusion and thermal conduction are much greater than the typical plasma expansion time [52, 82]. Similarly, we have also neglected the plasma ion viscosity [52, 82]. Therefore, the non-linear evolution of the modes might be the consequence of other non-linear effects such as mode saturation [101], interaction of different modes (mode coupling) and harmonic mode generation.

In order to understand coupling between different modes, we have used a cross-

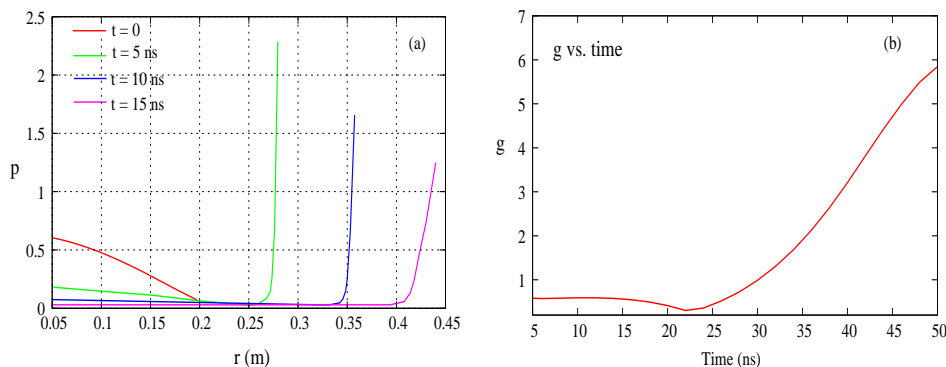


Figure 4.3: (a) Plasma pressure (normalized to 10^7 Pa) vs radius at different times during the initial phase of the plasma expansion. The plasma forms a shell like geometry [52,82]. (b) The temporal evolution of g of the outer surface (normalized to 10^{14} ms^{-2}) during the initial phase of plasma expansion.

correlation (f_{cr}) analysis, as explained in Ref. [102]. First the FFT spectrum is obtained for a large number of time points. This yields a time-series of the amplitudes of different modes in the spectrum. We have calculated f_{cr} between these time series using the following expression [103].

$$f_{cr} = \frac{\sum(\alpha_j^n - \bar{\alpha}_j) \times \sum(\alpha_k^n - \bar{\alpha}_k)}{\sqrt{\sum(\alpha_j^n - \bar{\alpha}_j)^2} \sqrt{\sum(\alpha_k^n - \bar{\alpha}_k)^2}} \quad (4.1)$$

Here, α_j^n and α_k^n are the time series for modes j and k , $\bar{\alpha}_j$ and $\bar{\alpha}_k$ are the respective average values. Fig. 4.5 shows f_{cr} for a few important modes ($n = 22, 34, 38$ and 50) with other modes in the spectrum. The results indicate strong cross-correlation between different modes. This coupling causes the transfer of energy between different modes. A detailed study would be required to analyze this non-linear mode coupling between different modes. This, however, lies beyond the scope of this thesis. The main objective of this multi-mode analysis is to qualitatively identify the dominant modes and the corresponding wavelength regime in the amplitude spectrum. This dominant wavelength range is next explored using

single mode analysis with an initial sinusoidal perturbation.

It is noteworthy that since the number of modes (n_θ) are fixed, the λ corresponding to a mode number increases with time due to the plasma expansion (r_p and hence C changes with respect to time). Thus the shortest λ (highest n) that can be studied increases with time due to geometric divergence. Fig. 4.6 shows the temporal variation of λ for $n = 80$. The λ for this mode changes from 4 mm to 22.5 mm. That is, as the plasma expands radially outwards, the shorter wavelength spectrum is continuously eliminated even though the number of modes/cells are fixed. Therefore, we have repeated the analysis with $n_\theta = 600$. This allows study of the shortest λ ($n = 300$) that varies from ~ 0.1 –5.8 mm. This study will also help us to see the sensitivity of the results with respect to the mesh-size.

Fig. 4.7 shows snapshots of the Fourier spectrum at different times for this case. Similar to the earlier case, the FFT spectrum has comparatively larger initial amplitudes for longer λ modes and as the plasma expands the shorter λ modes in the spectrum evolve faster and saturate. A progressive transition to longer λ regime is observed. Similar trends have been observed in the simulations of Z-pinch implosions [104]. The wavelength regime of the dominant modes and their amplitudes are consistent with the previous results obtained for $n_\theta = 160$. This means that there is no significant change in the results by increasing the number of cells and hence by including shorter wavelength modes (0.1–5.8 mm) in the simulation.

Let us now consider the effect of initial amplitude. We have already obtained results for $\alpha_n = 5 \mu\text{m}$. We have repeated the analysis with two different amplitudes, viz., $\alpha_n = 50 \mu\text{m}$ and 0.5 mm, a variation by two orders of magnitude. Fig. 4.8 shows the Fourier spectrum obtained for these two cases. The initial spectrum obtained for these two cases are as shown in the first plot of Fig. 4.4 with a

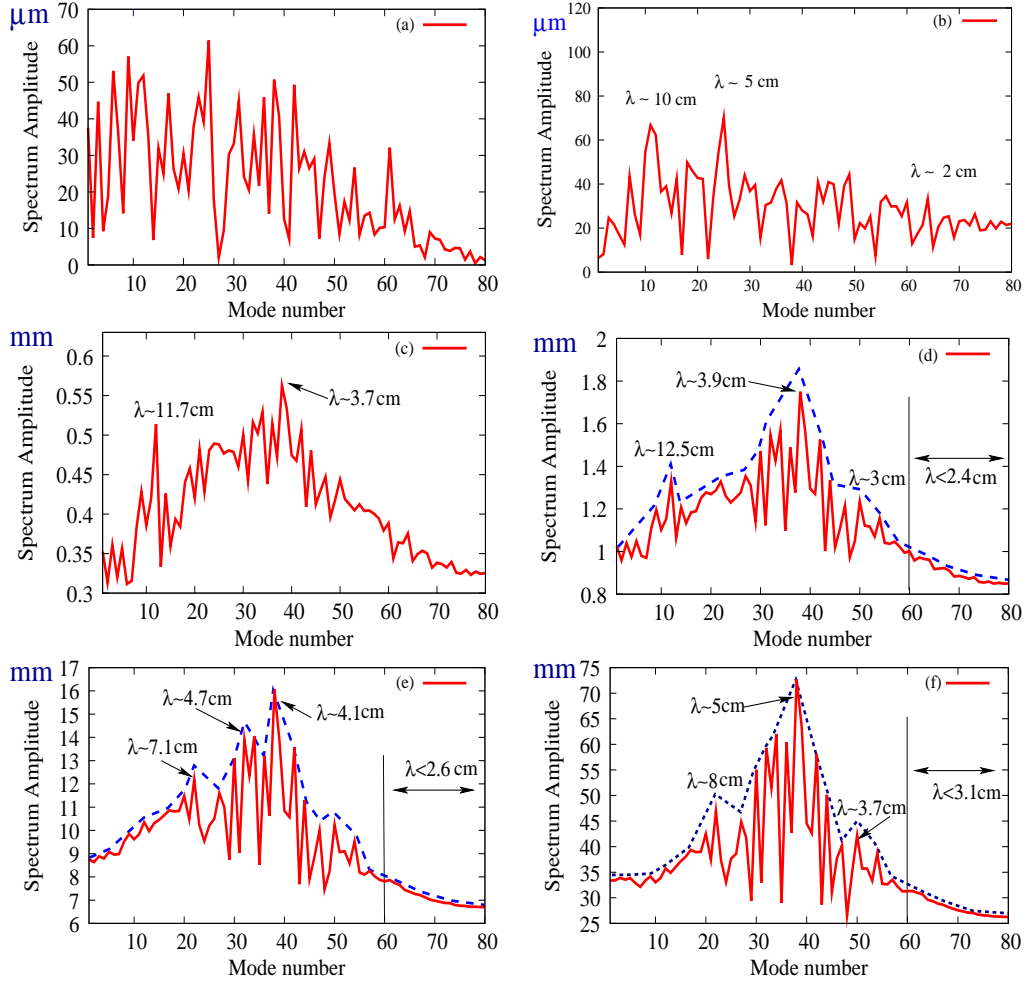


Figure 4.4: Spectral evolution of perturbations in plasma liner at different times, starting with an initial random perturbation. We have drawn an envelope over the wave structure, adapted from [104], (dashed blue line) to easily identify the dominant modes and corresponding wavelength regime. Figures (a)–(f) are at $t=0$, $0.04 \mu\text{s}$, $0.044 \mu\text{s}$, $0.048 \mu\text{s}$, $0.058 \mu\text{s}$ and $0.081 \mu\text{s}$, respectively. The corresponding average plasma radii are 0.2 m, 0.78 m, 0.9 m, 0.95 m, 1.0 m and 1.2 m respectively.

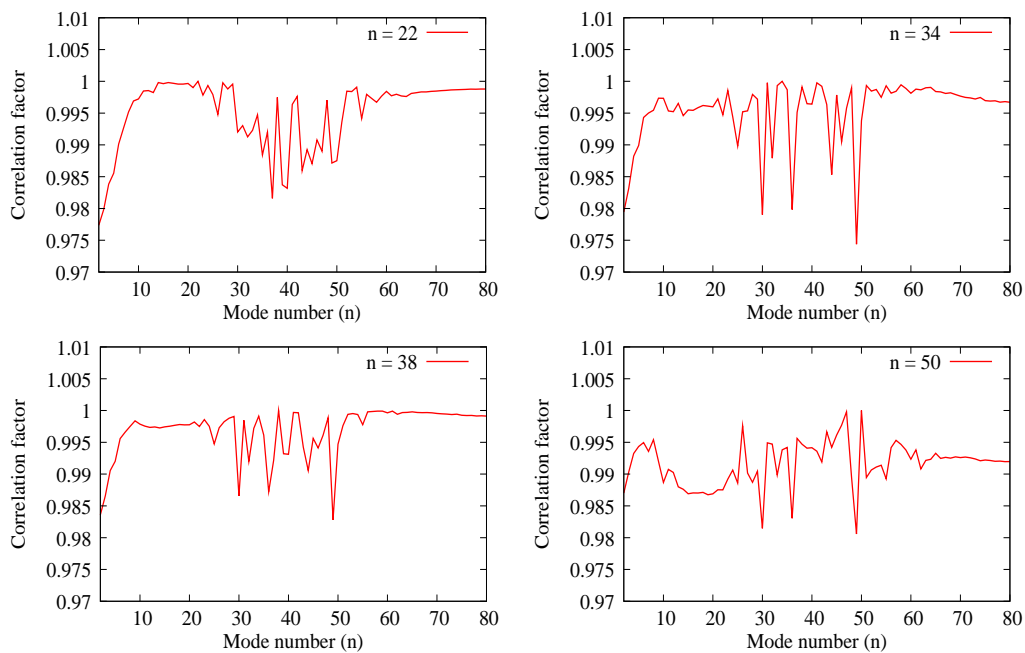


Figure 4.5: Cross-correlation factor (f_{cr}) for few dominant modes ($n = 22, 34, 38$ and 50) with other modes in the spectrum.

multiplication factor of 10 and 100 respectively. The dominant modes and their λ regime obtained for these two cases are in good agreement with the previous case ($\alpha_n = 5 \mu\text{m}$). However, with $\alpha_n = 0.5 \text{ mm}$, the spectrum amplitudes of the dominant modes are $\sim 60\text{--}80$ times higher than the short λ modes ($n > 60$) compared to $\sim 2\text{--}3$ times for the previous case. This is because the higher initial amplitude of short λ modes leads to their reaching saturation faster than for lower initial amplitudes.

The spectral evolution obtained clearly demonstrates its complex nature for the case with random initial perturbations. The large number of modes make it difficult to follow individual mode evolution and distinguish between the various factors influencing the γ . As mentioned in the beginning, the primary objective of this random seed perturbation analysis is to find out the dominant modes and their λ regime in the spectrum. These wavelengths are then subsequently used in the

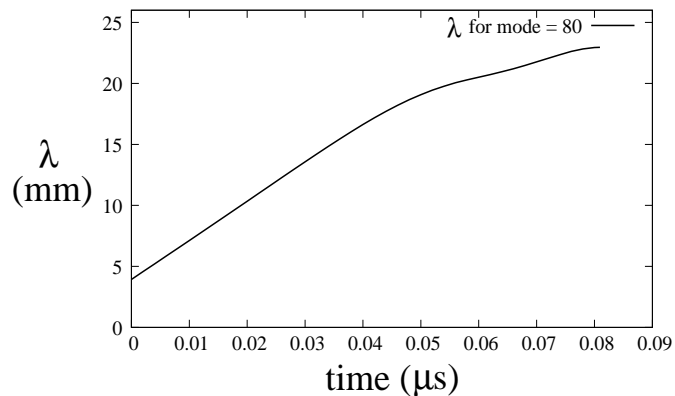


Figure 4.6: Temporal variation of λ for mode number 80. The λ for this mode changes from 4 mm to 2.25 cm.

single mode analysis. Inspecting Fig. 4.4, it is clear that towards the stagnation time the dominant modes shift towards intermediate wavelengths $\lambda = 3.7\text{--}8$ cm (mode number $n = 20\text{--}50$ for $n_\theta = 160$). Also, the higher wavelength modes (λ ranging from 10–100 cm) have comparatively lower amplitudes from $t = 0.05 \mu\text{s}$ to t_s . The dominant wavelength regime obtained in this analysis is consistent with the observations in our earlier work using a 2D Eulerian MHD scheme [82]. In Ref. [82], the instabilities grow from numerical perturbations and the λ of the dominant mode observed towards t_s is ~ 6.8 cm [82].

The evolution of the dominant modes to intermediate wavelength regime is the consequence of non-linear mode saturation and/or mode coupling effects. Other effects, such as B diffusion into the plasma, thermal conduction and viscosity, are not significant for the present MFC system parameters [52, 82]. The shorter wavelength modes, which grow more rapidly, saturate at an earlier time. With saturation, their growth rate becomes close to a constant value [101], so that they are eventually overtaken by intermediate λ modes. For longer λ modes ($n = 1\text{--}10$ for $n_\theta = 160$), the growth rate $\gamma \propto 1/\sqrt{\lambda}$ is slower than the γ of the intermediate modes. Apart from these, the non-linear coupling of different modes which occurs

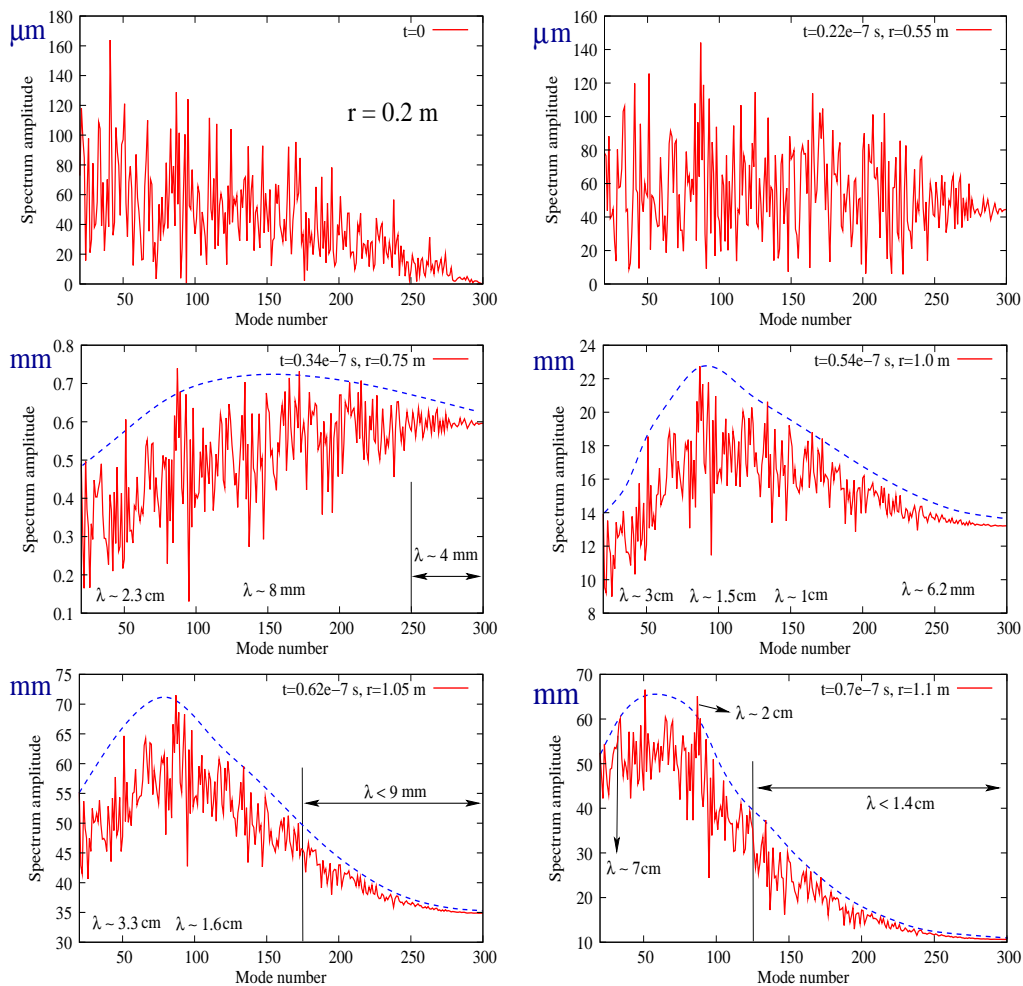


Figure 4.7: Spectral evolution of plasma liner at different times from an initial random amplitude perturbation (with $n_\theta = 600$). We have drawn an envelope over the wave structure (dashed blue line) to easily identify the dominant modes and corresponding wavelength regime.

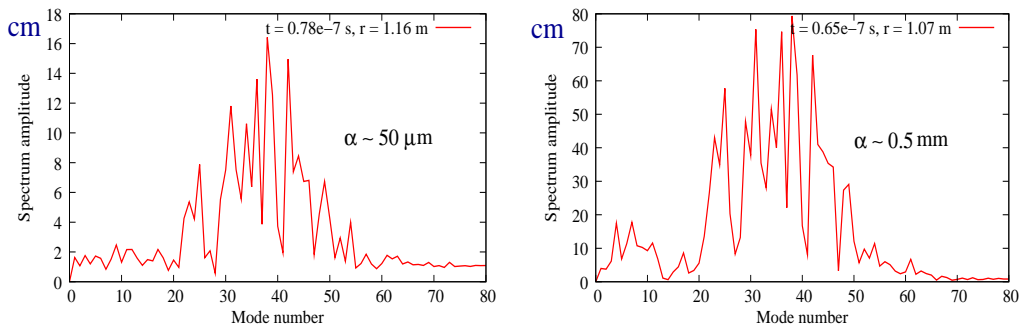


Figure 4.8: Fourier spectrum obtained for two different values of α_n (random initial perturbation). The initial spectrum obtained for these two cases are as shown in the first plot of Fig. 4.4 with a multiplication factor of 10 and 100 respectively.

simultaneously, as seen by the cross-correlation analysis, contributes to the growth of other modes in the spectrum. This makes the numerical picture more difficult to interpret. Therefore, in the next section, we have described the instability analysis with a single-mode initial perturbation. The initial wavelength (λ_{in}) of this perturbation is varied typically around the wavelength of the dominant modes found in this section.

4.4.2 Single mode sinusoidal perturbation

The initial perturbation is taken to be sinusoidal, as described in Sec. 4.3. λ_{in} is varied from 6.9 mm–6.28 cm ($n = 5–45$). These modes are chosen in such a way that the corresponding λ_{in} lies within the dominant λ regime found in the previous study. For each λ_{in} , four values of α_{in} are used; $\lambda_{in}/1000$, $\lambda_{in}/100$, $\lambda_{in}/50$ and $\lambda_{in}/10$. Note that for the cases with $\alpha_{in} \sim \lambda_{in}/10$, the mode amplitude and the wavelength are comparable. This means that α_{in} is close to the mode saturation limit [101]. This value, however, is included in the test cases by considering the fact that the λ of a given mode increases due to plasma expansion. Also, we have observed that for a short initial period of time, the α decreases – this is examined

in later sections. Apart from these, the following fact also need to be considered. In reality the plasma expands from a radius of $\sim 200 \mu\text{m}$ after fusion energy release is completed. However, as mentioned above, we have started our simulation with a radius of 0.2 m (1000 times expansion). Therefore, modes with comparable α and λ would pre-exist on the plasma surface.

Fig. 4.9 shows the density profile near the plasma surface and the corresponding Lagrangian mesh towards $t = t_s$ for the case with $\lambda_{in} = 3.14 \text{ cm}$ ($n = 10$) and $\alpha_{in} = \lambda_{in}/10$. The plasma forms a shell like geometry near the stagnation time. This is consistent with the observations in Refs. [52, 82]. The evolution of the FFT spectrum amplitude is shown in Fig. 4.10. Inspecting the plots, it is clear that apart from the fundamental imposed mode, the evolution of other harmonic modes (nk where $n = 2, 3, \dots$) with $\lambda_n = \lambda_{in}/n$ are also taking place. We have observed that, in all the test cases presented here, the evolution of harmonic modes (the non-linear phase of instability growth) occur significantly when $\alpha_{in} \sim \lambda_{in}/10$.

In order to understand the mode coupling and harmonic mode generation in detail, we have performed a multi-mode analysis by imposing two fundamental modes having different λ . Initially two fundamental modes, numbers 10 and 40, are imposed with the same initial amplitude $\alpha_{in} \sim 500 \mu\text{m}$ for each mode, i.e. $\alpha_{in} \sim \lambda_{in}/65$ for mode 10 and $\alpha_{in} \sim \lambda_{in}/15$ for mode 40. The right side plot in Fig. 4.10, shows the FFT spectrum (normalized to the highest amplitude in the spectrum) at $t \sim 0.04 \mu\text{s}$ for this case. For single mode perturbation with $\alpha_{in} = \lambda_{in}/10$ and $n = 40$, only one harmonic mode ($n = 80$) is appeared at $t = 0.04 \mu\text{s}$, see Fig. 4.10(b). The amplitude of this harmonic mode is $\sim 20\%$ of the fundamental mode. Also, note that the FFT spectrum obtained in the single mode analysis for $n = 10$ with $\alpha_{in} = \lambda_{in}/50$ shows negligible amplitude for its harmonic modes at $t = 0.04 \mu\text{s}$. However, with multi-mode perturbation (modes

10 and 40), the evolution of other modes due to the interaction between different primary and harmonic modes are observed. The appearance of a mode $n = 30$ which is the difference of fundamental modes is also observed. Note that for single mode perturbation with $n = 40$, the spectrum amplitude of the modes 20 and 30 were negligible.

Further, to observe the mode coupling between two fundamental short wavelength modes (say n_1 and n_2), we have repeated the multi-mode analysis for two different sets of fundamental modes $(n_1, n_2) = (30, 40)$ & $(60, 80)$ with $\alpha_{in} \sim 500 \mu\text{m}$. The FFT spectrum (α/α_{peak}) obtained for these two cases are shown in Fig. 4.11. Note the appearance of inverse cascade modes 10 and 20 corresponding to the difference $n_2 - n_1$ for these two cases respectively (the generation of inverse cascade modes in a Z-pinch implosion system with multi-mode perturbation analysis is reported in Ref. [104]). That is the short wavelength modes upon saturation generate higher wavelength modes along with other short wavelength harmonic modes. Note that the amplitude of harmonic modes are found to be insignificant for all the cases of multi-mode analysis when the value of α_{in} for each mode is set equal to $\sim 5 \mu\text{m}$ (this is true even with increased spatial resolution). That is the evolution of harmonic modes and their interactions with both the primary and other harmonic modes are found to be significant only when the value of α_{in} is comparable to λ_{in} . This implies upon saturation these modes evolve non-linearly with the generation of harmonic and inverse cascade modes.

Our aim with this multi-mode perturbation study was to qualitatively analyze the non-linear evolution of the modes (particularly the short λ modes) when α is comparable to λ (close to mode saturation). It is clear that the non-linear evolution of the modes upon saturation is characterized by the generation of harmonic modes and mode coupling. Detailed analysis of the evolution of these harmonic modes

for various initial conditions in terms of number fundamental modes, their initial amplitudes and wavelength lies beyond the scope of this work. For these studies, more computational efforts with increased spatial resolution to resolve the highest harmonic mode [104] in the spectrum are required.

In Fig. 4.12, we have shown the temporal evolution of the perturbation amplitude α and the wavelength λ . As mentioned earlier, α decreases till $t \sim 0.03 \mu\text{s}$ due to the geometric divergence effect, comparatively low growth rate $\gamma_L \sim (2\pi g/\lambda)^{1/2}$ (g is comparatively low during the initial phase of the expansion) and the high pressure region created near the surface of the plasma. However, as the plasma expands further, the B outside the plasma and hence g increases due to MFC. This increases the γ value. Therefore, at a time $\sim 0.03 \mu\text{s}$ the α begins to grow.

The temporal evolution of the α predicted by the linear theory with a constant growth rate γ_L is also shown in Fig. 4.12. Since, both the λ and g varies with time, we have used their time averaged values ($\lambda_{avg} \sim 10 \text{ cm}$, $g_{avg} \sim 3 \times 10^{14} \text{ m/s}^2$) for calculating the growth rate $\gamma_L \sim (2\pi g_{avg}/\lambda_{avg})^{1/2} \sim 1.4 \times 10^8 \text{ s}^{-1}$. Note that λ_{avg} and g_{avg} are also averaged along the θ direction. It is clear from the figure that the assumption of linear growth for α from $t = 0$ to t_s with a growth rate γ_L tends to overestimate the final amplitude by orders of magnitude. The magnetic deceleration g and hence the γ value, as mentioned earlier, becomes significant at a time $\sim 0.03 \mu\text{s}$. Therefore, we have also plotted the temporal evolution of α starting from $t \sim 0.03 \mu\text{s}$ by using both γ_L (shifted line in the Fig. 4.12) and $\gamma_L(t) \sim (2\pi g(t)/\lambda(t))^{1/2}$, where $g(t)$ and $\lambda(t)$ are the instantaneous values of the interface deceleration and wavelength respectively. These plots are close to the simulation result, except towards the stagnation time t_s , where the simulation result shows a non-linear evolution. Clearly, the assumption of linear growth from $t = 0$ produce a much larger amplitude than is observed computationally.

The temporal evolution of α for a few other cases of sinusoidal perturbation ($n = 5, 25$ and 45) with $\alpha_{in} = \lambda_{in}/1000$ is shown in Fig. 4.13. The evolution of α starting from $t = 0.03 \mu\text{s}$ is found to be in agreement with the predictions of linear theory. However, similar to the earlier case, non-linear evolution of the modes is observed towards the time $t = t_s$. For short wavelength modes, this onset of non-linearity occurs at an earlier time. For example the onset of non-linearity for mode $n = 45$ occurs at a time $t \sim 0.05 \mu\text{s}$, whereas for mode $n = 5$ this occurs at a time $t \sim 0.07 \mu\text{s}$. In short, the growth of the modes near stagnation time, although exponential in nature, occurs at a lower rate than that predicted by linear theory.

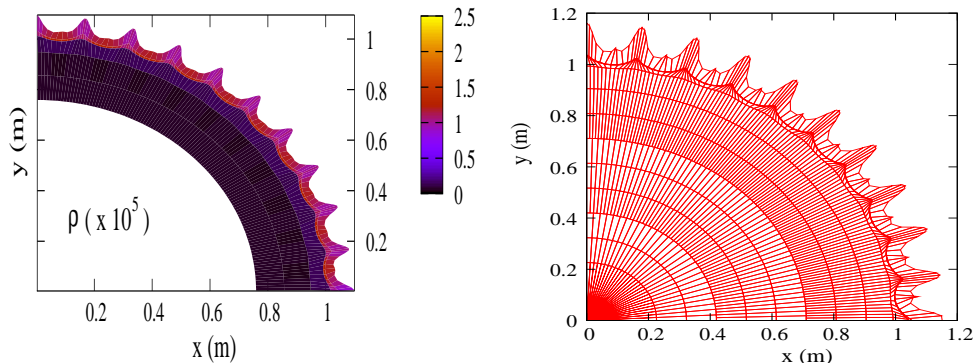


Figure 4.9: Density ($\times 10^5 \text{ kg/m}^3$) profile near the plasma surface towards $t = t_s$ for the case with $\lambda_{in} = 3.14 \text{ cm}$ ($n = 10$) and $\alpha_{in} = \lambda_{in}/10$. Right side plot is the corresponding Lagrangian Mesh with a mesh-size $\sim \lambda/12$.

For a plasma of given mass, its radial expansion velocity increases with its initial energy E_p . Therefore, the plasma energy determines (for fixed B) the stagnation time, plasma stopping radius and hence the growth of the modes. Typical plasma energy E_p and mass m_p reported for inertial fusion plasmas vary from 140–300 MJ and 1.2–6 mg respectively [25–27, 31, 32, 52, 82]. Fig. 4.15 shows the results of a sample calculation ($n = 10$, $\alpha_{in} = \lambda/1000$) with two different values for E_p (140 and 280 MJ) with $m_p \sim 4.4 \text{ mg}$. No significant difference in the final amplification factor (at $t \sim t_s$) is observed between these two cases despite having different

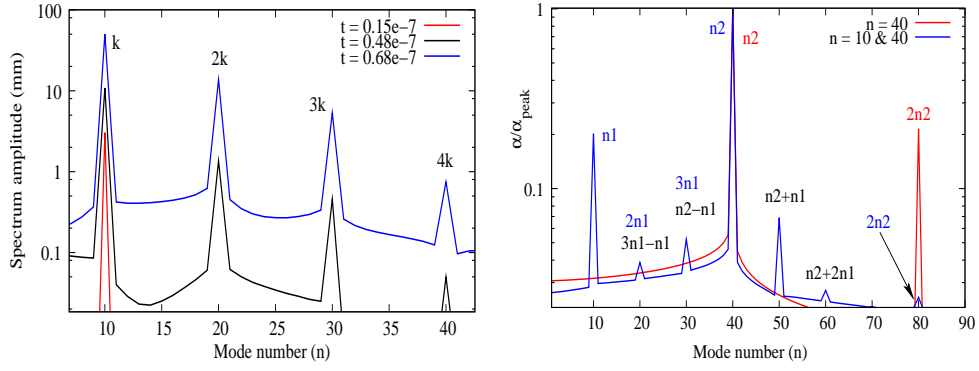


Figure 4.10: The left side plot shows the spectrum amplitude (mm) at different times (single mode analysis) with $\lambda_{in} = 3.14$ cm ($n = 10$) and $\alpha_{in} = \lambda_{in}/10$. The FFT spectrum shows the evolution of harmonic modes. Right side plot shows the normalized spectrum amplitude (α/α_{peak}) at $t \sim 0.04 \mu\text{s}$ obtained in the multi-mode analysis (modes 10 & 40, $\alpha_{in} = 500 \mu\text{m}$) and single mode analysis ($n = 40$, $\alpha_{in} = \lambda/10$).

operational time, interface deceleration and plasma stopping radius. The decrease in g (hence γ) and the increase in overall operational time (more growth) makes the final α/α_{in} factor nearly the same for this particular system parameters with $B \sim 5$ T. A similar trend is observed for other cases with different n , α_{in} and m_p . A more comprehensive analysis with different plasma mass, energy (different fusion yield), mode number, α_{in} and initial B lies beyond the scope of this work.

The results can now be summarized. Fig. 4.14 shows the values of maximum α/α_{in} and α obtained at $t = 0.09 \mu\text{s}$ (close to the stagnation time) for different values of initial mode number n and perturbation amplitude α_{in} . The final amplitude amplification factor α/α_{in} obtained is typically higher for the cases with lower α_{in} values. Also, small wavelength modes have comparatively higher α/α_{in} value. For a given n , the final α/α_{in} value obtained (at $t \sim t_s$), when $\alpha_{in} \sim \lambda/10$, is found to be much lower than the α/α_{in} values obtained for $\alpha_{in} \sim \lambda/100$ and $\lambda/1000$. This difference increases towards higher n (mode saturation for short λ modes happens at an earlier time). However, inspecting the actual amplitude (α) variation, com-

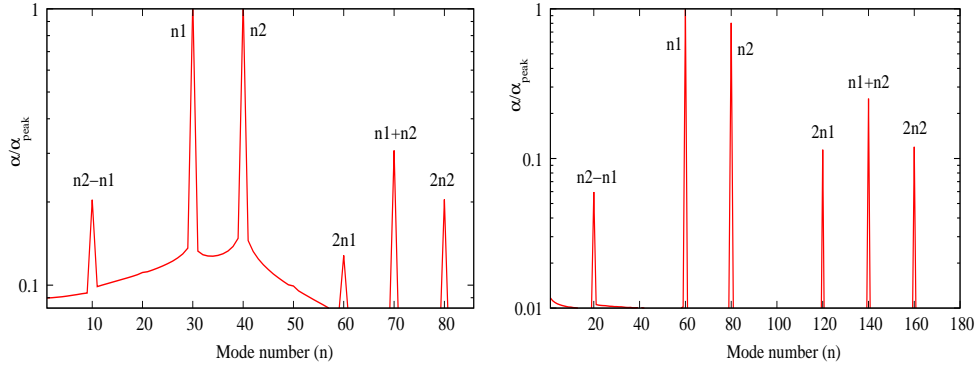


Figure 4.11: The normalized spectrum amplitude (α/α_{peak}) obtained in the multi-mode perturbation analysis with $\alpha_{in} \sim 500 \mu\text{m}$. The left and right side plots are for modes 30 & 40 at $t = 0.04 \mu\text{s}$ and modes 60 & 80 at $t = 0.03 \mu\text{s}$ respectively.

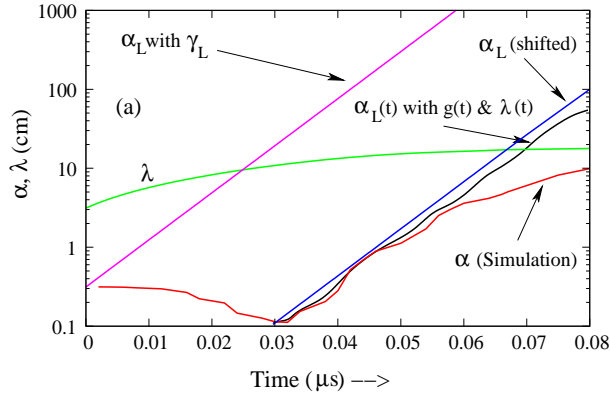


Figure 4.12: The evolution of perturbation amplitude α (single mode analysis) for $n = 10$ with $\alpha_{in} = \lambda_{in}/10$. Here, α_L is the analytical variation assuming constant linear growth rate $\gamma_L \sim (2\pi g_{avg}/\lambda_{avg})^{1/2}$. Similarly $\alpha_L(t)$ is obtained by using instantaneous values for $\gamma_L(t) \sim (2\pi g(t)/\lambda(t))^{1/2}$.

paratively larger α values (despite having lower α/α_{in} values) are observed for the cases with $\alpha_{in} \sim \lambda/10$. Furthermore, as the mode number n increases (shorter wavelength modes), the α values tend to decrease for $\alpha_{in} \sim \lambda/10$.

It is worth mentioning here that the conversion of plasma energy into electrical energy across a resistive load, during several expansion and compression cycles of the plasma [25–27], are for an unperturbed initial plasma with $B \leq 0.6 \text{ T}$. Such operation would be inefficient/challenging for the present system parameters

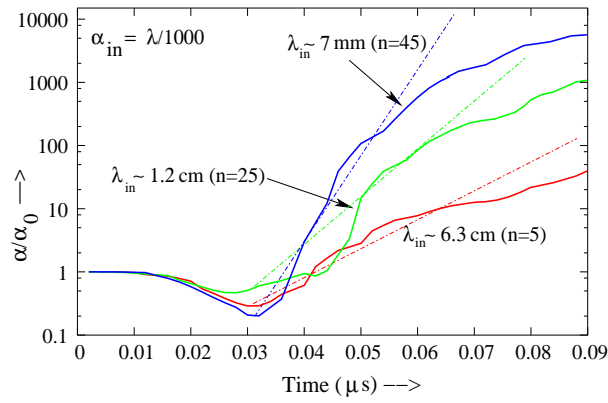


Figure 4.13: The temporal evolution (single mode analysis) of the spectrum amplitude (normalized to initial value) for modes 5, 25 and 45 with $\alpha_{in} = \lambda_{in}/1000$.

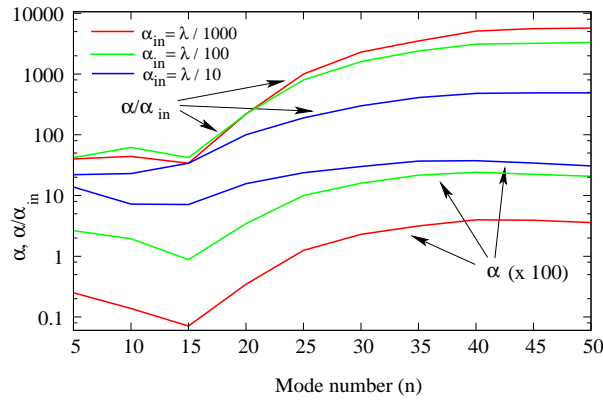


Figure 4.14: The variation of maximum α/α_{in} and $\alpha (\times 10^2 \text{ m})$ for different values of initial mode number n and perturbation amplitude α_{in} ($\lambda/1000$, $\lambda/100$ and $\lambda/10$).

since the plasma outer surface, after the first expansion phase, would have high-amplitude perturbations. During the next implosion phase of the plasma, after the turn-around, these perturbations grow further and may generate plasma jetting or extremely large amplitude wave structures, which could affect the smooth implosion of the plasma (the compression phase) and damage the cavity wall. Therefore, further studies are required to explore the concept of plasma energy recovery across a resistive load with several expansion and compression phases [25–27].

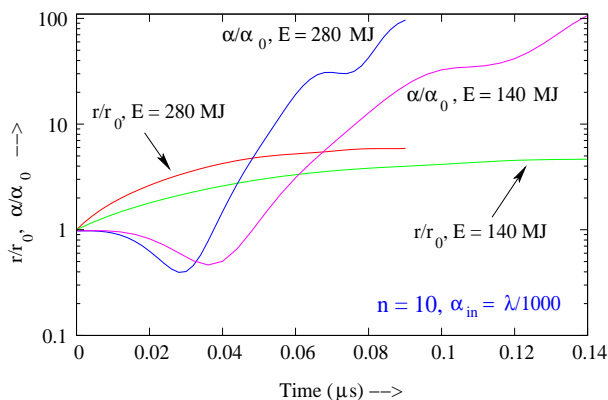


Figure 4.15: Temporal evolution of spectrum amplitude (single mode analysis with $n = 10$) and plasma outer surface radius (both normalized to their initial values) with $m_p \sim 4.4$ mg and $E_p = 140$ and 280 MJ.

The implications for the proposed MFC system (for the present plasma and system parameters) from the results summarized above are as below: The instability amplitudes are not large enough to severely disturb smooth compression of B for initial perturbations with $\alpha_{in} \leq \lambda_{in}/10$. Comparatively large wave structures are observed for the short wavelength modes with $\alpha_{in} \sim \lambda_{in}/10$.

Next, it is desirable to determine the threshold value of initial amplitude beyond which instability growth would significantly degrade operation due to large flute structures and jetting. Hence we have next conducted the instability analysis with $\alpha_{in} \geq \lambda_{in}$ for modes 5, 10, 20 and 40. The present Lagrangian scheme, however, has failed to simulate the plasma dynamics till the stagnation time for $\alpha_{in} \geq \lambda_{in}$ due to large plasma deformation (plasma jetting). Fig. 4.16 shows such a situation for $n = 10$ with $\alpha_{in} = \lambda_{in}$.

Beyond this time point, the Lagrangian scheme fails due to severe mesh tangling. Therefore, we have continued the analysis with an Eulerian MHD model described in Chapter 3. It is necessary to validate the Eulerian MHD model before we can believe its prediction of MRT instability growth rate. This has been

done by comparing the final α predicted by both models for different perturbation wavelengths (modes 5 – 40) with $\alpha_{in} \sim \lambda_{in}/10$. The differences in the final α thus obtained were not more than $\sim 6\%$ of the peak value, the Eulerian model predicting higher growth.

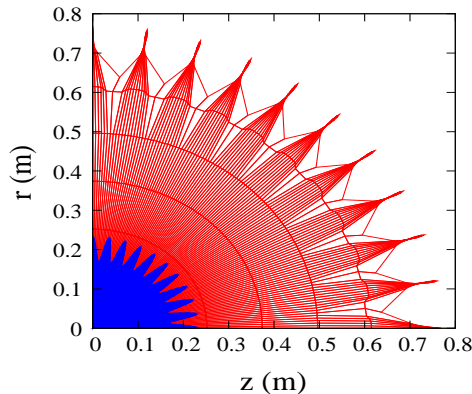


Figure 4.16: Initial plasma configuration (blue color plot) and the plasma configuration at $t = 0.033\mu\text{s}$ obtained in the single mode analysis for $n = 10$ with $\alpha_{in} = \lambda_{in}$.

Fig. 4.17 shows snapshots of MRT instability evolution, using Eulerian simulation, at different times, for $n = 10$ with $\alpha_{in} = \lambda_{in}$. Zoomed in plots of plasma density and pressure near the surface of the plasma at $0.09\mu\text{s}$ are shown in Fig. 4.18 and Fig. 4.19 respectively. Large plasma deformation, plasma jetting, flute breaking (towards t_s) etc are observed. Also, for this case, the instability amplitude is large enough to reach the coil inner surface before the stagnation time, leading to inefficient flux compression. In order to quantify the decrease in the flux compression efficiency, we have plotted the value of $\eta = B_f/B_{t_s}$ vs mode number for different values of α_{in} . Here, B_f and B_{t_s} are the B at a time when the plasma instability amplitude (jetting) first reaches the coil inner surface and the peak magnetic field obtained (~ 9.5 T) at t_s assuming ideal operation, respectively.

Fig. 4.20 shows the η calculated for modes 5, 10, 20 and 40 with two different

values of α_{in} (λ_{in} and $2\lambda_{in}$). For modes 5–10, the decrease in efficiency is $\sim 15\text{--}20\%$ when $\alpha_{in} \sim \lambda_{in}$ and $\sim 30\text{--}40\%$ when $\alpha_{in} \sim 2\lambda_{in}$. However, for a given α_{in} (related to λ_{in}), the decrease in η is found to be smaller for short λ modes. In general, a loss of efficiency $\sim 20\%$ is expected for longer λ modes ($n \leq 20$) and short λ modes ($n > 20$) when $\alpha_{in} \sim \lambda_{in}$ and $\alpha_{in} \sim 2\lambda_{in}$ respectively.

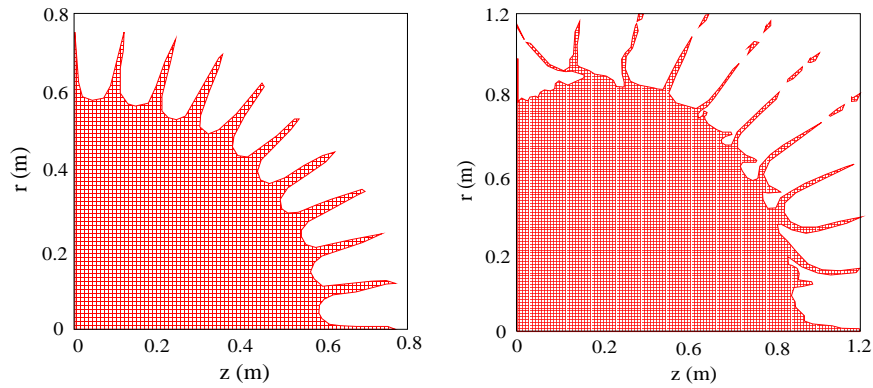


Figure 4.17: The snap shots of MRT instability evolution at different times (left and right side plots are at $0.035\mu\text{s}$ and $0.09\mu\text{s}$ respectively.) with an Eulerian MHD scheme for $n = 10$ with $\alpha_{in} = \lambda_{in}$.

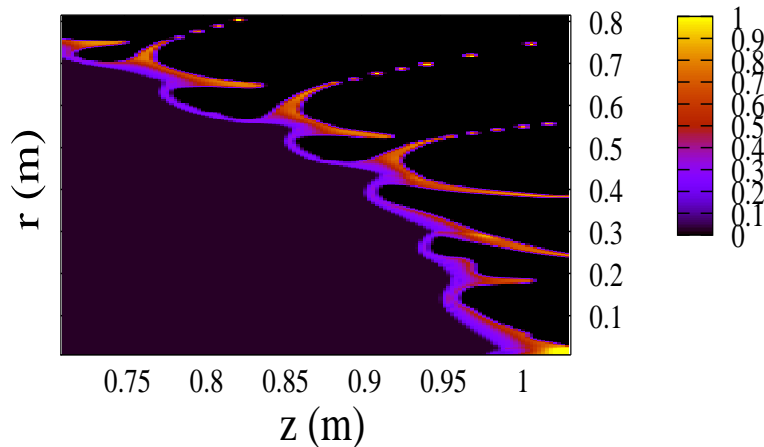


Figure 4.18: The plasma density (normalized to $1.0 \times 10^{-5} \text{ kg/m}^3$) at $0.09 \mu\text{s}$ obtained with an Eulerian MHD scheme for $n = 10$ with $\alpha_{in} = \lambda_{in}$. The plot is shown only near the surface of the plasma for better clarity.

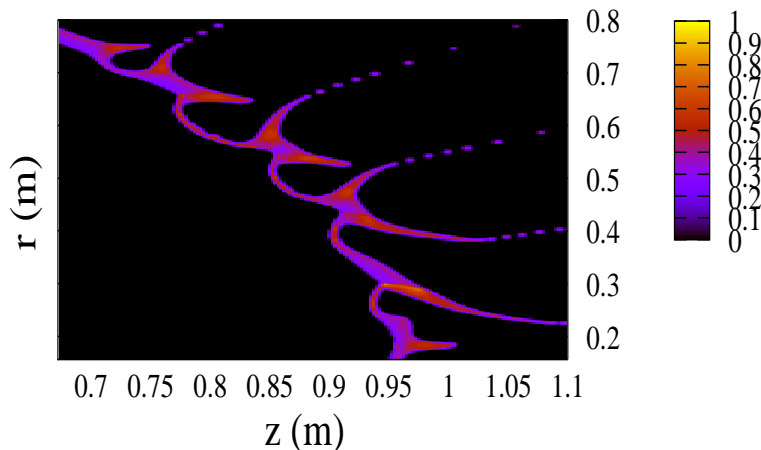


Figure 4.19: The plasma pressure (normalized to 7.0×10^7 Pa) at $0.09 \mu\text{s}$ obtained with an Eulerian MHD scheme for $n = 10$ with $\alpha_{in} = \lambda_{in}$. The plot is shown only near the surface of the plasma for better clarity.

4.5 Conclusions of this study

Two-dimensional MHD simulations of random, single and multi-mode perturbation growth in an MFC system driven by a fusion plasma sphere have been carried out for different initial perturbation amplitudes and wavelengths. The simulation takes into account the effects of magnetic flux compression and geometric divergence due to spherical plasma expansion.

In the random seed perturbation analysis, we have found that the dominant modes in the spectrum show a progressive transition from the short-wavelength to the intermediate-wavelength regime, $\lambda \sim 4\text{--}8$ cm – this is consistent with the observations in Ref. [82]. The cross-correlation analysis indicates the mode coupling between dominant modes and other modes in the spectrum.

The multi-mode (sinusoidal) analysis, with two different fundamental modes, and with $\alpha_{in} \sim 500 \mu\text{m}$, shows the appearance of higher harmonics of the individual modes, as well as the shorter wavelength ($n_1 + n_2$) and higher wavelength inverse cascade ($n_2 - n_1$) modes created by non-linear interaction of fundamental and

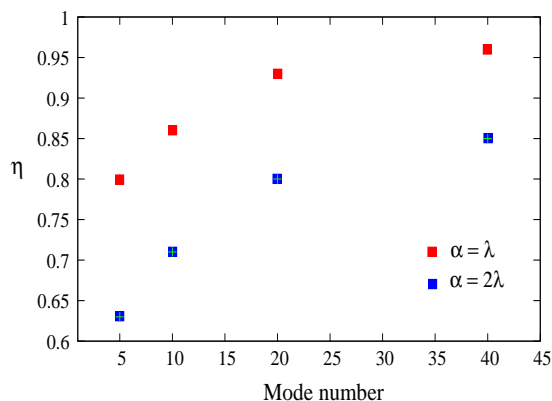


Figure 4.20: Flux compression efficiency (defined in the text) vs mode number for two different values of α_{in} .

harmonic modes.

In the case of single-mode perturbation, the modes continue to grow exponentially with nearly constant γ and make a transition into the non-linear phase (mode saturation). That is the amplitude growth of the modes towards stagnation time, although exponential in nature, is lower than the growth predicted by linear theory. We also note that extremely large flute structures and plasma jetting, which could damage or reach the cavity-wall/coil and to severely disturb the smooth compression of the magnetic field, are not seen during the time period of our interest, viz., the first expansion phase of the plasma. This means that it is feasible to have efficient flux compression during the first expansion phase in the proposed system, for perturbation amplitudes $\alpha_{in} \leq \lambda_{in}/10$. However, for $\alpha_{in} \geq \lambda_{in}$, the instability amplitudes are large enough, especially for longer λ modes, to cause plasma jetting leading to significant reduction in the flux compression efficiency.

There are a number of remaining issues that need to be addressed to obtain a complete description of the evolution of MRT instability in MFC systems driven by fusion plasma. The extension of the present work to three dimensions may give a better understanding of mode coupling and non-linear evolution. Future work

should quantify the effect of MRT instability in terms of conversion efficiency by using MHD models that are coupled with external circuit equations [52].

5

FDTD based first principle analysis of MFC systems

5.1 Introduction

So far in this thesis, we have focused on an MHD description of plasma behaviour. No attention has been paid to accurate modelling of the outer coil, which produces the seed magnetic field and also acts as the pickup coil. In all real-life MFC generators, such as helical flux compression generators [107], it is necessary to perform accurate calculations of the inductance and resistance of complex geometries, such as arbitrarily-wound helical coils, including the effects of multiple materials, conductors as well as insulators. The resistance calculations must take into account phenomena such as skin and proximity effects. For high-frequency (short pulse) operation, capacitive effects in the coil could also become significant. Furthermore, the requirement of self-consistent coupling between the MHD computational domain to external circuit solver can be eliminated by using a 3D FDTD simulation of the whole system. The evolution of electromagnetic field components in the

MFC system and the currents in the moving armature and the stator coil can be self-consistently updated by using FDTD scheme for electromagnetics. In this chapter, we report, for the first time, on the application of an advanced electromagnetics technique (FDTD scheme for electromagnetics) for accurate modelling of MFC generator coils.

Analytical, closed-form expressions are available, and have long been used, for calculating the coil resistance, taking into account skin and proximity effects [107–109]. Similarly, the filamentary technique has been applied to model skin and proximity effects in flux compression systems by Novac et al. [110, 111]. For an arbitrarily-wound coil, involving a variable pitch, loosely-wound coils (3D helical effects), turn splitting and inter-turn potting, calculation of the proximity and skin effects is complicated by a complex geometry and the presence of multiple materials, conductors as well as dielectrics. One example of such a dielectric is the inter-turn potting material used in conventional FCGs [107]. Note that the inter-turn potting cannot be used in the MFC systems described in previous chapters due to high inter-turn voltage ~ 25 MV. Even if these factors were not a consideration, the analytical methods are applicable for a single frequency, while flux compression systems typically involve complex temporal waveforms which cannot be approximated by a single frequency. To our knowledge, none of the closed-form expressions can handle these complexities.

The most general method is to solve the magnetic field diffusion equation for the system [57]. Such a solution yields the spatio-temporal distribution of the magnetic field, and hence the current density, throughout the domain, from which the resistance can be calculated. However, the electrical conductivity, and hence the magnetic field diffusion coefficient, can vary by orders of magnitude through the coil assembly. This leads to numerical problems in obtaining this solution using

“standard” solvers for such equations. In particular, the inter-turn insulation has a near-infinite magnetic field diffusion coefficient, requiring a near-zero time-step. This last problem can be handled by using flux-limited transport, but the problem of small time-steps remains. The problem is further complicated by imperfectly-known boundary conditions for the magnetic field. There is thus a need for a more general method that can handle real-life problems with all the complexities listed earlier.

We have used the three-dimensional (3-D) Finite Difference Time Domain (FDTD) method for electromagnetics [112] to handle such problems. This method directly updates Maxwell’s curl equations in time, using an explicit algorithm, to yield the 3-D variation of electric and magnetic fields. It allows setting up of complex, multi-material configurations. Furthermore, the time domain analysis allows handling of arbitrary time-dependent waveforms of current. This technique thus allows a study of real-life configurations with practically no limitations on the geometric complexity, the materials used or the temporal waveforms. To our knowledge, this is the first application of this powerful technique to such systems.

5.2 Application to problems with stationary conductors

5.2.1 Computational method

The past decade has seen rapidly-increasing growth of the Finite Difference Time-Domain (FDTD) method for electromagnetics to calculate scattering and absorption of electromagnetic waves from lossy dielectrics as well as conducting objects [118, 119, 122]. The FDTD method is an explicit time-domain approach for

solving Maxwell's curl equations

$$\nabla \times \vec{E} = -\mu \frac{\partial \vec{H}}{\partial t} \quad (5.1)$$

$$\nabla \times \vec{H} = \varepsilon \frac{\partial \vec{E}}{\partial t} + \sigma \vec{E} \quad (5.2)$$

on spatial grids, based on a technique introduced by Yee [114], see Fig. 5.1. Here, \vec{E} and \vec{H} represent the electric field and magnetic field intensities, respectively, while σ , μ and ε represent the electrical conductivity, magnetic permeability and permittivity of the medium, respectively. The six finite-difference equations are stepped in time, alternately updating the electric and magnetic field components at each grid point. This method has been applied to a wide range of problems, including scattering cross-section calculations for arbitrarily-shaped objects [115], scattering from materials with frequency-dependent properties [117], and a variety of other areas [116].

The FDTD technique yields the 3-D variation of electric and magnetic fields, $E(\vec{r},t)$ and $B(\vec{r},t)$ throughout a specified domain [112]. Using the field distribution computed for a given coil and a specified driving voltage waveform, we can determine the inductance from the magnetic field distribution and the resistance from the computed current. We can also determine the current density distribution $J(\vec{r},t)$ throughout the conductor, which provides physical insight into the role of proximity and skin effects.

The object to be modeled is set up in a Cartesian computational grid. The time-step is governed by the Courant criterion for speed-of-light transit through the smallest computational cell and it is calculated using Eq.(5.3) [112,114].

$$\Delta t = \frac{1}{c \sqrt{\frac{1}{\Delta x^2} + \frac{1}{\Delta y^2} + \frac{1}{\Delta z^2}}} \quad (5.3)$$

where, $c = 1/\sqrt{\mu\epsilon}$ is the velocity of light. Since the present problem is related to magnetic field diffusion, the standard finite difference form used in FDTD [112,114] is replaced by an explicit exponentially differenced form, to avoid the possibility of diffusion instability [105,106].

$$\begin{aligned}
 E_x^{n+\frac{1}{2}}(I, J, K) = & e^{\frac{-\sigma\Delta t}{\epsilon}} E_x^{n-\frac{1}{2}}(I, J, K) + \left[\frac{1 - e^{\frac{-\sigma\Delta t}{\epsilon}}}{\sigma} \right] \\
 & \times \left[\frac{H_z^n(I, J, K) - H_z^n(I, J - 1, K)}{Y(J) - Y(J - 1)} \right. \\
 & \left. - \frac{H_y^n(I, J, K) - H_y^n(I, J, K - 1)}{Z(K) - Z(K - 1)} \right]
 \end{aligned} \tag{5.4}$$

This modification increases computational accuracy in the presence of dissipation and this scheme reduces to a standard differencing form when $\sigma\Delta t\epsilon \ll 1$ so that $e^{\sigma\Delta t/\epsilon} \approx 1 - \sigma\Delta t/\epsilon$. This approach was taken to handle large values of σ and first published for the 3-D FDTD equations by Holland *et al.* [106]. Its 1-D application in the electromagnetics literature was given in Ref. [123]. A more detailed analysis of exponential time-differencing for FDTD in lossy dielectrics is given in Ref. [121]

A second-order outer radiation boundary condition has been used [112,113].

5.2.2 Geometry setup and excitation

Figure 5.2 shows a sample setup of the coil, along with the excitation by an applied voltage.

For problems of interest in the present work, we consider a time-harmonic applied voltage with a peak value V_p and angular frequency ω . The coil resistance (R), inclusive of proximity and skin effects, as well as the coil inductance (L), can then be calculated by ‘measuring’ the peak current (I_p) flowing through the coil

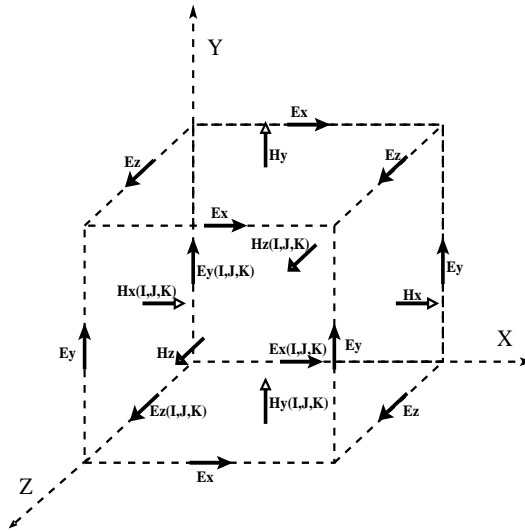


Figure 5.1: Yee cell with electric and magnetic field locations

and the phase angle (ϕ) between the applied voltage and the current.

$$V_p^2/I_p^2 = \omega^2 L^2 + R^2 \quad (5.5)$$

$$\tan(\phi) = \omega L/R \quad (5.6)$$

5.2.3 Important issues

FDTD modeling requires the calculation of optimum values for the size of a computational cell, the total number of cells required in the simulation and time-step.

The following issues must be kept in mind whilst setting up a magnetic field diffusion problem using FDTD. Firstly, the modeling of curved geometries, such as coils, in a Cartesian grid, leads to ‘staircase’ errors that must be minimized by using a sufficient number of cells [112]. Secondly, the cell size must not exceed 10% of the free-space wavelengths λ corresponding to the frequencies of interest [112]. Thirdly, since an outer radiation boundary condition is used, it is necessary to maintain a distance of at least 1-2 λ between the object and the domain boundary in all directions [112]. Fourthly, there must be a sufficient number of cells in one

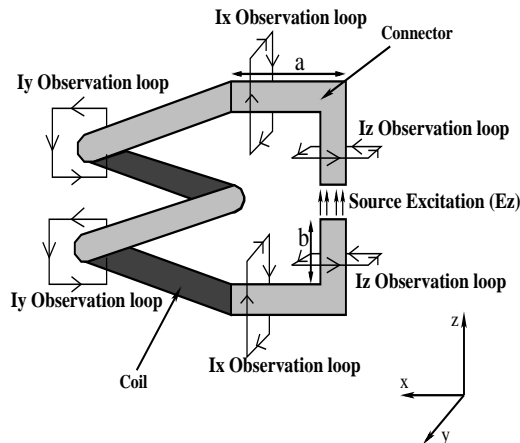


Figure 5.2: Schematic of a typical two turn coil geometry setup used in FDTD modeling, including different current observation loops as well as the applied electric field driving a current through the coil.

skin depth, for proper resolution of the penetration of the magnetic field. Fifthly, the wavelength corresponding to the applied frequency should be very different from system dimensions, to eliminate the possibility of radiation, which would not be significant in a real-life system.

These criteria, put together, lead to a rather large computational load in 3-D calculations, which is best illustrated by an example. Consider the copper coil shown in Figure 5.3, having a wire diameter $D=3$ mm and a mean coil diameter of 15 mm. For an applied voltage of frequency 1 MHz, the skin depth is 0.066 mm. This leads to a cell size of 0.0132 mm even if we use the bare minimum of five cells per skin depth. Even for a single-turn coil, a $1363 \times 1363 \times 227$ mesh is required, a total of 400 million cells. For a real-life problem involving multi-turn coils, the number would increase substantially. To this must be added the mandatory distance to the domain boundary, typically $1-2\lambda$. Since $\lambda = 3 \times 10^5$ mm, this leads to a prohibitively large mesh requirement. Another important parameter is the time-step. For a cell size of 0.0132 mm, in free space, the Courant-limited time-step Δt is $\approx 2.5 \times 10^{-14}$ s, leading to $\approx 3.9 \times 10^7$ steps per cycle. This is again

prohibitively large.

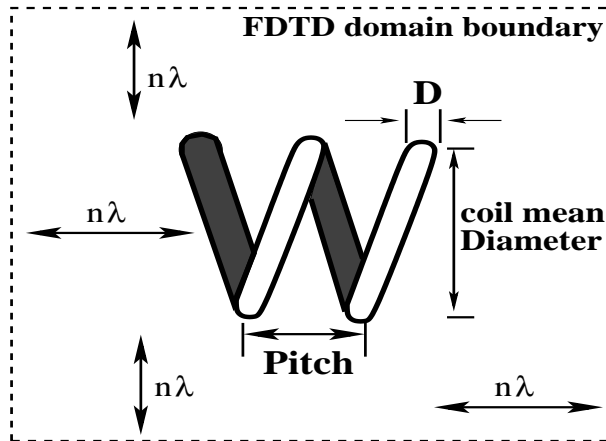


Figure 5.3: A typical two turn coil, $n\lambda$ is the distance to the FDTD domain boundary ($n = 1, 2, 3 \dots$)

This problem can be solved by using an artificially increased permittivity for the medium by a large factor, which reduces the speed of light and thereby permits much larger time-steps [105, 106]. The scaling factor used for the permittivity ϵ throughout the computational domain varies from 10^4 to 10^8 , depending upon the problem. This permits an increase in the time-step by a factor of 10^2 to 10^4 . Since λ is proportional to the speed of light, the cell size required to resolve the wavelength becomes a few mm. However, the cell size required to resolve the skin-depth is 10-1000 times smaller, depending upon the conductivity and frequency. The only solution is to have variable meshing, which is constant through the conductor region, but progressively expands in the free-space region surrounding the coil. With the use of variable meshing, a typical simulation involves $360 \times 360 \times 210$ cells, and a typical time-step of 10 ns.

Clearly, there is a great reduction in computational demand by increasing ϵ . However, one constraint must be kept in mind while increasing ϵ . In a real-life helical generator coil made out of good conductor, e.g. copper, the ratio of the conduction current to the displacement current $\sigma/\epsilon\omega \gg \gg 1$, i.e., the conduction

current dominates, by far, over the displacement current. The maximum enhancement in ϵ must be limited to a range that satisfies the above condition.

Another issue is to ensure the magnetic diffusion timescale in good conductors is not affected by the use of an artificially large permittivity to achieve higher time-steps in the simulation. The magnetic diffusion time to a conductor having thickness 'L' and conductivity σ is given by $t_d = \mu\sigma L^2$. This time scale will not be affected by increasing ϵ in the medium. However, the time-step used in the computation should not exceed the magnetic diffusion time scale and it should be able to resolve the magnetic diffusion time. In our simulation we have scaled permittivity keeping these constraints in mind.

Despite these changes, due to the large number of constraints that have to be satisfied, the computational demand is too large to be handled on one CPU. Hence the computer code has been parallelized in three directions with the flexibility to independently specify the number of CPUs in each direction.

The present work is an exploratory study of the use of FDTD for such problems. Hence the method has been applied to simple geometries, such as single-turn and two-turn coils. Coil dimensions, as well as parameters such as ϵ , ω and electrical conductivity σ , are chosen so as to minimize the computational demand. Also, in the present work, the coil geometries simulated are extremely small compared to those of interest for practically relevant MFC generators.

5.2.4 Important new constraint observed in simulations

Apart from the constraints mentioned in Section 5.2.3, which are known from the literature, our simulations have indicated a new constraint that must also be satisfied. This is discussed below.

Consider electromagnetic (EM) waves, driven by the exciting gap voltage, trav-

eling along the inner and outer surfaces of a coil, as illustrated in Figure 5.4.

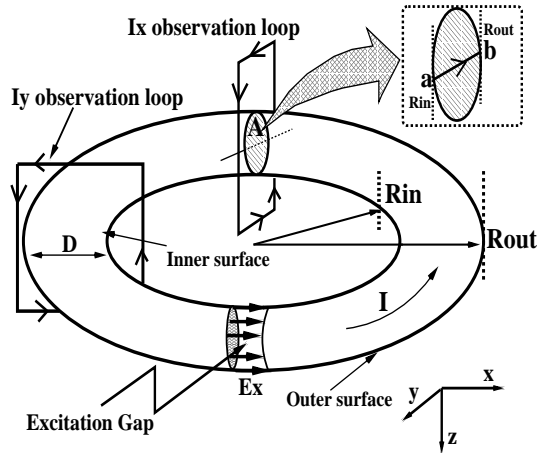


Figure 5.4: Schematic of a typical single-turn coil geometry setup with different current observation loops and source excitation gap. Inset shows line ‘ab’ along which electric field measurements are reported.

These two surfaces define transit paths with different path lengths. This difference can become significant for “thick” coils, i.e., coils where the conductor diameter is a significant fraction of the average coil diameter. For example, in a coil with an average diameter of 15 mm and a conductor diameter of 6 mm, the path lengths are $2\pi \times 18$ and $2\pi \times 12$ mm, respectively. These path lengths imply a transit time difference $\Delta t_{trans} = 0.13$ ns, taking the velocity of light in a vacuum. This is negligible in comparison with a cycle time of $1 \mu\text{s}$ corresponding to an applied frequency of 1 MHz, the highest typically encountered in helical generators. Hence, even with thick coils, this Δt_{trans} does not affect field propagation through the coil.

With a large enhancement in ϵ , however, the resulting decrease in the speed of light increases Δt_{trans} , and can make it significant in comparison with cycle times. This is bound to affect the distribution of EM fields through the conductor, leading to erroneous results. Hence ϵ should be chosen so that this error remains small.

5.2.5 Quasi-DC Excitation

We first studied the diffusion problem with a quasi-DC excitation by using a half Gaussian ramp-up pulse followed by a flat top. We expect the magnetic field to diffuse into the conductor and finally relax to a steady-state distribution. A gradual ramp-up of the applied voltage is necessary, since a jump in the electric field from zero to a finite value would lead to numerical instabilities [112]. The reasons for using a half-gaussian ramp-up waveform are explained in Ref. [120].

Single Turn Coil

We first studied diffusion into a single turn coil having the following parameters: coil mean radius $R = 7.5$ mm, conductor radius $r = 1.5$ mm, relative permittivity $\epsilon_r = 10^8$, conductivity $\sigma = 5 \times 10^5$ Siemens/m. This value of ϵ_r implies that the speed of light is reduced by a factor of 10^4 . The half-gaussian pulse had a rise time of $1 \mu\text{s}$, as shown in Figure 5.5. The coil is assumed to lie in the x-y plane, its thickness extending in the z direction as shown in Fig 5.4. The excitation is applied over a 3-cell gap in the x-direction. A $360 \times 360 \times 210$ mesh was used in the x, y and z directions, respectively. Variable mesh sizes were used, the smallest being 0.1 mm in the conductor region, increasing to a maximum of 3 mm in the free space region. The number of cells used along the x, y and z directions, and their variations, are mentioned in Table 5.1.

The computed mean current from currents observed at different observation locations is shown in Figure 5.6.

The currents have been computed by an application of Ampere's law along paths of the form shown in Figure 5.4. The difference between currents observed at two different locations are found to be very small for this particular case. However, at early times, up to $\sim 2 \mu\text{s}$, we see a small difference in the waveforms, which

Region	NX, DX (mm)	NY, DY (mm)	NZ, DZ (mm)
1	50, 3	50, 3	50, 3
2	10, 1.5	10, 1.5	10, 1.5
3	8, 0.8	8, 0.8	8, 0.8
4	2, 0.4	2, 0.4	2, 0.4
5	5, 0.2	5, 0.2	5, 0.2
6	5, 0.15	5, 0.15	5, 0.15
7	100, 0.1	100, 0.1	50, 0.1
8	5, 0.15	5, 0.15	5, 0.15
9	5, 0.2	5, 0.2	5, 0.2
10	2, 0.4	2, 0.4	2, 0.4
11	8, 0.8	8, 0.8	8, 0.8
12	10, 1.5	10, 1.5	10, 1.5
13	50, 3	50, 3	50, 3

Table 5.1: No. of cells and cell-size used in each directions

is due to a propagation delay between the two observation points at the reduced speed of light. However, once the applied voltage stabilizes at its peak value, propagation delay becomes irrelevant, and the waveforms merge.

At steady state, the current at different locations is found to be the same, as expected. The current at steady state was 24.5 mA and the excitation gap voltage was 0.3 mV, corresponding to a 3-cell gap with a cell size of 0.1 mm. The DC resistance, calculated from the steady state values, was 12.2 m Ω , yielding good agreement with the analytical value of 12.8 m Ω , and the analytical inductance value is 18.3 nH, leading to an analytical L/R time of 1.4 μ s.

It takes the current 2.23 μ s and 3.91 μ s to reach 60% and 90% of its steady-state value, respectively. This compares well with the analytical L/R time of 1.4 μ s.

The inductance can also be calculated from the magnetic energy stored. We have calculated the inductance from the energy of the magnetic field and mean current. The calculated value of 18.29 nH agrees well with the analytical value.

It is also interesting to examine the electric field distribution across the conductor cross-section, after steady state is achieved. Consider the inset shown in

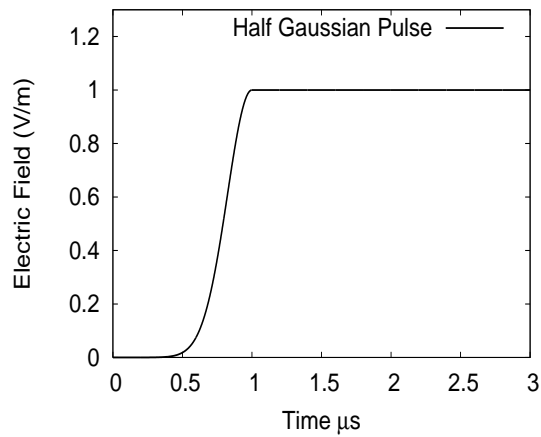


Figure 5.5: Applied Half-gaussian pulse for Quasi-DC excitation with a rise-time of $1 \mu s$

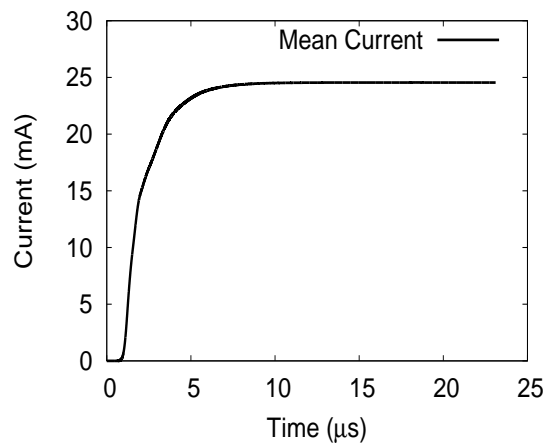


Figure 5.6: Mean current for single-turn coil with quasi-DC excitation

Figure 5.4. Since the applied voltage is the same across the coil cross-section (y - z plane), the electric field is expected to exhibit a strong variation with radial position, due to coil curvature. Figure 5.7 shows the steady-state distribution of electric field E_x as a function of radial position inside the conductor. The electric fields are plotted along the line \vec{ab} inside the conductor as shown in Figure 5.4. For the dimensions used in this study, the expected ratio $E_{in}/E_{out} = R_{out}/R_{in} = 1.5$, while the ratio determined from FDTD calculation is 1.53.

Hence we conclude that the FDTD technique yields good agreement with an-

alytical results in the case of quasi-DC excitation.

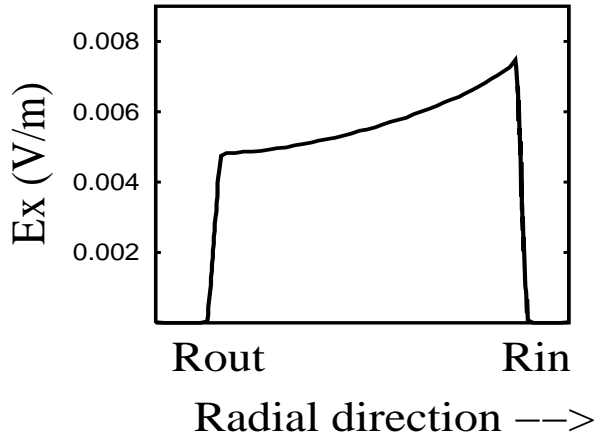


Figure 5.7: Steady-state electric field E_x (V/m) distribution through the conductor as a function of radial position (along the line \vec{ab} as shown in Figure 5.4) inside the conductor, for a single turn coil with Quasi-DC excitation.

Two Turn Coil

We next studied a two-turn coil with a Pitch/Diameter (P/D) ratio of 1.5, where D refers to the conductor diameter. The other dimensions are the same as in the single-turn coil, and the connectors are arranged as shown in Figure 5.2 with an excitation gap of 0.09 mm. A $640 \times 580 \times 390$ mesh was used, expanding from 0.09 mm to 3 mm. The number of cells used along the x, y and z directions and their variations are mentioned in Table 5.2. The 2D meshing near the conductor cross-section is shown in Figure 5.8.

The connectors have the same cross-section as the coil conductor, with $a = 4$ mm and $b = 3$ mm. $\sigma = 5 \times 10^2$ Siemens/m, the gaussian pulse has a rise-time of 10 ns, and $\epsilon_r = 10^2$ in the entire computational domain. The mean current, calculated using the currents recorded at different observation locations, is shown in Figure 5.9. The absolute value of the difference in currents with respect to the mean current is depicted in Figure 5.10. The reason for this change in current

Region	NX, DX (mm)	NY, DY (mm)	NZ, DZ (mm)
1	100, 3	100, 3	100, 3
2	6, 1	6, 1	6, 1
3	2, 0.4	2, 0.4	2, 0.4
4	2, 0.2	2, 0.2	2, 0.2
5	10, 0.1	10, 0.1	10, 0.1
6	400, 0.09	340, 0.09	150, 0.09
7	10, 0.1	10, 0.1	10, 0.1
8	2, 0.2	2, 0.2	2, 0.2
9	2, 0.4	2, 0.4	2, 0.4
10	6, 1	6, 1	6, 1
11	100, 3	100, 3	100, 3

Table 5.2: No. of cells and cell-size used in each directions

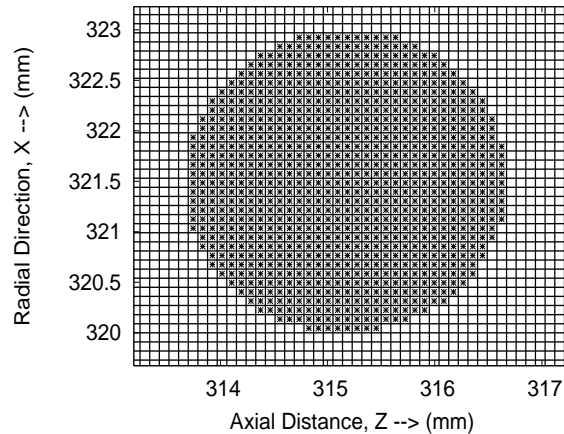


Figure 5.8: Meshing used near the conductor cross-section with mesh size of 0.09 mm

waveforms is the propagation delay between the observation points at the reduced speed of light. However, it is clear from the Figure 5.10 that at steady state the waveforms merge and the difference goes to zero.

The calculated DC resistance, inclusive of the connectors, is 28.7Ω , matching well with the analytical value of 29.1Ω . The inductance, calculated from the energy of the magnetic field and the mean current, is 33.78 nH , in reasonable agreement with the analytical value of 36.7 nH .

Having obtained a match in the gross resistance, we next examine the current density distribution through the conductor cross-section. Figure 5.11 shows the orientation of the coil in space and the cross-sections in each turn that have been used to record the current density distribution \mathbf{J} . The variation of \mathbf{J} over the conductor cross-section, at different times during current ramp-up, is shown in Figure 5.12. The following points are noteworthy:

1. The conductor cross-section for each turn lies in the x-z plane. It is clear from the plots that current densities are higher near the inner radius of the coil and decrease as we move radially outwards. This is consistent with the curvature effect that was seen in the single-turn coil.
2. As expected, the current gradually fills-up the entire cross-section as it approaches steady state. It is also clear that at early times, current densities are lower in the sections of the two turns adjacent to each other. This is the so-called ‘proximity effect’, which pushes apart the current from neighboring areas of two adjacent conductors if the current flows in the same direction. Such current concentration tends to increase the coil resistance, and plays a major role in determining the flux efficiency of helical MFC generators [108, 109].

To show the proximity effect in greater detail, the current density is calculated as a function of axial distance along the line \vec{cd} , which is indicated in Figure 5.11. The results are shown in Figure 5.13. The last frame in Figure 5.13 is close to steady state, where the current density distribution is uniform.

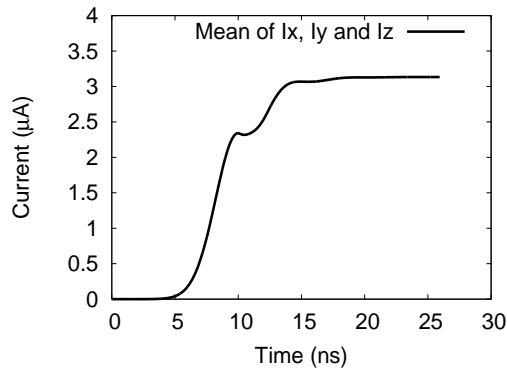


Figure 5.9: Mean Current calculated for two-turn coil with quasi-DC excitation

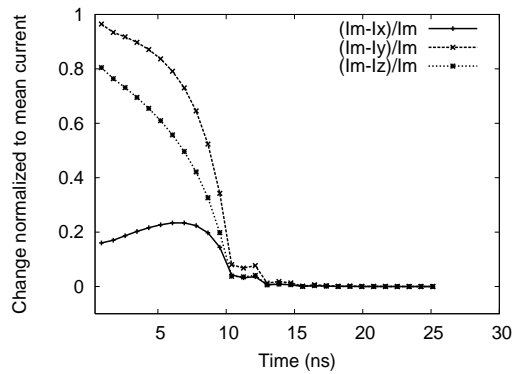


Figure 5.10: Absolute value of the difference in currents with respect to the mean current

5.2.6 AC Excitation

We continue to study simple coil geometries for the cases with AC excitation, coil parameters being chosen so as to minimize the demand for computational resources.

Single Turn Coil

We next study a single-turn coil with AC excitation. The coil dimensions are the same as those used with quasi-DC excitation, with $\sigma = 5 \times 10^6$ Siemens/m, a frequency of 0.1 MHz, yielding a skin-depth of 0.7 mm. A $360 \times 360 \times 210$ mesh was used, the smallest being 0.1 mm in the conductor region, and expanding to

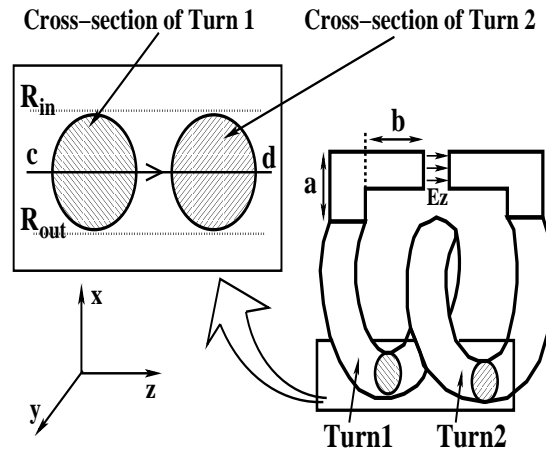


Figure 5.11: Schematic of a typical two-turn coil which shows the current density observation planes across the conductor cross-section for individual turns in the coil

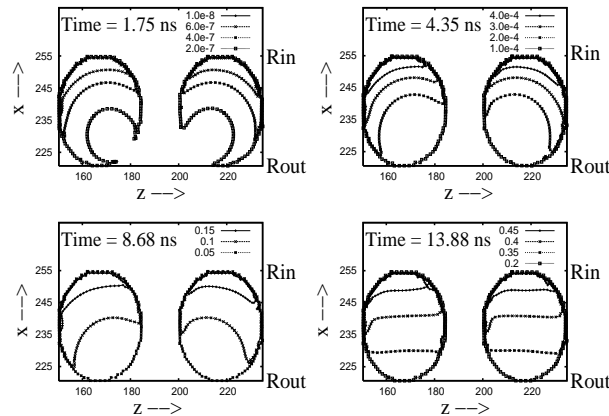


Figure 5.12: Current density distribution (A/m^2) over the conductor cross-section for a two turn coil at different times during current ramp-up. The last frame is close to steady state.

3 mm in free space. The applied voltage, and the measured current waveforms at two locations, are shown in Figure 5.14. As expected, there is an initial transient in the current waveforms, settling down to harmonic variation after a few cycles. From the observed current waveform, and its phase difference with the voltage, the inductance was found to be 18.3 nH, in excellent with the analytical value of 18.3 nH. The inductance calculated from the magnetic energy stored and mean current was 18.24 nH. The ratio of AC to DC resistance (R_{AC}/R_{DC}) calculated from

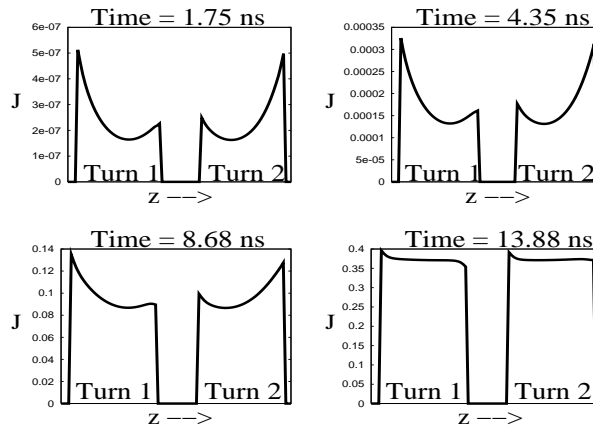


Figure 5.13: The current density (A/m^2) diffusion in to the conductor cross-section as a function of axial distance (along the line \vec{cd} as shown in Figure 5.11) for a two turn coil at different times during current ramp-up. The last frame is close to steady state.

the simulation is 1.36, matching very well with the analytical value of 1.364 from Arnold's expression [109]. However, Arnold's formulae for resistance calculations are approximations as well, especially for non-perfect conductors. Also, it fails to give accurate results for coils with gap, loosely wound coils and variable pitch coils. Arnold's method does not include non-linear heating of conductors.

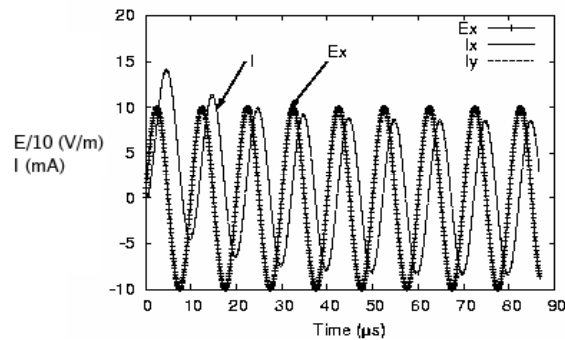


Figure 5.14: Currents (mA) observed at different locations and the applied voltage (scaled up by 10) for a single-turn coil with AC excitation

Two Turn Coil

We next studied a two-turn coil with the same coil dimensions as in quasi-DC excitation, with an applied voltage frequency of 100 MHz and conductivity $\sigma = 5 \times 10^3$ Siemens/m. A $640 \times 580 \times 390$ mesh was used, expanding from 0.09 mm to 3 mm. The current waveforms observed at three different observation locations are shown in Figure 5.15. The simulation yields a value of 1.54 for the ratio of

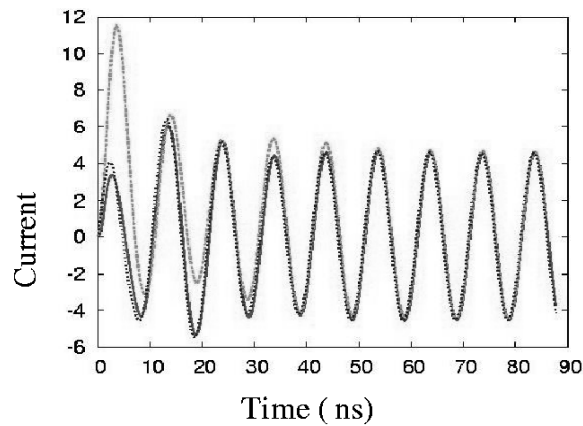


Figure 5.15: Currents (μA) observed at different locations for two-turn coil for AC excitation

AC to DC resistance (R_{AC}/R_{DC}), matching well with the analytical value of 1.49 from Arnold's expression [109]. The inductance calculated is 33.6 nH, while the analytical value is 36.7 nH – however, it should be noted that the analytical value assumes a uniform current density distribution through the conductor, which is bound to yield a higher inductance.

Figure 5.16 shows the variation of time-dependent inductance up to the steady state. The inductances are functions of time because of the diffusion of field into the conductors. At steady state the coil inductance calculated from the magnetic energy stored and mean peak current is 33.59 nH. Consider the conductor cross-sections depicted in Figure 5.11. The distribution of current density over these

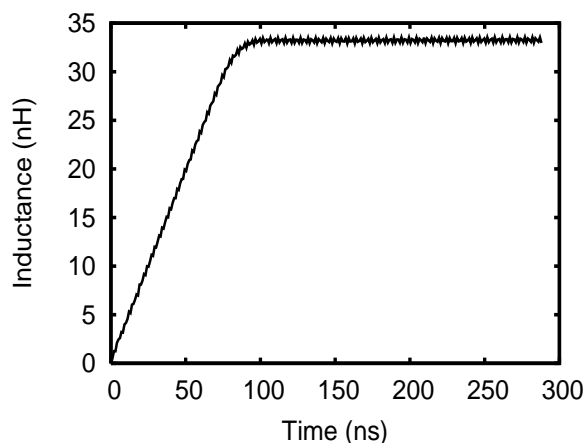


Figure 5.16: Time dependent inductance (nH) for two-turn coil with AC excitation

cross-sections is shown in Figure 5.17 at various times covering one cycle. The results are shown after the simulation settles down to a harmonic variation. The variation of current density distribution along the axial direction (line \vec{cd} in Figure 5.11) of the coil, illustrating the proximity effect for this case, is shown in Figure 5.18. It is clear from the plots that the magnitude of current densities are lower in the sections of the two turns adjacent to each other. Also, the the magnitude of current density fluctuation in a cycle are found to be less at these locations.

5.2.7 Sample calculations for different P/D ratios

It is also interesting to know how the ratio of AC to DC resistance, R_{ac}/R_{dc} , varies with the P/D ratio of the coil. For this, we have used a simple two-turn coil with dimensions used in previous calculations, along with a fixed frequency of 1 GHz and conductivity $\sigma = 10^3$ Siemens/m. The P/D ratio is varied from 1.2 to 5.2. The R_{ac}/R_{dc} calculated using FDTD method and the analytical values from [109] are shown in Figure 5.19.

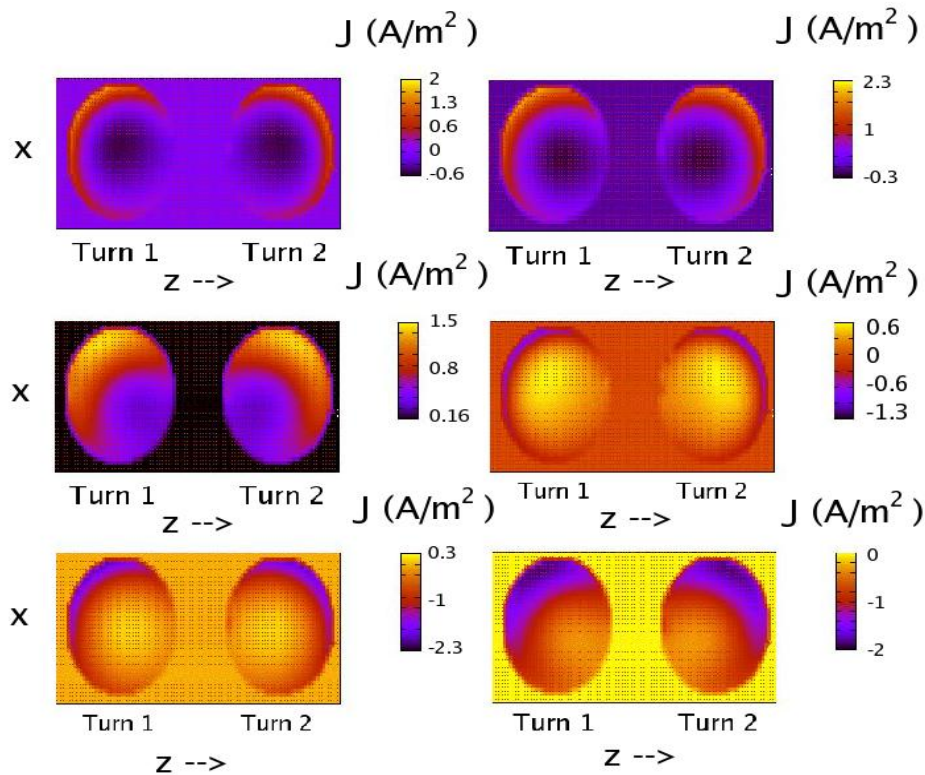


Figure 5.17: Current density (A/m^2) distribution over conductor cross-section for two-turn coil for AC excitation. The snap-shots are for a typical cycle after reaching steady state.

5.2.8 Sample Calculations for different applied frequencies

Finally, we consider a two-turn coil having the same parameters as earlier, but with the following changes. The P/D ratio is held constant at 1.3, the frequency being varied from 0.5 to 1.3 GHz. The variation of R_{ac}/R_{dc} is shown in Figure 5.20. Fairly good agreement is seen.

5.2.9 Sample calculation with a variable pitch coil

We have studied a typical problem with a simple coil structure having two sections with different P/D ratios. The first section of the coil is with a P/D ratio of 1.5 and the other with 3.0. Both sections have the same number of turns (two). Fig. 5.21

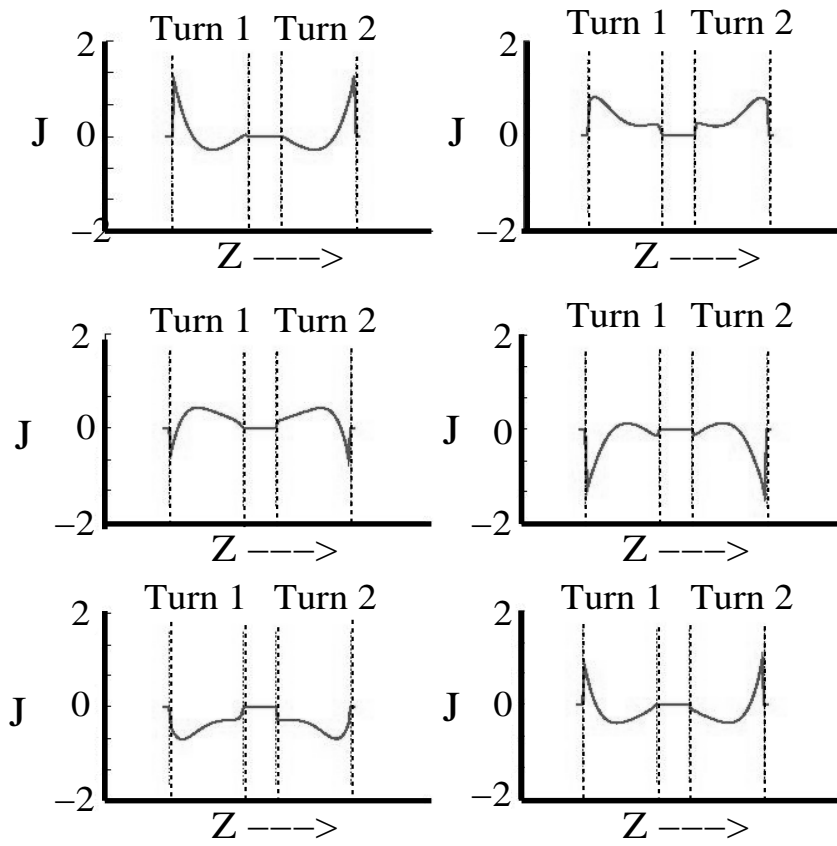


Figure 5.18: Current density (A/m^2) distribution over conductor cross-section for two-turn coil for AC excitation. The snap-shots are for a typical cycle after reaching steady state.

shows a schematic of the coil. The coil mean diameter and wire diameter are the same as mentioned in previous sections for the two-turn coil, with a conductivity of $\sigma = 5 \times 10^3$ Siemens/m. A mesh size of $640 \times 580 \times 1170$ was used with an applied voltage frequency of 100 MHz. To calculate AC to DC resistance (R_{AC}/R_{DC}) for this case using Arnold's expression, we have to use the average P/D ratio for the coil, which is equal to 2.25 for the case with four turns. R_{AC}/R_{DC} calculated using Arnold's formula with the average P/D ratio is 1.49. Another way is to calculate R_{AC}/R_{DC} independently for the two sections and then take the average, which yields 1.44. Both the calculations using Arnold's formula only approximately

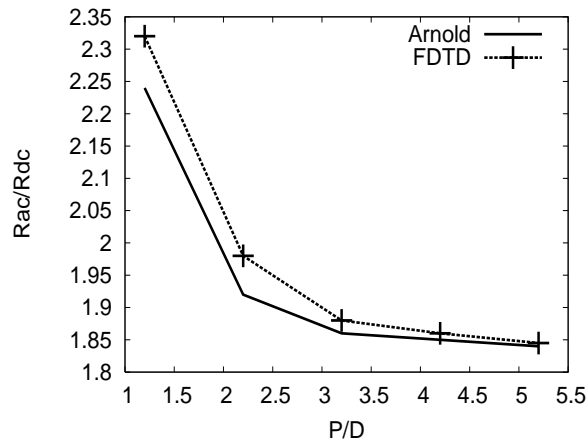


Figure 5.19: Comparison of R_{ac}/R_{dc} using FDTD calculations with those obtained from Arnold's expression, as a function of the P/D ratio. Calculations are reported for a two-turn coil with an applied frequency of 1 GHz.

account for variable pitch, so the estimate is subject to some error. The value yielded by FDTD is 1.59.

5.2.10 Parallel Performance of the 3D-Code

3-D FDTD calculations are very demanding. Hence it is necessary to parallelize the computer code using the Message Passing Interface (MPI) for communication between processors. The speedup achievable with the parallelized code is discussed in this section.

Consider the two-turn coil system mentioned earlier. This requires a mesh size of $640 \times 580 \times 390$ in x, y and z directions respectively. The performance study were performed on a 33 node 3.0 GHz, Dual core and Dual Socket Xeon cluster with an Infiniband interconnect and 4 GB memory per node. The network bandwidth is 20+20 (send+receive) Giga bits per second (Gbps). The performance of the code in terms of speedup is given in Table 5.3. In that Table, NPx, NPy and NPz refer to the number of segments in the domain in the x-, y- and z-directions. It is clear from the table that three-way parallelization gives better performance compared

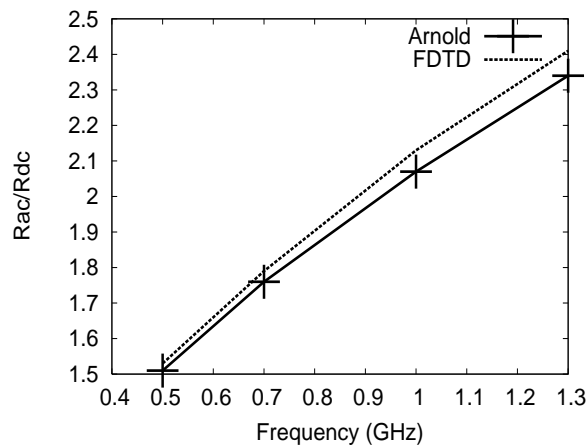


Figure 5.20: Comparison of R_{ac}/R_{dc} using FDTD calculations with those from Arnold's expression, for a two-turn coil having a P/D ratio of 1.3. The frequency is varied from 0.5 to 1.3 GHz

to parallelized performance in one direction, typically when the dimensions of the unparallelized directions are larger. For example, speedup achieved for 20 processors along the z-direction is only about 16.2, while with the same number of processors (10 along x-direction, 2 along y-direction and 1 along z-direction) gives a speedup of 18. Still better performance, a speedup of 19.4, is achieved with a combination of $NPC_x=5$, $NPC_y=2$ and $NPC_z=2$ (Total 20). A plot showing the speedup achieved for two cases, namely, parallelization along one direction and parallelization along multiple directions, is shown in Fig. 5.22. It is clear that for a given number of processors, a better performance can be achieved by multi-directional parallelization. Total computational time required for this particular problem with 10 processors (along z-direction) was ≈ 28 hours for completing 12 harmonic wave cycles with a computational time-step of 1.7×10^{-12} sec.

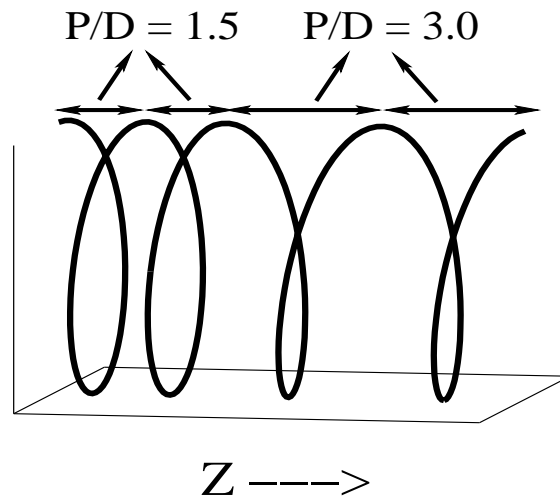


Figure 5.21: Sketch of a typical 4 turn variable pitch coil having two sections with different P/D ratio

5.3 Application to dynamic problems

So far in this chapter, we have considered the application of the FDTD technique to problems involving static conductors. MFC systems involve the motion of conductors (liner, armature or expanding plasma) across a magnetic field. The FDTD calculations performed so far include only the coil (stator); the inclusion of material movement in standard FDTD equations is, therefore, necessary. Worldwide, the FDTD algorithms for electromagnetics are used mainly for problems with static conductors.

We have, therefore, developed a new 2D-FDTD algorithm for electromagnetics by including motional e.m.f terms in the standard FDTD update equations, which can be applied to flux compression systems with moving parts. A leapfrog method [114] is used to update electric and magnetic fields, and a Flux Corrected Transport (FCT) algorithm [59,125] is used for magnetic field transport. This new method can be used for electromagnetic problems involving material movement.

NPx	NPy	NPz	Total	Speedup
1	1	5	5	4.5
1	1	10	10	9.1
1	1	15	15	12.1
1	1	20	20	16.2
1	1	25	25	15.6
3	2	1	6	5.9
5	2	1	10	9.4
7	2	1	14	13.6
10	2	1	20	18.0
12	2	1	24	21.4
3	3	1	9	8.9
4	4	1	16	15.8
5	5	1	25	23.2
2	2	2	8	7.9
3	2	2	12	11.9
4	2	2	16	15.8
5	2	2	20	19.4
6	2	2	24	23.8
3	3	2	18	17.9
4	3	2	24	23.9
3	3	3	27	26.9

Table 5.3: Speedup achieved with no. of processors used in each directions

In the following, we report details of this modified FDTD method for electromagnetic problems involving material movement and validation of the new technique. We restrict our calculations to two spatial dimensions (2D), although its three dimensional (3D) implementation is straightforward. To our knowledge, this is the first application of this powerful technique to systems involving material movement.

5.3.1 Algorithm

Similar to the case for static problems described in the earlier sections, the standard scheme is replaced by an explicit exponentially-differenced form, to avoid the

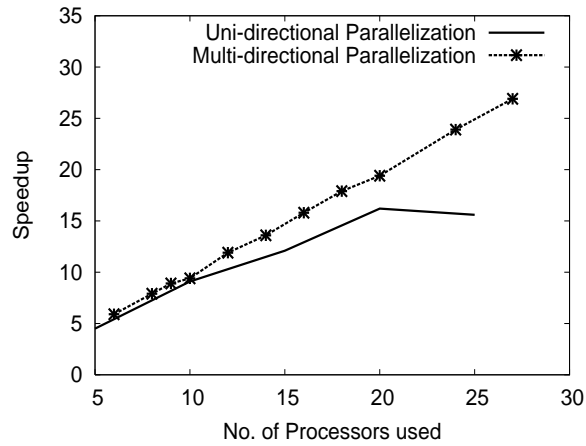


Figure 5.22: Speedup vs. no. of processors used for two different cases, namely, parallelization along one direction and parallelization along multiple directions

possibility of diffusion instability [105, 106, 121, 123].

Let us now consider problems involving magnetic field diffusion through moving conductors. We limit ourselves to non-relativistic cases, which is sufficient for practical systems such as magnetic flux compression systems. Hence the effect on displacement current can be neglected. The motion of a conductor in an external magnetic field can create an electric field or voltage (motional emf) that can induce a flow of current in the conductor. This can be expressed mathematically by the relation

$$\vec{E}' = \vec{E} + \vec{v} \times \vec{B} \quad (5.7)$$

The conduction current density \vec{J} must now include the motional emf:

$$\vec{J} = \sigma \left[\vec{E} + \vec{v} \times \vec{B} \right]$$

where, $\vec{B} = \mu \vec{H}$. This corresponds to a motional electric field, $\vec{E}_v = \mu(\vec{v} \times \vec{H})$, induced in materials having finite conductivity and velocity.

For most problems in time-dependent field problems, where currents are induced by non-relativistic velocities, $\vec{D}' \approx \vec{D}$ and $\vec{B}' \approx \vec{B}$, (see, e.g., Sommerfield, 1952) [128]. Thus the electric field and hence conduction current density are the only variables that differ significantly. The relevant theories followed and its mathematical formulations can be found in Ref. [129].

The addition of motional electric field leads to the following equation for magnetic field update.

$$\frac{\partial \vec{H}}{\partial t} = -\frac{1}{\mu} \nabla \times \vec{E}' + \nabla \times \vec{v} \times \vec{H} \quad (5.8)$$

Applying some mathematical treatment, along with the condition $\nabla \cdot \vec{H} = 0$, the final form of Eq. 5.8 becomes:

$$\frac{\partial \vec{H}}{\partial t} + \nabla \cdot (\vec{v} \vec{H}) = S_H \quad (5.9)$$

where, $\nabla \cdot (\vec{v} \vec{H})_j = \Sigma_i \partial(v_i H_j) / \partial x_i$ in Cartesian coordinates. The source term S_H is given by

$$S_H = \nabla \cdot (\vec{H} \vec{v}) - \frac{1}{\mu} \nabla \times \vec{E}' \quad (5.10)$$

The advection terms in Eq.(5.9) can be solved using special algorithms like the Total Variation Diminishing (TVD) scheme [130–132] or the Method of Characteristics (MOC) [133]. A comparative study on TVD scheme and the flux-corrected transport (FCT) method can be found in Ref. [132], which also lists some advantages of the FCT algorithm over the TVD scheme. The FCT procedure adds higher order anti-diffusive terms to the stable but diffusive low-order solution and a limiter ensures that no new minima or maxima with respect to the low order solution are created [59,125]. This method ensures a monotonic solution. A detailed discussion can be found in Refs. [59,125]. The FCT algorithm satisfies $\nabla \cdot \vec{H} = 0$ condition fairly accurately, limited only by round off errors. It is also efficient at

resolving sharp spatial gradients. Finally, its implementation is simple. We have, therefore, opted to use the FCT algorithm to modify the standard FDTD equations for magnetic field diffusion through moving conductors. We have also used a multi-dimensional flux limiter suggested in Refs. [134, 135].

The electric field equation can be updated using the following equation which include $\vec{v} \times \vec{B}$ term.

$$\frac{\partial \vec{E}}{\partial t} = -\frac{\nabla \times \vec{H}}{\varepsilon} + \frac{\sigma}{\varepsilon} \vec{E} \quad (5.11)$$

A variety of boundary conditions are available for FDTD algorithms [122]. It turns out that in the problems of interest here, the choice of boundary condition is not very critical, as long as the boundary is far from the the object through which magnetic field diffusion is taking place. Hence we have used Mur's second order outer radiation boundary condition (ORBC) [112, 113]. For other problems, more appropriate boundary conditions could be used.

Due to material movement through the mesh, the electrical conductivity throughout the domain must be updated at every time-step. This is particularly critical at conductor-insulator interfaces, where the conductivity changes by orders of magnitude. The conductivity in each computational cell is calculated based on the mass density – details are given in Sec. 5.3.3. Hence it is necessary to evolve material density throughout the domain, given the spatio-temporal distribution of velocity. This is done using the continuity equation:

$$\frac{\partial \rho}{\partial t} + \nabla \cdot (\vec{v}\rho) = 0 \quad (5.12)$$

where \vec{v} is the material/conductor velocity. The velocity distribution in space and time, throughout the computational domain, must be externally specified. In the

present study, the velocity distribution required throughout the domain in space and time is given as an input parameter. Self-consistent updation of the velocity profile with the hydrodynamics lies beyond the scope of the present work.

Due to the large number of constraints that have to be satisfied, the computational demand is too large to be handled on one CPU. Hence the computer code has been parallelized using Message Passing Interface (MPI) [136] in all directions, with the flexibility to independently specify the number of sub-divisions in each direction.

5.3.2 Theoretical Model for a simple system

This new method has been validated against analytical solutions for the spatio-temporal distribution of the magnetic field, given in Refs. [79–81]. These solutions apply to a simple flux compression system having a slab geometry shown in Fig. 5.23. The system consists of a slab with a finite conductivity σ and thickness a , placed inside two ideally conducting walls with infinite conductivity. The slab moves across a transverse magnetic field with a uniform velocity, v . B_{10} and B_{20} are the initial transverse (z -component) magnetic fields to the left and right of the conductor. In Figure 5.23, L is the length of the ‘compression volume’. As the slab moves to the right, it reduces L , leading to an amplification in the external magnetic field B_{20} by flux compression and a dilution of magnetic field B_{10} behind the slab [80, 81].

The processes involved are a) the induction of electromagnetic fields in the conductor resulting from its motion across $B(x, t)$, and b) diffusion of this magnetic field through the moving conductor, etc [79–81]. The extent of field amplification depends on two competing effects. Diffusion of flux through the conductor reduces the total flux left in the compression volume. The remaining flux is compressed

into a progressively smaller volume, leading to an increase in magnetic field. The efficiency of flux compression in the compression volume is related to a dimensionless number

$$R_d = \frac{\mu\sigma a^2 v}{L} \quad (5.13)$$

which is the ratio of the diffusion time $t_d = \mu\sigma a^2$ to the compression time $t_v = L/v$. The higher the value of R_d , the better is expected to be the conservation of flux in the compression volume.

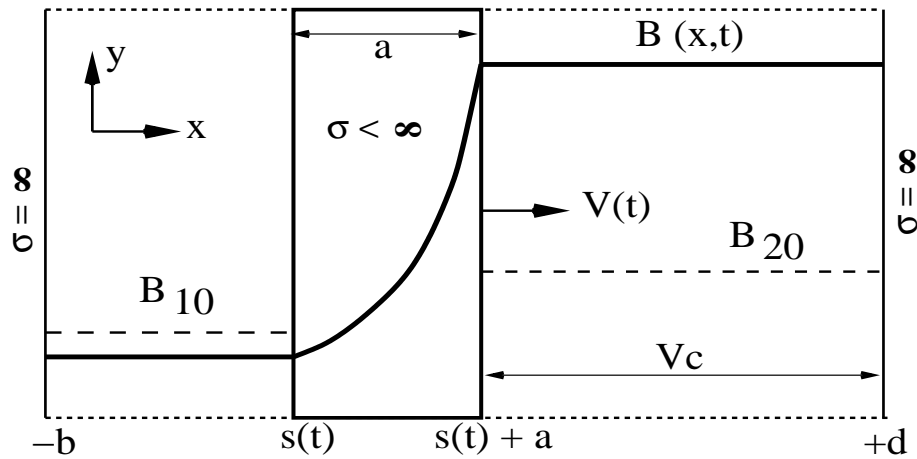


Figure 5.23: Electromagnetic induction model with a moving conductor and fixed end conductors at $x = -b$ and $x = +d$. B_{10} , B_{20} are the initial transverse magnetic fields to the left and right of the conductor. The symbol V_c marks the ‘compression volume’.

This is an initial-boundary-value-problem (IBVP) and can be solved analytically as in Refs. [80, 81]. The displacement current is neglected in Refs. [80, 81] while deriving analytical solutions, since the electromagnetic field changes are produced by non-relativistic conductor motion. Also, the diffusion of electromagnetic field through the moving conductor is described by the linear parabolic diffusion equation, since joule heating is neglected for the present study. More details can be found in Refs. [80, 81].

In order to remain consistent with [79–81], we have neglected the deceleration

of the moving conductor and its compression due to magnetic pressure, which becomes significant at high fields. However, it is easy to include both effects in the FDTD calculation.

5.3.3 Computational Model

The FDTD setup is shown in Fig. 5.24. The object is modeled in a 2D Cartesian grid. For the present problem, only E_x and E_y components of the electric field and the H_z component of the magnetic field exists. The electric and magnetic field components are located according to a 2D Yee cell configuration, as shown in Fig. 5.25. Material quantities like conductivity, σ and density, ρ are specified at the center of a computational cell, while velocities are specified at the faces of the cell. The specification of field locations in this manner requires boundary conditions only for electric field components. In order to remain consistent with FCT algorithms [59,125], the velocities are specified on the edge faces.

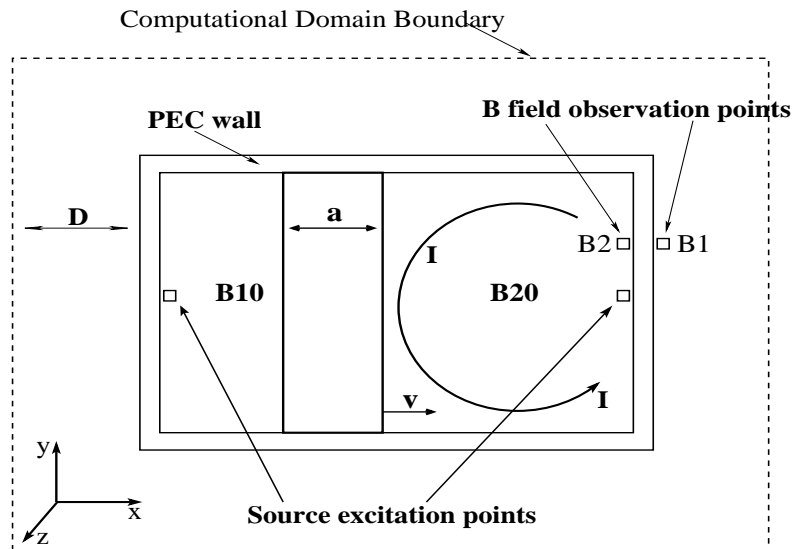


Figure 5.24: FDTD setup, with source excitation points and magnetic field observation points (B_1 and B_2). D is the distance to computational boundary.

The conductor, having a thickness a , is enclosed by a Perfectly Electrically Conducting (PEC, $\sigma = \infty$) wall. Mur's outer radiation boundary condition (ORBC) [112, 113] has been used to terminate the computational domain. In order to avoid unphysical reflections from the termination boundary due to ORBC, a minimum distance D must be maintained between the PEC wall and the computational boundary in all directions. D is typically 1-2 λ [112]. A gap of 20-40 cells has been found to be sufficient for the present problem.

For the present problem we found that no field get diffused through the PEC wall and therefore the number of cells between the object (PEC wall) and the boundary can be reduced considerably. The initial magnetic fields B_{10} and B_{20} are specified analytically at two different source excitation points, see Fig. 5.24, with one computational cell for each source excitation point. The field observation points B_1 and B_2 are used for recording magnetic fields at different times.

In the FDTD method, the highest frequency that can be handled is limited by the mesh-size. From stability considerations, the free-space wavelength λ corresponding to that frequency should not be smaller than 4 computational cells [112]. For reasonable accuracy, it is desirable to have at least 10 cells in one λ . Now, a step-change in any quantity contains all frequencies, so it cannot be handled by any practical mesh-size. Hence it is not acceptable to start the simulation with a jump in B_1 and B_2 to their desired values B_{10} and B_{20} . Starting from zero values of all field components, a gradual increase becomes necessary. We have used a quarter-wave sinusoidal excitation function given by Eq.(5.14).

$$B_z = B_0 \sin(\omega t), B_0 = B_{10}, B_{20}, 0 < t < t_B \quad (5.14)$$

where, t_B is the 0-100% rise-time of the magnetic field, corresponding to the

quarter-wave time, when $\omega = 2\pi/(4t_B)$ is the angular frequency. This will fill up uniform magnetic fields B_{10} and B_{20} at the left and right side of the conductor respectively.

Apart from satisfying the stability criterion, the field rise-time for both source excitation points is determined in such a way that negligible diffusion takes place into the slab before the movement, so as to trap most of the flux between the conductor and PEC wall.

The conducting slab is held stationary until $t = t_B$, at which point it suddenly starts moving to the right with a constant specified velocity, compressing the initial magnetic field along the x-direction. The material density in each computational cell is evolved using Eq.(5.12). A multi-dimensional Flux corrected Transport (FCT) method is used for this purpose [134]. The material conductivity (σ^m) for material m in each computational cell is calculated using an approximate expression given by Eq.(5.15), which is based on the assumption that the material is uniformly filled in the entire region of the cell.

$$\sigma^m(i, j) = \sigma_0^m \times \frac{\rho^m(i, j)}{\rho_0^m} \quad (5.15)$$

where ρ_0^m , $\rho^m(i, j)$ are the normal density of material ‘m’ and its instantaneous material density, respectively. Similarly σ_0^m , $\sigma^m(i, j)$ are electrical conductivities corresponds to normal density and instantaneous density, respectively. Here, cell indices i and j correspond to the x- and y-directions, respectively. The total conductivity in a computational cell is calculated using the weighted average of individual conductivities of all materials present in that cell, which can be expressed as:

$$\sigma_T(i, j) = \frac{\sum_{m=1}^M \rho^m(i, j) \sigma^m(i, j)}{\sum_{m=1}^M \rho^m(i, j)} \quad (5.16)$$

where M is the total number of materials present in a cell.

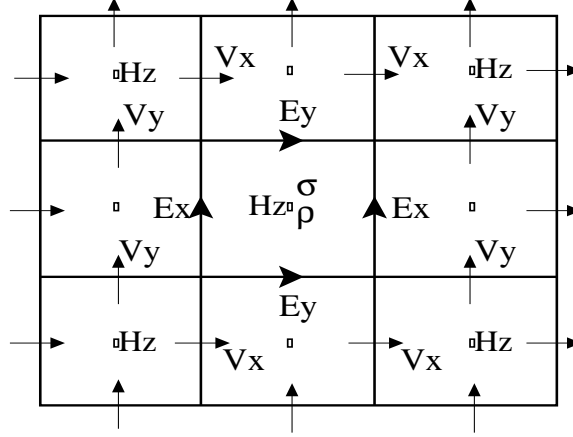


Figure 5.25: Two-dimensional (2D) Yee cell, showing locations of field components and material quantities.

Finally, the equations to be solved for the present problem in two dimensions can be summarized in finite difference form as below:

$$E_x^n(i, j) = E_x^{n-1}(i, j) + \frac{\Delta t}{\epsilon_0} \left[\frac{H_z^{n-\frac{1}{2}}(i, j) - H_z^{n-\frac{1}{2}}(i, j-1)}{\Delta y} \right] \quad (5.17)$$

$$E_y^n(i, j) = E_y^{n-1}(i, j) + \frac{\Delta t}{\epsilon_0} \left[\frac{H_z^{n-\frac{1}{2}}(i, j) - H_z^{n-\frac{1}{2}}(i-1, j)}{\Delta x} \right] \quad (5.18)$$

$$E_x^n(i, j) = E_x^{n-1}(i, j) e^{-\sigma(i, j) \Delta t / \epsilon(i, j)} + (1 - e^{-\sigma(i, j) \Delta t / \epsilon(i, j)}) \times \left[\frac{H_z^{n-\frac{1}{2}}(i, j) - H_z^{n-\frac{1}{2}}(i, j-1)}{\sigma(i, j) \Delta y} - \mu v_y(i, j) H_z(i, j) \right] \quad (5.19)$$

$$E_y^n(i, j) = E_y^{n-1}(i, j)e^{-\sigma(i, j)\Delta t/\epsilon(i, j)} + (1 - e^{-\sigma(i, j)\Delta t/\epsilon(i, j)}) \times \left[\frac{H_z^{n-\frac{1}{2}}(i, j) - H_z^{n-\frac{1}{2}}(i-1, j)}{\sigma(i, j)\Delta x} + \mu v_x(i, j)H_z(i, j) \right] \quad (5.20)$$

$$H_z^{n+\frac{1}{2}} = H_z^{n-\frac{1}{2}} - \frac{\Delta t}{\mu_0} \times \left[\frac{E_y^n(i+1, j) - E_y^n(i, j)}{\Delta x} \right] - \frac{\Delta t}{\mu_0} \times \left[\frac{E_x^n(i, j+1) - E_x^n(i, j)}{\Delta y} \right] - \frac{\partial F_x^{n+\frac{1}{2}}}{\partial x} - \frac{\partial F_y^{n+\frac{1}{2}}}{\partial y} \quad (5.21)$$

Here, Equations (5.17) and (5.18) are for free space, while Equations (5.19) and (5.20) are for lossy dielectrics. $F_x^{n+\frac{1}{2}} = v_x(i, j)H_z(i, j)$ and $F_y^{n+\frac{1}{2}} = v_y(i, j)H_z(i, j)$ are x -directed and y -directed fluxes evaluated at the faces of the Yee cell, using the FCT algorithm. n is the time index and i, j are the space indices. The conductivity values required at various electric field locations (cell faces) are obtained by taking the average of cell-centered conductivities surrounding that face.

The computational algorithm can be described as follows.

Initialize time, $t = 0$

(i) initialize $E_x, E_y, H_z, \rho, \sigma$ etc.

1. E update

(i) Update electric fields using Eq. (5.17), (5.18), (5.19) and (5.20)

(ii) if ($t < t_B$) then, apply source terms for electric fields, if any

(This section will be used if one has an applied voltage excitation [54–56] rather than magnetic field excitation for establishing current flow in the system. For the present problem we have used magnetic field excitation)

Advance time, $t = t + \frac{\Delta t}{2}$

2. *H update*

(i) *transport magnetic field using FCT; Eq. (5.9).*

(ii) *if ($t < t_B$) then, apply source terms for magnetic fields using Eq. (5.14).*

The source fields B_{10} and B_{20} are specified at two different excitation points with one computational cell for each. See Fig. 5.24. This will establish a current flow in the system.

Advance time, $t = t + \frac{\Delta t}{2}$

3. *Material movement at full time-step*

(i) *advect material using FCT; Eq. (5.12)*

(ii) *update conductivity in each cell using convected density; Eq. (5.15) and Eq. (5.16).*

If $t < t_{stop}$ go to step 1

4. *Stop*

Basic steps involved in the FCT algorithm are as follows

1. *Calculate and apply the convective and diffusive fluxes in x-direction*

2. *Calculate and apply the convective and diffusive fluxes in y-direction*

3. *Add source terms, if any*

4. *Calculate the anti-diffusive fluxes in x and y direction*

5. *Limit and apply correction factors to the anti-diffusive fluxes in x and y direction*

6. *Compute the solution*

Details of each step and its evaluation schemes can be found in Refs. [59, 125].

Multi-dimensional problems in FCT are solved by using directional splitting [59].

We have used a fully multi-dimensional flux limiter suggested in Refs. [134, 135] for

performing step 5 above, which does not require a directional splitting algorithm.

For the present problem, $\nabla \cdot \vec{H} = \left(\frac{\partial H_x}{\partial x} + \frac{\partial H_y}{\partial y} + \frac{\partial H_z}{\partial z} \right) = 0$ is clearly maintained, since we only have one component of the magnetic field, H_z , which is perpendicular to x-y plane and symmetry along z-direction is assumed.

The present study aims at introducing a modified form of the FDTD equations for electromagnetics involving material motion, and its validation against analytical solutions. Another aim is to study the sensitivity of results to computational parameters such as the permittivity scaling factor. The application of this technique to sample problems involving a plasma armature is given in later sections. Similar to static problems discussed earlier, arbitrary parameters are chosen for material conductivity σ , velocity v and system dimensions so as to minimize the overall computational demand. These parameters, of course, meet the necessary conditions discussed earlier.

5.3.4 Application to 2D planar MFC systems

As a first step, we have chosen a flux compression system similar to the one given in Ref. [81]. The initial magnetic field outside the compression volume is zero ($B_{10} = 0$), with a compression length of 50 mm in both x and y directions. The dimensions of the B10 region and thicknesses of walls are 20 mm and 1 mm respectively. The initial magnetic field inside the compression volume, B_{20} is 1.256×10^{-2} Tesla. The total flux injected into the system is thus $3.14 \times 10^{-5} Tm^2$ (Weber). The thickness and conductivity of slab are 10 mm and 1×10^6 S/m respectively. Cell-sizes are taken as $\Delta x = 0.1$ mm and $\Delta y = 1$ mm, leading to a problem size of 860×110 cells, including the distance to the boundary. A uniform velocity of 100 km/s in the positive x-direction is given to the slab when the field reaches its peak value B_{20} . This velocity lies in the range (20-400 km/s) offered by plasma armatures [81, 137].

This implies $R_d \approx 251$. The permittivity of the medium is artificially increased by a factor of 100, relative to free space, to allow a larger time-step while satisfying all the constraints discussed earlier.

The temporal amplification of the initial magnetic field B_{20} due to flux compression, and the analytical solution given in Ref. [81], is shown in Fig. 5.26. Good agreement is observed.

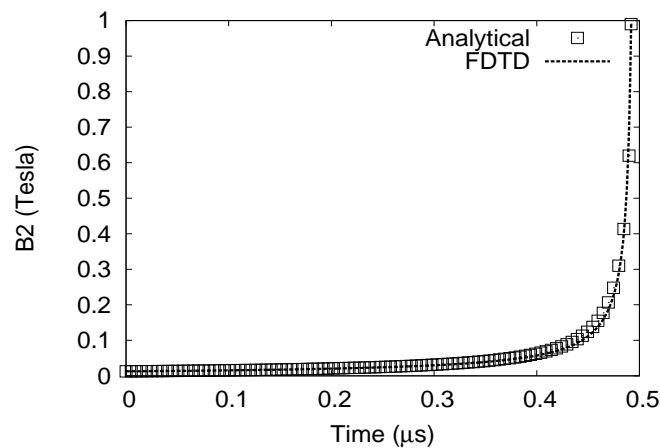


Figure 5.26: Magnetic field inside the compression volume, B_2 , as a function of time. Dotted curve is the analytical solution and solid line represents results from the FDTD calculation. $t=0$ refers to the time when the source magnetic field reaches its peak value.

A plot showing the normalized flux inside the system is shown in Fig. 5.27. The total flux is evaluated for the entire computational domain. It is clear that the total flux inside the system is conserved during the compression stage. A small decrease in the flux ($\approx 0.02\%$) towards the end of operation is observed, which is in the acceptable range.

There is an induced electric field (motional EMF, $E_v = v_x B_z$) on the surface of the conductor moving across the magnetic field. The computed result is compared with analytical solutions given in Ref. [81] and reasonable agreement is found, as shown in Fig. 5.28.

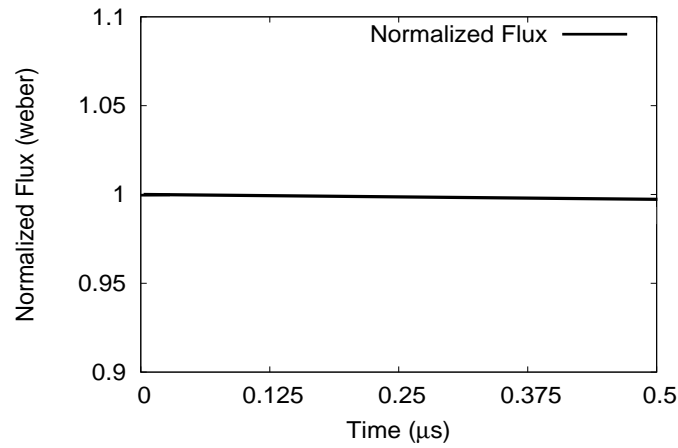


Figure 5.27: Time history of normalized magnetic flux inside the system. The normalization factor is the initial flux in the system = $3.14 \times 10^{-5} \text{ Tm}^2$ (Weber)

The spatial variation of magnetic field inside the compression volume at three different times during the compression stage is shown in Fig. 5.29. Data points to the left of the flat-top, at any given time, show field diffusion into the moving conductor.

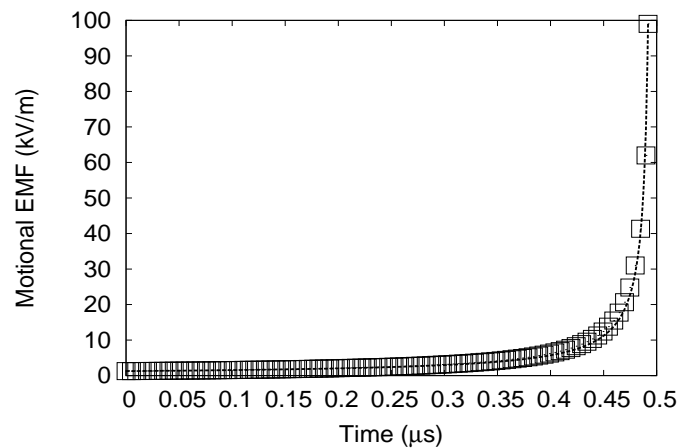


Figure 5.28: Magnitude of induced EMF (kilo volts/m) on the surface of the slab ($E_v = v_x \times B_z$). Both analytical and computed values are shown.

The inductance per unit width in the z-direction, i.e., perpendicular to the plane of Fig. 5.24, can be calculated using Eq. (5.22).

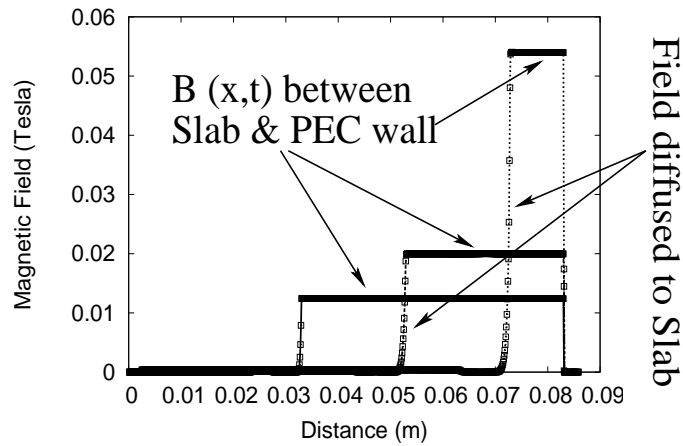


Figure 5.29: Spatial variation of magnetic field inside the compression volume, illustrating field amplification. Three different plots correspond to field variations at three different times during compression. Points represent analytical solutions while line plots shows numerical results.

$$L = \frac{\Phi_{total}}{I} = \frac{\int_s \vec{B} \cdot d\vec{S}}{I} \quad (5.22)$$

where I is the total current per unit width of the conductor, $d\vec{S}$ is an area element in the x-y plane and Φ_{total} is the total flux linked with the compression volume. Here, the total area \vec{S} include only the compression volume. The variation of inductance with time is plotted in Fig. 5.30, along with analytical solutions from [4]. Good agreement can be seen.

We next investigate a flux compression problem described in Ref. [80], where the field outside the compression volume B_{10} is non-zero. System dimensions and material parameters are the same as described previously, with $B_{10} = 1.256 \times 10^{-3}$ Tesla, i.e., 10% of B_{20} . The spatial variation of the magnetic field inside the compression volume at two different times during the compression is shown in Fig. 5.31. The FDTD results are found to be in good agreement with analytical results given in Ref. [80]. Figure 5.32 shows the normalized magnetic fields inside ($B_2(t)/B_{peak}$) and outside ($B_1(t)/B_{10}$) the compression volume. Reasonable agreement between

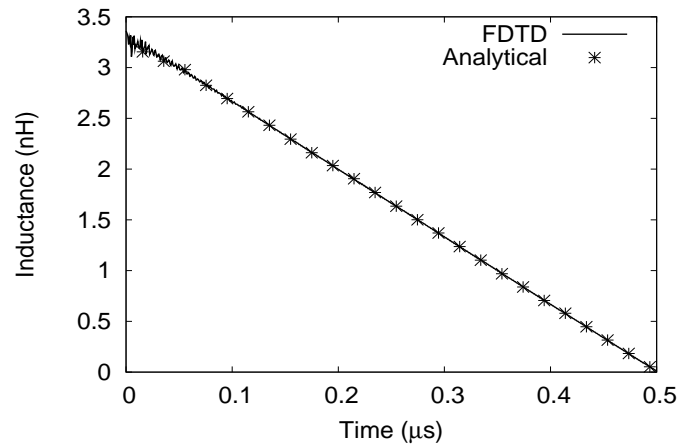


Figure 5.30: Inductance as a function of time. Analytical and FDTD results match well.

FDTD results and analytical solutions is observed.

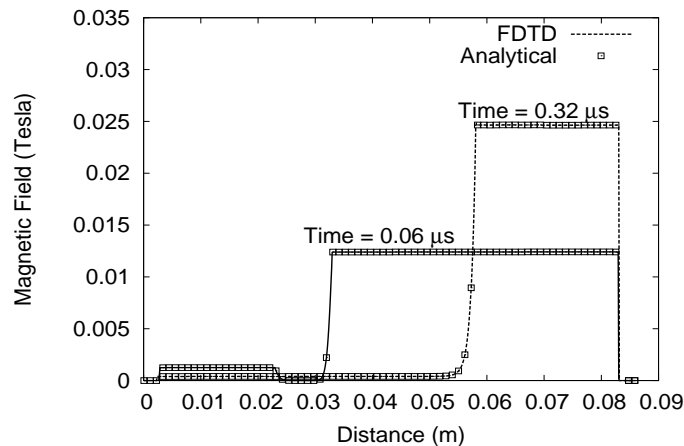


Figure 5.31: Spatial variation of magnetic field inside the compression volume. Dots and solid lines represent analytical and computational solutions, respectively.

5.3.5 Sensitivity to permittivity scaling factor

The permittivity of the medium is scaled-up artificially as in Ref. [54, 105, 106] to achieve higher time-step by meeting all the constraints mentioned earlier in this chapter. It is important to determine the maximum extent of scaling that can be achieved without introducing significant errors in physical quantities of practical

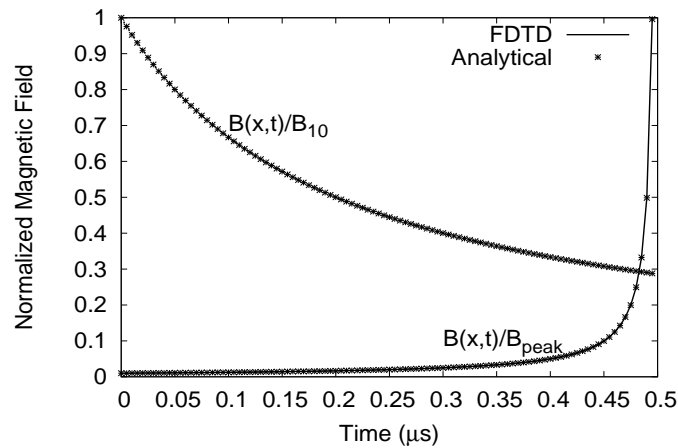


Figure 5.32: Normalized magnetic fields inside ($B_2(t)/B_{peak}$) and outside ($B_1(t)/B_{10}$) the compression volume, as functions of time. B_{peak} is the peak magnetic field reached in the compression volume. Dots and solid lines represent analytical and computational solutions, respectively. $t=0$ refers to the time when the source magnetic field reaches its peak, and conductor motion starts.

interest, e.g. compressed magnetic field.

Hence we next examine the sensitivity of computational results to the scaling factor used for the permittivity of free space, i.e., ϵ_r . We consider the problem described in Ref. [81], with system dimensions described earlier in this section. The scaling factor is varied from 10 to 10000. For each scaling factor, we compute the percentage difference between the analytical and numerical solutions for the magnetic field inside the compression volume at the end of the compression. Fig. 5.33 shows the result. For the case examined here, the overall error remains a few percent, although there is a monotonic increase with ϵ_r . Furthermore, the error only changes by a few percent for a change of three orders of magnitude in ϵ_r . Hence, while a higher ϵ_r would certainly help increase the time-step and reduce the computational load, it comes at the cost of reduced accuracy. Note also that this may significantly change for other system parameters where the diffusion scales are different.

The conclusion is that the acceptable scaling factor that can be used for achiev-

ing higher time-steps needs to be selected carefully, depending upon system parameters and the desired accuracy level.

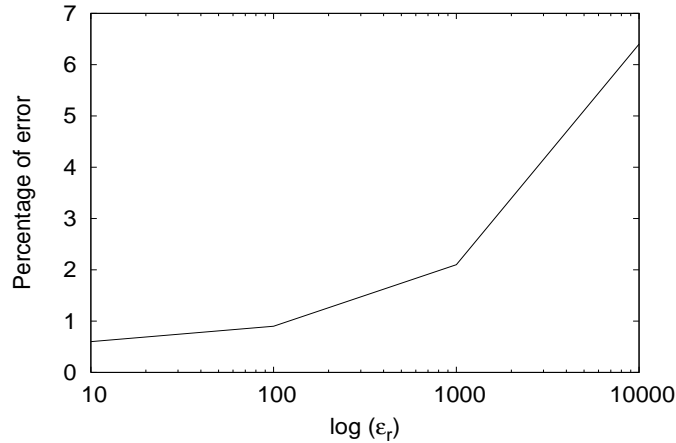


Figure 5.33: Percentage error between analytical and numerical solutions, as a function of the permittivity scaling factor (ϵ_r).

5.3.6 Convergence Test

Next, we have performed a convergence test by comparing analytical solutions and FDTD simulated results for different mesh-size. To investigate the sensitivity of mesh-size on the convergence of numerical results, a test problem mentioned in Ref. [81] with system dimensions described in the previous section has been used with permittivity scaling factor equal to 100. The mesh-size is varied from 0.025 mm to 0.4 mm along the direction of velocity. The numerical error estimated is plotted against mesh-size, See Fig.5.34. For the case examined here, the numerical results have converged with respect to the mesh-size ($\Delta x \approx 0.1$ mm). The variation of numerical error estimated with respect to permittivity scaling factor for different mesh-size shows similar trend as discussed in Ref. 5.3.5. The acceptable mesh-size may vary for different system parameters depending on conductivity (skin-depth), velocity etc. Therefore, an acceptable mesh-size that can be used needs to be

selected carefully, depending upon system parameters and the desired accuracy level.

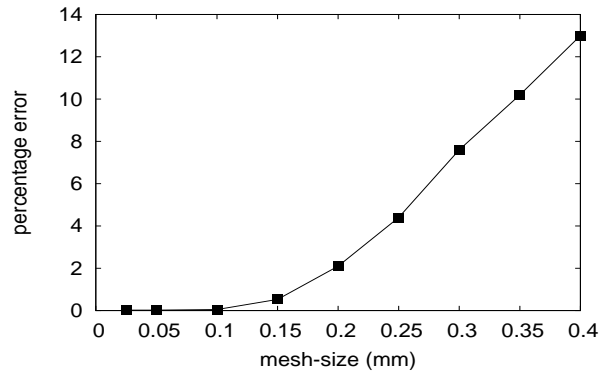


Figure 5.34: Percentage error between analytical flux conservation factor and numerical solutions, as a function of mesh-size.

5.3.7 Parallel Performance of the 2D-Code

Even sample problems of the kind discussed above require a fairly large mesh. Simulations for practical flux compression problems would thus impose a much greater computational load. Hence it is important to examine the performance of a parallelized version of this algorithm on a parallel cluster.

The algorithm has been parallelized using Message Passing Interface (MPI) [136]. The flux compression system mentioned in the Sec. 5.3.4 requires a mesh size of 860×110 in x and y directions respectively. Computer code performance has been studied on a 33 node, 3.0 GHz, Dual core, Dual Socket Xeon cluster with Infiniband interconnect. The speedup achieved as a function of the number of processors is shown in Fig. 5.35. It can be seen that the speedup varies approximately linearly with the number of processors used.

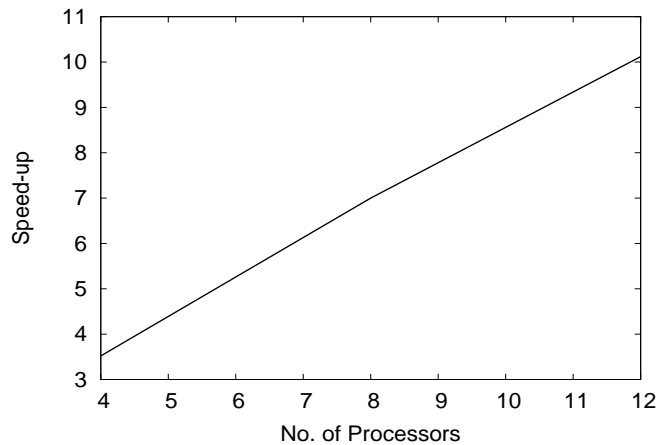


Figure 5.35: Speedup achieved as a function of the number of processors, for the problem described in Sec. 5.3.4.

5.4 MFC by an expanding cylindrical plasma

Finally, in order to demonstrate the utility of the powerful FDTD-based scheme to MFC problems, we have applied it to a sample problem involving plasma armatures [25]. Here, an ideal cylindrical plasma expansion in an applied magnetic field ~ 0.27 T is considered. The initial conditions are taken from Ref. [25] with plasma energy, $E_p = 270$ MJ, plasma mass ~ 0.2 mg and pickup coil (single turn) radius 8.25 m. In Ref. [25], the electrical energy is extracted across a resistive load connected to the pickup coil. The axial length of the cylindrical plasma was 15 m. The schematic of FDTD setup for the simulation of MFC by an expanding cylindrical plasma is depicted in Fig. 5.36. The hydrodynamic calculation provides the spatial variation of plasma conductivity and velocity at a given instant of time. This information is used in the FDTD calculation to update electromagnetic fields. The updated electromagnetic fields are then used in the hydrocode for calculating magnetic deceleration on the surface of the plasma.

The 2D-FDTD algorithm mentioned in the previous section has been modified to make it compatible for cylindrical geometry by including other field components.

Since systems dimensions are of the order of a few meters, the FDTD simulation with fixed 2D Eulerian grid would be prohibitively expensive. Therefore, we have solved the FDTD equation in a Lagrangian manner, where high-resolution is used in the conductor and plasma region, and a comparatively coarse mesh in the surrounding vacuum region. The surrounding vacuum is modeled by an extremely low density ($\rho \sim 10^{-14}$ kg/m³) medium. In the Lagrangian phase, we assume the frozen field approximation (flux being constant for a fluid element). New magnetic field, B_z , values after the Lagrangian step are determined by using the flux conservation equation in the old and new mesh ($B_z^{n+1} \cdot dS^{n+1} = B_z^n \cdot dS^n$, where the superscript represent the time point and dS is the cross-section area). This step is followed by the standard FDTD calculations to update field components. Apart from these, boundary conditions for the field components are explicitly specified near the axis, for example $(E_\theta)_{r=0} = 0$. That is, the standard MUR's radiation boundary condition has been replaced by an explicit boundary condition at the axis.

An unstructured Lagrangian scheme (see Chapter 4 and Appendix B) is used for solving fluid equations. The pickup coil is a single turn cylindrical coil. The current in the coil is determined by constructing an integration loop around the cross-section of the loop in 2D r-z plane. The initial magnetic fields B_z is specified analytically (with a rise-time as described in the previous section) at a source excitation point above the plasma cylinder, see Fig. 5.36.

The radial plasma density profile at two different times during the first expansion phase is depicted in Fig. 5.37. The results are similar to the case described in Chapters 2 and 3. The plasma forms a shell like geometry at stagnation point, where the outer surfaces slow down due to magnetic pressure and the inner region catch up to the outer region. The results presented in Ref. [25] shows several com-

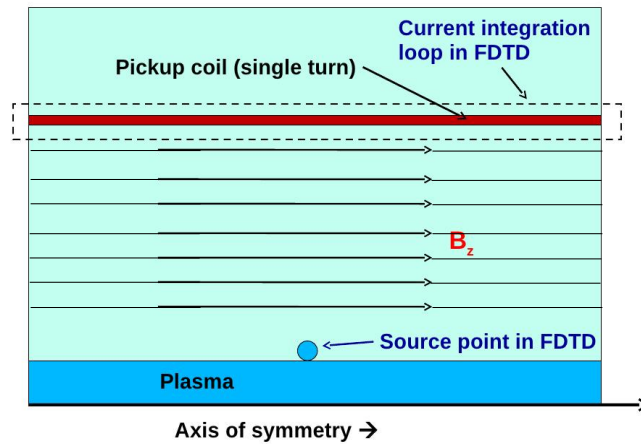


Figure 5.36: Schematic of FDTD setup for the simulation of MFC by an expanding cylindrical plasma. The pickup coil is a single turn cylindrical coil. The current in the coil is determined by constructing an integration loop around the cross-section of the loop in 2D r - z plane.

pression and expansion phases of plasma and the energy is assumed to be extracted throughout these phases. However, the dynamics of the plasma after the first expansion phase in our simulation is found to be different from the predictions made by the 0D-model described in Ref. [25]. This is due to the neglect of plasma compressibility in their 0D-model. The model described in Ref. [25], assume plasma as a point mass and hence the behavior of plasma as a fluid is neglected. It also neglect the plasma instabilities. Our simulation results clearly indicate the evolution of plasma instability after the first expansion phase, see Fig. 5.38. The evolution of plasma outer radius till the stagnation time (with load resistance $R = 100 \Omega$) is shown in Fig. 5.39, which is in reasonable agreement with the results given in Ref. [25].

We have compared the conversion efficiency ($I^2 R t / E_p$) obtained in our simulation with the results given in Ref. [25]. Since the instabilities are observed after the first expansion phase, the comparison is made only at the end of the first expansion phase. We have compared the plasma energy conversion efficiency ($\sim 28\%$)

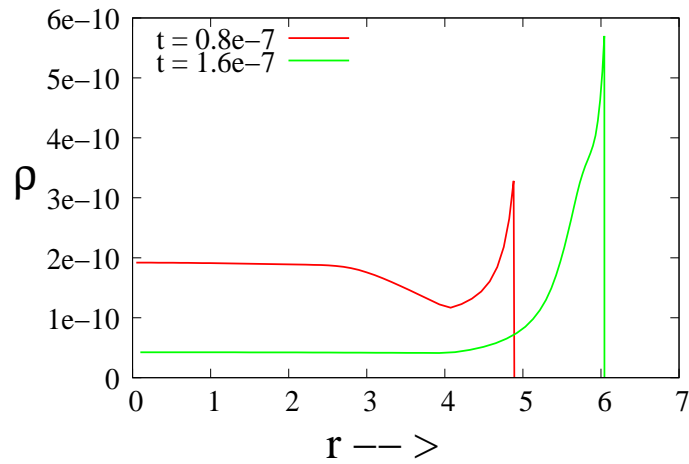


Figure 5.37: Radial profile of plasma density (kg/m^3) at different times during the first expansion phase

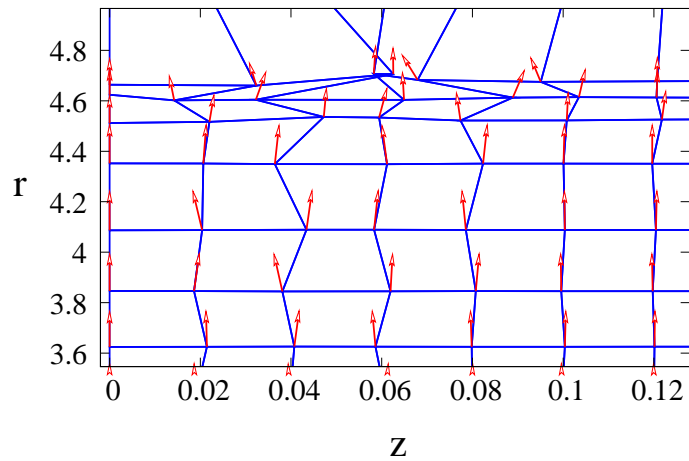


Figure 5.38: The plot of velocity vector defined at nodes along with the distorted Lagrangian mesh (plotted on a coarse mesh for clarity) indicates the evolution of instability.

at the end of first expansion phase with the reported values $\sim 30\%$ in Ref [25] for a load resistance of 100Ω . Reasonable agreement with the results is obtained. As expected, the diffusion of magnetic field into the plasma is found to be negligible during the first expansion phase.

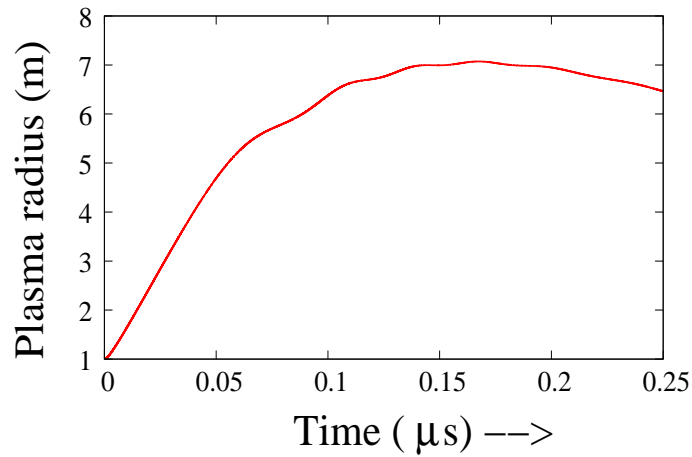


Figure 5.39: The variation plasma outer surface radius w.r.t time during the first expansion phase.

5.5 Limitations of the Study

The present study suffers from the following major limitations. Firstly, it is extremely demanding in terms of computational power. Therefore, at present, the calculation of resistance and inductance using FDTD scheme are performed only for simple coil geometries. Hence the work should be regarded as a first, exploratory step rather than as a mature technique ready for application to design. Secondly, the spatial variation of conductivity inside the conductor, due to effects like Joule heating, has been neglected in the present work. It is straightforward to include an arbitrary conductivity distribution in the FDTD model. However, self-consistent inclusion of that effect will require coupling to a complete model for helical generators, which is still inaccessible due to the high computational cost.

5.6 Conclusions

The Finite Difference Time Domain (FDTD) method for electromagnetics, adapted for magnetic field diffusion problems, has been applied for accurate calculation of

the resistance and inductance of coils (single turn, two turns and four turns with variable pitch). These simulations have been performed using a locally-developed three-dimensional variable-mesh FDTD code that has been parallelized along three directions. This technique allows the study of complex, multi-material configurations, and the time domain analysis allows handling of arbitrary temporal waveforms of current. This technique thus allows a study of real-life configurations with practically no limitations on the geometric complexity, the materials used or the temporal waveforms.

Resistance calculations based on this technique automatically take account of skin and proximity effects. The simulations also yield a detailed 3-D picture of magnetic field diffusion through a complex coil in the presence of arbitrary time-dependent current waveforms. Hence they can provide critical insight into coil performance in real-life systems. We have identified the critical issues that must be kept in mind for such simulations and the results of test problems with simple coil geometries.

The modified algorithm, by including velocity dependent terms, has been applied to study the electromagnetic induction in moving materials similar to magnetic flux-compression systems in planar geometry. In order to demonstrate the utility of the powerful FDTD-based scheme to MFC problems, we have applied it to a sample problem involving plasma armatures [25]. We have compared the energy conversion efficiency (with a resistive load) reported in Ref. [25] with our simulation results for a typical set of plasma parameters. Reasonable agreement in the results is obtained.

This technique allows the study of complex, multi-material configurations with arbitrary non-relativistic material velocity. To our knowledge, this is the first application of this powerful technique to electromagnetic problems involving material

motion.

However, the technique also suffers from the disadvantage of being extremely demanding in terms of computational power. Hence the present work should be regarded as a first, exploratory step rather than as a mature technique ready for application to design.

6

Summary and conclusions

6.1 Overall summary

The objective of this thesis work is to computationally examine the physics of magnetic flux compression using expanding plasma armatures. Starting with an MHD-based approach, we have extended the study to Finite Difference Time Domain (FDTD)-based electromagnetics calculations, involving direct solution of Maxwell's equations, as a computational tool for MFC systems.

The following studies have been performed in this thesis:

- *Development of a Lagrangian MHD scheme coupled self-consistently with external circuit equations for the analysis of MFC inside a solenoid driven by a fusion plasma sphere.*
- *Preliminary analysis of the conversion of plasma energy into pulsed electrical energy using the above mentioned MHD scheme.*

- *Development of an Eulerian MHD model using volume-of-fluid material interface tracking for studying plasma dynamics across the magnetic field.*
- *The study of large-deformation plasma dynamics in the proposed MFC system using an Eulerian MHD model.*
- *Analysis of Magnetic Rayleigh-Taylor instability in an MFC system driven by a fusion plasma sphere.*
- *Development and validation of computational algorithms relevant to MFC systems based on the FDTD scheme for electromagnetics.*
- *Application of FDTD scheme for electromagnetics for the analysis of MFC by an expanding cylindrical plasma.*

In Chapter 2, we have reported on a conceptual study of magnetic flux compression (MFC) inside a solenoid by an expanding IFE plasma sphere. The study has been performed numerically using two-dimensional (2D) magneto-hydrodynamic (MHD) simulations. A 2D Lagrangian code has been developed to solve the governing two-dimensional MHD equations. A filamentary model, which includes the effect of plasma dynamics, is used to update the coil current and the induced currents in the plasma. The plasma dynamics, and the efficiency of the proposed system with different inductive and resistive load conditions, are studied numerically. An overall efficiency $\sim 56\%$ is obtained for a typical set of plasma and system parameters. The concept is found to be promising in terms of conversion efficiency. However, ultrahigh coil inter-turn voltages (~ 25 MV) are predicted. Therefore, the application of magnetic self-insulation to avoid coil inter-turn breakdown is considered. Even-though voltage levels are within the theoretically acceptable range, for a typical case considered here, a detailed optimization study may

be required to avoid coil inter-turn break-down without reducing the system efficiency. Such a detailed optimization, however, lies beyond the scope of the present work.

It is observed that during the final stage of MFC, the plasma shape becomes distorted (non-spherical) due to non-uniform deceleration caused by the magnetic field outside the plasma sphere. In particular, there is elongation of the plasma in the axial direction. These effects, collectively, lead to non-spherical expansion of the plasma with large deformation. Hence, in order to examine the large deformation plasma dynamics in the proposed MFC system, we have next developed an Eulerian multi-material algorithm with Volume-of-Fluid (VOF) based material interface tracking. In Chapter 3, we have described the details of this Eulerian MHD model and the analysis of the MFC system using this model. The Eulerian code is then extended to MHD form. The magnetic induction equation is solved implicitly using magnetic vector potential. An iteration procedure using Alternating Direction Implicit (ADI) scheme is used for free space field calculation. The validated algorithm is applied to study the dynamics of plasma inside an MFC system. Simulations indicate the development and evolution of MRT instabilities at the plasma-vacuum interface near stagnation time, i.e., close to the time when the outer surface comes to a halt. In the $r - z$ plane, these instabilities are more marked near the center of the solenoid where the magnetic deceleration is comparatively higher. We start with a spherically-symmetric initial plasma, which means that the MRT instability is seeded by numerically-generated perturbations. The plasma sphere forms a shell-like geometry near the stagnation point as the outer surface slows down due to \vec{B} and the inner region catches up with the outer surface. The resulting high temperature plasma region has high electrical conductivity. Therefore the \vec{B} diffusion into the plasma is found to be negligible even

around stagnation time.

The plasma armature, expanding across a magnetic field, is subject to the Magnetic Rayleigh Taylor (MRT) instabilities. The studies described in Chapter 3, starting with an unperturbed initial plasma state, indicate the growth of MRT instability as stagnation time is approached. In reality, perturbations with different wavelengths and amplitudes would exist on the surface of the plasma sphere even before it starts expanding. For a real-life system, therefore, it is necessary to study the growth of pre-existing perturbations with different wavelengths and amplitudes. In Chapter 4, therefore, a study has been performed for different cases of applied initial perturbations (different wavelengths and amplitudes), taking into account the effects of magnetic field amplification (time dependent g) and geometric divergence due to spherical plasma expansion. For this, we have developed an unstructured Lagrangian MHD scheme. Two-dimensional MHD simulations of random, single and multi-mode perturbation growth in an MFC system, driven by an expanding fusion plasma sphere, have been carried out for different initial perturbation amplitudes and wavelengths. In the random seed perturbation analysis, we have found that the dominant modes in the spectrum show a progressive transition from the short-wavelength to the intermediate-wavelength regime, $\lambda \sim 4-8$ cm, which is consistent with the results obtained in Chapter 3. A cross-correlation analysis indicates mode coupling between dominant modes and other modes in the spectrum, leading to energy transfer to weaker modes. The multi-mode (sinusoidal) analysis, with two different fundamental modes (say n_1 & n_2) and with $\alpha_{in} \sim 500 \mu\text{m}$, shows the appearance of higher harmonics of the individual modes, as well as the shorter wavelength ($n_1 + n_2$) and higher wavelength inverse cascade ($n_2 - n_1$) modes created by non-linear interaction of fundamental and harmonic modes. In the case of single-mode perturbation, the modes con-

tinue to grow exponentially with nearly constant γ and make a transition into the non-linear phase (mode saturation). This means that the amplitude growth of the modes towards stagnation time, although exponential in nature, is lower than the growth predicted by linear theory.

A major concern in such systems is the formation of large flute structures and plasma jetting, which could damage or reach the cavity-wall/coil and could severely disturb smooth compression of the magnetic field [25–27]. We find that these are not seen during the time period of our interest, viz., the first expansion phase of the plasma. This means that it is feasible to have efficient flux compression during the first expansion phase in the proposed system, for perturbation amplitudes $\alpha_{in} \leq \lambda_{in}/10$. However, for $\alpha_{in} \geq \lambda_{in}$, the instability amplitudes are large enough, especially for longer λ modes, to cause plasma jetting leading to significant reduction in the flux compression efficiency.

It is worth mentioning here that the conversion of plasma energy into electrical energy across a resistive load, during several expansion and compression cycles of the plasma given in Refs. [25–27], are for an unperturbed initial plasma with $\vec{B} \leq 0.6$ T. Such operation would be inefficient/challenging for the present system parameters since the plasma outer surface, after the first expansion phase, would have high-amplitude perturbations. During the next implosion phase of the plasma, after the turn-around, these perturbations grow further and may generate plasma jetting or extremely large amplitude wave structures, which could effect the smooth implosion of the plasma (the compression phase) and damage the cavity wall. Therefore, further studies are required to explore the concept of plasma energy recovery across a resistive load with several expansion and compression phases [25–27].

In Chapter 5, we have investigated the application of finite-difference time-domain (FDTD) schemes to electromagnetics calculations in MFC systems. As a first step, a computational tool has been developed, allowing for variable-mesh 3D, time-dependent FDTD calculations of electromagnetic field components. This is then used for calculating accurate resistance and inductance of arbitrarily-wound helical coils of interest. The resistance calculations automatically take account of skin and proximity effects and are capable of handling arbitrarily complex multi-material systems. The simulations also yield a detailed 3D picture of magnetic field diffusion through a complex multi-material coil in the presence of arbitrary time-dependent current waveforms. Hence these methods can provide critical insight into coil performance in real-life MFC systems. In the second step, we have modified the FDTD algorithm (in 2D), by including motional e.m.f terms, so that it can be applied to flux compression systems with moving surfaces. This new approach has been validated against standard analytical solutions for planar flux compression systems and magnetic field diffusion in moving conductors with non-relativistic velocity. Finally, in order to demonstrate the utility of the powerful FDTD-based scheme to MFC problems, we have applied it to a sample problem involving plasma armatures. Analysis is done by coupling a hydrodynamic module (for plasma dynamics) and FDTD scheme (for field update). We have compared the plasma energy conversion efficiency at the end of first expansion phase with the reported values. Reasonable agreement in results is obtained. We have identified, through extensive numerical tests, critical constraints that must be satisfied (e.g. cell-size, distance to computational boundary, maximum permittivity scaling factor, etc) while performing magnetic diffusion problems using FDTD scheme for electromagnetics. The FDTD scheme is found to be promising in predicting magnetic field diffusion in complex geometries as well as in predicting magnetic

induction in moving conductors. However, the technique also suffers from the disadvantage of being extremely demanding in terms of computational power. To our knowledge, this is the first application of this powerful technique to such systems.

6.2 Suggestions for future work

In future work one can optimize the proposed MFC system for higher efficiency, to reduce inter-turn voltage and to yield optimum coil parameters and system dimensions for a typical initial plasma parameters. With detailed numerical and theoretical study, it is possible to formulate a model which can suggest, for given initial plasma parameters, the coil and other system parameters that have to be used for optimum operation.

A possible improvement of the proposed concept is the use of spherical coils instead of a solenoid. The use of spherical coils may yield symmetric spherical plasma expansion (i.e. without a considerable axial plasma distortion) and hence a higher conversion efficiency. The second advantage by using a spherical coil is that it may lower the initial energy requirement. This study can be a potential future scope of the present work.

The instability analysis must be repeated in three dimensions, since a 2D analysis may be ignored 3D modes altogether. Hence the results of the present study are likely to be slightly optimistic. A 3D study would help to make a more accurate assessment of instability-related problems. Further more, a detailed study would be required to analyze the non-linear mode coupling between different modes. The growth of instabilities is also likely to be different for different kinds of loads, viz., resistive, inductive and capacitive. The study must be repeated. Future work should also quantify the effect of MRT instability in terms of conversion efficiency

for different kinds of loads by using MHD models that are coupled with external circuit equations.

The application of first principle FDTD calculation (including velocity dependent terms) to MFC systems, though computationally very expensive, can give a detailed picture of the evolution of electromagnetic fields inside the MFC system. These simulations, however, can only be performed through massively parallel computer simulations.

A

Volume-of-fluid (VOF) scheme

We have developed a volume-of-fluid (VOF) scheme [60] for material interface tracking in Eulerian simulations. The details of the algorithm and several validation tests are given in Ref. [60]. Here, we have described important features of the algorithm in brief. The overall VOF formulation can be split into three major parts: Interface construction, Lagrangian deformation of material interfaces and Eulerian transport step. All calculations presented here are one-dimensional in nature and therefore a ‘directional-split’ advection algorithm is used to extend it into two-dimensional case.

A.1 Structured Staggered Mesh

A spatially staggered grid: where volume fractions (f^m , m = material number), density (ρ^m), cell mass etc are cell-centered, whereas the velocity components (u, v) are specified at the mid point of cell edges. See Fig. A.1 for details.

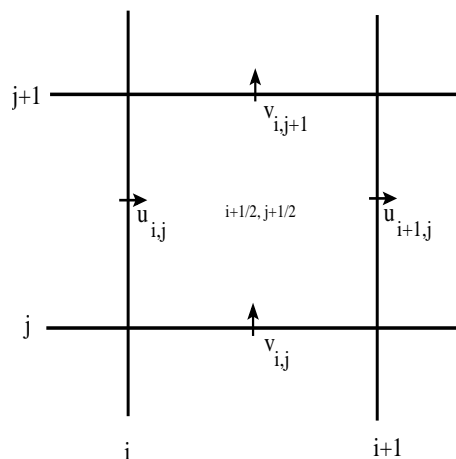


Figure A.1: Schematic of staggered computational grid

A.2 Interface Construction

A Piecewise Linear Interface Construction (PLIC) method is used. An interface line can be represented by Eq. (A.1) [67, 139], where $\vec{n} = \hat{i}n_x + \hat{j}n_y$ is the exterior normal to the line and α is the perpendicular distance from a local origin, see Fig. A.2 (a general case) and Fig. A.3 (for different possible material orientations). It is worth to note that the distance α is always measured from a local origin in our method. It is possible to define α as distance from a common origin. The local origin is defined as per material orientation. For some special cases, e.g. lines parallel to any co-ordinate axis, any one of the possible two origins can be selected.

$$\vec{n} \cdot \vec{x} - \alpha = 0 \tag{A.1}$$

The slope of a material interface line and hence the normal vector ($\vec{n} = \vec{\nabla} f^m / |\vec{\nabla} f^m|$) can be estimated by using different known existing methods. One such algorithm is the LVIRA [72] scheme. In LVIRA algorithm one minimizes $E_{i,j}^2$ as a function of slope by rotating the line under the constraint that this line exactly reproduces the volume fraction in the cell. $E_{i,j}^2$ is defined as follows

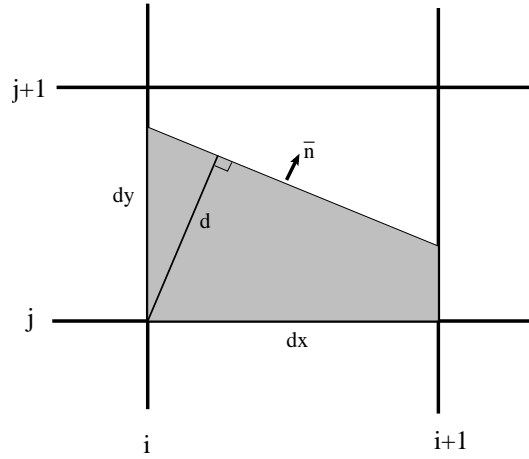


Figure A.2: Geometry of linear interface construction for Material interface

$$E_{i,j}^2 = \left(\sum_{k,l=-1}^1 (\tilde{f}_{i+k,j+l}(\tilde{m}) - f_{i+k,j+l})^2 \right)^{\frac{1}{2}} \quad (\text{A.2})$$

where, \tilde{f} be a linear approximation to a curve passes through the cell (i,j) with slope \tilde{m} and volume fractions $\tilde{f}_{k,l}$. Similarly, $f_{k,l}$ represent the volume fractions due to a true linear function f . The basic logic in the LVIRA algorithm is to minimize some measure of the error between the volume fractions given by the true and approximate interfaces. This method generally exhibits second order accuracy.

A.3 Volume behind interface line

We have developed a generalized algorithm (in order to treat all possible material orientations) for evaluating volume behind material interface line for arbitrary material orientation. The algorithm outline is given below.

Algorithm outline

1. Adjust normal depending on orientation

$$\begin{aligned} & \text{if } (n_x < 0); \alpha = \alpha + n_x \Delta x \\ & \text{if } (n_y < 0); \alpha = \alpha + n_y \Delta y \end{aligned} \tag{A.3}$$

2. Get the two intersection points with cell edges

3. Collect all cell-nodes lies behind an interface line

$$\text{if } n_x(x - x_i) + n_y(y - y_i) \leq \alpha \tag{A.4}$$

4. Construct a polygon using nodes from step 2 and 3

5. Calculate volume of this polygon

$$V_{xy} = \frac{1}{2} \sum_{i=1,n} (x_i y_{i+1} - x_{i+1} y_i) \tag{A.5}$$

n_x = normal component along x-direction

n_y = normal component along y-direction

α = perpendicular distance to interface line from local origin

Δx = mesh-size along x-direction

Δy = mesh-size along y-direction

n = no. of polygon nodes

A.4 Volume Iteration

Having obtained interface normals the interface parameter α has to be determined (See Eq. (A.1)) so that volume behind the interface line is equal to the material

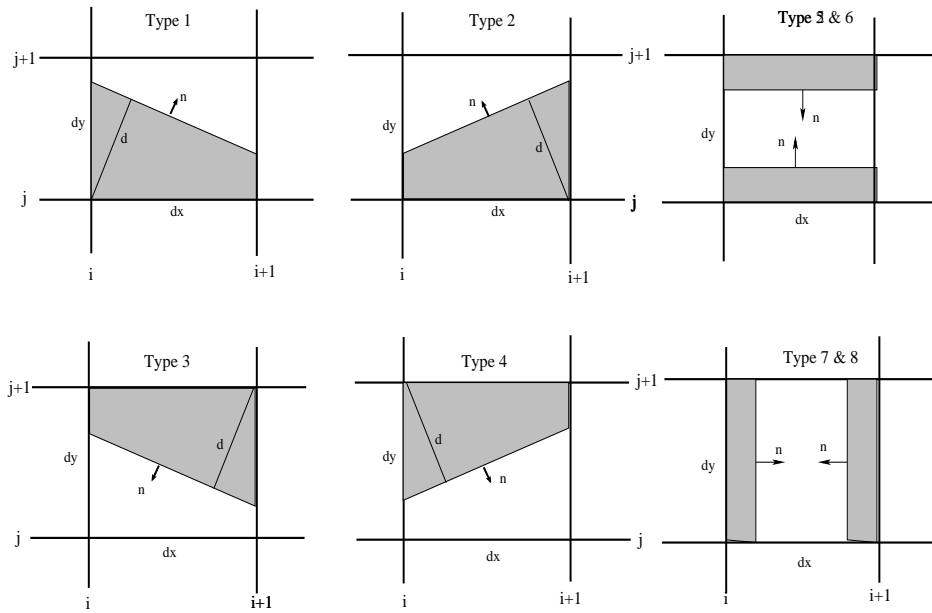


Figure A.3: Different types of possible material interface orientation. Here, $d = \alpha$ (in the text) is the perpendicular distance from a local origin and \vec{n} is the exterior normal to the interface line.

volume. If there are more than two materials in a cell a material order has to be determined and all materials are layered in that order so that volume behind i^{th} and $i - 1^{th}$ material interface is equal to the sum of volume of materials from 1 to $i - 1$. Different methods for evaluating ‘material order’ will be discussed in later sections. The interface parameter α is found when the function $f(\alpha) = V(\alpha) - V_{actual}$, becomes zero. Here, $V(\alpha)$ is the material volume in the cell bounded by the interface line with line parameter α . An efficient *root-finding* algorithm can be used to find α . We have used *Brents* method for root-finding as suggested in [67]. In our calculation we have used $\alpha_{min} = 0$ and $\alpha_{max} = d$ as initial bracket for root-finding system, where ‘d’ is the cell diagonal distance. For each iteration in root-finding system a function which evaluate volume behind an interface line with a given interface parameters has to be used. We have used our new volume evaluation algorithm mentioned in section A.3.

A.5 Multi-material interface construction

In this section we describe a ‘non-intersecting’ material interface construction method. Once the ‘material order’ is defined (how to define material order is discussed in later sections), the material interfaces are constructed using methods given in Section A.2 using ‘onion-skin’ model (See Fig. A.4). Given a material order, material m_1 to m_N , the first interface, between m_1 and m_2 , is calculated by putting the volume of m_1 behind the interface [138]. The slope of this particular material is evaluated by using the volume fractions of material m_1 in a 3×3 block element surrounding it.

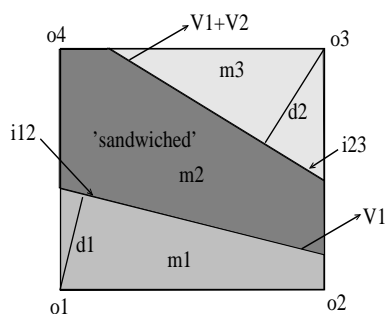


Figure A.4: Onion-skin order of material interfaces in a computational cell

The second interface, between m_2 and m_3 , is calculated by putting the volumes of m_1 and m_2 behind the interface. This time the sum of volume fractions between m_1 and m_2 in 3×3 block is used for evaluating slope. In general, the interface of material i is constructed by putting the sum of the volumes of materials m_1 through m_i behind interface i and same logic is applied for slope estimate.

To avoid intersection between a pair of interfaces we have used the following repair algorithm. Once the interface reconstruction is completed, we check for an intersection among them in order. If there is an intersection, the scalar product of their normal vector ($\vec{n}_{m_1} \cdot \vec{n}_{m_2}$) is evaluated [62]. If the scalar product is negative, we determine a new interface for material having lesser volume fraction among

them by using Eq. (A.6) (In Eq. (A.6) we have assumed $f^{m_1} > f^{m_2}$).

$$\vec{n}_{m_2} = \frac{\vec{n}_{m_2}}{|\vec{n}_{m_1}|} - \frac{\vec{n}_{m_1}}{|\vec{n}_{m_2}|} \quad (\text{A.6})$$

If the scalar product is positive, we adjust the normal of least stiff material equal to the normal of other material. Thereafter, new interface parameter, α is evaluated.

A.6 Dynamic Material Ordering

In this section we have summarized different material ordering methods.

Niem's intersection check method

In this section we discuss on a method given in [62]. This method is based on an intersection check between material interface lines. This method works only for three-material configuration in a mixed-cell. First, an independent interface reconstruction for each material is performed. Second step is to test for an intersection point of each pair of interface lines within a cell. This can be performed by a simple line intersection check with known interface line parameter α and their slopes. The final goal is to eliminate one out of three interface lines to partition the cell into an 'onion-skin'. Counting each intersection among a particular pair of interface lines independently, there are $2^3 = 8$ different cases [62]. These are listed in Table. A.1. Third step is to reject the interface line of one of the materials. The rejected material is then 'sandwiched' in between the two others.

Table A.1: Different cases of intersection among pairs of interface lines [62]; ‘y’ and ‘n’ stands for an intersection and non-intersection respectively.

case	line 1 & 3	line 2 & 3	line 1 & 2	action
1	n	n	n	reject 1, 2 or 3
2	n	n	y	reject 1 or 2
3	n	y	n	reject 2 or 3
4	y	n	n	reject 1 or 3
5	n	y	y	reject 2
6	y	n	y	reject 1
7	y	y	n	reject 3
8	y	y	y	adjust normal

Centroid check method by Mosso and Clancy

Mosso and Clancy [73] developed a formulation based on approximate center-of-mass of materials. They evaluate the centroid (x_m) from a nine-cell stencil centered by the mixed cell from the material volume fractions and cell centroids (x_c) as given Eq. A.7.

$$x_m = \frac{\sum_{i=1}^9 f^m(i)x_c(i)}{\sum_{i=1}^9 f^m(i)}, m = 1, \dots, M \quad (\text{A.7})$$

Once all the centroids are evaluated, the materials are arranged in the ascending order of their centroid distances from a ‘local origin’. This ‘local origin’ is determined by checking slope of lines connecting material centroids. A positive slope is a vote for the lower left corner and a negative slope is a vote for the lower right corner [138], see Fig. (A.5).

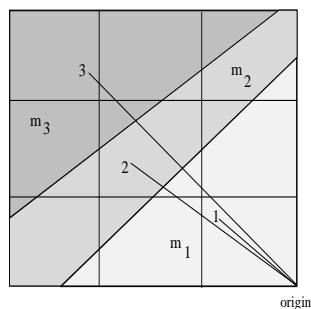


Figure A.5: Priority checking by Mosso-Clancy method

A simple combination of Centroid check and Benson's least squares fit to centroid

A similar approach is described by Benson in [74]. He adds the locations of the centroids as solution variables. They are transported using some higher-order transport algorithm, e.g. MUSCL algorithm [74]. Using the centroids of the materials (\vec{x}_m) in the current element, a least squares fit to a line is calculated by solving the least squares problem given in Eq. (A.8).

$$\min J = \frac{1}{2} \sum_{m=1,M} f^m [n_x(x_m - \tilde{x}) + n_y(y_m - \tilde{y})]^2 \quad (\text{A.8})$$

The projections of the centroid locations onto this line are sorted in ascending order. There after few *heuristic rules* are applied to define 'material order', details of these rules and their purpose can be found in [74]. See Fig. (A.6).

This method is found to be more accurate in determining 'material order'. We actually did not transport material centroids, instead an approximate centroid for each material is evaluated at each time-step using method given by Mosso and Clancy [73]. Remaining procedures follows method given by Benson in [74].

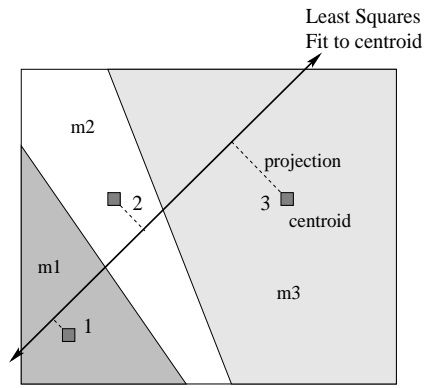


Figure A.6: Priority checking by Benson's method of least square fit to the set of the centroids

A.7 Calculation of transport volume

The calculation of advected volume ($V_i^{m,a}$) for each material is basically the evaluation of the area of the overlap region between Eulerian and Lagrangian positions after deformation (see Fig. (A.7)). This is determined by using the algorithm mentioned in Appendix A.3.

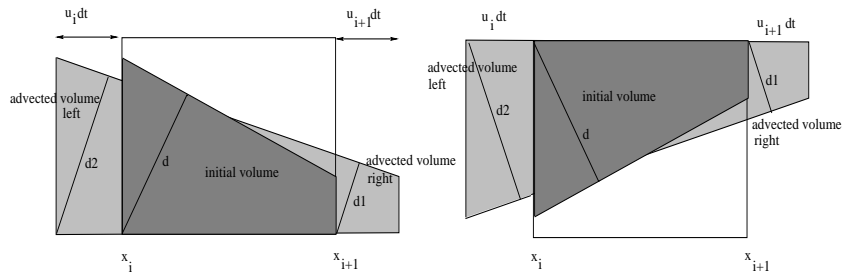


Figure A.7: Material polygon before and after Lagrangian deformation for two different orientations

The volume fraction, f^m for each material is updated at each time-step by solving an advection equation (color advection) of the form given by Eq. (A.9), see [62, 66, 67, 140].

$$\frac{\partial f^m}{\partial t} + u \frac{\partial f^m}{\partial x} + v \frac{\partial f^m}{\partial y} = 0 \quad (\text{A.9})$$

The above equation can be solved by using a flux difference scheme described in Refs. [60, 62].

B

Unstructured compatible Lagrangian hydrodynamics scheme

B.1 Introduction

The compatible unstructured Lagrangian hydrodynamics algorithm used in Chapter 4 is a staggered mesh, finite-difference scheme for solving the equations of fluid dynamics in Lagrangian form. The compatible algorithm is formulated [98] in a such a way that it exactly conserves momentum and internal energy. The unstructured mesh offers more flexibility especially when the geometry is complex. We have also included the sub-zonal pressures and masses [99] to control artificial grid distortion. Further, to stabilize the grid a node based tensor viscosity [100] is used. In the following we have described the details of this compatible unstructured Lagrangian hydrodynamics scheme.

B.2 Staggered unstructured mesh

Spatially staggered unstructured mesh is constructed as follows. The construction of the grid begins with arbitrary placement of nodes which define the geometry of interest. The velocities and the accelerations are defined at these nodes. In order to define computational cells or zones uniquely, a connectivity among the nodes which define arbitrary shaped polygons are specified, see Fig. B.1. The density, pressure and internal energy are defined at the zone centers. The sub-cell or sub-zone of each node is formed by connecting the zone centroid and edge centers. The sub-zonal cell will be always a quadrilateral regardless of the shape of the unstructured mesh, see Fig. B.1. With node positions, their connectivity and the cells defined, an unstructured mesh is completely specified. Following conventions are used: The cells are denoted by z , and nodes are indexed by p . The set of nodes that defines a cell z are $p \in S(z)$, where the nodes are ordered counterclockwise. Similarly, the set of cells that shares a node p is denoted by $z \in S(p)$.

B.3 Discrete Lagrangian hydrodynamics

In the Lagrangian framework, the equations of conservation of mass, momentum and energy are written

$$\frac{d\rho}{dt} = -\rho \nabla \cdot \mathbf{v} \quad (\text{B.1})$$

$$\frac{d\mathbf{v}}{dt} = -\frac{\nabla P}{\rho} \quad (\text{B.2})$$

$$\rho \frac{de}{dt} = P \nabla \cdot \mathbf{v} \quad (\text{B.3})$$

where ρ is density, P is pressure, \mathbf{v} is the velocity vector and e is the internal

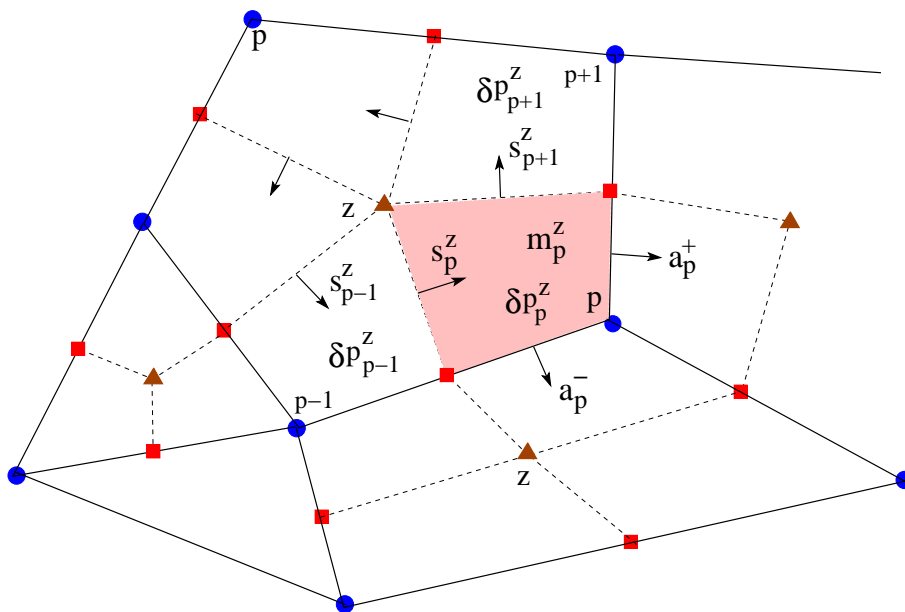


Figure B.1: A typical unstructured staggered mesh, including zone z and point p . The solid lines define the mesh and the dashed lines show the sub-cell or median mesh. The sub-cell of each node is formed by connecting the zone centroid and edge centers.

energy. In Lagrangian scheme, the mass of the cell is assumed to be constant. The same assumption is used for the sub-cell, leading to the definition of sub-zonal corner volume, mass and pressure. The cell volumes, V_z , are related to the sub-cell volumes, V_p^z , by

$$V_z = \sum_{p \in S(z)} V_p^z \quad (\text{B.4})$$

Let us denote the mass of this corner volume as m_p^z , where the indices define the zone and point with which it is associated. Also, define $m_p^z = m_z^p$, with a convention that the summation in any mathematical expression is always with respect to the lower index.

The corner mass is used to define both the zone m_z and point mass m_p .

$$\begin{aligned}
m_z &= \sum_{p \in S(z)} m_p^z \\
m_p &= \sum_{z \in S(p)} m_z^p
\end{aligned}
\tag{B.5}$$

Since, the mass of a cell is constant the discrete forms for mass conservation equation is as below.

$$\begin{aligned}
\rho_z &= \frac{m_z}{V_z} \\
\rho_p^z &= \frac{m_p^z}{V_p^z}
\end{aligned}
\tag{B.6}$$

The algorithm is written in terms of corner forces. A corner force is the contribution of one computational zone to the total force at a point or node. The discrete momentum equation at a node p in terms of corner force, \mathbf{f}_z^p , is as given below.

$$m_p \frac{d\mathbf{v}_p}{dt} = \mathbf{F}_p = - \sum_{z \in S(p)} \mathbf{f}_z^p
\tag{B.7}$$

The corner force, \mathbf{f}_z^p , is the force from zone z that acts on point p . The summation of all the corner forces around a point p gives \mathbf{F}_p . The corner force due to hydrostatic pressure is evaluated as

$$\mathbf{f}_p^z = P_z (\mathbf{s}_{p+1}^z - \mathbf{s}_p^z)
\tag{B.8}$$

where \mathbf{s} is the area vector defined in Fig. B.1. The change in mass specific internal energy can be calculated as below [98].

$$m_z \frac{de_z}{dt} = - \sum_{p \in S(z)} \mathbf{f}_p^z \cdot \mathbf{v}_p \quad (\text{B.9})$$

The derivation of the above equation and proof of energy conservation can be found in Ref. [98]. Since the conservation of total energy is used to derive the above equation, it ensures total energy is conserved to numerical round-off in calculations.

B.4 Sub-zonal pressure method

The sub-zonal pressure method [99] is developed to control artificial grid distortion. The difference between the sub-zonal and the zonal density and hence in the pressure (assuming same specific internal energy for sub-zone and zone) is used to formulate a corner force which oppose the hourglass motion. The details of this formulation and physical backgrounds are described in Ref. [99]. For each sub-zone the pressure difference between the zone and sub-zone, δP_p^z , is calculated using the following equation.

$$\delta P_p^z = (\rho_p^z - \rho_z) c_z^2 \quad (\text{B.10})$$

Here, c_z is the zone sound speed. The corner force due to these pressure difference is then calculated by integrating around the boundary of the sub-zonal volume.

$$\mathbf{f}_{p,h}^z = C_h \left(\delta P_p^z (\mathbf{a}_p^+ + \mathbf{a}_p^-) + \frac{1}{2} [(\delta P_p^z - \delta P_{p+1}^z) \mathbf{s}_{p+1}^z + (\delta P_{p-1}^z - \delta P_p^z) \mathbf{s}_p^z] \right) \quad (\text{B.11})$$

Here, $0 < C_h \leq 1$ is a dimensionless factor and the \mathbf{a} vectors are outward edge normals to the zone, see Fig. B.1. This sub-zonal corner force, $\mathbf{f}_{p,h}^z$, is added to

corner force, \mathbf{f}_p^z .

B.5 Tensor artificial viscosity

To resolve shocks over just a few zones, the tensor artificial viscosity of Campbell and Shashkov [100] is included in the hydrodynamic equations. It assume that the artificial viscosity tensor is a combination of a scalar coefficient and the gradient of the velocity tensor, $\nabla\mathbf{v}$. The sub-zonal artificial viscous force, $\mathbf{f}_{p,v}^z$, thus calculated is added to the corner force, \mathbf{f}_p^z . The details of the algorithm can be found in Ref. [100].

- [1] L. L. Altgilbers et al, Magnetocumulative Generators, Springer-Verlag, (2000)
- [2] G. Knoepfel, Pulsed High Magnetic Fields, North-Holland Publishing Company, Amsterdam, (1970)
- [3] C. M. Fowler et al, Megagauss Technology and Pulsed Power Applications, Plenum Press, New York, (1987)
- [4] C. M. Fowler and R. S. Caird and W. B. Garn, *An Introduction to Magnetic Flux Compression Generators*, LANL Report LA-5890-MS, (1975)
- [5] A. I. Pavlovskii, Magnetic cumulation—A Memoir for Andrei Sakharov, Megagauss Magnetic Field Generation and Pulsed Power Applications, Ed. by M. Cowan and R. B. Spielman, Nova Science Publ., New York, pp 9-22, (1994)
- [6] Ia. P. Terletskii, Production of very strong magnetic fields by rapid compression of a conducting shell, *Sov. Phys. JETP*, **32**, pp 301, (1957)
- [7] B. M. Novac and I. R. Smith, Brief history and classification of magnetic flux compression generators, *Electromagnetic Phenomena*, **3**, pp 358-365, (2004)
- [8] I. R. Smith, B. M. Novac and H. R. Stewardson, Flux-compression generators, *Engineering Science & Technology Journal*, **4**, pp 52-56, (1995)
- [9] I. R. Smith and B. M. Novac, Flux compression generators, *Power Engineering Journal*, **9**, pp 97-101, (1995)
- [10] B. M. Novac, I. R. Smith, H. R. Stewardson, P. Senior, V. V. Vadher and M. C. Enache, Design, construction and testing of explosive driven helical generators, *J. Phys. D Appl. Phys.*, **28**, pp 807-823, (1995)

- [11] L. I. Rudakov et al, A. Chuvatin, A. L. Velikovich and J. Davis, Confinement and compression of magnetic flux by plasma shells, *Physics of Plasmas*, **10**, pp 4435-4447, (2003)
- [12] F. S. Felsber, M. A. Liberman and A. L. Velikovich, Methods for producing ultrahigh magnetic fields, *Appl. Phys. Lett.*, **46**, pp 1042, (1985)
- [13] M. Hohenberger, P. Y. Chang, G. Fiksel, J. P. Knauer, R. Betti, Inertial confinement fusion implosions with imposed magnetic field compression using OMEGA Laser, *Physics of Plasmas*, **19**, pp 56306, (2012)
- [14] O. V. Gotchev et al., Laser driven magnetic flux compression in high energy density plasmas, *Physical Review Letters*, **103**, pp 215004-(1-4), (2009)
- [15] A. L. Velikovich et al, S. M. Golberg, M. A. Liberman and F. S. Felsber, Hydrodynamics of compression of a plasma with a frozen-in magnetic field by a thin cylindrical wall, *Sov. Phys. JETP*, **61**, pp 261, (1985)
- [16] F. S. Felsber, M. A. Liberman and A. L. Velikovich, Magnetic compression by dynamic plasmas. I. Subsonic self-similar compression of a magnetized plasma-filled liner, *Phys. Fluids.*, **31**, pp 3675, (1988)
- [17] F. S. Felsber, M. A. Liberman and A. L. Velikovich, Magnetic compression by dynamic plasmas. II. Supersonic self-similar solutions for a magnetic cumulation, *Phys. Fluids.*, **31**, pp 3683, (1988)
- [18] F. S. Felsber, F. J. Wessel, N. C. Wild, H. U. Rahman, A. Fisher and C. M. Fowler, Ultrahigh magnetic fields produced in a gas-puff Z pinch, *J. Appl. Phys.*, **64**, pp 3831, (1988)

- [19] F. S. Felsber et al, Compression of ultrahigh magnetic fields in a gas-puff Z pinch, *Phys. Fluids.*, **31**, pp 2053, (1988)
- [20] C. M. Fowler, W. B. Carn and R. S. Caird, Production of very high magnetic fields by implosion, *J. Appl. Phys.*, **31**, pp 588, (1960)
- [21] L. A. Artsimovich, The magnetic flux in a contracting cylinder, *Plasma physics and the problems of Controlled Thermonuclear Reactions*, Ed. by M. A. Leontovich, translated from Russian by A. J. Meadows et. al, Pergamon Press, London, **2**, pp 39-125, 1959
- [22] A. F. Haught, D. H. Polk and W. J. Fader, Magnetic Field Confinement of laser irradiated solid particle plasmas, *Phys. of Fluids*, **13**, pp 2842-2857, 1970
- [23] Yu. P. Raizer, On the retardation and energy transformations for plasma expanding in vacuum in the presence of a magnetic field, *Prikl. Mekh. Tekh. Fiz.*, **6**, pp 19-28, 1963
- [24] R. Hyde, L. Wood and J. Nuckolls 1972, Prospects for rocket propulsion with laser-induced fusion micro-explosions, *AIAA Conf. Paper* (New York), **72**, pp 1063
- [25] K. Mima, K. Yoshikawa, O. Moriyama, H. Takase, Y. Kitagawa, T. Tajima, Y. Kosaki and S. Nakai, Preliminary studies of direct energy conversion in a D-3He inertial confinement fusion reactor, *Fus. Tech.*, **22**, pp 56, 1992
- [26] H. Shoyama, H. Nakashima and Y. Kanda, Plasma energy recovery from a D-3He inertial confinement fusion reactor, *Fusion Engineering and Design*, **69**, pp 1250-1259, 1993

- [27] H. Nakashima, Masaya Takada and Y. Kanda, Plasma energy recovery by using pickup coil system from a D-3He inertial confinement fusion reactor, *Fusion Engineering and Design*, **15**, pp 225-262, 1992
- [28] Yu. P. Zakharov, A. V. Melekhov, V. G. Posukh and I. F. Shaikhislamov, Direct conversion of the energy of laser and fusion plasma clouds to electrical energy during expansion in a magnetic field, *J. Appl. Mech. and Tech. Phys.*, **42**, pp 185-195, 2001
- [29] Yu. P. Zakharov, A. M. Orishich, A. G. Ponomarenko and V. G. Posukh, Effectiveness of slowing of expanding clouds of diamagnetic plasma by magnetic field (experimental), *Fiz. Plazmy.*, **12**, pp 1170-1176, 1986
- [30] Yu. P. Zakharov, A. G. Ponomarenko and A. V. Melekhov, Plasma confinement and direct energy conversion of ICF-micro-explosion in open magnetic systems, *Trans. Fusion Technol.*, **35**, pp 283-287, 1999
- [31] T. Honda, Y. Nakao, Y. Honda, K. Kudo and H. Nakashima, Burn characteristics of inertially confined D-3He fuel, *Nuclear Fusion*, **31**, pp 851-865, (1991)
- [32] T. Shiba, H. Nakashima, Y. Yoshioka and K. Kanda, Burn characteristics of D-T ignited D-D and D-3He fuel pellets for inertial confinement fusion reactors, *Nuclear Fusion*, **28**, pp 699-705, (1991)
- [33] H. Nakashima, Y Inoue and Y. Kanda, Instability analysis of a magnetically protected cavity in a D-3He inertial confinement fusion reactor, *Fus. Tech.*, **22**, pp 73-81, 1992
- [34] M. Cowan, W. K. Tucker, D. L. Wesenberg and E. C. Snare 1975, Pulsar-A Field Compression Generator for Pulsed Power, *Proc. 6th Symp. Engineering*

- Problems of Fusion Research* (Sheraton Inn, San Diego, California), **1**, IEEE Pub. No. 75CH1097-5-NPS, pp 308
- [35] E. C. Snare, M. Cowan, T. P. Wright and W. K. Tucker 1977, Pulsed Power conversion with inductive storage, *Proc. 7th Symp. Engineering Problems of Fusion Research*, **2**, pp 1049
- [36] M. Cowan, E. C. Snare, W. K. Tucker and D. L. Wesenberg, Multimegajoule Pulsed Power Generation from a Reusable Compressed Magnetic field Device, in *Energy Storage, Compression and Switching*, W.H. Bostick, V. Nardi and O.S.F. Zucker, eds., Plenum, NY, pp 131, (1976)
- [37] T. P. Wright, L. Baker, M. Cowan and J.R. Freeman, Magnetic Flux Compression by Expanding Plasma Armatures, in *Magagauss Physics and Technology*, P.J. Turchi, ed., Plenum, NY, pp 241, (1980)
- [38] M. L. Wilkins 1999, *Computer Simulation of Dynamic Phenomena* (Springer-Verlag, Berlin)
- [39] R. P. Drake 2006, *High-Energy-Density Physics* (Springer-Verlag, Berlin)
- [40] D. Winske, Development of flute modes on expanding plasma clouds, *Phys. Fluids B*, **1**, 9, pp 1900, 1989
- [41] F. Winterberg, On the concept of Magnetic Insulation, *The Review of Scientific Instruments*, **43**, 5, pp 814, 1972
- [42] F. Winterberg, Magnetically Insulated Transformer for Attaining Ultrahigh Voltages, *The Review of Scientific Instruments*, **41**, 12, pp 1756, 1970
- [43] E. H. Hirsch, The concept of Magnetic Insulation, *The Review of Scientific Instruments*, **42**, pp 1371, 1971

- [44] B. M. Novac, I. R. Smith and J. Brown, Magnetically self-insulated transformers, *J. Phys. D: Appl. Phys.*, **35**, pp 1467, 2002
- [45] M. Istenic, B. M. Novac, J. Luo, R. Kumar and I. R. Smith, A 0.5 MV magnetically self-insulated pulsed transformer, *J. Phys. D: Appl. Phys.*, **39**, pp 4529, 2009
- [46] R. Hawley, The electrical properties of high vacuum, *High-Voltage Technology* (Edited by L. L. Alston, Oxford University Press, Oxford), pp 59-94, 1968
- [47] A. B. Hassam, J. D. Huba, Magnetohydrodynamic equations for systems with large Larmor radius, *Phys. Fluids*, **31**, 2, pp 318, 1988
- [48] J. D. Huba, J. G. Lyon and A. B. Hassam, Theory and simulation of the Rayleigh-Taylor instability in the limit of large Larmor Radius, *Phys. Rev. Lett.*, **59**, pp 2971, 1987
- [49] B. M. Novac and I. R. Smith, Advances in the filamentary modeling of electromagnetic flux compression, *Jap. J. Appl. Phys.*, **45**, pp 2807, 2006
- [50] B. M. Novac, I. R. Smith and M. Hubbard, 2-D modeling of electromagnetic flux compression in theta pinch geometry, *IEEE Trans. Plasma Sci.*, **32**, pp 1896, 2004
- [51] B. M. Novac and I. R. Smith, Numerical studies of electromagnetic flux compression in θ -pinch geometry, *Electromagnetic Phenomena*, **5**, pp 44-57, 2005
- [52] C.D. Sijoy and Shashank Chaturvedi, Conversion of plasma energy into electrical pulse by magnetic flux compression, *Fusion Eng. Des.*, **86**, pp. 174-182, (2011)

- [53] C.D. Sijoy and Shashank Chaturvedi, Finite difference time domain algorithm for electromagnetic problems involving material movement, *J. Comp. Phys.*, **228**, pp 2282-2295, (2009)
- [54] C. D. Sijoy and Shashank Chaturvedi, Calculation of Accurate Resistance and Inductance for Complex Magnetic Coils Using the Finite-Difference Time-Domain Technique for Electromagnetics, *IEEE. Trans. on Plasma. Sci.*, **36**, pp 70-79, (2008)
- [55] C. D. Sijoy and D. Sharma and S. Chaturvedi, Use of 3-D FDTD Method for Magnetic Field Diffusion Calculations in Complex Pinch Geometries, Presented at VIII Khariton Readings, RFNC-VNIIF, Russia, (2006)
- [56] C. D. Sijoy and S. Chaturvedi, Three-Dimensional Calculations of Electrical Parameters in Flux Compression Systems, *Int. Conf. on Megagauss Mag. Field Gen. and Rel. Topics*, USA (5-10 Nov, 2006)
- [57] John R. Freeman and Samuel L. Thompson, Numerical methods for studying compressed magnetic field generators, *J. Comp. Phys.*, **25**, pp 332-352, (1977)
- [58] P. Cornille, Numerical Study of a Cylindrical Plasma Expansion in a Magnetic field, *J. Comp. Phys.*, **14**, pp 371-390, (1974)
- [59] J. P. Boris and D. L. Book, Flux-corrected transport. I. SHASTA, a fluid transport algorithm that works, *J. Comp. Phys.*, **11**, pp 38-69, (1973)
- [60] C. D. Sijoy and Shashank Chaturvedi, Volume of fluid algorithm with different modified dynamic material-ordering methods and their comparisons, *J. Comp. Phys.*, **229**, pp 3848-3863, (2010)

- [61] G. H. Miller and E. G. Puckett, High-Order Godunov Method for Multiple Condensed Phases, *J. Comp. Phys.*, **128**, pp 134-164, (1996)
- [62] D. de Niem, E. Kuhrt and U. Motschmann, A volume-of-fluid method for simulation of compressible axisymmetric multi material flow, *Comp. Phys. Comm.*, **176**, pp 170-190, (2007)
- [63] D. J. Benson, Computational methods in Lagrangian and Eulerian hydrocodes, *Comput. Meth. Appl. Mech. Eng.*, **99**, pp 235-394, (1992)
- [64] B. Van Leer, Toward the ultimate conservative difference scheme. II. Monotonicity and conservation combined in a second-order scheme, *J. Comp. Phys.*, **14**, pp 361-370, (1974)
- [65] H. M. Antia, Numerical methods for scientists and engineers, Tata McGraw-Hill Publishing Company Limited, New Delhi, (1991)
- [66] C. W. Hirt and Nicholas B. D., Volume of Fluid (VOF) method for the dynamics of free boundaries, *J. Comp. Phys.*, **39**, pp 201-225, (1981)
- [67] W. J. Rider and D. B. Kothe, Reconstructing Volume tracking, *J. Comp. Phys.*, **141**, pp 112-152, (1998)
- [68] D. Gueyffier, J. Li, R. Scardovelli and S. Zaleski, Volume-of-Fluid interface tracking with smoothed surface stress methods for three-dimensional flow, *J. Comp. Phys.*, **152**, pp 423, (1999)
- [69] J. E. Pilliod and E. G. Puckett, Second-order accurate volume-of-fluid algorithms for tracking material interfaces, *J. Comp. Phys.*, **199**, pp 465, (2004)

- [70] E. Aulisa, S. Manservigi, R. Scardovelli and S. Zaleski, A geometrical area-preserving volume-of-fluid advection method, *J. Comp. Phys.*, **192**, pp 355, (2003)
- [71] D. J. Benson, Volume of fluid interface reconstruction methods for multi-material problems, *Appl. Mech. Rev.*, **55**, pp 151, (2002)
- [72] E. G. Puckett, A Volume-of-Fluid interface tracking algorithm with applications to computing shock wave refraction, Proceedings of the Fourth International Symposium on Computational Fluid dynamics, H. Dwyer (Ed.), Davis, CA, pp 933-938, (1991)
- [73] S. Mosso and S. Clancy, A geometrically derived priority system for Youngs interface reconstruction, Technical Report LA-CP-95-81, LANL, (1994)
- [74] D. J. Benson, Eulerian finite element methods for the micromechanics of the heterogeneous materials: Dynamic prioritization of material interfaces, *Comput. Meth. Appl. Mech. Eng.*, **151**, pp 343-360, (1998)
- [75] M. Holt, Numerical methods in fluid dynamics, Springer, Berlin, Heidelberg, New York, Tokyo, (1984)
- [76] L.I. Sedov, Similarity and Dimensional Methods in Mechanics, Academic Press, New York, (1959)
- [77] Aamer Haque, The Sedov Analytical Solution Program, <http://flash.uchicago.edu/~ahaque/sedov.html>
- [78] A. L. Cooper and D. L. Book, Magnetic flux compression in imploding liquid liners, *Phys. Fluids*, **21**, pp 34-41, (1978)

- [79] H. E. Wilhelm, Electromagnetic Induction in Accelerated Conductors, *Phys. Rev. E*, **25**, pp 2913-2922, (1982)
- [80] H. E. Wilhelm, Electromagnetic induction in accelerated conductors with frontal compression and rear dilution of magnetic flux, *J. Appl. Phys.*, **58**, pp 1285-1292, (1984)
- [81] H. E. Wilhelm, Electromagnetic induction in conductors Accelerated in Magnetic field Amplified by Flux Compression, *Appl. Phys. B*, **31**, pp 107-113, (1983)
- [82] C. D. Sijoy and Shashank Chaturvedi, An Eulerian MHD model for the analysis of magnetic flux compression by expanding diamagnetic fusion plasma sphere, *Fusion Eng. Des.*, **87**, pp. 104-117, (2012)
- [83] S. Chandrasekhar, Hydrodynamic and hydromagnetic stability, Oxford: Oxford Univ. Press, (1961)
- [84] H. Dickinson, W. H. Bostick, J. N. DiMarco and S. Koslov, Experimental study of Rayleigh-Taylor instability in plasma, *Phys. fluids.*, **5**, pp 1048-1056, (1962)
- [85] J. D. Huba, A. B. Hassam and D. Winske, Stability of sub-Alfvenic plasma expansions, *Phys. fluids B*, **2**, pp 1676-1697, (1990)
- [86] A. B. Hassam and J. D. Huba, Magnetohydrodynamic equations for systems with large Larmor radius, *Phys. fluids*, **31**, pp 318, (1988)
- [87] J. D. Huba, A. B. Hassam and P. Satyanarayana, Nonlocal theory of the Rayleigh-Taylor instability in the limit of unmagnetized ions, *Phys. fluids B*, **1**, pp 931, (1989)

- [88] B. H. Ripin, J. D. Huba, E. A. McLean, C. K. Manka, T. Peyser, H. R. Burris and J. Grun, Sub-Alfvenic plasma expansion, *Phys. fluids B*, **5**, pp 3491-3506, (1993)
- [89] S. Okada, K. Sato and T. Sekiguchi, Behaviour of Laser-Produced Plasma in a Uniform Magnetic Field—Plasma Instabilities, *Jpn. J. Appl. Phys.*, **20**, pp 157-165, (1981)
- [90] W. G. Pilipp, Expansion of an ion cloud in the earth's magnetic field, *Planet. Space Sci.*, **19**, pp 1095, (1971)
- [91] K. Akimoto, M. Galvez, S. P. Gray and D. Winske, Prompt structuring of a plasma expanding in an external magnetic field, *J. Geomag. Geoelectri.*, **40**, pp 1161-1191, (1988)
- [92] A. G. Sgro, S. P. Gray and D. S. Lemons, Expanding plasma structure and its evolution towards long wavelengths, *Phys. fluids B*, **1**, pp 1890-1899, (1989)
- [93] Byung-Il Jun, Michael L. Norman and J. M. Stone, A numerical study of Rayleigh-Taylor instability in magnetic fluids, *The Astrophysical J.*, **453**, pp 332-349, (1995)
- [94] G. L. Kalra and S. N. Kathuria, Nonlinear Rayleigh-Taylor instability in hydromagnetics, *J. Plasma Physics*, **15**, pp 239-244, (1976)
- [95] Bhimsen K. Shivamoggi, Rayleigh-Taylor instability of a plasma in a magnetic field: nonlinear theory, *J. Plasma Physics*, **27**, pp 129-134, (1982)
- [96] J. D. Huba and D. Winske, Rayleigh-Taylor instability: Comparison of hybrid and nonideal magnetohydrodynamic simulations, *Phys. Plasmas*, **5**, pp 2305-2316, (1998)

- [97] G. Dimonte and L. G. Wiley, Dynamics of exploding plasmas in a magnetic field, *Phys. Rev. Lett.*, **67**, pp 1755-1758, (1991)
- [98] E. J. Caramana, D. E. Burton, M. J. Shashkov and P. P. Whalen, The construction of compatible hydrodynamics algorithms utilizing conservation of total energy, *J. Comp. Phys.*, **146**, pp 227-262, (1998)
- [99] E. J. Caramana and M. J. Shashkov, Elimination of artificial grid distortion and hourglass-type motions by means of Lagrangian subzonal masses and pressures, *J. Comp. Phys.*, **142**, pp 521-561, (1998)
- [100] J. C. Campell and M. J. Shashkov, A tensor artificial viscosity using a mimetic finite difference algorithm, *J. Comp. Phys.*, **172**, pp 739-765, (2001)
- [101] D. L. Youngs, Numerical simulation of turbulent mixing by Rayleigh-Taylor instability, *Physica D: Nonlinear Phenomena*, **12**, pp 32-44, (1984); and references therein.
- [102] P. V. Subhash, S. Madhavan and Shashank Chaturvedi, Effect of liner non-uniformity on plasma instabilities in an inverse Z-pinch magnetized target fusion system: liner-on-plasma simulations and comparison with linear stability analysis, *Physics of Plasmas*, **77**, 035501, (2008)
- [103] W. H. Press, S. A. Teukolsky, W. T. Vetterling and B. P. Flannery, Numer. Recipes, pp 631, (1992)
- [104] M. R. Douglas, C. Deeney and N. F. Roderick, Computational investigation of single mode vs multimode Rayleigh-Taylor seeding in Z-pinch implosions, *Physics of Plasmas*, **5**, pp 4183, (1998)

- [105] Richard Holland, FDTD Analysis of Nonlinear Magnetic Diffusion by Reduced c , *IEEE Transactions on Antennas and Propagation*, **43**, pp 653-659, (1995)
- [106] R. Holland and L. Simpson and K. S. Kunz, Finite-Difference analysis of EMP coupling to lossy dielectric structures, *IEEE Trans. Electromagn. Compat.*, **22**, pp 203-209, (1980)
- [107] M. Jones, An Equivalent Circuit Model of a Solenoidal Compressed Magnetic Field Generator, *Proc. Megagauss II*, pp 249-264, (1978)
- [108] Glenn S. Smith, Proximity Effect in Systems of Parallel Conductors, *Journal of Applied Physics*, **43**, pp 2196-2203, (1972)
- [109] Arnold A.H.M, Proximity Effects in Solid and Hollow Round Conductors, *J. I. E. E.*, **88**, pp 349-359, (1941)
- [110] B. M. Novac, I. R. Smith, M. Enache and H. R. Stewardson, Simple 2D model for helical flux compression generators, *Laser and Particle Beams*, **15**, pp 379-395, (1997)
- [111] B. M. Novac, I. R. Smith and M. Hubbard, 2D modelling of electromagnetic flux-compression in θ -pinch geometry, *IEEE Trans. Plasma Science*, **32**, pp 1896-1901, (2004)
- [112] K.S. Kunz and R.J. Luebbers, The Finite Difference Time-Domain Method for Electromagnetics, CRC press, (1993)
- [113] Mur, G, Absorbing boundary conditions for the finite difference approximation of the time domain electromagnetic field equations, *IEEE. Transactions on Electromagnetic Compatibility*, **23**, pp 377, (1981)

- [114] K. S. Yee, Numerical Solutions of initial value problems involving Maxwell's equations in isotropic media, *IEEE Trans. on Antennas and Propagation*, **AP-14**, pp 302-307, (1966)
- [115] A. Taflove and K. Umashankar, Radar cross section of general three-dimensional scatterers, *IEEE Trans. Electromagn. Compatibility*, **25**, pp 433-440, (1983)
- [116] K. Shlager and J. Schneider, A selective survey of the finite-difference time-domain literature, *IEEE Trans. on Antennas and Propagation*, **37**, pp 39-57, (1995)
- [117] R. Luebbers and H. Hunsberger, FDTD for Nth-order dispersive media, *IEEE Trans. on Antennas and Propagation*, **40**, pp 1297-1301, (1992)
- [118] D. Sullivan and O. Gandhi and A. Taflove, Use of the finite-difference time-domain method for calculating EM absorption in man models, *IEEE Trans. Bioengineering*, **35**, pp 179, (1988)
- [119] R. J. Speigal and M.B.E. Fatmi and K.S. Kunz, Application of a finite-difference technique to the human radiofrequency dosimetry problem, *J. Microwave Power and Electromagnetic Energy*, **20**, pp 241-254, (1985)
- [120] Shahid Ahmed and Deepti Sharma and Shashank Chaturvedi, Modeling of an EMP simulator using a 3-D FDTD code, *IEEE Trans on Plasma Science*, **31**, pp 207-215, (2003)
- [121] Peter G. Petropoulos, Analysis of Exponential Time-Differencing for FDTD in lossy Dielectrics, *IEEE Trans. on Antennas and Propagation*, **45**, pp 1054-1057, (1997)

- [122] Allen Taflove and Susan C. Hagness, Computational Electrodynamics The Finite-Difference Time-Domain Method, Artech House, Norwood 3rd Ed., (2000)
- [123] H. J. Longley and C. L. Longmire, Development of the GLANC EMP code, Defence Nuclear Agency, DNA3221T, Dec, (1973)
- [124] Richard Holland, Finite-Difference Time-Domain (FDTD) Analysis of Magnetic Diffusion, *IEEE Transactions on Electromagnetic Compatibility*, **36**, No. 1, pp 32-39, (1994)
- [125] J. P. Boris, Flux-Corrected Transport Modules for Solving Generalized Continuity Equations, NRL Memorandum Report 3237, (1976)
- [126] J. P. Berenger, A perfectly matched layer for the absorption of electromagnetic waves, *J. Comput. Phys.*, **114**, pp. 185-200, (Oct. 1994)
- [127] D. S. Katz and E. T. Thiele and A. Taflove, Validation and extension to three dimensions of the berenger PML absorbing boundary condition for FDTD meshes, *IEEE Microwave Guided Wave Lett.*, **4**, pp 268-270, (Aug. 1994)
- [128] Moon Francis C, Magneto-solid Mechanics, Wiley Interscience Publication, John-Wiley, New York, (1984)
- [129] J. D. Jackson, Classical Electrodynamics, John Wiley and Sons Inc., New York, 3rd Ed., (1998)
- [130] A. Harten, High resolution schemes for hyperbolic conservation laws, *J. Comp. Phys.*, **49**, pp 357, (1983)

- [131] D. Ryu and F. Miniati and T. W. Jones and A. Frank, A Divergence-free Upwind Code for Multidimensional Magnetohydrodynamic Flows, *Astro. Phys. Journ.*, **509**, pp 244-255, (Dec. 1998)
- [132] Gabor Toth and Dusan Odstreil, Comparison of Some Flux Corrected Transport and Total Variation Diminishing Numerical Schemes for Hydrodynamic and Magnetohydrodynamic Problems, *J. Comp. Phys.*, **128**, pp 82-100, (1996)
- [133] J. M. Stone, A radiation magnetohydrodynamics code for astrophysical flows in two space dimensions. I - The hydrodynamic algorithms and tests, *The Astrophys. Journ. Supp. Series*, **80**, pp 791, (June 1992)
- [134] S. T. Zalesak, Fully multidimensional flux-corrected transport algorithms for fluids, *J. Comp. Phys.*, **31**, pp 335-362, (1979)
- [135] C. R. DeVore, Flux-corrected transport techniques for multidimensional compressible magnetohydrodynamics, *J. Comp. Phys.*, **110**, pp 310-319, (1994)
- [136] Marc Snir, MPI: The Complete Reference, Vol. 1, 2nd Ed, MIT Press, (1998)
- [137] R. J. Litchford and G. A. Robertson, Magnetic Flux Compression Reactor Concepts for Spacecraft Propulsion and Power, NASA Tech. Report, NASA/TP-2001-210793, (2001)
- [138] D. J. Benson, Volume of fluid interface reconstruction methods for multi-material problems, *Appl. Mech. Rev.*, **55**, 2, pp 151, (2002)
- [139] D. L. Youngs, Time dependent multi-material flow with large fluid distortions, Numerical methods for Fluid dynamics, K. W. Morton and M. J. Baines (eds), Academic Press, pp 273-285, (1982)

- [140] Keh-Ming Shyue, A wave-propagation based volume tracking method for compressible multicomponent flow in two space dimensions, *J. Comp. Phys.*, **215**, pp 219-244, (2006)
- [141] S.J. Sackett, EFFI: A code for calculating the electromagnetic field, force, and inductance in coil systems of arbitrary geometry, Lawrence Livermore National Lab, CA, ed., S.J. Sackett, (1978)